Imperial College London
Department of Materials

Understanding the Proton Transport in a Barium-Based Perovskite: From Incorporation to Dynamics

Chenyang Liao

Supervisors: Prof. Stephen Skinner (Imperial College London), Dr Miguel Angel Gonzalez (Institut Laue-Langevin), Dr Robert Leah (Ceres Ltd.)

Date of submission: 2025.10.29

This thesis is submitted in fulfilment of the requirements for the degree of Doctor of Philosophy (PhD), Imperial College London

Declaration of Originality

I hereby declare that this thesis is the result of my own work. All sources of information and any contributions from others have been appropriately acknowledged and referenced. An AI-based language editing tool (ChatGPT) was employed solely for the purpose of improving grammar and clarity. The research content, data, analysis, and conclusions presented in this thesis are entirely my own and have not been generated or altered by AI.

Copyright

The copyright of this thesis rests with the author. Unless otherwise indicated, its contents are licensed under a Creative Commons Attribution-Non Commercial 4.0 International Licence (CC BY-NC).Under this licence, you may copy and redistribute the material in any medium or format. You may also create and distribute modified versions of the work. This is on the condition that: you credit the author and do not use it, or any derivative works, for a commercial purpose. When reusing or sharing this work, ensure you make the licence terms clear to others by naming the licence and linking to the licence text. Where a work has been adapted, you should indicate that the work has been changed and describe those changes. Please seek permission from the copyright holder for uses of this work that are not included in this licence or permitted under UK Copyright Law.

Acknowledgement

Four years may sound like a long journey, yet the time has passed far more quickly than I could have imagined.

First and foremost, I would like to express my deepest gratitude to my supervisors, Stephen and Miguel, for their generosity in offering me the opportunity to pursue my own scientific interests. Over these four years, I have come to realise how rare and valuable such freedom is, particularly when accompanied by their unwavering support. I am especially grateful for the way they have shaped me as a scientist and an independent researcher. Instead of rushing to celebrate "good results," they constantly encouraged me to ask whether the data were rational, reproducible, and truly explainable. From them I learned to treat "bad results" with patience and "good results" with caution. The most common phrase I remember hearing from them, "Think a little bit more about this", has left me with a habit of critical thinking that I believe will benefit me for the rest of my life.

To my parents, no words can ever be strong enough to convey my gratitude for their love and support. Though they know little about academia, fuel cells, or hydrogen energy, they were always eager to listen to every detail of my PhD journey. I will never forget their comforting words during one of my lowest moments, when I felt my PhD had completely failed: "No matter what you achieve in the end, remember you will always have a home to return to."

The most important personal milestone of this period was meeting and marrying my wife, Yao, who began her PhD in the same year. She is the most positive and patient researcher I have ever met. Although every PhD comes with pressure and challenges, she faced them with remarkable resilience. Even though her research is in a different field, she has always been willing to listen to my presentations, ideas, and experimental sparks. I cannot imagine this journey without her, and I will always be thankful that we found each other.

I am also grateful to the EU Marie Curie programme for funding this PhD project. It was an exceptionally enriching scheme, offering countless "first-time" experiences: my first time living in France, my first exposure to neutron techniques, and my first formal training in essential skills such as scientific presentation. I would also like to thank Ceres Power for providing me with an internship, which offered valuable insights into the industrial applications of fuel cell technologies. This experience broadened my perspective and helped me connect scientific progress with market-driven needs.

I have been fortunate to receive support and guidance from many generous scientists

along the way. My thanks go to Andrey (XRD), Sarah (SIMS), Gwilherm (XPS), Mahmoud (SEM), and neutron experts Markus, Matthew, and Niina, among many others. They not only shared their expertise with patience and kindness but also showed me what it means to be a mentor to the next generation of researchers.

I feel lucky to have worked in two inspiring institutions: Imperial College London and the Institut Laue-Langevin, both provided me with wonderful colleagues and a vibrant scientific atmosphere. Many of the ideas that shaped this project were born from casual conversations with colleagues in these communities.

Finally, I would like to thank myself for persevering to the end. A PhD is often jokingly said to stand for "Permanent Head Damage," and indeed, it is never an easy journey. But here I am.

Abstract

Proton-conducting solid oxide fuel cells (PCFCs) are considered a promising next-generation energy conversion technology due to their high efficiency and compatibility with hydrogen as a clean fuel. Among the various candidate materials, the barium-based perovskite $BaZr_{0.1}Ce_{0.7}Y_{0.1}Yb_{0.1}O_{3-\delta}$ (BZCYYb1711) system has attracted significant attention because of its outstanding proton conductivity. However, despite extensive studies on its electrochemical performance, the fundamental origin of its exceptional conductivity has not been systematically investigated. This lack of mechanistic understanding hampers the rational design of improved PCFC materials.

In this thesis, a systematic multi-scale experimental strategy was developed to elucidate the mechanisms underpinning the outstanding performance of BZCYYb1711. The approach centred on assessing the impact of hydration annealing on proton dynamics, with particular emphasis on its relationship to crystal structure, chemical composition, proton incorporation, and both localised and long-range transport processes. Structural information was examined using X-ray diffraction (XRD), while the chemical composition was determined by inductively coupled plasma optical emission spectroscopy (ICP-OES) and energy-dispersive X-ray spectroscopy (EDS). Proton incorporation was quantified through thermogravimetric analysis (TGA) and neutron-based methods, including prompt gamma activation analysis (PGAA), providing direct measurements of mobile proton concentrations within the lattice. Transport dynamics across multiple timescales were further investigated using neutron Compton scattering (NCS), quasielastic neutron scattering (QENS), and electrochemical impedance spectroscopy (EIS). Together, this integrated methodology established a direct connection between proton concentration quantification, structural analysis, and proton dynamics spanning both localised and long-range regimes.

Based on the comparison of proton concentrations between the as-calcined sample (BZCYYb-cal) and the humid-annealed sample (BZCYYb-HA), it was discovered that the as-cacined BZCYYb1711 system possessed a significant amount of protons even without intentional humid treatment. This challenges the long-standing assumption in the PCFC field that existence of protons originates from deliberate humidification.

The EIS results of Pt-electrode BZCYYb symmetric cells reproduce a frequently reported yet insufficiently explained phenomenon: the measured total conductivity under humid (3 vol%) conditions is not significantly higher than that obtained under dry ($P_{H_2O} < 10^{-5}$ mbar) conditions. This observation appears counterintuitive, as humid environments are generally expected to promote proton incorporation, thereby increasing the overall conductivity. This phenomenon suggested the excellent conductivity of BZCYYb1711 was not majorly contributed by external humidity, though from QENS measurements it

showed that the humid annealing can facilitate the localised proton hopping. Beyond elucidating the mechanisms in BZCYYb1711, this thesis establishes a transferable framework for systematically investigating proton transport in other proton-conducting oxides. This approach not only deepens the fundamental understanding of proton conduction but also provides a rational basis for the development of next-generation PCFC electrolytes with enhanced performance.

Contents

List of Figures **10**

List of Tables **21**

1 Introduction **23**

2 Solid Oxide Fuel Cells State of the Art: From Oxide-ion Conducting to Proton Conducting Systems **25**

2.1 Growing Importance of Hydrogen Energy 25
2.2 Introduction of Fuel Cells 28
2.3 Oxide-ion Conducting and Proton Conducting Solid Oxide Fuel Cells 32
2.4 Review of Fuel Cells Performance 38
2.4.1 Bilayer Electrolyte Coatings for Stability and Conductivity 38
2.4.2 Effect of Sintering Aids on Processing and Performance 40
2.4.3 Electrolyte Geometry Optimisation (Micro-tubular Cells) 40

3 Research Gaps and Suitable Techniques **42**

3.1 Research Gaps of Current $BaZr_{0.1}Ce_{0.7}Y_{0.1}Yb_{0.1}O_{3-\delta}$ Studies 42
3.2 Suitable Techniques to Address Research Gaps 44

4 Material Synthesis and Sample Preparation **49**

4.1 Material Synthesis 49
4.2 Pellet Pressing 50

5 Characterisation Techniques **51**

5.1 Archimedes Density Measurement 51
5.2 Scanning Electron Microscopy 52
5.3 Energy Dispersive X-ray Spectroscopy 56
5.4 X-ray Diffraction 57
5.5 Inductively Coupled Plasma Optical Emission Spectroscopy 60
5.6 Thermogravimetric Analysis 61
5.7 Residual Gas Analysis 62
5.8 Fourier Transform Infrared Spectroscopy 63
5.9 Isotopic Exchange Secondary-ion Mass Spectrometry Depth Profiling 63
5.10 Prompt Gamma Rays Activation Analysis 68
5.11 Electrochemical Impedance Spectroscopy 70
5.12 Neutron Compton Scattering 74
5.13 Quasielastic Neutron Scattering (QENS) 80

6 Existence of Protons in As-calcined $BaZr_{0.1}Ce_{0.7}Y_{0.1}Yb_{0.1}O_{3-\delta}$ **85**

6.1 Crystal Structure and Composition Analysis 85

6.2 Indirect Probing of Incorporated Protons 95
6.3 Neutron Techniques to Measure Proton Concentrations 101
6.4 Summary 106

7 Effect of Humid Annealing on Proton Dynamics in $BaZr_{0.1}Ce_{0.7}Y_{0.1}Yb_{0.1}O_{3-\delta}$ 107
7.1 Effect of Humid Annealing on Localised Proton Dynamics 107
7.2 Effect of Humid Annealing on Total Conductivity 126
7.3 Summary 136

8 Effect of Partial Pressure of Oxygen on Proton Dynamics in $BaZr_{0.1}Ce_{0.7}Y_{0.1}Yb_{0.1}O_{3-\delta}$ 137
8.1 Effect of Partial Pressure of Oxygen on Total Conductivity 137
8.2 Effect of Partial Pressure of Oxygen on Localised Proton Hopping 137
8.3 Summary 143

9 Conclusions and Outlook 147
9.1 Conclusions 147
9.2 Outlook 149

References 151

List of Figures

Figure 2.1 Sources of global energy supply in 2024, reported by energy institute[11]. 25

Figure 2.2 Pathway of the damages caused by the usage of fossil fuels to the human health. Reproduced with permission from Elsevier, open access CC BY license[14]. 26

Figure 2.3 The increase of global energy consumption over past years[20]. Reproduced with permission from Elsevier, open access CC BY license. 28

Figure 2.4 Schematic of alkaline fuel cell (AFC). 29

Figure 2.5 Schematic of phosphoric acid fuel cell (PAFC). 29

Figure 2.6 Schematic of proton exchange membrane fuel cell (PEMFC). 30

Figure 2.7 Schematic of molten carbonate fuel cell (MCFC). 31

Figure 2.8 Schematic of solid oxide fuel cell (SOFC). 31

Figure 2.9 The temperature-dependent conductivity of yttrium-stabilised zirconia (YSZ), gadolinium-doped ceria (GDC) and lanthanum gallate-based systems (LSGM). Reproduced with permission from Springer Nature[38]. 33

Figure 2.10 Illustration of (a) Oxide-ion conducting SOFC and (b) proton conducting SOFC[43]. Reproduced with permission from Wiley, open access CC BY license. 35

Figure 2.11 Conductivity under wet (3 vol% H_2O) oxygen of BZCYYb1711, BZCY ($BaZr_{0.1}Ce_{0.7}Y_{0.2}O_{3-\delta}$), YSZ ($Y_{0.15}Zr_{0.85}O_{2-\delta}$) and GDC ($Gd_{0.1}Ce_{0.9}O_{2-\delta}$) from 400-750°C[8]. From [Yang, L., Wang, S., Blinn, K., Liu, M., Liu, Z., Cheng, Z., & Liu, M. (2009). Enhanced Sulfur and Coking Tolerance of a Mixed Ion Conductor for SOFCs: $BaZr_{0.1}Ce_{0.7}Y_{0.2-x}Yb_xO_{3-\delta}$. Science. https://doi.org/1174811]. Reprinted with permission from AAAS. 37

Figure 2.12 Chemical stability assessment of the bilayer electrolytes. (a) The XRD patterns of untreated BZCYYb1711 and BHYb-BZCYYb bilayer electrolytes after exposed in 100% CO_2 for 100 hours at 500°C. The SEM image of (b) untreated BZCYYb1711 and (c) the 110-BHYb after exposing to 100% CO_2 for 100 h at 500°C. (d) Raman spectra of untreated BZCYYb1711 and BHYb-BZCYYb bilayer electrolytes after exposing to 100% CO_2 for 100 hours at 500°C. (e) The normalised ASR (area specific resistance) over time of untreated BZCYYb1711 and BHYb-BZCYYb bilayer electrolytes with various thickness measured in 97% CO_2 with 3% H_2O at 500°C. (f) The XRD patterns of untreated BZCYYb1711 and BHYb-BZCYYb bilayer electrolytes after exposed in 97% CO_2 with 3% H_2O at 500°C for 1000 hours [59]. Reproduced with permission from American Chemical Society, open access CC-BY-NC-ND 4.0 license. 39

Figure 2.13 Schematic illustration of the production of micro tubular fuel cells with BZCYYb1711 as the electrolyte[67]. Reprinted from International Journal of Hydrogen Energy, Volume 44, Chen et al., Electrochemical properties of micro-tubular intermediate temperature solid oxide fuel cell with novel asymmetric structure based on $BaZr_{0.1}Ce_{0.7}Y_{0.1}Yb_{0.1}O_{3-\delta}$ proton conducting electrolyte, Pages 16887-16897, Copyright 2019, with permission from Elsevier. 41

Figure 3.1 Proton concentration derived from the increase of mass measured by TGA in the water uptake experiment under humid (0.02 atm H_2O) Ar, O_2 (3%) atmosphere, versus temperature[79]. Reprinted from Solid State Ionics, Volume 180, Ricote et al., Water vapour solubility and conductivity study of the proton conductor $BaCe_{0.9-x}Zr_xY_{0.1}O_{3-\delta}$, Pages 990-997, Copyright 2009, with permission from Elsevier. . . . 45

Figure 3.2 TGA curve for as-prepared $BaZr_{1-x}In_xO_{3-\delta}$, x = 0.50, taken at 1.5°C/min under an Ar gas flow saturated with water, square data represents heating cycle, while the circle data represents cooling cycle[80]. Reprinted from Solid State Ionics, Volume 177, Ahmed et al., Synthesis and structural characterisation of perovskite type proton conducting $BaZr_{1-x}In_xO_{3-\delta}$ ($0.0 \leq x \leq 0.75$), Pages 1395-1403, Copyright 2006, with permission from Elsevier. 46

Figure 3.3 The PGAA spectra of dry and saturated $BaPr_{0.9}Y_{0.1}O_{3-\delta}$ illustrates signal from (a) Y and Ba, and (b) H[90]. Reprinted from Journal of Applied Physics, Volume 97, Jones et al., Hydrogen content in doped and undoped $BaPrO_3$ and $BaCeO_3$ by cold neutron prompt-gamma activation analysis, Pages 114908, Copyright 2005, with permission of AIP Publishing. 47

Figure 5.1 The relationship between the backscattered electron coefficient and the atomic number of pure elements with constant incident electron energy of 20 keV[120]. Reproduced with permission from Springer Nature. 54

Figure 5.2 The relationship between the secondary electron coefficient and the atomic number of pure elements with constant incident electron energy of 5 keV[120]. Reproduced with permission from Springer Nature. 55

Figure 5.3 The schematic diagram illustrates the locations of inlens detector and normal SE detector, and the origins of different types of SE (SE_1, SE_2 and SE_3)[120]. Adapted and reproduced with permission from Springer Nature. 55

Figure 5.4 The relationship between the secondary electron coefficient and the energy of incident electrons on different metals[123]. Reproduced with permission from Wiley. 56

Figure 5.5 Schematic of Bragg diffraction. 58

Figure 5.6 The schematic of RGA set up. 63

Figure 5.7 The Schematic of Secondary Ion Mass Spectrometry. Reproduced with open access CC-BY 4.0 license[135]. 66

Figure 5.8 The instrument layout of TOF-SIMS 5 with the dual beam configuration. EF is the electron floodgun, R is the reflectron and D is the detector. Reproduced with open access CC-BY 4.0 license[135]. 67

Figure 5.9 The process of sample preparation for line scan analysis, where the sample is exchanged with deuterium. 68

Figure 5.10 The example of typical Nyquist plot with three separate processes (each process follows the resistor-capacitor parallel equivalent circuit model). 71

Figure 5.11 The illustration of ideal semicircle in Nyquist plot in theory (dashed line) and the measured deformed semicircle (solid line)[142]. Reprinted from Solid State Ionics, 180, Shoar Abouzari et al., “On the physical interpretation of constant phase elements”, 922-927, (2009), with permission from Elsevier. 73

Figure 5.12 The schematic of Vesuvio beamline[97]. Electron-volt neutron spectroscopy: beyond fundamental systems, Andreani et al., Advances in Physics, copyright at 2017, reprinted by permission of Informa UK Limited, trading as Taylor & Francis Group. 75

Figure 5.13 The example of NCS data and fit of recoil peaks from multiple elements: hydrogen (olive line and shaded area), carbon (red line and shaded area), nitrogen (blue line and shaded area), and aluminium from the sample container (grey line and shaded area). The top figure shows the data and fitting for backscattering, while the bottom figure shows the forward scattering results[146]. Reproduced with permission from American Chemical Society, open access CC-BY-NC-ND 4.0 license 77

Figure 5.14 The flow diagram illustrates the scheme of data fitting, connecting the measured ToF spectrum and the J(y) (Compton profile) which describes the NMD (nuclear momentum distribution) of targeted atom. 79

Figure 5.15 (a) The schematic example of neutron scattering spectrum contains elastic peak (grey), inelastic peak (blue) and quasielastic broadening peak (red), classified based on different change of energy transfer value. (b) The example plot of energy transfer ($\hbar\omega$) versus momentum transfer (q) of the $\delta - Bi_2O_3$ sample at 730°C[153]. (c) The schematic demonstrates that the total scattering signal can be classified into the coherent signal and the incoherent signal, where the coherent scattering contains the peak shape pattern in the q range, while the incoherent signal appears as a flat background. Reproduced with permission from American Chemical Society, open access CC-BY-NC-ND 4.0 license, copyright credit to 2025 Schwaighofer et al.[92] 82

Figure 6.1 The measured count rate of prepared Ba standard solutions with eight different known concentrations (Blue dots). The purple dot represents the measured barium concentration in dissolved BZCYYb-HA powder which was diluted to approximately 15 ppm concentration (details of diluting procedure are available in section 5.5), and the barium concentration was interpolated based on the linear relationship of prepared Ba standard solution. 86

Figure 6.2 The SEM-EDS result of dense BZCYYb-pellet sample. (a) The secondary electron image of a selected region for EDS mapping, and the EDS elemental mapping of (b) barium, (c) cerium, (d) yttrium, (e) ytterbium, (f) zirconium 88

Figure 6.3 XRD patterns of sintered BZCYYb pellet (green), BZCYYb-cal powders (yellow), and BZCYYb-HA powders (blue) measured at 25°C from 20° to 90°. Intensity of all XRD patterns was normalised in [0,1]. The red stick pattern represents the BZCYYb1711 tetragonal crystallography model reported by Hamze et al.[157]. All observable peaks in XRD patterns are indexed. The small inverse triangle marks out the additional peak which was only visible in the XRD pattern of BZCYYb-HA sample. 89

Figure 6.4 XRD patterns of BZCYYb-HA(blue) and the literature reported $BaCO_3$ (red) powders measured at 25°C from 20° to 90°. Intensity of both XRD patterns was normalised in [0,1]. The replotted $BaCO_3$ XRD pattern with the Pmcn symmetry was reported by Cai et al.[160]. 90

Figure 6.5 The FTIR spectra of BZCYYb-HA powder (blue) and BZCYYb-cal powder (orange). 90

Figure 6.6 The Rietveld refinement of BZCYYb-cal powder with I4/mcm tetragonal phase model. Same powder was measured under room temperature and the scan time per step were both 250 seconds per step, but with different scanning angle, (a) is the XRD pattern scan from 20° to 90° , and (b) is the XRD pattern scan from 20° to 135°. The statistical parameters of the refinements for pattern in (a) was $R_{wp} = 9.99\%$ and $\chi^2 = 2.53$, and in (b) was $R_{wp} = 9.74\%$ and $\chi^2 = 1.81$. 92

Figure 6.7 The Rietveld refinement of BZCYYb-HA XRD pattern with $BaCO_3$ phase. The BZCYYb-HA phase was refined by I4/mcm tetragonal space group reported by Hamze et al.[157], and the $BaCO_3$ phase was refined by the Pmcn orthorhombic space group reported by Cai et al.[160]. The statistical parameters of this Rietveld refinement were $R_{wp} = 9.73\%$ and $\chi^2 = 1.76$. 94

Figure 6.8 The illustration of the TGA set up with the drying tube. 96

Figure 6.9 The mass loss of BZCYYb-cal powders heated from 100°C to 700°C under argon atmosphere, the red curve in data corresponds to the measured temperature, and the blue and orange curves represent the mass change percentage of measured samples. Orange curve represents the mass loss of heated BZCYYb-cal sample without applying the drying tube, while the blue curve represents the mass loss with the set up containing the drying tube. 97

Figure 6.10 The mass loss of BZCYYb-cal powders heated from 100°C to 700°C under air (orange) and argon (blue) atmosphere with the application of drying tube. Two TGA measurements were applied on the same batch of BZCYYb-cal sample, and all experimental settings were kept the same (e.g. gas flow rate = 50 ml/min, heating rate = 10 K/min). 98

Figure 6.11 (a) The pressure of gas species with molar mass = 18 in the closed system containing BZCYYb-pellet at 67°C (blue) and 700°C (orange), and the pressure of gas species (molar mass = 18) of the empty quartz tube was measured at 700°C as the background reference (green). (b) The pressure of gas species with molar mass = 18 in the closed system containing BZCYYb-pellet at 67°C (blue) and 700°C (orange). The green curve represents the pressure of gas (mass = 18) measured when heated BZCYYb-pellet was cooled from 700°C to 67°C at 2°C/min cooling rate. One hour stabilisation period was applied before performing the RGA measurement 100

Figure 6.12 The mass loss of BZCYYb-cal (orange) and BZCYYb-HA (blue) powders heated from 100°C to 700°C under dry argon atmosphere with the application of drying tube. The gas flow rate was 50 ml/min, and the heating rate was 10 K/min 101

Figure 6.13 An energy spectrum measured by the PGAA technique with peak fitting and element labelling. The peak fitting includes the characteristic γ peaks of barium and hydrogen determined by the Hyperlab software. The normalised residual which was calculated based on Equation 6.12 is illustrated at the bottom to show the fitting quality. 103

Figure 6.14 The PGAA spectra of BZCYYb-cal and BZCYYb-HA powders at room temperature. (a) The PGAA spectrum includes peaks corresponding to ^{138}Ba, ^{92}Zr with the characteristic hydrogen (H) signal presented after subtraction of the background hydrogen contribution inherent to the PGAA setup. (b) The PGAA spetrum includes the peak corresponding to ^{140}Ce, two little humps besides the ^{140}Ce peak were due to the teflon packaging of powders. 105

Figure 7.1 The raw ToF spectrum of BZCYYb-HA measured by (a) backward detectors and (b) forward detectors. The NCS experiment was performed at room temperature and the BZCYYb-HA powders was sealed in the aluminium sample holder. 108

Figure 7.2 The fitting of BZCYYb backward scattering data. Recoil peaks of all elements except hydrogen were fitted based on the normalised 1D Gaussian function (Equation 5.50), and then all fitted recoil peaks were convoluted and converted back to the ToF domain to form the final fit (Grey line). 108

Figure 7.3 The hydrogen peak in the ToF spectra of BZCYYb-cal sample at room temperature fitted (a) without masking the ToF range locating absorption resonance peaks, (b) with masking the ToF range locating absorption resonance peaks. And the corresponding Compton profile J(y) of hydrogen fitted (c) without masking the ToF range locating absorption resonance peaks with reduced chi-squared value = 0.47, (d) with masking the ToF range locating absorption resonance peaks with reduced chi-squared value = 0.53. All fittings were performed based on the normalised 1D Gaussian function shown in Equation 5.50. 110

Figure 7.4 The NCS spectrum consists of the fitted recoil peaks of atomic species in (a) BZCYYb-cal based on normalised 1D Gaussian model and (b) BZCYYb-HA based on anisotropic Gaussian model at room temperature. The Al recoil peak comes from the aluminium sample container provided by Vesuvio beamline. 112

Figure 7.5 Timescale and length scale of different neutron spectroscopy techniques[181].114

Figure 7.6 The illustration of the QENS spectra broadening of BZCYYb-HA powders measured at RT, 310°C, 370°C and 450°C in IN16b beamline (ILL, France). The indicating lines demonstrate the focused energy transfer value of elastic fixed window scan (EFWS) at 0 meV and inelastic fixed window scan (IFWS) at 0.002 meV. 115

Figure 7.7 (a) The elastic fixed window scan (EFWS) of BZCYYb-HA sample from 50°C to 450°C. (b) The inelastic fixed window scan (IFWS) at energy transfer ($\hbar\omega$) = 0.002 meV of BZCYYb-HA sample from 50°C to 450°C. Both FWS experiments were performed at the IN16b beamline, ILL, France. 115

Figure 7.8 The calculation of the attenuation coefficients based on Palmann Ping's method[182] via the *PaalmanPingsMonteCarloAbsorption* algorithm in MANTID software[183, 184]: (a) the attenuation coefficient of container from container itself (A_C^C) (b) the attenuation coefficient of container from container itself and the sample (A_{S+C}^C), (c) the attenuation coefficient of container from the sample from itself and the container(A_{S+C}^S). 118

Figure 7.9 (a) Room temperature QENS spectra of BZCYYb-cal (green) and empty quartz container (red) at q = 0.59 $Å^{-1}$ in IN16b beamline, ILL, France. (b) The integration of the room temperature QENS spectra of BZCYYb-cal and empty quartz container over all energy channels. 119

Figure 7.10 (a) The example of the QENS spectra of empty quartz container measured at 25°C, 300°C and 600°C at q = 0.83 $Å^{-1}$ measured in IN16b beamline (ILL, France). (b) The linear fitting between the ratio of the integration to the whole energy transfer range ($\hbar\omega = \pm 0.03$ meV) at each measured temperature to the integration value at 25°C at q = 0.83 $Å^{-1}$ of measured empty quartz container in IN16b beamline (ILL, France). (c) The linear fitting between the ratio of the integration to the whole energy transfer range ($\hbar\omega = \pm 0.03$ meV) at each measured temperature to the integration value at 25°C at q = 0.94 $Å^{-1}$ of measured empty quartz container in IN16b beamline (ILL, France). 120

Figure 7.11 (a) The integration of vanadium QENS spectrum in the elastic energy tranfer range ($\hbar\omega = \pm 0.002$ meV) at different q values. (b) The integration of the normalised vanadium QENS spectrum after the division by the integration of raw vanadium QENS spectrum in the elastic energy tranfer range ($\hbar\omega = \pm 0.002$ meV), this result proves the correct normalisation of detectors' efficiencies. 121

Figure 7.12 The example of QENS spectra of BZCYYb-HA powders and vanadium standard at q = 0.59, both experiments were measured at room temperature in IN16b beamline(ILL, France). 122

Figure 7.13 The neutron diffraction pattern of BZCYYb-cal sample with normalised intensity [0,1] measured at RT in XTREMED beamline (ILL, France), the wavelength of the incident neutron was 2.45 Å. The q-range of IN16b beamline is outlined by red dashed line. . . . 124

Figure 7.14 (a) The fit of the QENS spectrum of BZCYYb-HA sample measured at 310°C in IN16b (ILL, France) using a flat background, a delta function for the elastic term and a Lorentzian function for the quasielastic term which both are convoluted with the resolution function. (b) The fit of the QENS spectrum of BZCYYb-cal sample measured at 310°C using a flat background, a delta function for the elastic term and a Lorentzian function for the quasielastic term which both are convoluted with the resolution function. (c) The HWHM of the BZCYYb-HA sample measured at 310°C in IN16b (ILL, France) fitted with the Chudley-Elliot jump diffusion model, the reduced χ^2 value is 1.458. (d) The HWHM of the BZCYYb-HA sample measured at 310°C in IN16b (ILL, France) fitted with the Hall and Ross jump diffusion model, the the reduced χ^2 value is 1.682. (e) The HWHM of the BZCYYb-cal sample measured at 310°C in IN16b (ILL, France) fitted with the Chudley-Elliot jump diffusion model, the reduced χ^2 value is 1.708. (f) The HWHM of the BZCYYb-cal sample measured at 310°C in IN16b (ILL, France) fitted with the Hall and Ross jump diffusion model, the the reduced χ^2 value is 2.213. 125

Figure 7.15 The effect of selected measured frequency on the data validity tested by Lin-KK tool. The BZCYYb-cal symmetric cell with Pt electrodes was measured at 150°C under dry compressed air condition. (a) The Nyquist plot of EIS data measured from 1 MHz to 1 Hz. (b) The Nyquist plot of EIS data measured from 3 Mhz to 1 Hz. (c) The residual, representing the difference of measured and calculated real and imaginary part of impedance, of data measured from 1 MHz to 1 Hz. (d) The residual, representing the difference of measured and calculated real and imaginary part of impedance, of data measured from 3 MHz to 1 Hz. 129

Figure 7.16 The fitted EIS data of BZCYYb-cal symmetric cell measured under dried (passed through drying tube) compressed air from 1 MHz to 1 Hz at (a) 426°C, (b) 166°C with chi-squared value of fitting $= 4.4 \times 10^{-5}$ and (c) 118°C with chi-squared value of fitting $= 1.6 \times 10^{-5}$. The measured temperatures were probed by the thermocouple positioned close to the measured symmetric cell. 130

Figure 7.17 The total conductivity of BZCYYb symmetric cells coated with Pt electrodes measured under humid air (3 vol% H_2O) and dry air ($pH_2O \approx 10^{-5}$ mbar) condition from temperature range 517°C to 95°C. 131

Figure 7.18 (a) SIMS mass spectrum of the exchanged BZCYYb pellet and the unexchanged pristine reference. (b) 2D SIMS image of the cross-sectional side of exchanged BZCYYb sample. In the 2D scanning, the SIMS technique measured the intensity of m/z = 2.014 signal along each point with (x,y) position, and the blue arrows illustrate the X and Y directions. 132

Figure 7.19 (a) The fitted isotopic diffusion profile measured in BZCYYb pellet exchanged in $pD_2O = 22$ torr environment for 25 minutes at 260°C. The inset image shows the normalised isotopic fraction depth profile from the surface of the exchanged pellet. The fitted $D^* = 4.35(3) \times 10^{-8}\ cm^2s^{-1}$, fitted $k = 4.48(2) \times 10^{-7}\ cms^{-1}$, the R^2 value of the fitting is 0.99. (b) The fitted isotopic diffusion profile measured in BZCYYb pellet exchanged in $pD_2O = 22$ torr environment for 25 minutes at 320°C. The inset image shows the normalised isotopic fraction depth profile from the surface of the exchanged pellet. The fitted $D^* = 1.21(4) \times 10^{-7}\ cm^2s^{-1}$, fitted $k = 1.41(2) \times 10^{-8}\ cms^{-1}$, the R^2 value of the fitting is 0.99. The green dashed line represents the natural abundance of deuterium. 134

Figure 8.1 The comparison of total conductivities of Pt-coated BZCYYb pellet measured under humid (3vol% H_2O) air and humid (3vol% H_2O) hydrogen mixed gas (5%H_2/95%N_2) conditions from 517°C to 95°C. 138

Figure 8.2 The fitted HWHM (half width half maximum) versus q (change of momentum) of BZCYYb-HH measured at 310°C based on the Chudley-Elliot model[187]. The fitted constant jump length is 3.0(2) Å, fitted relaxation time of hopping is 652(43) ps, and the fitted diffusion coefficient is $2.3(4) \times 10^{-7}$ cm^2s^{-1}. The reduced chi-squared value of the fitting is 1.927. 138

Figure 8.3 (a) The fitted diffusion coefficients of BZCYYb-HA (annealed in humid air) sample measured by QENS at IN16b (ILL, France) at 310°C, 370°C and 450°C. The R^2 value of the linear relationship is 0.99, and the fitted activation energy is 0.46 eV. (b) The fitted diffusion coefficients of BZCYYb-HH (annealed in humid hydrogen) sample measured by QENS at IN16b (ILL, France) at 310°C, 370°C and 450°C. The R^2 value of the linear relationship is 0.98, and the fitted activation energy is 0.61 eV. 140

Figure 8.4 (a) QENS spectra of empty quartz container and BZCYYb-HH sample with q (change of momentum) = 0.9 measured at room temperature. (b) QENS spectra of empty quartz container and BZCYYb-HH sample with q (change of momentum) = 0.9 measured at 450°C. 142

Figure 8.5 The fitted HWHM (half width half maximum) versus q (change of momentum) of BZCYYb-HA sample based on Chudley-Elliot model measured by BASIS beamline at (a) 370°C and reduced chi-squared is 1.405, (b) at 450°C and reduced chi-squared is 2.889, (c) at 550°C, the red box highlights fitted HWHM which equal to the energy tranfer range of BASIS beamline (± 200 μeV), indicating the failure of fitted QENS broadening, thus the HWHM fitted results cannot be fitted by Chudley-Elliot model at this temperature. 144

Figure 8.6 The fitted HWHM (half width half maximum) versus q (change of momentum) of BZCYYb-HH sample based on Chudley-Elliot model measured by BASIS beamline at (a) 370°C and reduced chi-squared is 1.575, (b) at 450°C and reduced chi-squared is 2.483, (c) at 550°C and reduced chi-squared is 1.794, (d) at 650°C, the red box highlights fitted HWHM which equal to the energy tranfer range of BASIS beamline (± 200 μeV), indicating the failure of fitted QENS broadening, thus the HWHM fitted results cannot be fitted by Chudley-Elliot model at this temperature. 145

List of Tables

Table 5.1 Mass and natural abundance of hydrogen isotopes 64

Table 5.2 Bound scattering cross section of elements in the BZCYYb1711 system.[154] 83

Table 6.1 Measured concentrations from the diluted dissolved BZCYYb solutions and their corresponding molar ratio to measured barium in ICP-OES experiments. 86

Table 6.2 The stoichiometry of BZCYYb-pellet measured by EDS. 88

Table 6.3 The refined lattice parameters, barium positions and its anisotropic thermal parameters of BZCYYb diffraction pattern with different 2θ ranges, the reported refined parameters in literature are included as a reference. 93

Table 6.4 Refined UVWXY parameters based on the Rietveld refinement of standard LaB_6 sample. 93

Table 6.5 Refined unit cell parameters and phase fractions of BZCYYb-HA, BZCYYb-cal phases and $BaCO_3$ phase. 94

Table 6.6 The molar ratio calculated from the peak area of selected species in room temperature PGAA measurement. 105

Table 7.1 The fitted intensity of recoil peaks of atoms in BZCYYb-cal samples except hydrogen measured in backward scattering at room temperature (298K). The aluminium signal was originated from the sample holder, and its recoil peak width was well calibrated at 298K, hence the error value of fitted peak width of aluminium is zero. 109

Table 7.2 The fitted width and intensity of the H recoil peak in BZCYYb-cal and BZCYYb-HA samples at room temperature. 111

Table 7.3 The fitted jump diffusion length (l), mean residence time (tau) and corresponding calculated diffusion coefficient ($D = \frac{l^2}{6\tau}$) of BZCYYb-cal and BZCYYb-HA QENS results with Chudley-Elliot (CE) jump diffusion model and Hall and Ross (HR) jump diffusion model. The * represents the root mean square average jump diffusion length fitted based on HR model as shown in Equation 7.22 126

Table 7.4 Capacitance values and their possible interpretation of electrochemical process[193]. 128

Table 8.1 Fitted constant jump length and relaxation time based on the Chudley-Elliot model from BZCYYb-HA (annealed in humid air) and BZCYYb-HH (annealed in humid hydrogen mixed gas $5\%H_2/95\%N_2$) QENS results, which were measured at IN16b (ILL, France) at different temperatures. 139

Table 8.2 Fitted diffusion coefficients based on the Chudley-Elliot model between BZCYYb-HA samples measured at BASIS (BZCYYb-HA-BASIS) and at IN16b (BZCYYb-HA-IN16b) at 370°C and 450°C. . 143
Table 8.3 Fitted diffusion coefficients based on the Chudley-Elliot model between BZCYYb-HH samples measured at BASIS (BZCYYb-HH-BASIS) and at IN16b (BZCYYb-HH-IN16b) at 370°C, 450°C and 550°C. 143

Chapter 1: Introduction

The transition towards sustainable energy has accelerated the search for technologies that combine high efficiency with low environmental impact. Hydrogen is widely recognised as a central component of this transition due to its abundance, clean utilisation, and potential for integration with renewable energy systems[1, 2]. Fuel cells are central to the hydrogen economy, converting chemical energy directly into electricity through electrochemical reactions, and offering significant advantages over combustion-based technologies[3].

Among the various types of fuel cells, solid oxide fuel cells (SOFCs) are particularly attractive owing to their high efficiency, long-term stability, and ability to operate with a wide range of fuels[4]. However, conventional oxygen-ion conducting SOFCs typically operate above 800°C, where degradation of materials, high system costs, and slow thermal cycling remain major challenges[5]. Lowering the operating temperature into the intermediate regime of 400-700°C is therefore a major objective of recent research.

A promising route towards intermediate-temperature operation is the development of proton-conducting solid oxide fuel cells (PCFCs). In these systems, charge transport is achieved by protons migrating through the electrolyte lattice, which enables lower activation energies and efficient conduction at reduced temperatures[6]. Beyond improved efficiency and durability, PCFCs allow greater flexibility in electrode selection, enhancing overall device performance.

Considerable attention has focused on perovskite oxides of the general formula ABO_3. Barium cerate based compounds displayed high proton conductivity but poor chemical stability, while barium zirconate was chemically robust yet exhibited lower conductivity and poor sinterability[7]. To address these limitations, the co-doped system with four elements (Zr, Ce, Y, Yb) at the B-site of perovskite structure was developed with composition $BaZr_{0.1}Ce_{0.7}Y_{0.1}Yb_{0.1}O_{3-\delta}$ (BZCYYb1711). This system combined the advantages of both parent materials and was regarded as one of the highest conductivity materials, thus was studied as one of the most promising electrolytes for PCFCs[8].

The importance of understanding proton behaviour in this material has led to extensive studies of its structural, electrochemical, and transport properties[9, 10]. However, the reason for excellent performance of this BZCYYb1711 system is missing, and further systematic characterisation remains essential for optimising the protonic conductivity and for establishing the fundamental principles that underpin the outstanding performance.

Despite the progress made in developing proton-conducting oxides, many questions

remain concerning the fundamental mechanisms that govern their performance. While conductivity measurements confirm that BZCYYb1711 is a promising electrolyte, they provide only limited insight into how protons are incorporated into the system and how they migrate at the atomic scale. The degree of intrinsic proton uptake under dry conditions, the influence of hydration, and the microscopic dynamics of proton transport are still not fully understood. Addressing these questions is crucial for clarifying the mechanisms of proton conduction and for strengthening the scientific foundation of proton-conducting fuel cells.

The motivation for this research is therefore to move beyond the reported outstanding performance and to probe proton behaviour in BZCYYb1711 at multiple levels, from incorporation to dynamics. By systematically combining structural analysis, electrochemical measurements, and neutron scattering techniques, this thesis seeks to provide a coherent understanding of how protons are accommodated and transported in this material. Establishing such a mechanistic picture is essential not only for optimising BZCYYb1711 itself but also for guiding the development of future generations of proton-conducting oxides.

Chapter 2: Solid Oxide Fuel Cells State of the Art: From Oxide-ion Conducting to Proton Conducting Systems

2.1 Growing Importance of Hydrogen Energy

Fossil fuels unequivocally continue to supply the vast majority of global primary energy. As reported by energy institute, fossil fuels still contributed 86% of the global energy supply in 2024, indicating a significant reliance on coal, oil, and natural gas[11]. As illustrated in Figure 2.1, Despite a growing contribution of other energy sources (e.g. renewable energies and nuclear energy), the proportion of energy of non-fossil origin remains comparatively minor.

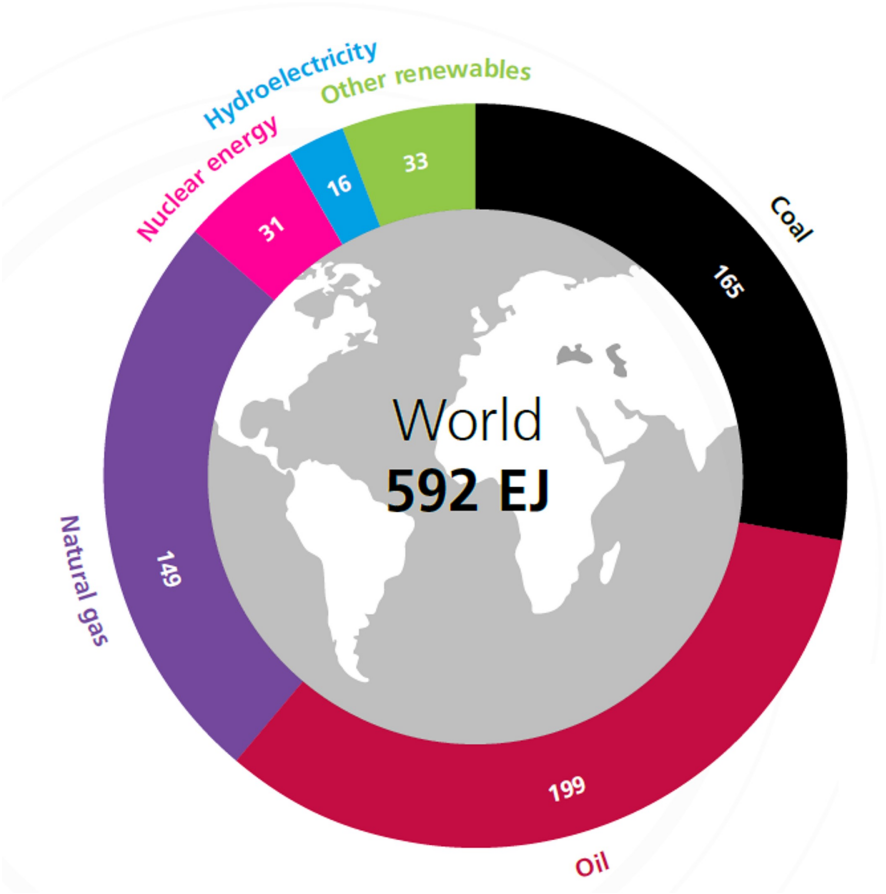


Figure 2.1: Sources of global energy supply in 2024, reported by energy institute[11].

Though the reliance on the combustion of fossil fuels is still heavy, it is vital to alleviate the reliance on their usage, as it exerts profound and multifaceted harm on the human health and the environment. Their extraction and utilisation are significant contributors

to global pollution and represent a major factor in the global burden of disease such as increasing respiratory problems and cancers. Emissions from fossil fuel combustion are responsible for approximately 8.7 million premature deaths annually worldwide[12]. Compared to the adults, the pollutions are particularly damaging to children. For example, from the study reported by Perera, pollutants can impair the cognitive and behavioral development of children, and affect their future well-being[13]. A more recent study reported by Zhang et al. summarised the pathway of the damages caused by the usage of fossil fuels to the health as shown in Figure 2.2[14].This figure highlights that pollution exerts a multi-stage impact on children's health. Beyond the direct consequences, such as diseases and the impaired neurodevelopment, pollution also contributes to secondary effects including learning difficulties and withdrawn personality. These indirect outcomes can severely hinder children's growth and limit their ability to adapt the society.

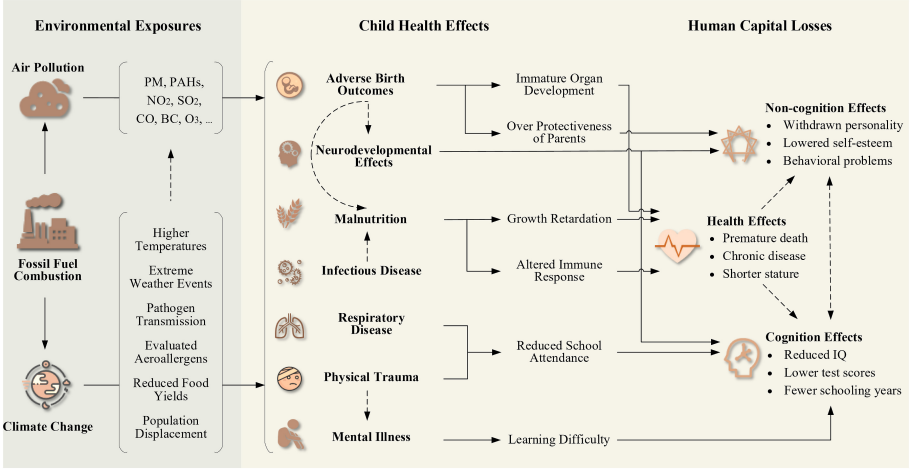


Figure 2.2: Pathway of the damages caused by the usage of fossil fuels to the human health. Reproduced with permission from Elsevier, open access CC BY license[14].

Apart from the harm on human health, the combustion of fossil fuels also significantly degrades environmental systems through a suite of mechanisms. Emissions of sulfur dioxide and nitrogen oxides lead to acid rain, damaging soils and aquatic ecosystems via acidification and nutrient overloading [15]. Moreover, the coal combustion emits hazardous heavy metals, including mercury, arsenic, and lead, which can enter food webs and groundwater systems, with long-term ecological consequences. The global warming caused by the emission from fossil fuel applications also becomes an increasingly severe problem to the environment: As reported by Pietrafesa et al., the rate of increasing temperature rose from 0.07°C/decade over the previous 100 years to the 0.18°C over the last 25 years[16].

Fossil fuels are non-renewable resources formed over millions of years from the remains of ancient plants and organisms. Their formation process is too slow to be replenished within a human timescale[17]. Holechek et al. suggested that coal, oil, and natural gas are nonrenewable and projected to be severely depleted within approximately 50 years if

current consumption levels persist[18].

Based on the concerns on human health, environment and resource sustainability mentioned above, pursuing a type of energy which is clean and renewable becomes key for the development of human society. Taking advantage on its low-carbon-emission nature, the application of hydrogen energy stands out as a more promising alternative to the combustion of fossil fuels. The high gravimetric energy density of hydrogen is also a huge advantage compared with the fossil fuels, as the energy density of hydrogen is approximately 120 MJ/kg, which is nearlly three times greater than that of gasoline ($\approx$ 46 MJ/kg)[19].

Figure 2.3 reported by Visvanathan et al. demonstrates the growth of the global energy consumption[20], reflecting the close link between rapid societal development and the escalating demand for energy. This increasing demand underscores the necessity of maximising efficiency in electricity generation. More recently, the proliferation of artificial intelligence (AI) technologies has further intensified electricity consumption, driven by the energy requirements of large-scale data centres and computationally demanding models such as GPT. In this context, technologies capable of converting energy into electricity with high efficiency have become particularly critical. Hydrogen fuel cells represent a promising solution, offering a highly efficient and clean alternative to conventional fossil fuel-based power generation. Unlike combustion engines, which are limited by the Carnot cycle and subject to significant thermodynamic losses, fuel cells convert hydrogen directly into electricity through electrochemical reactions[21]. In addition, hydrogen fuel cells operate emission-free at the point of use, producing only water vapour, and can function as both reliable backup and primary power sources for AI infrastructure. Taken together, these attributes position hydrogen fuel cells as a sustainable and efficient technology well-suited to meeting the rising energy demands associated with modern societal development and emerging technologies such as AI.

The global transition towards sustainable energy systems has placed hydrogen, particularly green hydrogen produced from renewable energy sources, at the forefront of energy policy and innovation. As nations strive to meet their climate goals and reduce dependence on fossil fuels, hydrogen energy has emerged as a critical enabler of decarbonization across various sectors, including industry, transportation, and power generation. The demand for green hydrogen is driven by its potential to provide a clean, versatile, and scalable energy solution, capable of addressing the dual challenges of energy security and environmental sustainability. This demand is further amplified by the ambitious policy frameworks and strategic initiatives adopted by many countries[22].

In summary, hydrogen energy is a promising solution to the problems caused by the combustion of fossil fuels in the concern of human society and environment. Meanwhile, fuel cell technologies, based on their ability to convert chemical energy from fuels (e.g. hy-

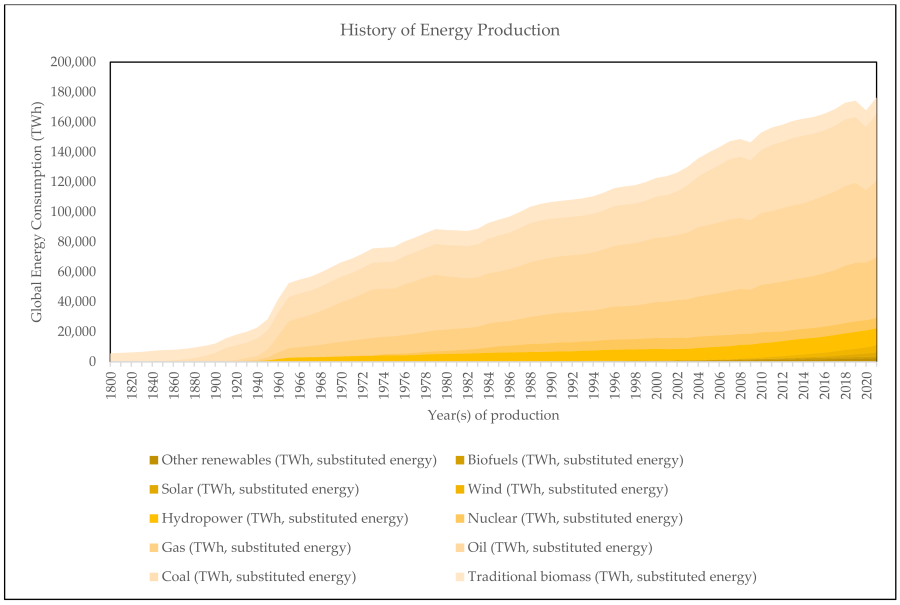


Figure 2.3: The increase of global energy consumption over past years[20]. Reproduced with permission from Elsevier, open access CC BY license.

drogen) to electricity, play an important role in the application sector of hydrogen energy market.

2.2 Introduction of Fuel Cells

A fuel cell is an electrochemical energy conversion device that directly transforms chemical energy from a fuel (commonly hydrogen) and an oxidant (typically oxygen) into electricity, heat, and water. Structurally, a fuel cell comprises three principal parts: an anode, an electrolyte, and a cathode[23].

The concept of the fuel cell dates back to 1839, when Welsh scientist Sir William Grove first demonstrated the principle of generating electricity through the electrochemical reaction between hydrogen and oxygen, which was regarded as the earliest practical example demonstrating the working principle of fuel cell technology. However, the first commercial application was not available until the development of first fully-operational fuel cell by Francis Thomas Bacon in 1959, and this fuel cell product was used by NASA in the 1960s in the Gemini and Apollo space programs[23].

Up to now, with the continuous developement of fuel cell technologies, based on different operating temperatures, efficiency, application, choice of fuels, type of conducting species and the electrolyte materials, fuel cells can be classified into six main groups: alkaline fuel cell (AFC), phosphoric acid fuel cell (PAFC), molten carbonate fuel cell (MCFC), proton exchange membrane fuel cell (PEMFC), and solid oxide fuel cell (SOFC).

The typical electrolyte used in an alkaline fuel cell (AFC) is potassium hydroxide (KOH) in water based solution. Figure 2.4 outlines the schematic of AFC. Hydroxyl ions generated by the reduction reaction at the cathode travel to the anode, where the oxidation reaction occurs[24]. AFC is regarded as the low-temperature fuel cell, the general operating temperature of AFC system is between 60°C to 90°C. The other advantage of AFC system is its low-cost catalyst, typically nickel. The lifetime of the AFCs is long as generally they can lasts over 5000 hours; howoever, this system suffers from the carbon poisoning problem[25]. The small amount of carbon dioxide (CO_2) can react with the KOH solution electrolyte to form carbonate salts, which reduce the conductivity and lead to the cell degradation, thus the required purity of input fuel and oxygen leads to extra operating costs. Moreover, the liquid phase of the electrolyte can increase the management and operational costs.

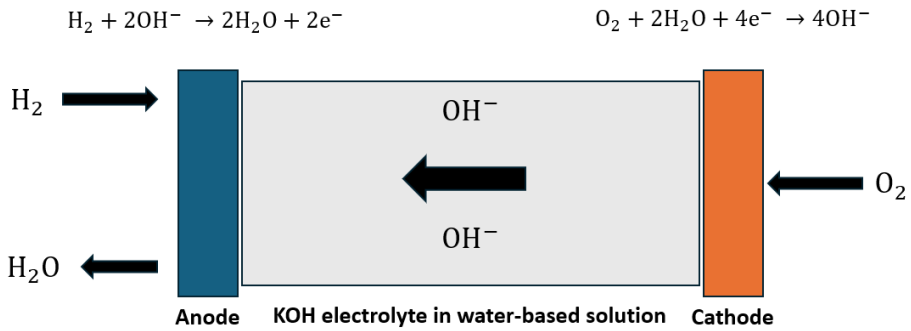


Figure 2.4: Schematic of alkaline fuel cell (AFC).

Similar to the AFCs, the phosphoric acid fuel cell (PAFC) system has a liquid phase electrolyte which is normally phosphoric acid (H_3PO_4). However, as shown in Figure 2.5, the conducting species is different, as the protons travel from the anode to the cathode. The operating temperature of PAFC is slightly higher than AFC, where the PAFC functions in the range of 150-220°C. The PAFC holds its advantage on its resistance to carbon dioxide, as CO_2 does not react with the electrolyte, but it suffers from the carbon poisoning problem on its platinum catalyst[26].

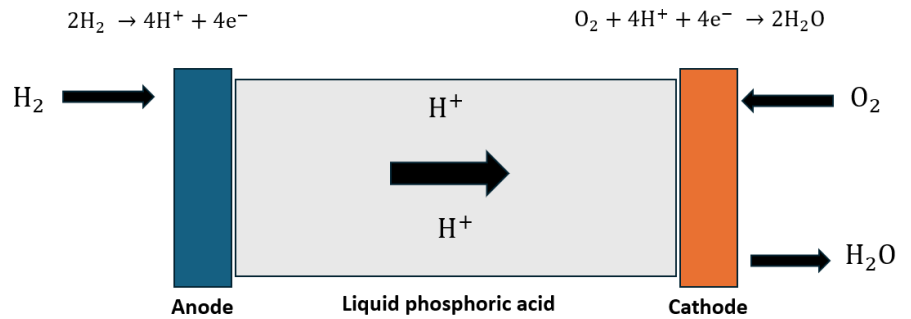


Figure 2.5: Schematic of phosphoric acid fuel cell (PAFC).

Proton exchange membrane fuel cells (PEMFC) are another system which has protons as the conducting species in the electrolyte, and the oxidation and reduction reactions occurring at anode and cathode are similar to PAFC (Figure 2.6). Unlike the other two low-operating-temperature fuel cells mentioned above, PEMFC has a polymer electrolyte instead of the liquid phase. One of the most popular PEMFC electrolytes is the Perfluorosulfonic Acid (PFSA) membrane (e.g. Nafion developed by Dupont). PEMFCs are known by their low operating temperatures ($\leq$80°C), which shorten the required start-up time and makes them suitable for rapid power delivery applications. However, PFSA membrane faces the limitation of the operating temperature, as its conductivity drops quickly when the humidity of the membrane is removed in higher operating temperature[27][28]. Additionally, the mechanical property and the stability of PFSA membranes will degrade at temperature $\geq$ 80°C, due to their relative low glass transition temperatures (80-120°C)[29].

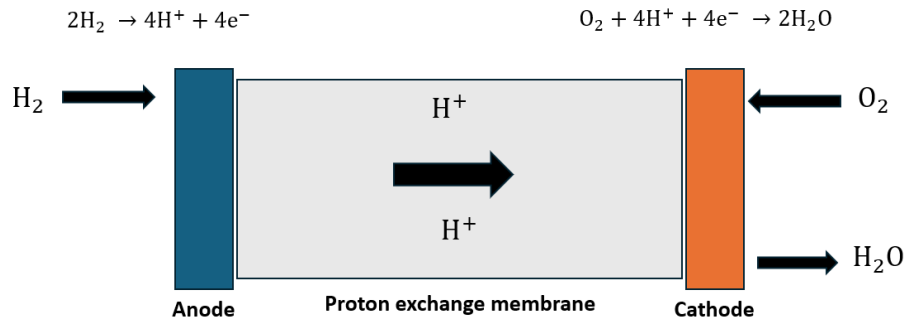


Figure 2.6: Schematic of proton exchange membrane fuel cell (PEMFC).

Despite the fuel cell systems operating at relatively low temperature, there are also some types of fuel cell which operates at much higher temperatures. Molten carbonate fuel cell (MCFC) holds much higher operation temperature (600-700°C). The transport species in the MCFCs electrolyte are the carbonate ions, which lead to the uniqueness of the involvement of carbon-related species (e.g. methane, carbon monoxide and carbon dioxide). The advantage of MCFC system is that it does not require external "reforming system" to convert fuels into hydrogen, which is demonstrated in the anode reforming reactions (Equation 2.1-2.2): At the anode side of MCFCs, the fed methane (CH_4) and water react to form hydrogen, carbon monoxide (CO) and carbon dioxide (CO_2)[30]. As shown in Fig 2.7, the CO_2 is one of the reactants at the cathode side, which makes the MCFCs ideal to play a role in capturing carbon dioxide species e.g. separating the CO_2 from a stream of supplied gas. Nevertheless, the MCFC system suffers from the limited durability due to the degradation at high temperatures and the possible evaporation of its liquid-phase electrolyte[31]

$$CH_4 + H_2O \rightarrow CO + 3H_2 \tag{2.1}$$

$$CO + H_2O \rightarrow CO_2 + H_2 \tag{2.2}$$

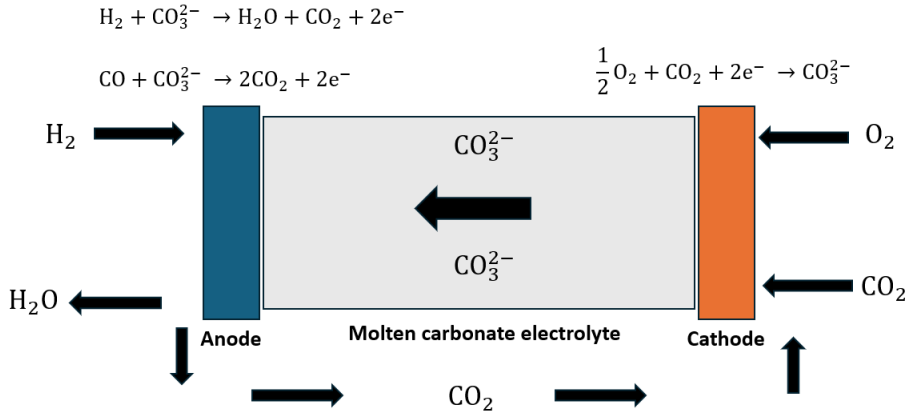


Figure 2.7: Schematic of molten carbonate fuel cell (MCFC).

While low-temperature fuel cells, such as alkaline fuel cells (AFCs), proton-exchange membrane fuel cells (PEMFCs), and phosphoric acid fuel cells (PAFCs), have demonstrated potential for various applications, their widespread adoption is hindered by challenges such as carbon poisoning and the inefficient usage of the exhaust heat generated during operation. Similarly, high-temperature fuel cells, such as molten carbonate fuel cells (MCFCs), though capable of operating at elevated temperatures, face their own set of limitations, including the cost risen from the management of input CO_2 gas and the handling of liquid-phase molten carbonate electrolytes. In this context, solid oxide fuel cells (SOFCs) emerge as a promising route of the hydrogen application, offering distinct advantages that address these limitations associated with both low and high-temperature fuel cell technologies.

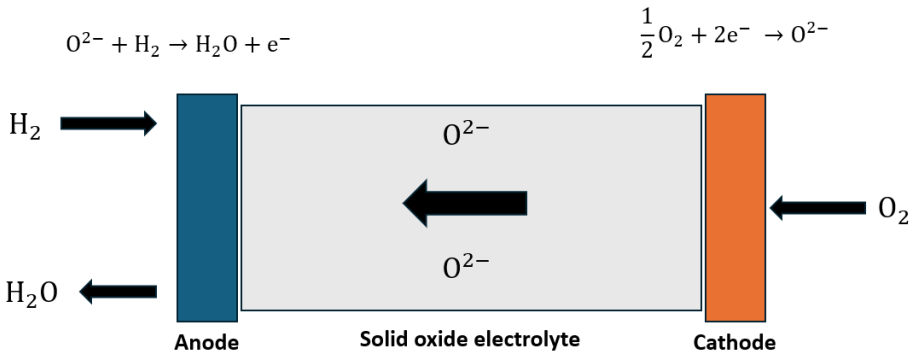


Figure 2.8: Schematic of solid oxide fuel cell (SOFC).

Figure 2.8 illustrates the layout of SOFCs. A key distinction of SOFCs lies in their solid-state oxide electrolyte, which eliminates the need for liquid-phase electrolyte management and the associated corrosion and containment issues. Moreover, the ceramic oxide nature of the electrolyte enables stable operation at high temperatures (typically 600-1000 °C). This elevated temperature provides several important advantages. First, it enables

significant fuel flexibility, allowing operation on a wide range of fuels, from pure hydrogen to hydrocarbons such as natural gas[4]. At high temperatures, internal reforming reactions can occur directly within the cell, reducing reliance on external reformers. Furthermore, carbon poisoning of catalysts (e.g., CO poisoning of Pt)[32] is thermodynamically less severe at elevated temperatures. As a result, SOFC systems can lower operational costs by reducing dependence on high-purity hydrogen, which remains expensive due to storage and transportation challenges[33]. In addition, the high operating temperature enables effective utilisation of exhaust heat in combined heat and power (CHP) systems, thereby improving overall system efficiency.

However, this high operating temperature also constitutes one of the principal disadvantages of SOFC technology. Elevated temperatures accelerate material degradation, impose stringent requirements on interconnects and sealing materials, and increase start-up time and system cost. Consequently, although the capability of operating in high-temperature regime provides SOFC multiple advantages, it simultaneously introduces challenges in durability, mechanical stability, and long-term reliability.

2.3 Oxide-ion Conducting and Proton Conducting Solid Oxide Fuel Cells

The development of oxide-ion conducting solid oxide fuel cells (O-SOFCs) has a long and significant history, originating from fundamental materials discoveries in the late 19th and early 20th centuries. In 1899, Walther Nernst invented a solid electrolyte material composed of 85 mol% ZrO_2 and 15 mol% Y_2O_3 named as yttria-stabilised zirconia (YSZ), and this invention laid the foundational understanding for ionic conduction in ceramics and formed the conceptual basis for SOFC electrolytes[34]. Subsequently, in 1937, Bauer and Preis demonstrated the first SOFC prototype employing the YSZ material, confirming the feasibility of using YSZ as an oxide-ion conducting electrolyte[35]. This was followed by more fundamental studies on the YSZ system, for example, Carl Wagner's pioneering work in 1943 linked the high ionic conductivity in doped zirconia to the formation and migration of oxygen vacancies, which further validated the suitability of YSZ for SOFC operation[36].

Driven by these early discoveries, a cathode-supported tubular SOFC design was developed and tested by scientists at Westinghouse Electric Corporation, which solidified the role of YSZ as the standard electrolyte material. YSZ exhibits excellent chemical and mechanical stability under both oxidising and reducing atmospheres and maintains compatibility with common electrode materials. However, its practical use is limited by the need for high operating temperatures (typically 800-1000°C), where the high temperature serves to reduce the ohmic resistance of the electrolyte and improve the performance[37]. Nevertheless, such elevated temperatures introduce significant engineering challenges, including increased thermal management requirements, expensive insulation, accelerated

material degradation, and slow system start-up times, which are undesirable for daily applications.

To improve the intermediate-temperature operation (500-700°C), alternative oxide-ion conductors with higher conductivity were subsequently developed. Gadolinium-doped ceria (GDC), retaining the fluorite framework, exhibits substantially enhanced oxygen vacancy mobility and achieves ionic conductivities one to two orders of magnitude higher than YSZ within this temperature range. Similarly, lanthanum gallate-based perovskites (LSGM) have demonstrated even higher oxide-ion conductivity owing to their favourable defect chemistry and lower activation energy for vacancy migration. These materials significantly improve electrolyte performance at intermediate temperatures, as illustrated in Figure 2.9[38].

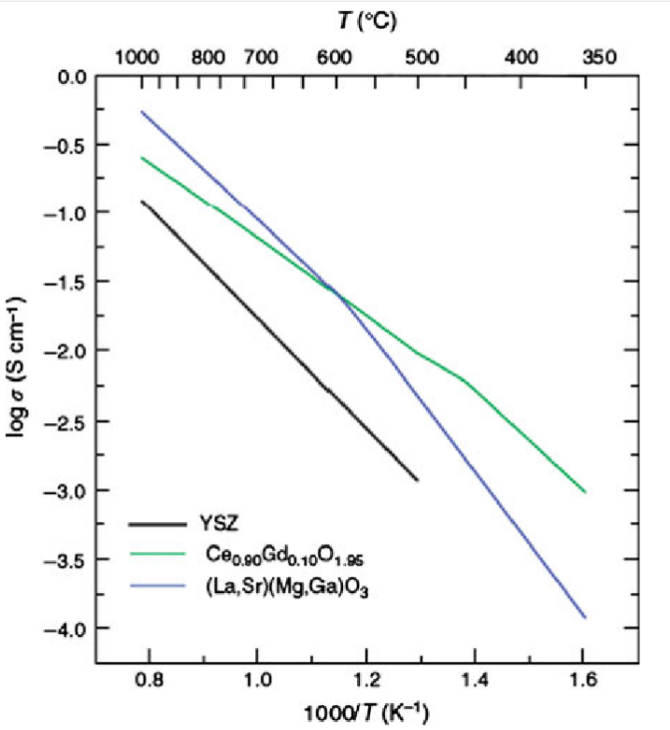


Figure 2.9: The temperature-dependent conductivity of yttrium-stabilised zirconia (YSZ), gadolinium-doped ceria (GDC) and lanthanum gallate-based systems (LSGM). Reproduced with permission from Springer Nature[38].

Despite these advances, both GDC and LSGM electrolytes present inherent limitations. GDC system may undergo partial reduction under low oxygen partial pressure, leading to electronic leakage and reduced open-circuit voltage[39], while LSGM can suffer from chemical incompatibility with common electrode materials (e.g. nickel-containing anode) and challenges associated with long-term stability[40]. These constraints have motivated the exploration of alternative structural frameworks capable of supporting faster or fundamentally different oxide-ion transport mechanisms.

In recent years, attention has shifted towards novel oxide-ion conductors beyond the classical fluorite and perovskite families. Notably, hexagonal perovskite-related oxides in the Ba-Nb-Mo system, such as $Ba_7Nb_4MoO_{20}$, have emerged as promising candidates for intermediate-temperature applications[41]. $Ba_7Nb_4MoO_{20}$ exhibit highly disordered oxygen sublattices and complex polyhedral connectivity, which facilitate rapid oxide-ion diffusion through non-conventional pathways distinct from simple vacancy migration[41]. The oxide-ion conduction mechanism was proposed by Schwaighofer et al. via computational route, suggesting that the out-of-plane oxygen mobility affect more in oxide-ion conductivity of $Ba_7Nb_4MoO_{20}$[42].

Nevertheless, despite its unconventional transport mechanism and structural novelty, the reported oxide-ion conductivity of $Ba_7Nb_4MoO_{20}$ at 600°C remains on the order of 10^{-3} S cm^{-1}, comparable to that of GDC under similar conditions. This observation suggests that even structurally innovative oxide-ion conductors may approach practical limits in achievable conductivity within the intermediate-temperature regime. Consequently, the exploration of alternative conduction mechanisms, particularly proton conduction, has gained research interests as a direction to further reduce operating temperatures without compromising performance.

In response to the limitations associated with high operating temperature required by O-SOFCs, proton-conducting solid oxide fuel cells (PCFCs) have emerged as a promising alternative for intermediate-temperature operation. Figure 2.10 schematically compares the working principles of O-SOFCs and PCFCs[43]. Unlike conventional O-SOFCs that rely on oxide-ion conduction, PCFCs conduct protons (H^+) under humidified conditions. This change in the mobile charge carrier underpins the lower operating temperatures achievable in PCFCs, since proton transport typically exhibits activation energies of 0.3-0.6 eV, compared with 0.6-1.2 eV for oxide-ion conduction[44, 45].

PCFCs possess another advantage in fuel management arising from the opposite migration direction of the charge carriers: In O-SOFCs, oxide ions migrate from the cathode to the anode and react with hydrogen to produce hydration. This water formation inevitably dilutes the fuel stream, lowering the effective partial pressure of fuels and thereby compromising the efficiency of operation. In contrast, in PCFCs, protons are transported from the anode to the cathode, where they react with oxygen to form water. As a result, water is generated exclusively at the cathode side, leaving the anode environment undiluted. This spatial separation of water formation preserves the hydrogen concentration at the anode, improves overall fuel utilisation efficiency, and reduces performance losses associated with fuel dilution, thereby offering operational benefits for high-performance energy conversion.

The first discovery of the proton conduction in strontium cerate ($SrCeO_{3-\delta}$) perovskite

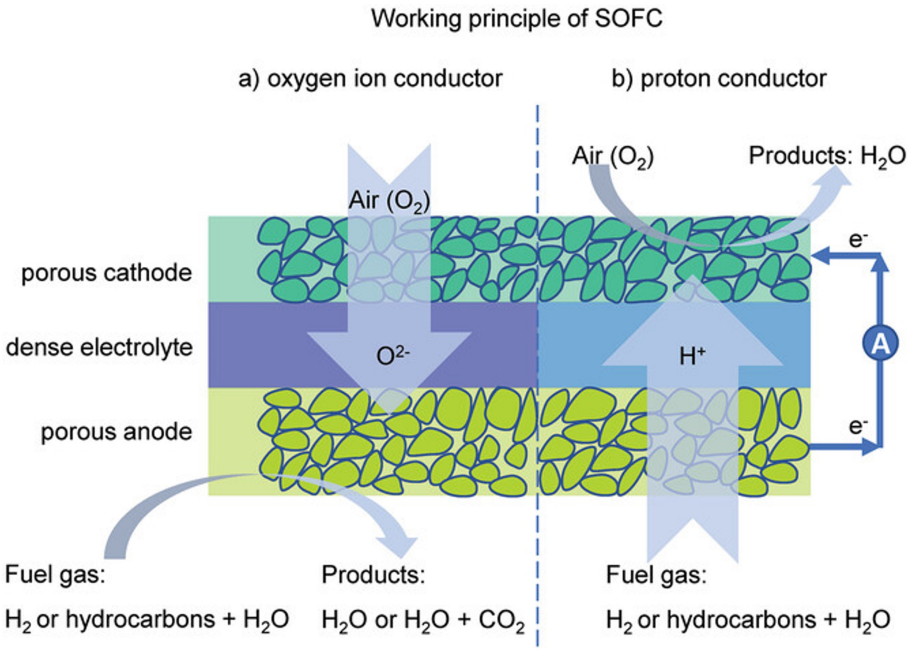


Figure 2.10: Illustration of (a) Oxide-ion conducting SOFC and (b) proton conducting SOFC[43]. Reproduced with permission from Wiley, open access CC BY license.

by Iwahara et al.[46] opened the field of research in protonic ceramics. Since then, a variety of crystal structures have been investigated as candidate electrolytes for PCFC applications, including simple perovskites with the ABO_3 structure, layered perovskites with the $A_{n+1}B_nO_{3n+1}$ Ruddlesden-Popper (RP) structure and Brownmillerites ($A_2B_2O_5$)[47]. Each of these structural families offers distinct features affecting the stability, defect chemistry, and conduction mechanism. For instance, RP phases exhibit pronounced structural flexibility owing to their inherently layered architecture, comprising alternating perovskite slabs and rock-salt layers, which allows compositional and stacking variations not available in simple perovskites[48]. Brownmillerites feature ordered oxygen-vacancy channels, which are embodied by alternating octahedral and tetrahedral layers and providing well-defined pathways facilitating proton incorporation and diffusion[49]. Among these structures, ABO_3 simple perovskite structure generally possesses the highest conductivity attributed to their large crystallographic volume that minimises lattice distortion and facilitates ion transport[50]. This superior performance of materials with the simple ABO_3 structure makes it one of the most promising structures for the development of practical PCFC electrolytes.

Among the ABO_3 perovskite family, barium cerate ($BaCeO_3$) was among the earliest compositions to be recognised for its high proton conductivity and therefore attracted significant attention as a potential PCFC electrolyte[51]. Building on this foundation, by the late 1980s Iwahara et al.[52] reported yttrium-doped barium cerate (BCY), which rapidly established itself as a benchmark material owing to its high protonic conductivity combined with a relatively low sintering temperature. These characteristics not only

facilitated its fabrication into dense electrolyte but also positioned BCY as a leading composition for early PCFC development[52]. Around the same period, Glockner et al. carried out computational studies to identify suitable B-site dopants for $BaCeO_3$, demonstrating that trivalent cations such as yttrium, gadolinium, and ytterbium possess favourable solution energies on the cerium site. This provided a theoretical basis for the effectiveness of yttrium substitution, rationalising the structural stability of BCY. Despite these advantages, however, barium cerate systems exhibit limited chemical stability, as they tend to become thermodynamically unstable in humid and CO_2-containing atmospheres. This susceptibility to degradation, often leading to the formation of barium carbonate and structural decomposition, significantly hinders their long-term durability and thereby constrains their practical application as PCFC electrolytes[53, 54].

Similar to the $BaCeO_3$, barium zirconate was studied as a proton conducting electrolyte candidate[55]. In contrast to BCY, yttrium-doped barium zirconate (BZY), in which zirconium occupies the B-site of the perovskite structure, was well known for its markedly superior chemical stability compared with barium cerate systems[56]. Nevertheless, the application of BZY has been hindered by its limited total conductivity. Although BZY exhibits excellent bulk protonic conductivity, its overall performance is significantly compromised by the presence of high grain boundary resistance, which reduces the effective total conductivity to values markedly lower than those of BCY[57]. This high grain boundary resistance of BZY is compounded by its poor sinterability as BZY requires exceptionally high sintering temperatures to achieve densification. The resulting low density and fine-grained microstructure intensify grain boundary resistance, thereby further limiting its practical application as a PCFC electrolyte[58].

To overcome the respective limitations of BZY and BCY in a complementary manner, considerable efforts have been devoted to developing solid solutions of barium cerate and barium zirconate. Among these, yttrium-doped barium zirconium cerate (BZCY) has attracted particular attention, as it aims to combine the high proton conductivity of cerates with the superior chemical stability of zirconates. A systematic study by Katahira et al.[56] demonstrated that increasing the cerium content enhances both conductivity and sinterability, whereas increasing the zirconium content improves chemical stability at the expense of electrochemical performance. By carefully tuning the cerium-to-zirconium ratio, the composition $BaZr_{0.1}Ce_{0.7}Y_{0.2}O_{3-\delta}$ (BZCY172) was identified as a stable proton-conducting electrolyte that offers an acceptable balance between conductivity and durability.[56].

In 2009, Yang et al. discovered a new composition $BaZr_{0.1}Ce_{0.7}Y_{0.1}Yb_{0.1}O_{3-\delta}$ (BZCYYb1711), which represented a significant breakthrough in the development of barium-based perovskite electrolytes for PCFCs[8, 50]. Figure 2.11 demonstrates that BZCYYb1711 system has approximately one order of magnitude higher conductivity than BZCY172

and substantially higher conductivity than conventional O-SOFC materials (e.g. YSZ and GDC). This enhancement was achieved by partially substituting ytterbium for yttrium in BZCY172, a modification that not only boosted protonic conductivity but also improved chemical stability in environments containing carbon and sulfur species[8]. However, subsequent studies have challenged the initially claimed chemical stability of BZCYYb1711, demonstrating that this composition is particularly vulnerable in CO_2-rich environments, where it readily decomposes to form barium carbonate[59, 60]. To address this limitation, Choi et al. proposed a modified stoichiometry with composition $BaZr_{0.4}Ce_{0.4}Y_{0.1}Yb_{0.1}O_{3-\delta}$ (BZCYYb4411)[61]. By increasing the Zr content relative to Ce, the material exhibited enhanced tolerance to CO_2 and therefore improved chemical stability, though this came at the expense of slight reduced proton conductivity, for example, Guo et al. reported that at 600°C under humid (3 vol%) H_2 condition, the total conductivity of BZCYYb1711 system was 0.016 Scm^{-1} and BZCYYb4411 was 0.009 Scm^{-1}[62]. Among the reported BZCYYb-based systems, the BZCYYb4411 composition shows improved chemical stability but at the expense of proton conductivity. Given that the central objective of this work is to study the proton transport mechanisms rather than chemical robustness, subsequent discussions focus on the BZCYYb1711 composition.

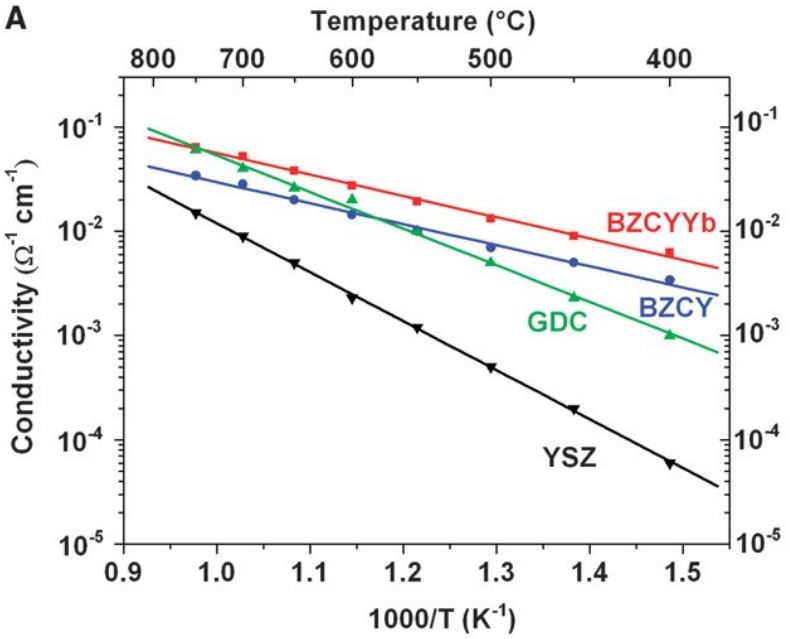


Figure 2.11: Conductivity under wet (3 vol% H_2O) oxygen of BZCYYb1711, BZCY ($BaZr_{0.1}Ce_{0.7}Y_{0.2}O_{3-\delta}$), YSZ ($Y_{0.15}Zr_{0.85}O_{2-\delta}$) and GDC ($Gd_{0.1}Ce_{0.9}O_{2-\delta}$) from 400-750°C[8]. From [Yang, L., Wang, S., Blinn, K., Liu, M., Liu, Z., Cheng, Z., & Liu, M. (2009). Enhanced Sulfur and Coking Tolerance of a Mixed Ion Conductor for SOFCs: $BaZr_{0.1}Ce_{0.7}Y_{0.2-x}Yb_xO_{3-\delta}$. Science. https://doi.org/1174811]. Reprinted with permission from AAAS.

2.4 Review of Fuel Cells Performance

Since its introduction, BZCYYb1711 has attracted considerable attention as one of the most promising proton-conducting electrolytes for intermediate-temperature protonic ceramic fuel cells (PCFCs). Its appeal derives from the combination of relatively high proton conductivity at 500-700°C and enhanced chemical stability. However, like most complex perovskite oxides, its practical deployment requires simultaneous optimisation of conductivity, chemical stability, electrode compatibility, and fabrication feasibility. Over the past decade, researchers have pursued multiple strategies to address these challenges. In the following sections, key approaches to performance enhancement are reviewed, including bilayer coatings, sintering aids techniques, and micro-tubular geometries.

2.4.1 Bilayer Electrolyte Coatings for Stability and Conductivity

One of the main drawbacks of Ce-rich electrolytes such as BZCYYb1711 is their vulnerability to chemical degradation under CO_2 and H_2O-rich environments, where the possible formation of $BaCO_3$ occurs. To mitigate this, Kane et al. introduced a bilayer electrolyte design in which a thin, dense layer of $BaHf_{0.8}Yb_{0.2}O_{3-\delta}$ (BHYb82) was deposited onto a BZCYYb1711 substrate. The rationale behind this architecture was to exploit the exceptional CO tolerance of Hf-based perovskites, while maintaining the superior bulk proton conductivity of the underlying BZCYYb1711[59].

By comparing the XRD patterns shown in Figure 2.12 (a) and Raman spectra illustrated in Figure 2.12 (d), it is evident that the protective BHYb layer functioned effectively, as the barium carbonate phase and signal were only observed in the untreated BZCYYb1711 sample after exposure to 100% CO_2 for 100 hours at 500°C. Similarly, the XRD patterns in Figure 2.12 (f) confirm that the BHYb protective layer also remains effective under humid conditions. The SEM images illustrated that the untreated BZCYYb1711 surface was completely covered by $BaCO_3$ (Figure 2.12 (b)), while the protected BZCYYb1711 surface only exhibited minor $BaCO_3$ formation (Figure 2.12 (c)). The protective effect was further validated by electrochemical measurements: as illustrated in Figure 2.12 (e), the untreated BZCYYb1711 exhibited a pronounced increase in area-specific resistance (ASR), indicating degradation in a humid (3% H_2O, 97% CO_2) atmosphere at 500°C. Importantly, impedance spectroscopy results demonstrated that the addition of the BHYb82 layer did not significantly compromise the high performance of the BZCYYb1711 electrolyte, with the total ASR of the bilayer structure remaining below 0.25 Ωcm^2 at 600°C. These findings suggest that the bilayer strategy effectively enhances the chemical stability of BZCYYb1711 while preserving its excellent electrochemical performance.

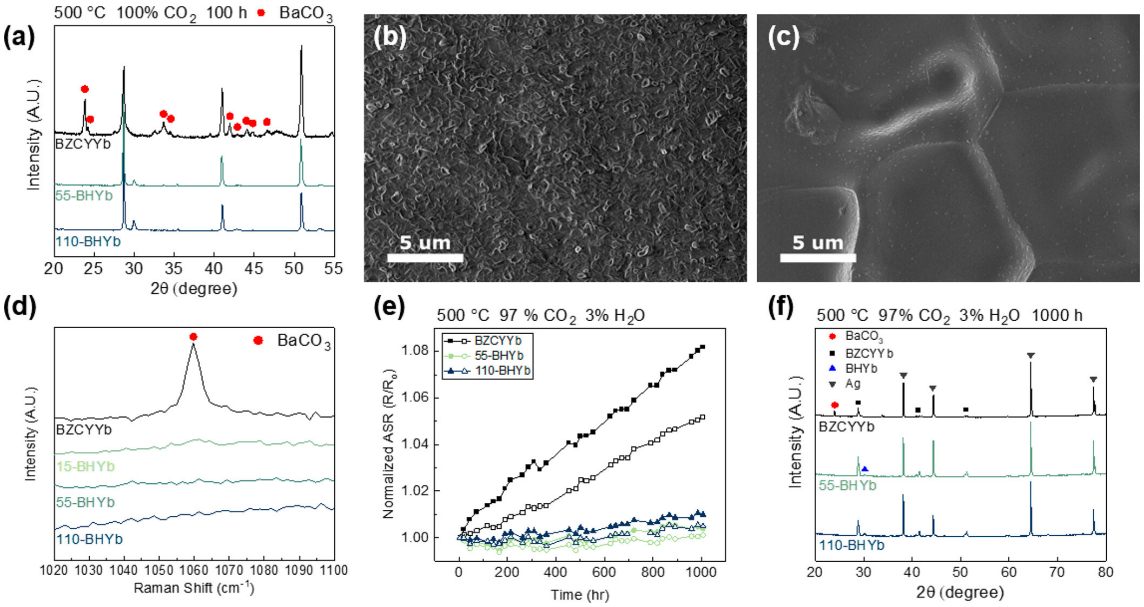


Figure 2.12: Chemical stability assessment of the bilayer electrolytes. (a) The XRD patterns of untreated BZCYYb1711 and BHYb-BZCYYb bilayer electrolytes after exposed in 100% CO_2 for 100 hours at 500°C. The SEM image of (b) untreated BZCYYb1711 and (c) the 110-BHYb after exposing to 100% CO_2 for 100 h at 500°C. (d) Raman spectra of untreated BZCYYb1711 and BHYb-BZCYYb bilayer electrolytes after exposing to 100% CO_2 for 100 hours at 500°C. (e) The normalised ASR (area specific resistance) over time of untreated BZCYYb1711 and BHYb-BZCYYb bilayer electrolytes with various thickness measured in 97% CO_2 with 3% H_2O at 500°C. (f) The XRD patterns of untreated BZCYYb1711 and BHYb-BZCYYb bilayer electrolytes after exposed in 97% CO_2 with 3% H_2O at 500°C for 1000 hours [59]. Reproduced with permission from American Chemical Society, open access CC-BY-NC-ND 4.0 license.

2.4.2 Effect of Sintering Aids on Processing and Performance

A challenge in the practical application of BZCYYb1711 as a proton-conducting electrolyte lies in its poor sinterability. Like other zirconate-cerate based perovskites, BZCYYb1711 requires exceptionally high sintering temperatures to achieve adequate densification, typically exceeding 1500°C. Such conditions consume lots of energy for heating, and introduce several deleterious effects, including abnormal grain growth, barium volatilisation, and the potential formation of secondary phases. These microstructural instabilities ultimately compromise the long-term performance and durability of the electrolyte. Consequently, much effort has been directed towards the development of sintering strategies that enable densification at lower temperatures without sacrificing significantly the conductivity or chemical stability. Among these strategies, the incorporation of sintering aids has proven to be particularly effective.

Among the barium-based perovskite PCFC family, commonly employed sintering aids include NiO, ZnO, and CuO. For instance, in the case of $BaZr_{0.85}Y_{0.15}O_{3-\delta}$, Babilo et al. demonstrated that the addition of ZnO as a sintering aid enabled the material to achieve 93% relative density at 1300°C[63]. Similarly, Liu et al. reported that the incorporation of NiO facilitated the densification of the BZCYYb1711 system, achieving 96% relative density while reducing the required sintering temperature by approximately 200°C compared with the pristine material[64].

Moreover, the quantity of added sintering aid can significantly influence both the density and electrochemical performance of barium-based perovskites. Liu et al. systematically investigated the effect of NiO content on the densification and conductivity of the $BaZr_{0.1}Ce_{0.7}Y_{0.2}O_{3-\delta}$ (BZCY172) system[65]. By varying the NiO addition from 0 to 1.5 wt%, they observed that the relative density increased when the NiO content was in the range of 0.5-1.0 wt%, but decreased once the amount reached 1.5 wt%. Furthermore, an increase in NiO content led to a reduction in the total conductivity of BZCY172. These results indicate that the optimal NiO concentration lies within 0.5-1.0 wt%, so as to achieve balancing and improved densification with minimal adverse effects on proton conductivity[65].

2.4.3 Electrolyte Geometry Optimisation (Micro-tubular Cells)

Regarding the overall performance of a fuel cell, the cell geometry plays a decisive role. Among the different geometrical configurations, micro-tubular designs offer significantly higher volumetric power density compared with conventional planar and tubular geometries[66].

Chen et al. fabricated anode-supported micro-tubular PCFCs using BZCYYb1711

electrolytes prepared via a phase-inversion technique, as illustrated in Figure 2.13[67]. In this configuration, the BZCYYb1711 electrolyte was formed into a thin tube, with the anode material (NiO-BZCYYb) deposited on the inner surface and the cathode material (LSCF-SDC) coated on the outer surface. This architecture enabled a maximum power density of 0.976 Wcm^{-2} at 700°C. By comparison, a planar BZCYYb1711 system achieved only 0.178 Wcm^{-2} at the same temperature, highlighting that the micro-tubular geometry delivers higher maximum power density. This significant increase in power density demonstrates that the micro-tubular geometry is an effective approach to enhancing the performance of PCFCs.

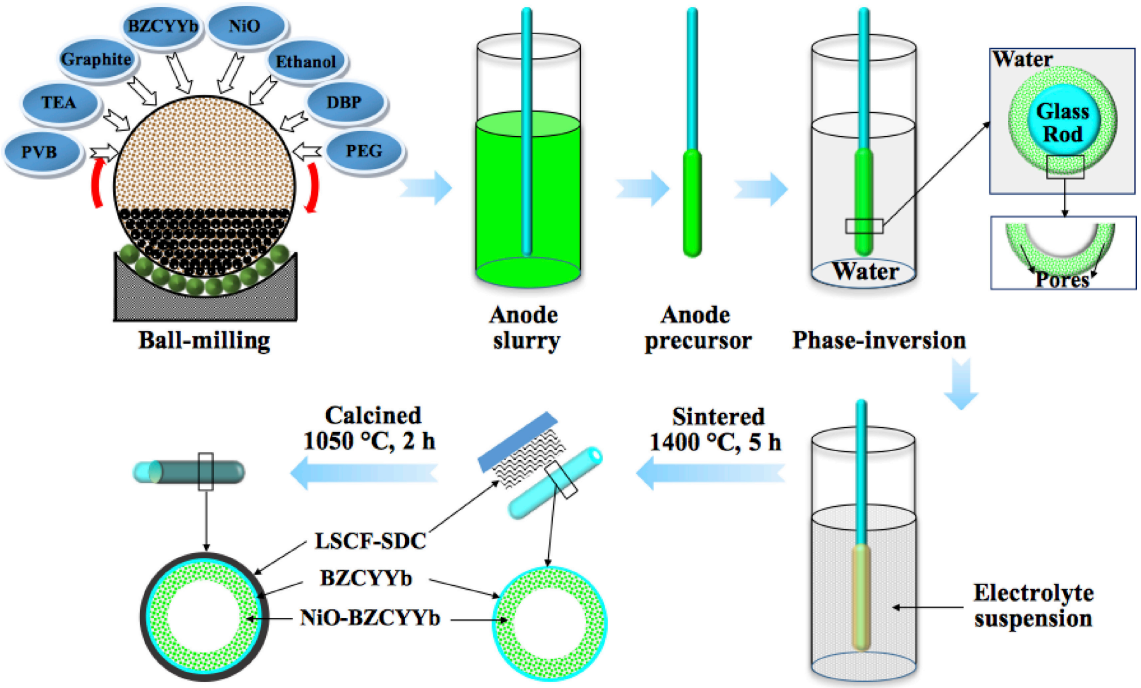


Figure 2.13: Schematic illustration of the production of micro tubular fuel cells with BZCYYb1711 as the electrolyte[67]. Reprinted from International Journal of Hydrogen Energy, Volume 44, Chen et al., Electrochemical properties of micro-tubular intermediate temperature solid oxide fuel cell with novel asymmetric structure based on $BaZr_{0.1}Ce_{0.7}Y_{0.1}Yb_{0.1}O_{3-\delta}$ proton conducting electrolyte, Pages 16887-16897, Copyright 2019, with permission from Elsevier.

Chapter 3: Research Gaps and Suitable Techniques

3.1 Research Gaps of Current $BaZr_{0.1}Ce_{0.7}Y_{0.1}Yb_{0.1}O_{3-\delta}$ Studies

Throughout the literature on BZCYYb1711, the majority of studies focused on strategies to enhance its electrochemical performance, while relatively a few have sought to elucidate the fundamental mechanisms responsible for its high conductivity, which is essential for the rational design of next-generation proton-conducting electrolytes with further improved properties.

In the attempt of attributing the improved conductivity to the dopping of ytterbium, Yang et al. carried out a direct comparison of the microstructure and conductivity of BZCY172 and BZCYYb1711, and suggested a possible correlation between the smaller grain size and the higher conductivity observed in the latter[68]. They further hypothesised that the improved conductivity may originate from the smaller ionic radius of Yb^{3+} relative to Y^{3+}, which could reduce lattice strain energy and thereby facilitate the migration of oxygen vacancies, although no direct experimental evidence has yet been reported to support this hypothesis[69, 70]. Additional insight focusing on the effect of ytterbium on proton conductivity was provided by Oishi et al., who compared $BaCe_{0.9}Y_{0.1}O_{3-\delta}$ (BCY10) with $BaCe_{0.9}Yb_{0.1}O_{3-\delta}$ (BCYb10), and found that Yb doping resulted in a slightly lower proton concentration than Y doping, but at the same time increased the oxygen vacancy concentration[71]. They concluded that although the reduced proton concentration might be expected to lower conductivity, this effect was offset by the enhanced defect mobility associated with the higher oxygen vacancy concentration, leading to an overall improvement in proton conductivity[71].

While this literature offers valuable insights into the possible origins of the enhanced conductivity in the BZCYYb1711 system, there were two limitations on studies related to the proton dynamics. First, the proton dynamics were only evaluated based on the conductivity measured by the electrochemical impedance spectroscopy (EIS) technique, whereas generally the EIS probed the total conductivity instead of the protonic conductivity of this mixed-ionic (protonic + oxide-ions) conducting system[8], thus the total conductivity did not exactly represent the protonic conductivity. Second, as the EIS measured the long-range (in micrometers) proton transport , the localised (in Angstroms) hopping information, such as the hopping distance and frequency were missing. These two research gaps suggest that some techniques which can probe exclusively the proton dynamics and the localised proton hopping are needed to further improve the understanding of the proton transport mechanism in BZCYYb1711 system.

Moreover, another research gap is related to an intriguing phenomenon, which relates to

the relatively small difference in the reported conductivity of BZCYYb1711 system under dry and humidified (3 vol% H_2O) atmospheres, is seldom-discussed. For example, Yang et al. reported that, at approximately 667 K ($1000/T = 1.5$), the conductivity under humid H_2 is $\approx 6.7 \times 10^{-3}$ Scm^{-1}, while the conductivity under dry H_2 condition is $\approx 4.1 \times 10^{-3}$ Scm^{-1}[68]. Similarly, this small difference in conductivities between the dry and humid hydrogen conditions was also reported by He et al.[72] and Zhang et al.[73], indicating this is the intrinsic property observed in the BZCYYb1711 system. Though there is no literature directly comparing the conductivity between the dry and humid condition other than in the hydrogen atmosphere, the effect of change of partial pressure of oxygen (pO_2) and partial pressure of hydration (pH_2O) on the total conductivity of BZCYYb1711 system reported by Kim et al. illustrated that the small dependency of the change of pH_2O still existed in the wide range of pO_2 conditions ($\log(pO_2/atm)$ = -0.7 to -26.6)[74], suggesting that the small conductivity difference under the change of pH_2O was not pO_2 sensitive.

As a proton-conducting material, it is counterintuitive to observe such a small difference in conductivities between dry and humid atmospheres, given the widely accepted mechanism of proton incorporation, namely the hydration dissolution reaction. As shown in Equation 3.1, protonic defects ($2OH_O^{\bullet}$) are generated via the dissolution and incorporation of the water vapour ($H_2O_{(g)}$) in the presence of oxygen vacancies ($V_O^{\bullet\bullet}$). This implies that the availability of external water (in the form of steam) is essential for proton incorporation in PCFC systems. Accordingly, a substantial difference in conductivity between dry and humid conditions would be expected, though the observed behaviour in BZCYYb1711 appears to contradict this expectation.

$$H_2O_{(g)} + V_O^{\bullet\bullet} + O_O^X = 2OH_O^{\bullet} \tag{3.1}$$

One possible explanation for this observed small difference in total conductivity between dry and humid atmospheres is that the protonic contribution to the overall conductivity in BZCYYb1711 may be minor, with the dominant charge carriers instead being oxide ions or electronic species. However, this hypothesis is challenged by the high ionic transport number (>97%) reported by Guo et al. at 600°C under humidified (pH_2O = 0.2 atm) oxygen atmospheres, as determined using the electromotive force (EMF) method [75]. This result indicates that electronic conduction does not significantly contribute to the high total conductivity observed.

Furthermore, Guo et al. also reported an oxide-ion transport number of approximately 10% at 600°C under the humid H_2 atmosphere, with this value decreasing with lower temperatures. A similar magnitude and temperature dependence of the oxide-ion transport number was also observed by Ishiyama et al. in a nickel-doped BZCYYb1711 system

(BZCYYb-Ni) [76], reinforcing the conclusion that oxide-ion conduction contributes minimally to the total conductivity, particularly lower than the intermediate temperatures (e.g. ≤ 600°C).

Since the total conductivity is not primarily governed by either electronic or oxide-ion transport, it is reasonable to hypothesise that, the similiarity in the total conductivity between dry conditions (e.g. in the absence of an external hydration source) and humid conditions is due to the similar amount of protons within BZCYYb1711 system under these two environments. However, according to the hydration dissolution reaction (Equation 3.1), only the BZCYYb1711 samples under humid conditions should exhibit significant incorporated protons, whereas the sample under dry conditions without purposefully exposed to humidity, should contain substantially fewer protons.

3.2 Suitable Techniques to Address Research Gaps

To address three research gaps outlined in section 3.1, a systematic framework, which integrates the effects of composition, crystal structure, microstructure, and proton-exclusive transport information (in both long-range and localised aspects) on the outstanding electrochemical performance, needs to be established.

This systematic framework requires experimental approaches that can disentangle the fundamental factors governing the conductivity. Proton conductivity can be expressed by Equation 3.2, where σ_{p} denotes the protonic conductivity, $\mathrm{n_p}$ the concentration of mobile protons, $\mathrm{q_p}$ the charge carried by a single proton, and μ_{p} the mobility of mobile protons. This relationship highlights that the macroscopic conductivity of a proton-conducting electrolyte is determined jointly by the number of mobile charge carriers and their ability to move through the structure. Consequently, a comprehensive investigation requires experimental techniques capable of probing these two contributions. This chapter therefore discusses two complementary categories of methods: those that quantify the concentration of mobile protons, and those that characterise their dynamics.

$$\sigma_p = n_p q_p \mu_p \tag{3.2}$$

Thermogravimetric analysis (TGA) is a widely used technique for studying weight changes in materials as a function of temperature or time. In proton-conducting oxides, it provides an indirect means of estimating proton concentration by measuring the weight change associated with dehydration, as the release of water upon heating directly reflects the number of incorporated protons[77]. One of the earliest systematic applications of this method was reported by Kreuer et al. in 1994, who used TGA to quantify the amount of protons incorporated into the $BaCeO_3$ system, thereby establishing a direct link between hydration

behaviour and proton uptake[78]. Building on this foundation, Ricote et al. applied TGA to investigate the correlation between zirconium substitution and proton concentration in $BaCe_{0.9-x}Zr_xY_{0.1}O_{3-\delta}$[79]. In their study, samples were first fully dehydrated by heating in dry Ar-O_2 (3%) at 1000°C for 12 hours, after which they were re-exposed to a humid Ar-O_2 (3%, $p_{H_2O} = 0.02$ atm) atmosphere, and the subsequent mass gain was attributed to hydration. As shown in Figure 3.1, the $BaCe_{0.9}Zr_0Y_{0.1}O_{3-\delta}$ (BCZY90) composition exhibited the highest proton concentration, while increasing zirconium content led to a systematic decrease in proton uptake. Similarly, Ahmed et al. used TGA to study hydration behaviour in $BaZr_{1-x}In_xO_{3-\delta}$ ($x = 0.5$), reporting that the largest mass change was observed at around 300°C, indicating that major water uptake takes place below this temperature, thus identifying 300°C as a critical point for proton incorporation in this system[80].

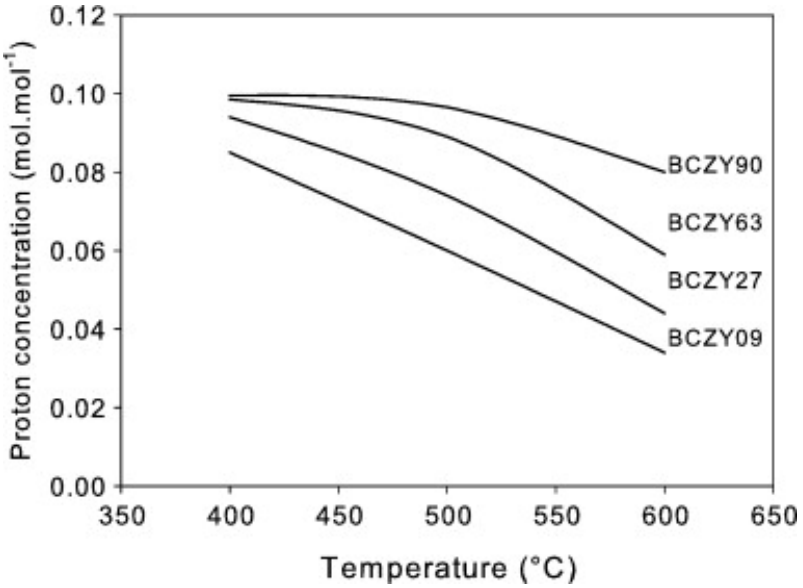


Figure 3.1: Proton concentration derived from the increase of mass measured by TGA in the water uptake experiment under humid (0.02 atm H_2O) Ar, O_2 (3%) atmosphere, versus temperature[79]. Reprinted from Solid State Ionics, Volume 180, Ricote et al., Water vapour solubility and conductivity study of the proton conductor $BaCe_{0.9-x}Zr_xY_{0.1}O_{3-\delta}$, Pages 990-997, Copyright 2009, with permission from Elsevier.

Despite its usefulness, TGA suffers from inherent limitations. It does not measure proton concentration directly but instead infers it indirectly from weight changes. This indirect route introduces uncertainties, as other processes such as decomposition of carbonates, loss of adsorbed species, or volatilisation of impurities may also contribute to mass variations. Furthermore, TGA cannot distinguish protons from other species involved in weight change, which restricts its reliability as a stand-alone method for quantifying proton concentration[81].

In contrast to the indirect nature of TGA, neutron-based techniques provide a more

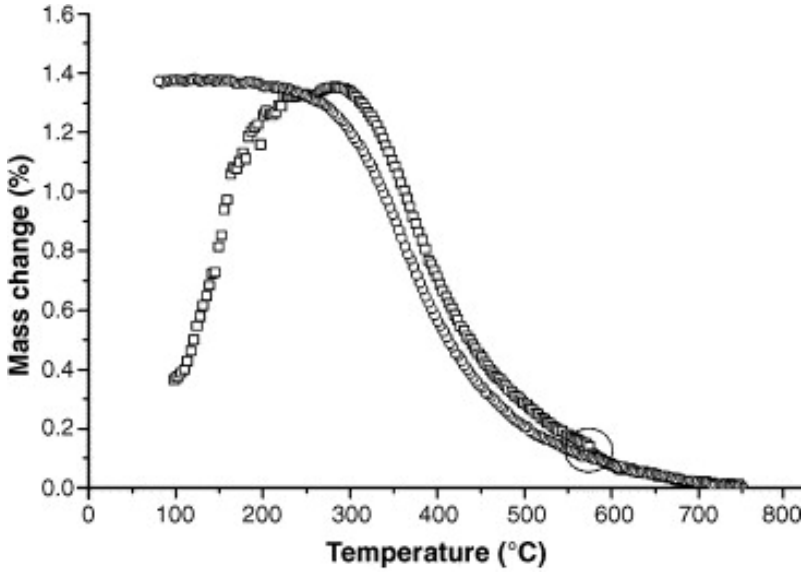


Figure 3.2: TGA curve for as-prepared $BaZr_{1-x}In_xO_{3-\delta}$, x = 0.50, taken at 1.5°C/min under an Ar gas flow saturated with water, square data represents heating cycle, while the circle data represents cooling cycle[80]. Reprinted from Solid State Ionics, Volume 177, Ahmed et al., Synthesis and structural characterisation of perovskite type proton conducting $BaZr_{1-x}In_xO_{3-\delta}$ ($0.0 \leq x \leq 0.75$), Pages 1395-1403, Copyright 2006, with permission from Elsevier.

explicit probe of proton concentration due to the exceptional sensitivity of neutrons to hydrogen nuclei. Among these, prompt gamma activation analysis (PGAA) has emerged as a powerful method for directly quantifying hydrogen incorporation in proton-conducting oxides. In this technique, a sample is irradiated with a neutron beam, and hydrogen atoms capture neutrons emitting prompt γ-rays with characteristic energies, enabling highly selective and quantitative determination of hydrogen content[82, 83, 84]. Depending on the energy of the incident neutrons, PGAA can be categorised into thermal neutron PGAA (higher neutron energy) and cold neutron PGAA (lower neutron energy)[85]. Thermal neutron PGAA is typically applied to samples with relatively high hydrogen content (mass fraction $\geq 1\%$), such as foods[86, 87], rock reference materials[88], and construction materials[89]. By contrast, cold neutron PGAA is particularly suited for detecting low levels (quantities) of hydrogen (down to $\sim$10 mg/kg), a sensitivity range that aligns with the hydrogen concentrations typically found in proton-conducting solid oxide materials. Jones et al. applied PGAA to directly and selectively probe the concentration of incorporated protons in the $BaPr_{0.9}Y_{0.1}O_3 - \delta$ system. As shown in Figure 3.3, PGAA clearly revealed the effect of hydration annealing by tracking changes in the hydrogen signal: a pronounced difference in peak intensity was observed between the humid-saturated and dried samples[90]. Since the intensity of the PGAA peak is proportional to the molar concentration of detected atoms, this method enables not only the qualitative detection of hydration effects but also the quantitative determination of proton concentration. By comparing the relative molar ratio of incorporated hydrogen atoms to reference matrix atoms (such as barium), PGAA provides a direct means of quantifying proton uptake in PCFC materials, thus overcoming the indirect limitations of techniques such as TGA.

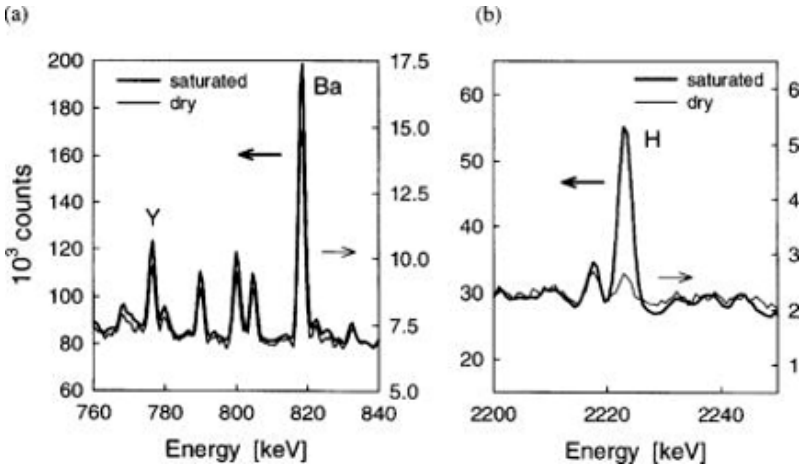


Figure 3.3: The PGAA spectra of dry and saturated $BaPr_{0.9}Y_{0.1}O_{3-\delta}$ illustrates signal from (a) Y and Ba, and (b) H[90]. Reprinted from Journal of Applied Physics, Volume 97, Jones et al., Hydrogen content in doped and undoped $BaPrO_3$ and $BaCeO_3$ by cold neutron prompt-gamma activation analysis, Pages 114908, Copyright 2005, with permission of AIP Publishing.

Although long-range proton conductivity can be effectively evaluated by electrochemical impedance spectroscopy (EIS), probing the localised proton hopping events that occur on the Angstrom length scale and nanosecond timescale remains challenging. Such local dynamic information is essential, as it can be bridged with the macroscopic conductivity to enable the formulation of a mechanistic picture of the proton transport. Neutron scattering techniques are well suited for measuring the localised dynamics due to their ability to probe processes at short timescales and length scales. In particular, quasielastic neutron scattering (QENS) provides direct access to localised proton hopping by enabling the estimation of parameters such as proton self-diffusion coefficients and relaxation times, thereby capturing atomic-scale dynamical behaviour. Complementarily, neutron Compton scattering (NCS) probes proton momentum distributions, offering insight into the local potential energy landscape and dynamics on ultrafast timescales ($\approx 10^{-15}$ s). Together, these neutron-based approaches overcome the intrinsic limitations of purely electrical measurements and allow for a systematic investigation of the interplay between proton mobility, structural features, and overall conductivity.

Quasielastic neutron scattering (QENS) is a powerful spectroscopic technique that probes atomic and molecular motions on picosecond to nanosecond timescales by analysing the small energy broadenings around the elastic line in neutron scattering spectra. By fitting the observed spectral broadening with appropriate jump-diffusion models, key local dynamical parameters such as proton hopping distances and relaxation times can be quantitatively extracted[91, 92].

Followed by the pioneering work reported by Hempelmann et al.[93], the QENS study reported by Karmonik et al. proved that the proton conduction in $BaCa_{0.39}Nb_{0.61}O_{2.91}$

system consists of simultaneous hopping and reorientational motions[94]. Malikova et al. revealed that the mobility of hydrogen strongly depends on the concentration of incorporated protons: in BCY samples, the mean square displacement of protons increased during hydration and decreased during dehydration, highlighting the coupling between proton content and dynamic behaviour[95]. More recently, Wallis et al. applied QENS to the $BaZr_{0.7}Ce_{0.2}Y_{0.1}O_{3-\delta}$ (BZCY) system and resolved the signal into two distinct contributions: a translational diffusion process and a localised rotational motion. They concluded that translational proton jumps are closely coupled with rotational displacements on a length scale comparable to the O-H bond, thereby confirming that proton transport in BZCY proceeds via a Grotthuss-type mechanism[96].

While QENS offers critical insights into proton hopping dynamics on the picosecond to nanosecond timescale and Angstrom length scale, neutron Compton scattering (NCS) enables the investigation of much faster and more localised dynamics. In contrast to QENS, which extracts information from quasielastic broadening, NCS measures the momentum distribution of protons on the femtosecond timescale ($\sim 10^{-15}$ s), thereby directly revealing the local quantum behaviour of protons in solids[97]. Applying this technique, Wallis et al. investigated the proton momentum distribution in $BaZr_{0.7}Ce_{0.2}Y_{0.1}O_{3-\delta}$ (BZCY72). Their results showed that the proton concentration in BZCY72 remained unchanged during the structural transition from the orthorhombic to rhombohedral phase. Moreover, the comparable proton kinetic energies extracted from NCS in both phases demonstrated that the local force field experienced by the protons was unaffected by the phase transition[98]. Similarly, Perrichon et al. employed NCS to investigate the localised dynamics of oxygen atoms in $BaZrO_3$. Analysis of the momentum distribution revealed direction-dependent mean square displacement values, indicating that the oxygen sublattice experiences an anisotropic local force field. This observation was further corroborated by complementary neutron diffraction data and density functional theory (DFT) simulations, together providing a consistent picture of anisotropic lattice dynamics of oxygen atoms in $BaZrO_3$[99]. These findings highlight the unique capability of NCS to probe the ultrafast, localised aspects of atom transport that remain inaccessible to QENS, thereby offering a more complete dynamic picture when the two neutron-based techniques are considered together.

In summary, although several studies have explored individual factors contributing to the high conductivity of the BZCYYb1711 system, a complete mechanistic understanding of its exceptional proton conduction remains lacking. To address this gap, this PhD study applied a systematic approach that integrates complementary experimental techniques to investigate both proton incorporation and proton dynamics, encompassing localised and long-range processes, in order to elucidate the proton transport mechanism in BZCYYb1711.

Chapter 4: Material Synthesis and Sample Preparation

This section details the synthesis of BZCYYb1711 using a sol-gel method and the subsequent preparation of pellets for experimental investigation. The aim is to obtain single phase material with correct stoichiometry, as well as to prepare dense and uniform samples suitable for the following characterisation.

4.1 Material Synthesis

The solid-state reaction method is regarded as the conventional route for synthesising solid oxide ceramics. In this approach, simple oxide or carbonate precursors are thoroughly mixed, often by ball milling, followed by repeated cycles of high-temperature calcination and grinding until a single-phase material is obtained[100]. While robust and straightforward, this method is limited by poor atomic-level mixing of the starting powders, which often results in inhomogeneous phases, incomplete reactions, and the requirement for prolonged calcination at elevated temperatures (typically above 1400°C)[101]. Moreover, such harsh thermal treatments can lead to exaggerated grain growth, which is detrimental to the densification and functional properties of the final ceramic.

By contrast, the sol-gel method mixes cation precursors through the hydrolysis and polycondensation of metal alkoxides or nitrates in solution, producing a homogeneous gel that converts into fine oxide powders upon calcination[102, 103, 104]. This route enables lower crystallisation temperatures, shorter heating cycles, and improved compositional control relative to the solid-state method. For example, sol-gel processing has been shown to yield highly dense and chemically homogeneous proton-conducting perovskites such as yttrium-doped barium cerate and barium zirconate with superior microstructural control[105, 106]. Owing to these advantages, sol-gel synthesis has become a preferred method for preparing advanced ceramic electrolytes, where precise phase control and minimisation of secondary phases are critical for optimising proton conductivity and overall electrochemical performance.

All $BaZr_{0.1}Ce_{0.7}Y_{0.1}Yb_{0.1}O_{3-\delta}$ (BZCYYb) powders were synthesised via the sol-gel method. The synthesis process was adapted from the work of Zhang et al.[73]. The preparation of a precursor solution began with dissolving the following metal nitrates, all obtained from Sigma Aldrich UK, stoichiometrically in deionised water: barium nitrate ($Ba(NO_3)_2$) (≥99%), cerium(III) nitrate hexahydrate ($Ce(NO_3)_3 \cdot 6H_2O$) (99%), zirconium(IV) oxynitrate hydrate ($ZrO(NO_3)_2 \cdot xH_2O$) (99%), yttrium(III) nitrate hexahydrate ($Y(NO_3)_3 \cdot 6H_2O$) (99.8%) and ytterbium(III) nitrate pentahydrate ($Yb(NO_3)_3 \cdot 5H_2O$)

(99.9%). Citric acid monohydrate (99%), as a chelating agent, was added into the precursor solution with the molar ratio between citric acid and total metal ions to be 1:1. To faciliate the dissolution process, the precursor solution containing the powders listed above was heated and stirred at 80°C on the heating plate (Corning, UK, PC-420D). As there was a significant temperature difference between the set temperature of the heating plate and the real temperature in the solution, the temperature of the solution was measured using a thermometer. Following the complete dissolution of added powders, the pH value of the solution was then adjusted to 7 with ammonium hydroxide solution (Sigma Aldrich, UK, 28.0-30.0% NH_3 basis) to improve the binding process between metal cations and the citrate species[103]. Subsequently, the solution was evaporated at 90°C with 500 RPM stirring speed. Once the solution was dried to a gel, it was heated at 265°C for 6 hours in decomposition furnace (Carbolite Gero, UK, AAF 1100) under ambient air to eliminate any remaining carbon species and form fine powders, which then was calcinated at 1100°C in a high-temperature chamber furnace (Carbolite Gero, UK, RHF 1600) under ambient air for 7 hours to achieve the final BZCYYb powders.

4.2 Pellet Pressing

For the preparation of dense BZCYYb pellets, the calcined powders were first compacted into cylindrical discs using a 10 mm diameter evacuable pellet die set (Specac, UK). Uniaxial pressing was carried out on a manual hydraulic press (Specac, UK) under a load of 19,620 N for 1 minute, ensuring sufficient packing density and mechanical stability of the pressed pellets. These pellets were then transferred to an alumina crucible (Almath Crucibles Ltd, UK) for high-temperature sintering, which was conducted at 1500°C for 10 hours in a high temperature chamber furnace (Carbolite Gero, UK, RHF 1600) under ambient air to achieve densification and grain growth.

To mitigate the risk of barium evaporation at such elevated temperatures, which is an issue known to induce secondary phase formation and significantly deteriorate proton conductivity, the pellets were carefully embedded in a protective bed of BZCYYb powders during the sintering process[107, 108]. This powder bed served the dual purpose: acting as a sacrificial source to maintain the barium vapour equilibrium, and shielding the pellet surfaces from direct interaction with the surrounding atmosphere and the alumina crucible, thereby preserving both phase purity and microstructural integrity.

Chapter 5: Characterisation Techniques

5.1 Archimedes Density Measurement

The Archimedes method is one of the most widely used experimental techniques for determining the bulk density of solid materials, especially ceramics and porous solids. Its popularity arises from its simplicity, reliability, and non-destructive nature, making it a standard method for evaluating sample quality during materials processing and sintering. The technique is particularly valuable in ceramic science, where density and porosity strongly influence mechanical strength, ionic conductivity, and chemical stability. By measuring the bulk density and comparing it with the theoretical crystallographic density, researchers can calculate the relative density, which provides insight into the degree of densification and the presence of pores in the microstructure[109, 110].

Theory

In order to evaluate the relative density of sintered ceramic pellets, both the theoretical density and the experimental density must be determined. The theoretical density is calculated from the crystallographic data obtained by diffraction refinement, according to Equation 5.1:

$$\rho_{theo} = \frac{M \cdot Z}{N_A \cdot V} \tag{5.1}$$

where ρ_{theo} is the theoretical density, M is the molar mass of one formula unit, Z is the number of formula units in one unit cell, N_A is Avogadro's constant, and V is the unit cell volume derived from the refined unit cell parameters. This value provides the maximum achievable density of the material, corresponding to a fully dense, pore-free sample.

The experimental density of the sintered pellets was measured using the Archimedes method. This technique is based on the principle of buoyancy, where a body immersed in a fluid experiences an apparent weight loss equal to the mass of fluid displaced. By measuring the mass of the sample in air (W_a) and its apparent mass when immersed in fluid (W_{fl}), the volume of the displaced fluid (V_{fl}) can be calculated, and thus the density

of the sample (ρ_s) is determined. The calculation can be expressed as follows:

$$\rho_s = \frac{Mass}{Volume} \tag{5.2}$$

$$\rho_s = \frac{W_a}{V_{fl}} \tag{5.3}$$

$$V_{fl} = \frac{W_a - W_{fl}}{\rho_{fl}} \tag{5.4}$$

$$\rho_s = \frac{W_a \cdot \rho_{fl}}{W_a - W_{fl}} \tag{5.5}$$

where ρ_{fl} is the density of the immersion fluid. To account for systematic effects, such as air buoyancy and the contribution of the sample holder or wire immersed in the fluid, correction terms are included in refined equations:

$$\rho_s = \frac{W_a \cdot [\rho_{fl} - \rho_{air}]}{W_a - W_{fl}} + \rho_{air} \tag{5.6}$$

$$\rho_s = \frac{W_a \cdot [\rho_{fl} - \rho_{air}]}{C \cdot [W_a - W_{fl}]} + \rho_{air} \tag{5.7}$$

where ρ_{air} is the density of air, and C is a correction factor accounting for the buoyancy of auxiliary parts of the setup (e.g. wires, sieves, or sample holders).

Thus, the relative density of the pellet can be expressed as the ratio between the experimentally determined density and the theoretical density, offering a quantitative measure of densification and porosity in sintered ceramics.

Experimental details

The density of the sintered pellets was measured using a density determination balance kit (Sartorius YDK01, Germany) with deionised water as the immersion fluid. Prior to measurement, the BZCYYb pellet was immersed in deionised water for 10 minutes to remove any surface-adhered air bubbles, as residual bubbles could artificially reduce the immersed weight (W_{fl}) and thereby compromise the accuracy of the calculated density. During the measurement, the temperature of the immersion fluid was monitored with a thermocouple to ensure stability, since fluid density is temperature dependent. For reliability, each pellet was measured three times, and the mean value was taken as the final experimental density to minimise random error.

5.2 Scanning Electron Microscopy

In ceramic and solid oxide electrolyte research, understanding the microstructure is crucial, as grain size, porosity, and grain boundary morphology significantly influence the

mechanical, electrical, and electrochemical properties of the material[111, 112]. While bulk density measurements provide a quantitative evaluation of densification, they cannot reveal local features such as residual porosity, intergranular connectivity, or microcracks. To obtain this complementary information, microstructural characterisation techniques are employed. Among these, scanning electron microscopy (SEM) is one of the most powerful and widely applied methods for investigating the morphology and surface features of sintered ceramics and electrolytes[113, 114]. SEM enables direct visualisation of grain structure and pore distribution with sub-micron resolution, offering insights into how processing conditions (e.g. sintering temperature, use of sintering aids, or dopant distribution) influence final material properties[115, 116].

In this project, SEM was therefore applied to complement Archimedes density measurements and to provide qualitative and spatially resolved assessment of the densification behaviour of BZCYYb pellets.

Theory

In SEM, a finely focused electron beam, typically with an accelerating voltage between 1-30 kV, is raster-scanned across the sample surface. The interaction between the primary beam electrons and the atoms of the specimen generates a variety of signals, including backscattered electrons (BSE), secondary electrons (SE), characteristic X-rays, Auger electrons, and cathodoluminescence photons[117, 118]. Among these, BSE and SE are the two most widely used signals for imaging applications.

When an energetic electron beam interacts with a solid sample, the electrons penetrate into the material and undergo elastic and inelastic scattering processes. The volume within which these interactions occur is known as the interaction volume, which depends strongly on accelerating voltage, atomic number, and density of the material[119]. Electrons scattered back from deeper regions provide compositional contrast, while those generated closer to the surface contribute more to the topographic imaging. By altering the accelerating voltage and the detector configuration, different types of information is obtained from SEM measurements.

Backscattered electrons (BSE) are primary beam electrons that undergo large-angle elastic scattering events with the atomic nuclei and are redirected out of the sample. Because the scattering cross-section increases with atomic number, the probability of backscattering is higher for heavier elements. This is quantitatively described by the backscattered electron coefficient (η), defined as:

$$\eta = \frac{N_{BSE}}{N_B} \tag{5.8}$$

where N_{BSE} is the number of backscattered electrons and N_B is the number of incident electrons. As shown in Figure 5.1, η increases with atomic number Z, making BSE signals highly sensitive to compositional variations within multiphase or doped ceramic systems[120]. Consequently, BSE imaging is frequently used to distinguish phases of different average atomic numbers and to investigate dopant segregation or secondary phase formation. However, the slope of η versus Z decreases at higher atomic numbers, meaning compositional contrast becomes less pronounced when elements have higher Z values.

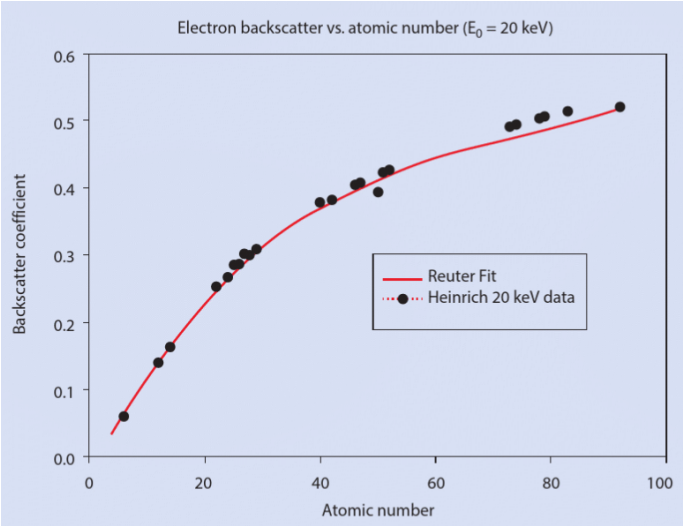


Figure 5.1: The relationship between the backscattered electron coefficient and the atomic number of pure elements with constant incident electron energy of 20 keV[120]. Reproduced with permission from Springer Nature.

Secondary electrons (SE), in contrast, are generated through inelastic scattering events, in which incident beam electrons transfer energy to loosely bound atomic electrons, ejecting them from the sample surface. SE typically possess kinetic energies below 50 eV and the escape depth of only a few nanometres[120]. This surface sensitivity makes SE signals particularly valuable for topographic imaging, as small variations in surface features, such as grain boundaries, cracks, or pores, strongly affect SE yield. Unlike BSE, the SE yield does not exhibit a strong dependence on atomic number (Figure 5.2), limiting its usefulness for compositional analysis. Instead, SE images provide fine structural details of the specimen surface, often at sub-nanometre spatial resolution when low accelerating voltages and immersion (inlens) detectors are employed[114, 121].

Another critical factor in SEM imaging is the geometry of the secondary electron (SE) detectors, where the illustration is demonstrated in Figure 5.3[120]. Conventional SE detectors, such as the Everhart-Thornley detector positioned laterally in the chamber, collect SE signals from inelastic interactions: SE_2 is originated from the interaction between backscattered electrons and the sample, while SE_3 is produced when backscattered electrons interact with the chamber metallic surface. Both SE_2 and SE_3 suffer from re-

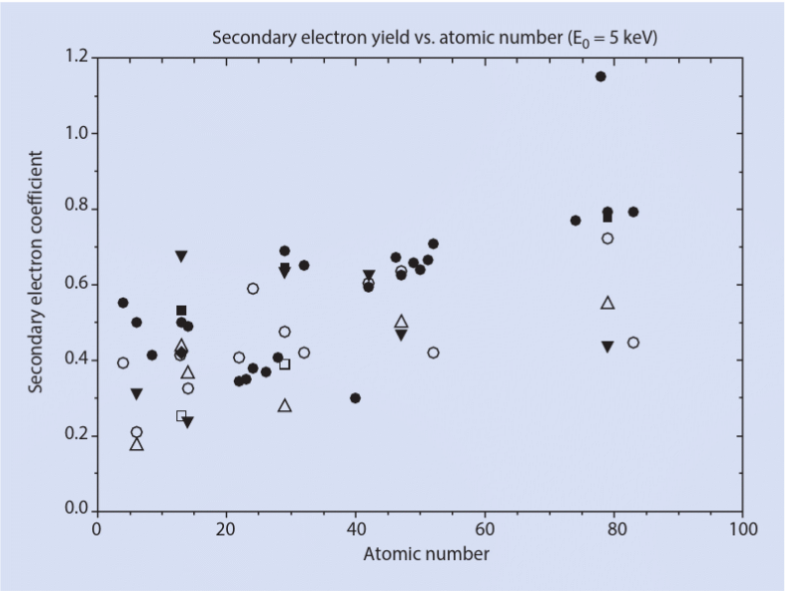


Figure 5.2: The relationship between the secondary electron coefficient and the atomic number of pure elements with constant incident electron energy of 5 keV[120]. Reproduced with permission from Springer Nature.

duced spatial resolution and introduce additional signal noise. By contrast, the inlens (or immersion) detector is located coaxially with the primary electron beam and is optimised for capturing SE_1, which are the high-resolution secondary electrons generated from the direct scattering between the incident electron beam and the sample.

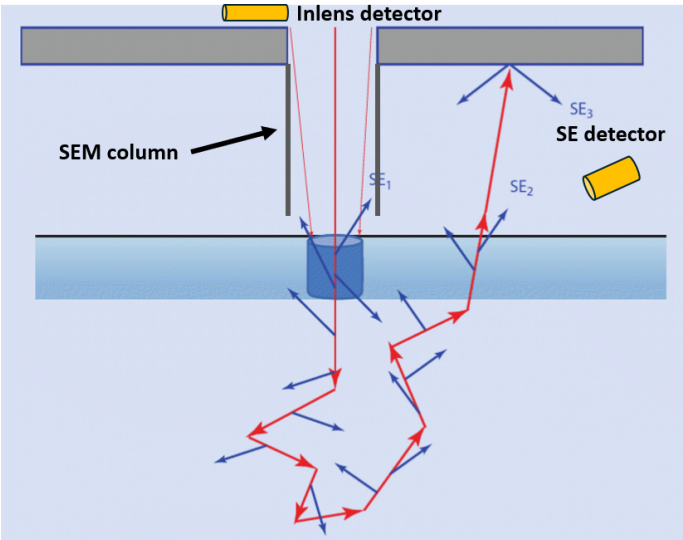


Figure 5.3: The schematic diagram illustrates the locations of inlens detector and normal SE detector, and the origins of different types of SE (SE_1, SE_2 and SE_3)[120]. Adapted and reproduced with permission from Springer Nature.

This geometry of the inlens detector enhances image resolution, particularly at low accelerating voltages, by preferentially collecting SE_1 while suppressing the lower-resolution contributions of SE_2 and SE_3[122, 123]. The accelerating voltage of the incident electron

beam plays a central role in this optimisation. As demonstrated by Moncrieff et al.[123], the secondary electron yield decreases with increasing beam energy (Figure 5.4). In conventional lateral SE detection, relatively high accelerating voltages (e.g. 20 kV) are typically employed to generate sufficient SE_2 and SE_3 from backscattered electrons and chamber interactions. In contrast, the inlens detector relies primarily on SE_1, which is produced directly at the beam–sample interaction and does not require such high beam energies. Consequently, operating at lower accelerating voltages (e.g. 5 kV) increases the relative yield of SE_1, thereby improving spatial resolution in SEM imaging.

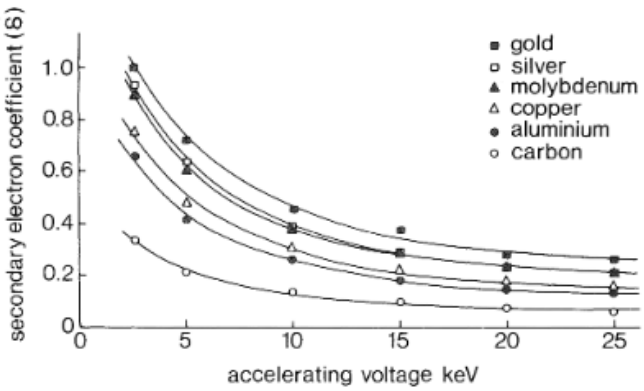


Figure 5.4: The relationship between the secondary electron coefficient and the energy of incident electrons on different metals[123]. Reproduced with permission from Wiley.

Experimental details

The SEM measurements were performed using a Zeiss Crossbeam microscope (Zeiss, Germany) equipped with both BSE and SE detectors. BZCYYb samples (pellets and powders) were mounted on a flat platinum holder with carbon tape and coated with a 15 nm chromium layer to minimise charging under the electron beam. For thick pellets, where only the top surface was chromium-coated, silver paste was applied along the pellet edge to ensure electrical contact between the coated surface and the carbon tape. High-resolution SEM images were obtained at an accelerating voltage of 5 kV, while BSE imaging was conducted at 20 kV to provide compositional contrast.

5.3 Energy Dispersive X-ray Spectroscopy

Energy Dispersive X-ray Spectroscopy (EDS) is a microanalytical technique commonly coupled with scanning electron microscopy (SEM) to provide elemental composition information. In ceramic systems, EDS is widely used to confirm phase purity, detect impurities, and assess dopant distribution or compositional variations [124, 125]. It serves as a valuable complement to structural techniques such as XRD and SEM imaging, bridging microstructural observations with compositional data.

Theory

The principle of EDS is based on the interaction between the high-energy incident electron beam and the atoms within the sample. When an incident electron possesses sufficient energy, it can ionise an atom by ejecting a core-shell electron, typically from the K or L-shell. This process creates an electronic vacancy, leaving the atom in an energetically unstable state.

To return to stability, an electron from a higher-energy outer shell fills the vacancy, and the energy difference between the two shells is released in the form of an X-ray photon. The energy of this emitted X-ray is unique to the specific electronic transition of the element and is therefore considered "characteristic" of that element. By collecting and analysing these X-rays, EDS provides a fingerprint that allows for unambiguous elemental identification[120].

Beyond qualitative analysis, the intensity of the characteristic X-ray peaks in the spectrum is directly related to the concentration of the corresponding elements present in the sample. However, accurate quantification requires correction procedures to account for factors such as X-ray absorption, fluorescence, and detector efficiency[126].

Experimental details

Similar to the SEM experiments, the BZCYYb pellets analysed by EDS were coated with a thin layer of chromium to minimise charging effects under the electron beam. The measurements were conducted using a Zeiss Crossbeam SEM (Zeiss, Germany) equipped with a 20 mm^2 X-Max silicon drift detector (Oxford Instruments, UK). The working distance was maintained at 10 mm from the sample surface to optimise X-ray collection efficiency.

An accelerating voltage of 20 kV was employed to provide the incident electrons with sufficient energy to ionise the relevant core levels of the constituent elements. In the case of BZCYYb, the highest excitation energy corresponds to the Ba Kα line (15.74 keV), and the chosen beam energy ensured reliable excitation of all characteristic X-rays required for accurate compositional analysis.

5.4 X-ray Diffraction

X-ray diffraction (XRD) is one of the most widely used characterisation techniques for crystalline materials, as it provides fundamental information on crystal structure, phase composition, and structural stability. In ceramic systems, XRD is routinely em-

ployed to verify phase purity, identify secondary phases, and monitor structural transitions that can directly affect functional properties such as ionic conductivity or mechanical integrity[127, 128]. In addition to qualitative phase identification, diffraction data allows determination of unit cell parameters, which can be refined to support the calculation of theoretical density and to track microstructural evolution during synthesis and reaction[129]. Overall, XRD serves as a critical tool for linking processing conditions to structural characteristics and, ultimately, to the resulting material properties.

Theory

XRD is commonly employed to determine the phase composition and crystal structure of materials. The appearance of diffraction peaks in an XRD pattern fundamentally arises from Bragg's law[130] (Equation 5.9):

$$n\lambda = 2d_{hkl} \sin\theta \tag{5.9}$$

Here, λ is the wavelength of the incident X-ray, n is the diffraction order, d_{hkl} is the interplanar spacing between crystallographic planes with Miller indices (hkl), and θ is the angle between the incident X-ray beam and the lattice plane, as illustrated in Figure 5.5. When a monochromatic X-ray beam impinges on a crystalline material, sets of parallel lattice planes with identical interplanar spacing scatter the incident radiation. Constructive interference occurs only when the conditions of Bragg's law are satisfied, producing diffraction peaks that reflect the material's crystal structure.

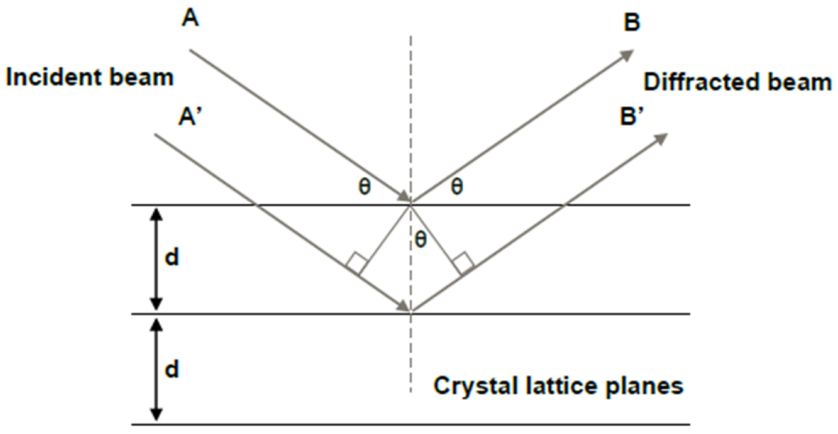


Figure 5.5: Schematic of Bragg diffraction.

However, compliance with Bragg's law alone is insufficient to determine the occurrence or intensity of a diffraction peak. The visibility and relative strength of a reflection are also governed by the structure factor, which accounts for the spatial arrangement of atoms within the unit cell and their respective scattering powers. The structure factor is defined

by Equation 5.10:

$$F_{hkl} = \sum_{n=1}^{N} f_n e^{2\pi i(hx_n + ky_n + lz_n)} \tag{5.10}$$

where F_{hkl} is the structure factor, N is the number of atoms in the unit cell, f_n is the atomic scattering factor of the nth atom, which describes the scattering power of the atom, h, k, l are the Miller indices of the crystallographic plane, x_n, y_n, z_n are the fractional coordinates of the nth atom within the unit cell, where $x_n = \frac{x}{a}$, $y_n = \frac{y}{b}$ and $z_n = \frac{x}{c}$ (a, b, c are the lattice parameters of the unit cell). In crystals with specific symmetries, certain reflections yield a structure factor equal to zero, leading to systematic absences in the diffraction pattern. These absences are crucial for identifying the space group symmetry of the crystal.

Experimental details

The X-ray diffraction (XRD) measurements were carried out on a high-resolution diffractometer (Malvern PANalytical X'Pert Pro MPD) operated in Bragg-Brentano geometry. A copper (Cu) anode served as the X-ray source, producing characteristic K_α ($\lambda \approx 1.5406$Å) and K_β ($\lambda \approx 1.3922$Å) radiations. To ensure the monochromatic incident radiation, a nickel (Ni) filter was employed to suppress the K_β component, leaving only the K_α radiation. The X-rays were generated under operating conditions of 40 mA filament current and 40 kV accelerating voltage.

A single-crystal silicon holder was used to minimise background contributions from the sample stage. In Bragg-Brentano geometry, only lattice planes parallel to the sample surface contribute to diffraction, which can lead to preferred orientation effects in dense sintered samples. To reduce this, the BZCYYb pellets were rotated at 60 RPM during measurements, ensuring more uniform sampling of crystallite orientations.

To obtain high-quality diffraction data suitable for Rietveld and Le Bail refinement analysed by GSAS-II software, several instrumental parameters were optimised. The 2θ scanning range was set between 15-135° to capture reflections from planes with both large and small interplanar spacings. A Soller slit with a divergence of 0.02 rad was employed to limit axial divergence and prevent peak asymmetry, particularly at low angles, albeit at the cost of intensity. In-plane divergence was controlled using a 0.25° divergent slit, ensuring that the interaction area of X-ray matched the sample area. A beam knife was also used to minimise background scattering from air, with its position carefully adjusted to avoid blocking peaks at high 2θ values. Finally, a step size of 0.004° and a counting time of 250 s per step were selected to achieve high resolution and adequate intensity across all diffraction peaks.

5.5 Inductively Coupled Plasma Optical Emission Spectroscopy

Inductively Coupled Plasma Optical Emission Spectroscopy (ICP-OES) is a powerful analytical technique widely employed for multi-elemental analysis of materials. By introducing samples into a high-temperature argon plasma, atoms and ions are excited, and the emitted light at element-specific wavelengths is detected to quantify elemental concentrations with high sensitivity and precision[131]. Unlike Energy Dispersive X-ray Spectroscopy (EDS), which probes only the near-surface region of a sample (typically within several micrometers)[132], ICP-OES provides information on the bulk composition of the sample. This complementarity allows ICP-OES to deliver accurate quantitative measurements of overall elemental concentrations, while EDS serves as a local, surface-sensitive technique to assess compositional distribution in microstructural features. Together, these methods provide a comprehensive characterisation of both surface and bulk chemistry.

Theory

Inductively Coupled Plasma Optical Emission Spectroscopy (ICP-OES) is an analytical technique employed to quantify elemental composition with high sensitivity. In this method, a high-temperature argon plasma is generated and serves as both the excitation and ionisation source, where electrons are promoted to higher energy states. As these excited species relax back to their ground states, they emit photons at characteristic wavelengths unique to each element. By detecting and analysing the intensity of this emitted light, both qualitative identification and quantitative determination of elemental concentrations can be achieved.

Experimental details

The ICP-OES measurements were performed using an iCAP 6000 Series ICP spectrometer (Thermo Scientific). Prior to analysis, BZCYYb samples were fully dissolved in dilute nitric acid (15%). The resulting solutions were then further diluted to a concentration range of 1 to 20 ppm in order to minimise matrix effects and improve measurement accuracy. Certified reference standards of elements in BZCYYb (Ba, Zr, Ce, Y and Yb) were supplied by Sigma Aldrich (UK) and applied to construct the calibration curves: The certified standard solutions were serially diluted by the dilute nitric acid (15%) to obtain a set of seven calibration solutions, including a blank reference. The concentrations were evenly spaced to ensure a linear calibration range for quantification. Elemental concentrations in the measured samples were determined by recording the emission intensities at the characteristic wavelengths of each element and interpolating these values against the corresponding calibration curves.

Selection of the target wavelengths for each element was guided by two criteria: The chosen wavelength had to exhibit the highest relative intensity for the element for reli-

able signals, and the selected wavelength was not overlap by an emission line of another element, thereby avoiding spectral interference. Following this approach, the optimised wavelengths were: Ba (455.403 nm), Zr (339.198 nm), Ce (404.076 nm), Y (371.030 nm), and Yb (328.937 nm).

5.6 Thermogravimetric Analysis

Thermogravimetric Analysis (TGA) is a thermal analysis technique widely used to monitor changes in the mass of a material as a function of temperature or time under controlled heating conditions. By measuring mass change during the change of temperature or gas atmosphere, TGA provides insights into processes such as dehydration, decomposition, oxidation, or reduction[133, 134].

Theory

TGA is a robust technique for monitoring mass changes in a material as a function of temperature and time under a controlled atmosphere. In the context of proton-conducting oxides, TGA is particularly useful for probing hydration behaviour, since proton incorporation is accompanied by measurable mass variations. The general mechanism of proton uptake is described by the hydration reaction:

$$\mathrm{H_2O_{(g)}} + \mathrm{V_O^{\bullet\bullet}} + \mathrm{O_O^x} \rightarrow 2\mathrm{OH_O^{\bullet}} \tag{5.11}$$

Here, water vapour from the atmosphere reacts with oxygen vacancies ($V_{\ddot{O}}$) and lattice oxygen (O_O^x) to form hydroxyl groups ($OH_{\dot{O}}$), thereby introducing protons into the crystal lattice. As a result, the mass gain detected during TGA can be directly associated with hydration and proton incorporation, provided that no competing processes (such as loss of lattice oxygen) occur simultaneously.

Experimental details

Thermogravimetric analysis (TGA) was performed using a Netzsch Jupiter F5 instrument (Netzsch). To maintain a low pH_2O environment during measurement, the carrier gases were passed through a drying tube suppplied by Sigma Aldrich, UK, filled with Drierite (anhydrous calcium sulfate), a desiccant widely used for removing residual moisture from gas streams. The BZCYYb sample was placed in an alumina crucible and subjected to heating from 25°C to 600°C at a constant rate of 10°C/min under a flowing atmosphere of argon and compressed air (50 ml/min). Once the temperature reached 600°C, the sample was held isothermally for 10 hours to ensure complete dehydration. Throughout the heating and holding stages, the mass of the sample was continuously recorded. The total mass loss observed was subsequently attributed to the release of

hydration water, enabling estimation of the proton concentration incorporated in the BZCYYb system.

5.7 Residual Gas Analysis

Residual Gas Analysis (RGA) is an analytical technique used to monitor and characterise gaseous species present within a closed system. It is typically performed using a mass spectrometer, which separates and detects gases based on their mass-to-charge ratio (m/z). By continuously tracking the intensity of selected m/z values, RGA provides time-resolved information on the evolution of specific species within the system. This enables the trace of interested gas species and the detection of outgassing processes during thermal treatments or reactions.

Theory

The working principle of RGA follows that of mass spectrometry. Ionised gas molecules are passed into a mass analyser, where an applied electric field influences the trajectories of ions according to their mass-to-charge ratio (m/z). As a result, ions with different m/z values are separated. These ions are subsequently collected at a detector, where the measured ion current is proportional to their abundance and, in turn, to the partial pressure of the corresponding gas species in the system. In this way, RGA enables identification of residual gases and determination of their relative concentrations.

Experimental details

The residual gas analysis (RGA) measurements were performed using a quadrupole mass spectrometer (Hiden Analytical), which was calibrated to convert the detected ion current of targeted charged species (e.g., OH^-) into partial pressure values (torr).

The experimental setup is illustrated in Figure 5.6. The sample was loaded into a quartz tube, which was first evacuated to $\sim 10^{-5}$ torr with the pump valve open. Once this vacuum level was reached, the pump valve was closed to maintain the pressure inside the quartz tube. The sealed quartz tube was then positioned inside a tube furnace (Carbolite) for heating. During analysis, the leak valve was carefully adjusted to allow a small portion of the enclosed gas to flow into the quadrupole mass spectrometer, enabling real-time monitoring of the residual gas composition.

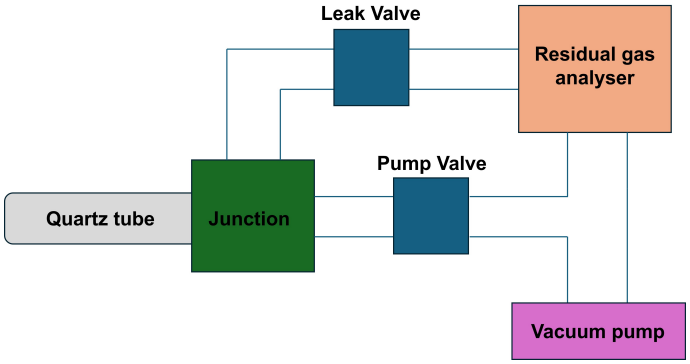


Figure 5.6: The schematic of RGA set up.

5.8 Fourier Transform Infrared Spectroscopy

Fourier Transform Infrared Spectroscopy (FTIR) is a versatile characterisation technique widely applied to investigate the chemical structure of materials. By probing the vibrational signatures of chemical bonds, FTIR provides direct information about the presence of functional groups, the degree of hydration, and possible structural changes during processing or treatment.

Theory

Fourier Transform Infrared Spectroscopy (FTIR) is based on the interaction of infrared (IR) radiation with matter, specifically the absorption of IR light by chemical bonds. When IR radiation passes through a sample, photons with energies matching the vibrational modes of chemical bonds are absorbed, producing characteristic absorption bands in the spectrum. These bands are directly related to the type of chemical bonds and functional groups present in the material.

Experimental details

The BZCYYb powders were analysed using a Bruker FTIR spectrometer. Before each measurement, a background spectrum was collected without the sample in place. This background spectrum was then subtracted from the sample measurement to eliminate atmospheric and instrumental contributions, ensuring that the resulting spectra reflected only the absorption features of the measured samples.

5.9 Isotopic Exchange Secondary-ion Mass Spectrometry Depth Profiling

Isotopic Exchange Depth Profiling (IEDP) is an advanced analytical technique that combines isotopic exchange with secondary-ion mass spectrometry (SIMS) to investigate tracer diffusion of selected isotopes in dense solid samples. In this method, the isotopic

exchange experiement introduces the isotopes into the sample. Subsequently, SIMS is employed to trace the diffusion of exchanged isotopes. This combined approach enables the determination of isotopic distribution and diffusion profiles within the material.

Isotopic Exchange: Theory

Due to the high natural abundance of hydrogen in the environment, probing and tracking its motion within a material is particularly challenging, as background signals from atmospheric hydrogen are unavoidable. To overcome this limitation, deuterium (D) is commonly employed as a labeled tracer to approximate protonic dynamics, taking advantage of the large difference in the natural abundances of hydrogen isotopes, as summarised in Table5.1

Table 5.1: Mass and natural abundance of hydrogen isotopes

Isotopes	Mass (amu)	Natural Abundance(%)
H	1.0078	99.9844
2H	2.0156	99.9844
D	2.0141	0.0156

To determine the protonic diffusion kinetics of the system, the materials are annealed at specific temperatures, pressures and durations in a deuterium-containing atmosphere, enabling the exchange of deuterium into the samples. The advantage of measuring the tracer diffusion kinetics lies in its ability to provide a more direct probing of hydrogen-isotopic dynamics compared to conventional techniques such as electrochemical impedance spectroscopy (EIS), where the EIS technique generally probes the total conductivity instead of protonic conductivity and kinetics exclusively.

Although there is a non-negligible difference in atomic mass between hydrogen (^{1}H) and deuterium (^{2}H) (see Table 5.1), their chemical compositions differ due to the presence of an additional neutron in deuterium. Consequently, a fundamental assumption must be made: the diffusion kinetics of deuterium can be approximated to those of hydrogen. This assumption is critical for interpreting the experimental results and correlating deuterium diffusion behaviour with protonic dynamics.

Isotopic Exchange: Experimental details

To ensure the valid isotopic exchange experiment and reliable diffusion results, the exchanged samples must be prepared according to the following criteria:

Shape — To simplify the diffusion model, deuterium should ideally diffuse only perpendicularly from the surface toward the centre of the sample. In practice, however, deuterium incorporation can occur through three-dimensional diffusion pathways. Therefore, a pellet-shaped sample with a sufficiently large diameter was preferred over a cube-shaped

sample to minimise the influence of lateral diffusions.

Thickness — To prevent the overlap of diffusion fronts originating from the top and bottom surfaces of the pellet, which would lead to an artificially enhanced isotopic signal, the samples must possess sufficient thickness. In this work, the minimum required thickness was set to exceed $4\sqrt{D^{*}t}$, where D^{*} is the tracer diffusion coefficient of deuterium at the target temperature and t denotes the isotopic exchange time.

Density — The open porosity can artificially enhance the measured isotopic diffusion, as exchanged deuterium atoms may migrate through pores rather than diffuse through the dense pellet. To avoid this effect, the relative density of the measured pellets was required to be higher than 95% to ensure the minimisation of open porosity.

Surface Roughness — The surface roughness of the sample can affect the reliability of diffusion measurements, as it introduces uncertainty in determining the diffusion distance from the surface and reduces the spatial resolution of SIMS analysis. To achieve an acceptable surface finish, the sintered pellets were first ground using progressively finer grades of SiC abrasive papers (Struers Co.) with grit sizes of 800, 1200, and 2000. The samples were then polished sequentially with water-based diamond suspensions (Struers Co.) of particle sizes 6 μm, 3 μm, 1 μm, and 0.25 μm.

During the isotopic exchange procedure, the prepared pellets were first subjected to pre-annealing under a controlled atmosphere of 23 torr P_{H_2O} (partial pressure of hydration) at the target temperature (identical to the subsequent exchange temperature) for 10 hours. This pre-annealing duration was selected to be at least eight times longer than the isotopic exchange period, ensuring complete hydration of the samples prior to deuterium exchange. Following this step, the samples were exposed to an atmosphere of 22 torr P_{D_2O} (partial pressure of deuterium oxide) at the temperature same as the pre-annealing temperature for 25 minutes for the isotopic exchange.

To minimise potential diffusion effects during thermal transitions, both the heating and cooling rates were carefully optimised. Specifically, the sample tube was rapidly inserted into a preheated tube furnace that had already stabilised at the target temperature, thereby significantly reducing the heating time. To maximise the cooling rate, the sample tube was swiftly removed from the furnace and air-quenched immediately after the exchange process.

Given the involvement of hydration in the exchange process, precautions were taken to prevent the condensation of H_2O and D_2O on the set up. Heating tapes were applied to maintain elevated temperatures in regions outside the furnace, thereby minimising the condensation occurred throughout the experimental procedure.

Secondary-ion Mass Spectrometry: Theory

Secondary-Ion Mass Spectrometry (SIMS) is an analytical technique used to characterise the surface chemical composition and elemental distribution of samples. In this study, SIMS was employed to investigate the diffusion of proton isotopic tracers in BZCYYb samples following the isotopic exchange.

The working principle of Secondary-Ion Mass Spectrometry (SIMS) is illustrated in Fig 5.7[135]. In this technique, primary ions such as Cs^+ and Bi^+ bombard the sample surface, inducing the sputtering of surface particles. Among these sputtered particles, less than one percent are ionised, forming what are known as secondary ions[136].

Once ejected, the secondary ions drift towards the mass spectrometer under the influence of an electric field generated by the accelerating potential. The mass spectrometer then separates the secondary ions based on their mass-to-charge ratio (m/z), enabling the determination of the sample's surface elemental composition.

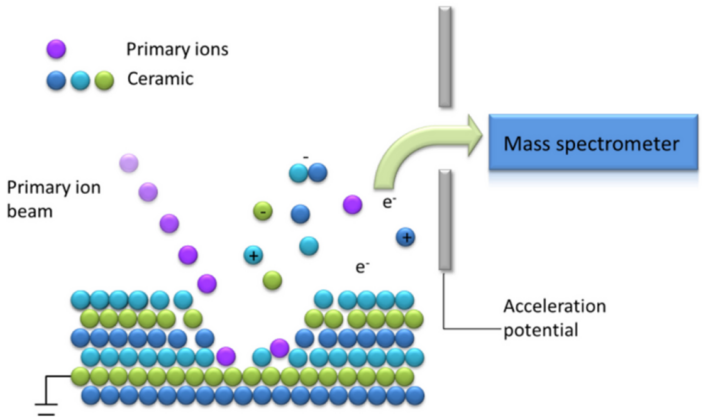


Figure 5.7: The Schematic of Secondary Ion Mass Spectrometry. Reproduced with open access CC-BY 4.0 license[135].

The generated signal from the secondary ion is affected by multiple factors, shown as below:

$$I_s = I_p S_m \alpha F C_m \tag{5.12}$$

where I_s is the current of secondary ion of species m (the measured secondary ion counts of species m), I_p is the primary ion current, S_m is the sputter yield of species m (the amount of species m removed due to the primary ion bombardment), α is the ionisation probability of species m, F is the transmission of the analysis system, and C_m is the concentration of species m on the sample surface.

Equation 5.12 illustrates the complexity of secondary ion generation. The ionisation process of sputtered particles is strongly influenced by the chemical environment of the sample surface, which is a phenomenon known as the matrix effect. However, when analysing the ratio of isotopes, the isotopic species exist within the same chemical environment, minimising the matrix effect. Consequently, SIMS is a practical technique for quantifying isotopic ratios.

Secondary-ion Mass Spectrometry: Experimental details

All SIMS experiments in this project were conducted using a TOF-SIMS 5 instrument (ION-TOF GmbH, Münster), equipped with a Time-of-Flight (ToF) analyser as the mass spectrometer. The instrument layout is presented in Fig 5.8.

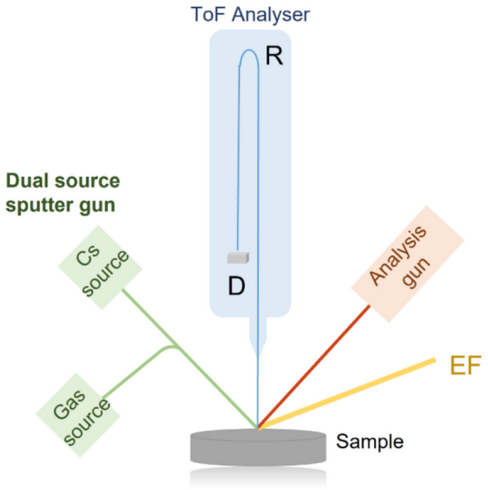


Figure 5.8: The instrument layout of TOF-SIMS 5 with the dual beam configuration. EF is the electron floodgun, R is the reflectron and D is the detector. Reproduced with open access CC-BY 4.0 license[135].

The analysis gun utilised in this study was the liquid metal ion gun (LMIG), which generated a focused ion beam, enabling secondary ion mapping with high lateral resolution. Bismuth was selected as the LMIG source due to its enhanced secondary ion yields[137]. To mitigate charge accumulation on the BZCYYb surface, an electron flood gun was employed.

Due to the high diffusion coefficient and extensive diffusion length of hydrogen (above 10 μm), the line scan analysis method was employed, with the sample preparation process outlined in Fig 5.9[138, 139]. Following isotopic exchange, the BZCYYb pellet was sectioned into two identical bars, as illustrated in Fig 5.9(b) to (c).

The surface sides of the two bars (highlighted in orange in Fig 5.9(c) and (d)) were then bonded together by superglue, leaving the cross-sectional sides exposed. The cross-

sectional surface was subsequently ground and polished to achieve a smooth finish, facilitating precise SIMS measurements.

Since deuterium was incorporated into the pellet during isotopic exchange, the isotopic ratio of deuterium (D) to hydrogen (H) was maximised at the bonded surface and gradually decreased along the cross-sectional direction in both bars, as depicted in Fig 5.9(d).

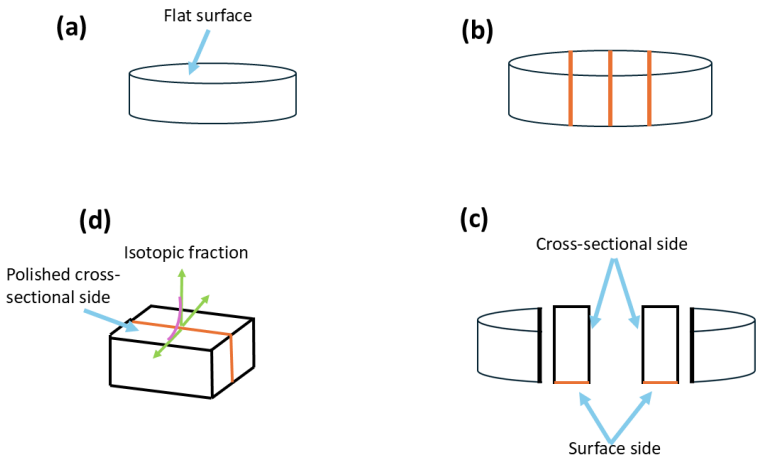


Figure 5.9: The process of sample preparation for line scan analysis, where the sample is exchanged with deuterium.

In addition to line-scan analysis, depth-profile analysis was also employed as a complementary technique. Whereas line-scan analysis is typically suited for measuring diffusion distances greater than 10 µm[139], depth profiling is more appropriate for diffusion lengths ranging from the nm ranges scale up to approximately 5 µm in most cases[135]. In depth profiling, a focused Cs^+ ion beam operated at 2 kV was rastered across a defined region of the sample surface to systematically sputter material. The depth of the sputtered region (the crater) was subsequently measured using a 3D optical interferometer (Zygo NewView 200), allowing the average sputtering rate to be determined. This rate was then used to convert sputtering time into sputtered depth for subsequent depth-profile measurements performed under identical experimental conditions, such as the same ion-beam voltage.

The targeted deuterium has m/z ratio = 2.0141, while the m/z ratio of 2H was 2.0156. To separate these two signals with close m/z ratio, the high current bunch mode (HCBM) was used to separating ions with close m/z ratio such as D and 2H[135].

5.10 Prompt Gamma Rays Activation Analysis

Prompt Gamma Activation Analysis (PGAA) is a versatile, non-destructive technique widely employed for multi-elemental analysis across a broad range of materials. It is particularly valued in materials science because it enables direct, bulk quantification of elements

without the need for dissolution or complex sample preparation[140]. PGAA is especially powerful for the detection of light elements such as hydrogen and nitrogen, which are often difficult to measure accurately with conventional analytical techniques. In studies of proton-conducting ceramics, PGAA provides a unique advantage by allowing the direct determination of hydrogen content within the bulk sample, offering complementary information to surface-sensitive techniques such as EDS and indirect methods such as TGA.

Theory

PGAA is a non-destructive nuclear analytical technique that determines elemental composition by detecting prompt gamma rays emitted during neutron capture reactions. The principle is based on the excitation and de-excitation of nuclei following neutron capture. When a low-energy (typically thermal or cold) neutron interacts with an atomic nucleus, it may be absorbed rather than scattered, forming a compound nucleus in an excited state. This unstable intermediate then relaxes to its ground state by emitting prompt gamma rays.

The energy of these emitted gamma rays is characteristic of the element and nuclear transition involved, thereby providing a direct fingerprint for elemental identification. Moreover, the intensity of the emitted gamma rays is proportional to the concentration of the element in the sample, enabling quantitative analysis.

Experimental details

Prompt Gamma-Ray Activation Analysis (PGAA) was carried out at the Budapest Neutron Centre (BNC). Two types of BZCYYb powder samples were prepared for analysis: a dehydrated sample and a hydrated sample.

For the dehydrated BZCYYb, the powder was annealed at 600°C for 10 hours to promote maximum removal of water. After treatment, the sample was stored in a sealed glass bottle wrapped with parafilm to minimise rehydration prior to measurement.

For the hydrated BZCYYb, the powder was annealed under a flow of humidified compressed air (3 vol% H_2O, introduced via a room-temperature water bubbler) at 450°C for 8 hours. Following annealing, this sample was also sealed in a glass bottle with parafilm to preserve its hydration state until the experiment.

During PGAA measurements, both dehydrated and hydrated powders were loaded into Teflon bags. Teflon was chosen as the container material because of its low neutron absorption cross-section and minimal gamma-ray background contribution, ensuring accurate hydrogen quantification.

5.11 Electrochemical Impedance Spectroscopy

Electrochemical Impedance Spectroscopy (EIS) is a powerful electrochemical technique widely used to characterise the transport and interfacial properties of functional materials. By applying an alternating current (AC) signal over a broad frequency range and measuring the resulting voltage response, the technique provides frequency-dependent information about resistance, capacitance, and other electrical processes occurring within the sample[141].

In ceramic electrolytes, EIS is particularly valuable for probing how proton transport responds to changes in the surrounding gas atmosphere. By monitoring conductivity under controlled environments such as dry air, humidified air, or hydrogen-rich atmospheres, EIS can reveal the contributions of hydration, proton incorporation, and defect interactions to the overall transport behaviour. This capability makes it a powerful tool for directly linking proton dynamics to environmental conditions, thereby providing critical insights into the operational behaviour of proton-conducting electrolytes in fuel cell applications.

Theory

EIS is a widely used technique for probing the electrical properties of materials. By applying a small alternating current (AC) signal over a broad frequency range and measuring the resulting voltage response, EIS enables separation of different electrical processes that occur simultaneously in a material. For ceramic electrolytes, these processes include bulk conduction, grain boundary conduction, and electrode-related phenomena.

The relationship between the applied AC voltage and the resulting current can be expressed using complex numbers notation. An AC voltage applied to the system can be written as a cosine function:

$$\mathrm{V(t)} = \mathrm{V_0 cos(\omega t)} \tag{5.13}$$

where V_0 is the voltage amplitude and ω is the angular frequency. The current response has the same frequency but is generally shifted in phase by an angle ϕ, reflecting resistive and reactive contributions of the material:

$$I(t) = I_0 \cos(\omega t - \phi) \tag{5.14}$$

To convert the these trigonometric expressions in exponential form, which is mathematically more convenient for impedance analysis, the Euler's formula is applied:

$$\mathrm{e^{j\theta}} = \cos(\theta) + \mathrm{j}\sin(\theta) \tag{5.15}$$

Hence, the AC voltage and its corresponding responding current can be expressed in the

exponential form:

$$\mathrm{V} = \mathrm{V}_0 \mathrm{e}^{\mathrm{j}\omega \mathrm{t}} \tag{5.16}$$

$$\mathrm{I} = \mathrm{I}_0 \mathrm{e}^{\mathrm{j}\omega \mathrm{t} - \phi} \tag{5.17}$$

which facilitates the expression of impedance (the ratio of voltage to current) in the exponential form:

$$\mathrm{Z} = \frac{\mathrm{V}}{\mathrm{I}} = \frac{\mathrm{V}_0 \mathrm{e}^{\mathrm{j}\omega \mathrm{t}}}{\mathrm{I}_0 \mathrm{e}^{\mathrm{j}\omega \mathrm{t} - \phi}} = \frac{\mathrm{V}_0}{\mathrm{I}_0} \mathrm{e}^{\mathrm{j}\phi} \tag{5.18}$$

and by rearranging the exponential form of impedance, it can be classified into real and imaginary components based on again the Euler's formula (Equation 5.15), as illustrated in Equation 5.19:

$$\mathrm{Z} = \frac{\mathrm{V}_0}{\mathrm{I}_0} \mathrm{e}^{\mathrm{j}\phi} = \frac{\mathrm{V}_0}{\mathrm{I}_0} \cos(\phi) + \mathrm{j} \frac{\mathrm{V}_0}{\mathrm{I}_0} \sin(\phi) = \mathrm{Z}' + \mathrm{j}\mathrm{Z}'' \tag{5.19}$$

where Z' represents the real part of impedance, equals to $\frac{V_0}{I_0} cos(\phi)$, while Z'' indicates the imaginary part corresponding to $j\frac{V_0}{I_0} sin(\phi)$, and j is the $\sqrt{-1}$, and the impedance data are typically represented in a Nyquist plot, where Z' is plotted against $-Z''$ as shown in Figure 5.10.

To interpret EIS spectra shown in the Nyquist plot, equivalent circuit models are em-

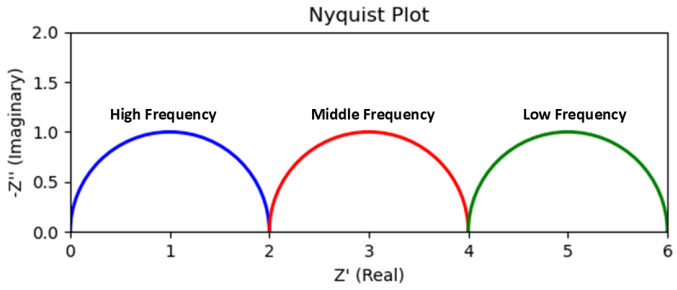


Figure 5.10: The example of typical Nyquist plot with three separate processes (each process follows the resistor-capacitor parallel equivalent circuit model).

ployed to represent electrochemical processes with simple electrical elements: resistors (R), capacitors (C), and inductors (L, which is a passive circuit element stores energy in the form of magnetic field and exhibit an impedance proportional to frequency of AC perturbation). For example, a parallel RC circuit is commonly used to describe processes such as bulk or grain boundary conduction. The most common applied mathematical model representing the electrochemical process is the parallel resistor-capacitor circuit, where the

impedance of a parallel-connected RC circuit is given by Equation 5.20:

$$\mathrm{Z_{RC}} = \frac{\mathrm{R}\frac{1}{\mathrm{j}\omega\mathrm{C}}}{\mathrm{R}+\frac{1}{\mathrm{j}\omega\mathrm{C}}} = \frac{\mathrm{R}}{1+\mathrm{j}\omega\mathrm{RC}} = \frac{\mathrm{R}}{1+(\omega\mathrm{RC})^2} - \mathrm{j}\frac{\omega\mathrm{R}^2\mathrm{C}}{1+(\omega\mathrm{RC})^2} \tag{5.20}$$

where the impedance of the resistor is R, the impedance of the capactior is $j\omega C$ with capacitance C value. This impedance of the RC parallel-connected circuit can be also separated into the real part (Equation 5.21) and imaginary part (Equation 5.22) with the ωRC subsituted by $tan(\theta)$ for introducing the trigonometry relationship:

$$\mathrm{Z'} = \mathrm{x} = \frac{\mathrm{R}}{1+(\omega\mathrm{RC})^2} = \frac{\mathrm{R}}{1+\tan^2(\theta)} \tag{5.21}$$

$$\mathrm{Z''} = \mathrm{y} = -\frac{\omega\mathrm{R}^2\mathrm{C}}{1+(\omega\mathrm{RC})^2} = \frac{\mathrm{R}\tan(\theta)}{1+\tan^2(\theta)} \tag{5.22}$$

Based on the trigonometry relationships shown in Equation 5.23-5.25, the real part of impedance can be expressed in Equation 5.26 and 5.27, which can then be rearranged by squaring both parts of x and y, yielding to relationship shown in Equation 5.28 and 5.29, which can be simplified by the Pythagorean equation (Equation 5.31) to the final equation (Equation 5.32) which satisfies the equation of a circle centred at $(\frac{R}{2}, 0)$ with radius $\frac{R}{2}$. Hence, the impedance of RC parallel-connected circuit expresses the semicircle geometry in the Nyquist plot.

$$1+\tan^2(\theta) = \frac{1}{\cos^2(\theta)} \tag{5.23}$$

$$\cos^2(\theta) = \frac{1+\cos(2\theta)}{2} \tag{5.24}$$

$$2\sin(\theta)\cos(\theta) = \sin(2\theta) \tag{5.25}$$

$$\mathrm{x} = \mathrm{R}\frac{1+\cos(2\theta)}{2} = \frac{\mathrm{R}}{2}(1+\cos(2\theta)) \tag{5.26}$$

$$\mathrm{y} = \mathrm{R}\frac{\sin(2\theta)}{2} = \frac{\mathrm{R}}{2}\sin(2\theta) \tag{5.27}$$

$$(\mathrm{x}-\frac{\mathrm{R}}{2})^2 = (\frac{\mathrm{R}}{2})^2\cos^2(2\theta) \tag{5.28}$$

$$\mathrm{y}^2 = (\frac{\mathrm{R}}{2})^2\sin^2(2\theta) \tag{5.29}$$

$$(\mathrm{x}-\frac{\mathrm{R}}{2})^2 + \mathrm{y}^2 = (\frac{\mathrm{R}}{2})^2(\cos^2(2\theta)+\sin^2(2\theta)) \tag{5.30}$$

$$\cos^2(2\theta)+\sin^2(2\theta) = 1 \tag{5.31}$$

$$(\mathrm{x}-\frac{\mathrm{R}}{2})^2 + \mathrm{y}^2 = (\frac{\mathrm{R}}{2})^2 \tag{5.32}$$

$$\tag{5.33}$$

As described by the preceding equations, an equivalent circuit consisting of a parallel

connection between an ohmic resistor (R) and a capacitor (C) can accurately reproduce the ideal semicircular Nyquist response in EIS measurements. However, in most practical cases, the measured semicircles appear distorted and exhibit noticeable broadening, as illustrated in Figure 5.11[142].

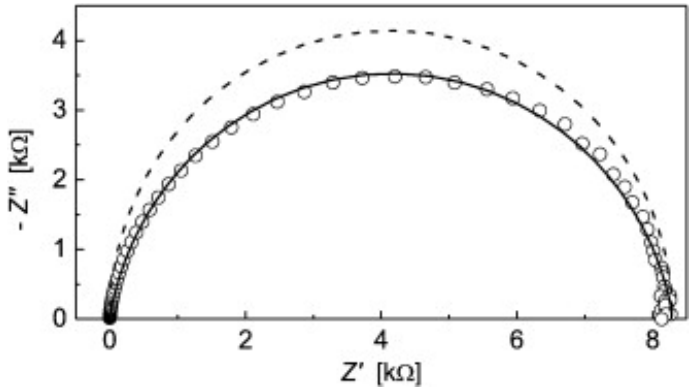


Figure 5.11: The illustration of ideal semicircle in Nyquist plot in theory (dashed line) and the measured deformed semicircle (solid line)[142]. Reprinted from Solid State Ionics, 180, Shoar Abouzari et al., "On the physical interpretation of constant phase elements", 922-927, (2009), with permission from Elsevier.

The origin of the deformed semicircle has been extensively investigated in previous studies and has been attributed to several factors, including the formation of an electrical double layer at the electrode interface[143], correlated ionic oscillations[142], and contributions from metal-electrode interfacial capacitance[144]. Although multiple explanations have been proposed, the most widely adopted approach is to introduce a constant phase element (CPE) in place of the ideal capacitor (C) to model the non-ideal semicircular response. The effective capacitance of the CPE (C_{eff}), as proposed by Hsu et al.[145], is expressed as follows::

$$C_{\text{eff}} = Q(\omega)^{\alpha-1} \tag{5.34}$$

where Q is the pseudo-capacitance term, α is the phase deviation, ω is the angular frequency of appliec AC signal. Hence, based on this relationship, the approximated capacitance of the deformed semicircle can be fitted in the EIS measurement.

Experimental details

A symmetric cell configuration was employed to investigate the electrical performance of BZCYYb1711 system. For this purpose, both the top and bottom surfaces of the sintered BZCYYb pellet were coated with a 200 nm platinum layer. Owing to the high electronic conductivity of platinum, the electrodes themselves served as both contact and current collector, eliminating the need for additional current-collecting layers.

The impedance response was recorded using a frequency response analyser (FRA, Solartron SI 1260, Solartron Analytical, UK) over a frequency range of 1 MHz to 1 Hz. The AC voltage applied on the measured sample was 12 mV. To investigate the effect of hydration on the total conductivity measured of BZCYYb1711 symmetric cell, EIS measurements were performed under dry and humid compressed air atmosphere with identical symmetric cell. The supplied compressed air (BOC, UK) was passed through a water bubbler at room temperature to provide 3 vol% H_2O to create the humid environment, while the drying tube containing Drierite (Sigma Aldrich, UK) was applied to form a reference dry compressed air atmosphere.

5.12 Neutron Compton Scattering

Neutron Compton Scattering (NCS), also known as Deep Inelastic Neutron Scattering (DINS)[97], is a powerful technique for probing the local dynamics of light atoms in condensed matter, particularly hydrogen. By measuring the energy and momentum transfer when neutrons scatter at very high energies, NCS provides direct access to the momentum distribution of nuclei on the femtosecond timescale ($\sim 10^{-15}$ s). This capability allows the technique to study very local dynamics of atoms such as hydrogen, enabling a quantitative and qualitative analysis on the localised environment and force fields experienced by hydrogen atoms in BZCYYb system.

Theory

The sensitivity of NCS to hydrogen can be better understood by considering the layout of a dedicated instrument. Vesuvio, the NCS beamline at the ISIS Neutron and Muon Source (UK), is equipped with detectors positioned in both forward and backward scattering geometries (Figure 5.12)[97]. This dual-detector configuration is central to the technique: it allows discrimination between scattering from light atoms, such as hydrogen, and heavier elements, thereby enhancing the element-specific resolution of the method. The hydrogen recoil peak appears prominently in the forward-scattering detectors, whereas signals from heavier elements (e.g. carbon, nitrogen, aluminium) dominate in the backscattering geometry[146]. This distinction originates from kinematic considerations: because neutrons are only slightly heavier than protons, forward scattering is energetically favourable for hydrogen, while heavier nuclei scatter more efficiently into the backward direction. Consequently, NCS provides a direct and selective probe of hydrogen in complex materials, making it highly suitable for studying proton incorporation in proton-conducting oxides.

In neutron Compton scattering (NCS), high-energy epithermal neutrons (in the eV range) are employed to probe nuclear momentum distributions (NMDs)[147]. The use of such energetic neutrons simplifies the description of the scattering process: collisions oc-

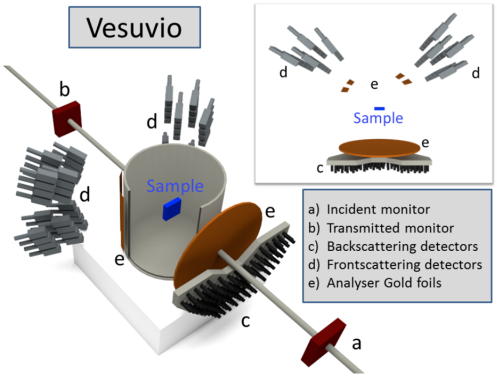


Figure 5.12: The schematic of Vesuvio beamline[97]. Electron-volt neutron spectroscopy: beyond fundamental systems, Andreani et al., Advances in Physics, copyright at 2017, reprinted by permission of Informa UK Limited, trading as Taylor & Francis Group.

cur over extremely short timescales and can be treated as instantaneous, while the large momentum transfer forces the struck atom to recoil almost freely, with negligible influence from neighbouring atoms. These assumptions underpin the impulse approximation (IA), which describes neutron scattering as instantaneous interactions with individual nuclei, where the transferred energy and momentum are unaffected by the surrounding lattice.

Within the IA framework, the dynamic structure factor S(q, ω), which in general represents the probability of a scattering event with momentum transfer q and energy transfer $\hbar\omega$, reduces to a single recoil peak centred at the recoil energy $\omega_r = \hbar^2 q^2/2M$, with M being the atomic mass of the recoiling nucleus. This recoil peak is directly related to the NMD of the scattering atom $n(p)$, as expressed in Equation 5.35. Furthermore, by applying the West scaling relation, which assumes the limits of infinite momentum and energy transfer ($q \to \infty$, $\omega \to \infty$)[148], S(q, ω) becomes independent of q and ω and can be expressed in terms of the Compton profile $J(y, \hat{q})$. The Compton profile describes the projection of the NMD along the direction of momentum transfer $\hat{q}$, where y is the West scaling variable defined in Equation 5.37. In this way, the measured scattering signal provides a direct representation of the atomic momentum distribution.

$$S_{IA}(q,\omega) = \int n_m(p)\delta(\omega + \frac{p^2}{2M} - \frac{(p+q)^2}{2M}) \tag{5.35}$$

$$S_{IA}(q,\omega) = \frac{m}{\hbar^2 q} J(y,\hat{q}) \tag{5.36}$$

$$y = p \cdot \hat{q} = \frac{m}{\hbar^2 q}(\omega - \omega_r) = \frac{M}{\hbar^2 q}(\omega - \frac{\hbar^2 q^2}{2m}) \tag{5.37}$$

The recoil peak is a central concept in analysing NCS spectra, as it provides three key pieces of information about the scattering atom: its identity, its kinetic properties, and its relative abundance in the sample. First, the position of the recoil peak in (q, ω)

space is determined by the atomic mass M of the scattering nucleus, meaning that atoms of different masses produce recoil peaks at distinct energies. This enables straightforward identification of the element responsible for a given peak. Second, under the impulse approximation, the effect of neighbouring atoms is negligible, so the width of the recoil peak reflects the intrinsic nuclear momentum distribution (NMD) of the atom. Since broader NMDs correspond to higher kinetic energies, the recoil peak width provides direct insight into the localised kinetic behaviour of atoms, allowing qualitative comparisons between species within the sample. Finally, the integrated intensity of the recoil peak carries quantitative information about atomic abundance. Atoms with the same mass M contribute collectively to a single recoil peak at the characteristic position for that mass. Consequently, the integrated intensity of the recoil peak, I_m, is directly proportional to the number of moles n_m of that element in the sample and its total bound neutron scattering cross-section σ_m, as expressed in Equation 5.38-5.39[149].

$$I_m \propto n_m \sigma_m \tag{5.38}$$

$$\frac{n_{m1}}{n_{m2}} = \frac{I_{m1}\sigma_{m2}}{I_{m2}\sigma_{m1}} \tag{5.39}$$

Building on the concept of recoil peaks and their role in analysing nuclear momentum distributions, it is important to outline how the Vesuvio instrument measures the relevant scattering parameters. As introduced in the section5.12, Vesuvio operates as a Time-of-Flight (ToF) inverse-geometry spectrometer. In this configuration, the final energy of scattered neutrons (E_1) is fixed by the analyser foils, while the incident energy (E_0) is determined from the neutron flight time. The relationship between the neutron travel time t and the instrument geometry is expressed in Equation 5.40, where L_0 is the source-to-sample distance, L_1 is the sample-to-detector distance, v_0 is the incident neutron velocity linked to E_0 through Equation 5.41, and v_1 is the detected neutron velocity corresponding to E_1 as in Equation 5.42. Thus, by measuring t together with the known E_1, and using the instrument parameters L_0 and L_1, the incident energy E_0 can be determined. From this, the energy transfer ω and momentum transfer q are readily obtained using Equations 5.43-5.44, which are the essential variables required to analyse the recoil peaks in NCS spectra.

$$t = \frac{L_0}{v_0} + \frac{L_1}{v_1} \tag{5.40}$$

$$v_0 = \frac{\sqrt{2E_0}}{m} \tag{5.41}$$

$$v_1 = \frac{\sqrt{2E_1}}{m} \tag{5.42}$$

$$\omega = E_0 - E_1 \tag{5.43}$$

$$q = \sqrt{2m}(E_0 + E_1 - 2cos\theta\sqrt{E_0 E_1}^{\frac{1}{2}}) \tag{5.44}$$

Because Vesuvio is a time-of-flight instrument, its raw data are naturally recorded and displayed as count rate versus ToF, as illustrated by Figure 5.13. Each recoil peak corresponds to the nuclear momentum distribution of a specific element, arising from scattering of the incident epithermal neutrons (in the eV energy range). Because the scattered neutron energy depends on the mass of the target nucleus, different elements can be resolved in the same measurement.

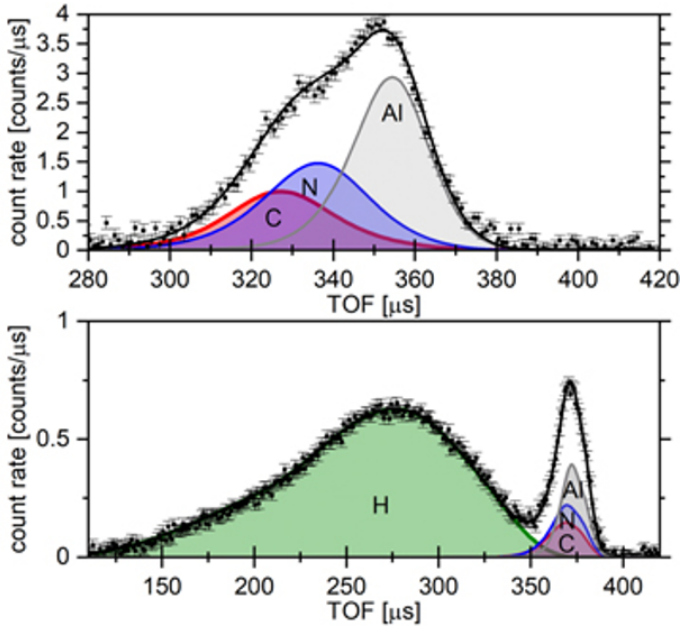


Figure 5.13: The example of NCS data and fit of recoil peaks from multiple elements: hydrogen (olive line and shaded area), carbon (red line and shaded area), nitrogen (blue line and shaded area), and aluminium from the sample container (grey line and shaded area). The top figure shows the data and fitting for backscattering, while the bottom figure shows the forward scattering results[146]. Reproduced with permission from American Chemical Society, open access CC-BY-NC-ND 4.0 license

Nevertheless, a discrepancy arises between the experimental output and the physical interpretation of NCS spectra. The measurable quantities are count rate and ToF, whereas the physically meaningful description of recoil peaks, which contain information on atomic identity, momentum distribution, and kinetic energy, is expressed in terms of momentum

transfer (q) and energy transfer (ω). To bridge this gap, the count rate describes the energy and momentum transfer $C(\theta = \text{const}, E_0)$ can be expressed as in Equation 5.45, where A is an instrumental constant, n is the number density of scatterers, b is the bound neutron scattering length, and $I(E_0)$ is the incident neutron energy distribution. Using the Jacobian factor dE_0/dt demonstrated in Equation 5.47, this count rate can then be converted into the time domain (Equation 5.46), as described by Mayers[150]. The resulting expression, shown in Equation 5.48, links the measured ToF spectrum directly to the integrated peak intensities I_m of atoms with mass m. These integrated intensities are in turn proportional to the nuclear momentum distribution (NMD) of the atoms, thereby connecting the experimentally accessible counts-ToF data with the physically interpretable recoil peaks in (q, ω) space.

As discussed in the previous paragraph, the measured TOF spectra on Vesuvio are first expressed in terms of count rate as a function of time, which can be related to the integrated recoil intensities of atoms with different masses (Equation 5.48). However, this expression is based on the idealised assumption of a fixed scattering angle. In real experimental conditions, the detected count rate $C(\theta, t)$ represents an average over a distribution of scattering angles and neutron trajectories. To account for these geometrical effects, a resolution function $R(y_m)$ is introduced, which describes the broadening and distortions imposed by the instrument. Within the standard data reduction scheme for NCS, this is addressed using the convolution approximation (CA). The CA assumes that the measured TOF spectrum is the convolution of the instrument resolution function $R(y_m)$ with the intrinsic neutron Compton profile $J(y_m)$ of the scattering atoms. This convolution is carried out in y-space for each atomic species of mass m, and the resulting contributions are summed to yield the total measured count rate $C(\theta, t)$, as expressed in Equation 5.49.

$$C(\theta = const, E_0) = Anb^2\sqrt{\frac{E_1}{E_0}}I(E_0)S(\theta = const, \omega) \tag{5.45}$$

$$C(t) = C(E_0)\frac{dE_0}{dt} \tag{5.46}$$

$$\frac{dE_0}{dt} = \frac{2}{L_0}\sqrt{\frac{2}{m}}E_0^{\frac{3}{2}} \tag{5.47}$$

$$C(\theta = const, t) = A'\frac{E_0(t)I[E_0(t)]}{q(t)}\sum_m I_m m J_m(y_m(t)) \tag{5.48}$$

$$C(\theta, t) = A'\frac{E_0(t)I[E_0(t)]}{q(t)}\sum_m I_m m J_m(y_m(t)) \otimes R_m[y_m(t)] \tag{5.49}$$

In summary, the experimentally measured ToF spectra and the physically meaningful energy-domain representation are interchangeable through the theoretical framework and transformations outlined above (e.g. Equation 5.49). To clarify the data processing

pathway for this complex neutron technique, a flow diagram is provided in Figure 5.14. It should be emphasised that, during Vesuvio data analysis, only the Compton profiles $J(y)$ of the atoms are directly fitted. The corresponding ToF spectra are obtained by converting the fitted energy-domain profiles back into the time domain, ensuring consistency between the physical interpretation and the experimental observables.

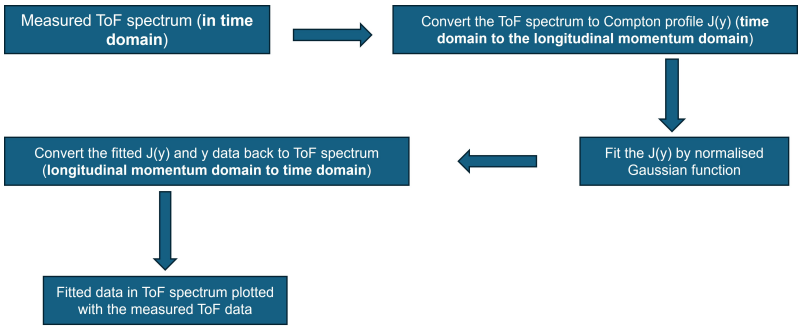


Figure 5.14: The flow diagram illustrates the scheme of data fitting, connecting the measured ToF spectrum and the J(y) (Compton profile) which describes the NMD (nuclear momentum distribution) of targeted atom.

Experimental details

NCS experiments were performed at the Vesuvio beamline, ISIS Neutron and Muon Source (UK). Two types of BZCYYb powder samples were prepared and analysed: a dried sample and a hydrated sample:

For the dried sample, BZCYYb powder was heated at 600°C for 10 hours in order to achieve complete dehydration. After cooling, the powder was immediately transferred into a sealed glass bottle and wrapped with parafilm to minimise rehydration prior to the measurement.

For the treated sample, BZCYYb powder was annealed at 450°C for 8 hours under a flow of humidified compressed air (20 vol % H_2O). Humidification was achieved by passing the carrier gas through a water bubbler maintained at 60°C, with heating tape applied to the connecting lines to prevent condensation. The annealed sample was then sealed in a glass bottle with parafilm to preserve its hydrated state until analysis.

In the NCS measurements, both powders were loaded into an aluminium sample holder. Aluminium was chosen because its nuclear momentum distribution is well characterised and routinely used as a calibration reference for the Vesuvio beamline.

The ability of NCS to discriminate between hydrogen and heavier elements through forward and backward detectors provides a practical means of improving the accuracy of hydrogen Compton profile $J(y)$ fitting. Generally, the NCS data is typically modelled as a

sum of the Compton profiles of all constituent atoms. However, simultaneously fitting multiple atomic species increases model complexity and often leads to large standard errors, particularly in multi-element systems such as BZCYYb. To mitigate this, a sequential fitting strategy was employed in the data processing step. First, the backward-detector data without hydrogen signal contribution was fitted to determine the Compton profiles of the heavier elements. These fitted parameters were then fixed during the analysis of the forward-detector spectrum, where the hydrogen recoil signal dominates. By decoupling the hydrogen contribution from that of other atoms, this approach improves both the robustness and accuracy of the extracted hydrogen $J(y)$.

In the case of NCS data fitting, an assumption was applied that the the Compton profile $J(y)$ exhibited the normalised 1D Gaussian format shown in Equation 5.50, where σ_p is the standard deviation linked with the width of the Compton profile $J(y)$ in y-scale[149]. This assumption describes that atoms are bound harmonically and isotropically with the small displacement from the harmonic position. At the room-temperature experiment, BZCYYb matrix elements (e.g. barium) possessed small displacements due to large atomic masses[151]. However, in the case of mobile hydrogen atoms, this ideal isotropic model may not be suitable, which will be described in more details in the following content.

$$J(y) = \frac{1}{\sqrt{2\pi\sigma_p^2} exp(\frac{-y^2}{2\sigma_p^2})} \tag{5.50}$$

5.13 Quasielastic Neutron Scattering (QENS)

Quasielastic Neutron Scattering (QENS) is a powerful spectroscopic technique used to probe the localised dynamics of atoms and molecules on the nanosecond to picosecond timescale and the Angstrom length scale. By analysing the small broadening of the elastic neutron scattering peak, QENS provides direct information about stochastic motions such as diffusion, rotational reorientation, or localised hopping processes.

In the context of solid-state ionics and proton-conducting oxides, QENS enables the quantitative determination of key dynamic parameters, such as self-diffusion coefficients and relaxation times, thereby bridging the gap between crystallographic structure and macroscopic conductivity, offering unique insight into the microscopic mechanisms of proton transport.

Theory

The principle of QENS is governed by two fundamental conservation laws that apply to incident and scattered neutrons during collision with the sample: conservation of

momentum and conservation of energy[152]:

$$\mathrm{E_{neutron}} = \frac{\hbar^2 \mathrm{k}^2}{2\mathrm{m}} \tag{5.51}$$

$$\hbar \mathrm{q} = \hbar(\mathrm{k_0} - \mathrm{k_1}) \tag{5.52}$$

$$\hbar\omega = \mathrm{E_0} - \mathrm{E_1} = \frac{\hbar^2}{2\mathrm{m}}(|\mathrm{k_0}|^2 - |\mathrm{k_1}|^2) \tag{5.53}$$

Equation 5.51 describes the neutron energy, where E is the energy of a neutron, $\hbar$ is the reduced Planck constant, m is the mass of a neutron, and k is the magnitude of the neutron wave vector, defined as $k = 2\pi/\lambda$, where λ is the neutron wavelength. Equation 5.52 demonstrates the relationship between the neutron wave vector (k) and momentum transfer (q), where q represents the momentum transfer between incident and scattered neutrons, k_0 is the wave vector of the incident neutron while k_1 is the wave vector of neutron scattered by the sample. Equation 5.53 shows the energy transfer fron the neutron to collided sample atoms, where $\hbar\omega$ denotes the energy transfer, E_0 is the incident nuetron energy and E_1 corresponds to the energy of scattered neutrons.

These relations show that when neutrons scatter from a sample, they may undergo a change in momentum (Equation 5.52) and/or a change in energy (Equation 5.53). When considering the change of energy transfer, the neutron scattering can be classified into three cases: elastic ($\hbar\omega = 0$), inelastic ($\hbar\omega \neq 0$) and quasielastic (where the small energy transfer occurs around the elastic peak), as illustrated in Figure 5.15 (a). The quasielastic pattern is the broadening of the elastic peak due to the non-zero energy transfer signal representing mobile species scattering. The term half-width-half-maximum (HWHM) is generally applied to quantify the width of the QENS broadening.

In a QENS experiment, the fundamental measured quantity is the double differential cross section $\frac{d^2\sigma}{d\Omega dE}$, which represents the number of scattered neutrons within the solid angle $d\Omega$ and change of energy dE. By integrating this term over all possible scattering angles and energy transfers, one obtains the total cross section per scatterer, which represents the effective areas of the nucleus observed by the incident neutrons. This is expressed in Equation 5.54:

$$\sigma = \int dE \int d\Omega \frac{d^2\sigma}{d\Omega dE} = 4\pi < b^2 > \tag{5.54}$$

where σ is the total cross section per scatterer, and b is the scattering length which determines the intensity of scattered neutrons.

Building on the definition of the double differential cross section, it is important to recognise that the total scattering signal can be separated into coherent and incoherent

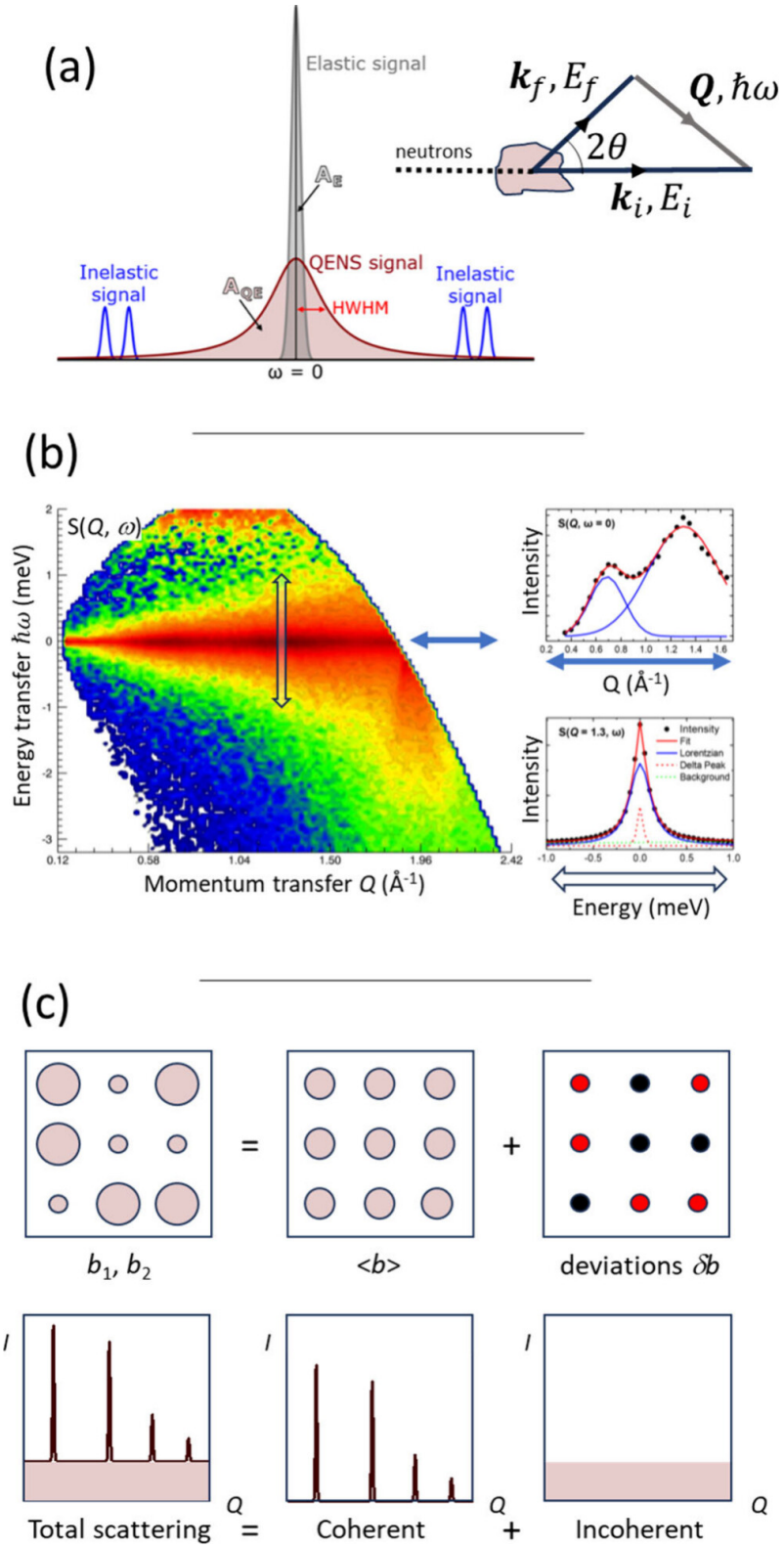


Figure 5.15: (a) The schematic example of neutron scattering spectrum contains elastic peak (grey), inelastic peak (blue) and quasielastic broadening peak (red), classified based on different change of energy transfer value. (b) The example plot of energy transfer ($\hbar\omega$) versus momentum transfer (q) of the $\delta - Bi_2O_3$ sample at 730°C[153]. (c) The schematic demonstrates that the total scattering signal can be classified into the coherent signal and the incoherent signal, where the coherent scattering contains the peak shape pattern in the q range, while the incoherent signal appears as a flat background. Reproduced with permission from American Chemical Society, open access CC-BY-NC-ND 4.0 license, copyright credit to 2025 Schwaighofer et al.[92]

contributions, as expressed in Equation 5.55:

$$\frac{d\sigma}{d\Omega dE} = \frac{k_1}{k_0}\frac{1}{4\pi\hbar}[\sigma_{coh}S_{coh}(q,\omega) + \sigma_{inc}S_{inc}(q,\omega)] \tag{5.55}$$

Here, σ_{coh} and σ_{inc} are the coherent and incoherent contributions to the total scattering cross section per nucleus, while $S_{coh}(q,\omega)$ and $S_{inc}(q,\omega)$ are the corresponding dynamic structure factors that describe the probability of neutrons being scattered with momentum transfer q and energy transfer $\hbar\omega$. The distinction between these two types of scattering is illustrated in Figure 5.15 (c). In constrast to the the coherent scattering signal, the incoherent signal does not produce peak-shape intensities, since it provides the dynamic information from individual atoms instead of the collective interference between atoms.

The strength of QENS in probing proton dynamics stems from the fact that hydrogen has a dominantly large incoherent scattering cross section relative to its coherent contribution (see Table 5.2). This ensures that the measured QENS signal is overwhelmingly sensitive to the motions of individual protons, allowing the extraction of localised dynamical information without interference from collective atomic correlations.

Table 5.2: Bound scattering cross section of elements in the BZCYYb1711 system.[154]

Element	σ_{coh}	σ_{inc}
H	1.757±0.001	80.26±0.06
O	4.232±0.006	0.000±0.008
Ba	3.23±0.04	0.2±0.1
Zr	6.44±0.05	0.01±0.05
Ce	2.94±0.02	0.0
Y	7.55±0.04	0.15±0.08
Yb	19.42±0.09	4.0±0.2

Experimental details

In the QENS experiments, the BZCYYb powders were sealed in quartz tubes to isolate the sample environment from external influences, such as the vacuum conditions within the beamline furnaces.

The QENS measurements were carried out in two neutron beam sources: IN16B beamline at the Institut Laue–Langevin (ILL) in France, and BASIS beamline at Oak Ridge in USA. Three types of samples were prepared for QENS measurements: first, BZCYYb powders annealed under humid hydrogen-nitrogen mixed atmopshere were refered as BZCYYb-HH. Second, powders annealed under humid air condition were refered as BZCYYb-HA. Third, the as-calcined BZCYYb powders acting as the pristine reference without humid

treatment (refered as BZCYYb-cal). BZCYYb-HH powders were annealed at 450°C for 8 h in 5% H_2/ 95% N_2 atmosphere (BOC, UK) with 20 vol% H_2O. The BZCYYb-HA powders were annealed at 450°C for 8 h in compressed air atmosphere (BOC, UK) with 20 vol% H_2O.

Chapter 6: Existence of Protons in As-calcined $BaZr_{0.1}Ce_{0.7}Y_{0.1}Yb_{0.1}O_{3-\delta}$

6.1 Crystal Structure and Composition Analysis

As discussed in section 3.1, one unresolved issue in the current literature is the unexpectedly similar conductivities observed under dry and humid atmospheres. A hypothesis is that BZCYYb1711 inherently contains a significant amount of protons even without deliberate humidification treatment. To examine this hypothesis, two types of BZCYYb1711 powders were prepared. The first type of sample, which was collected immediately after the calcination process (details provided in Section 4.1), was used as the nominally dry reference and is hereafter designated as BZCYYb-cal. The second type of samples was the as-calcined powder subsequently annealed in humid air (3 vol % H_2O) at 450°C for eight hours to serve as the humid reference, denoted as BZCYYb-HA. In addition, to determine whether the conductivity of the synthesised BZCYYb1711 exhibits the same limited variation between dry and humid atmospheres, a dense sintered pellet was fabricated from the BZCYYb-cal powder (preparation details provided in section 4.2) and is hereafter referred to as BZCYYb-pellet.

The chemical composition of the synthesised BZCYYb samples e.g. BZCYYb-cal, BZCYYb-HA, and the sintered BZCYYb pellet was examined due to the complexity introduced by the multi-element doping strategy. Inductively coupled plasma optical emission spectroscopy (ICP-OES) was employed to determine the bulk elemental composition, providing quantitative analysis of the overall stoichiometry. To complement this, energy-dispersive X-ray spectroscopy (EDS) was used for ahieving both local compositional assessment and elemental mapping of the sample surfaces.

Figure 6.1 presents the ICP-OES results, including both the barium calibration curve and the measured barium concentration in the dissolved and diluted BZCYYb-HA powder solution. To establish the calibration curve, eight barium standard solutions of known concentrations were prepared. The emission intensity at the selected barium wavelength (455.403 nm) was recorded for each standard, yielding a linear calibration curve. This curve was then used to interpolate the barium concentration in the sample solution.

Table 6.1 presents the elemental concentrations of the prepared BZCYYb sample solutions, as measured by ICP-OES, along with the corresponding molar ratios relative to barium. These ratios were used to assess the stoichiometry of the BZCYYb samples. To minimise the possibility of anomoly data, each sample was independently dissolved and diluted into three separate solutions. The mean of the three measured concentrations was reported as the final concentration in parts per million (ppm), while the standard devi-

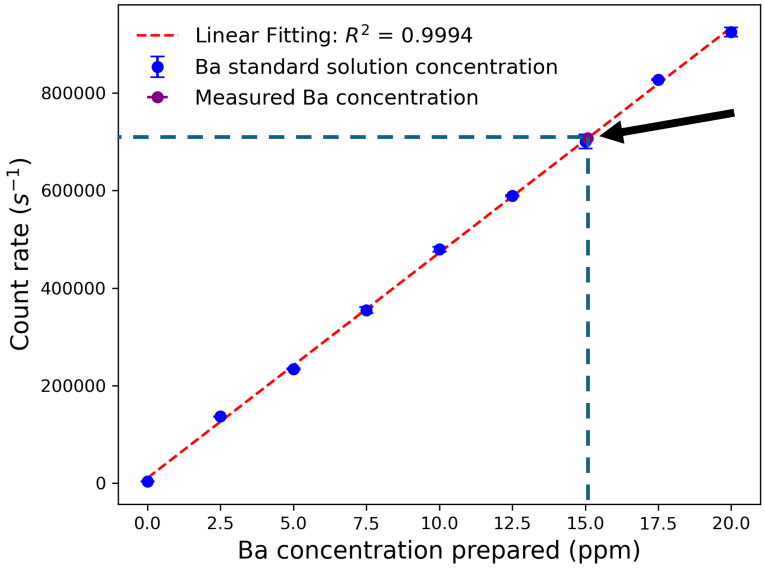


Figure 6.1: The measured count rate of prepared Ba standard solutions with eight different known concentrations (Blue dots). The purple dot represents the measured barium concentration in dissolved BZCYYb-HA powder which was diluted to approximately 15 ppm concentration (details of diluting procedure are available in section 5.5), and the barium concentration was interpolated based on the linear relationship of prepared Ba standard solution.

ation served as the associated uncertainty. For example, The average measured barium concentration in three BZCYYb-cal samples was 15.0812, with a standard deviation of 0.0602. Since the first significant digit of the standard deviation is 6, the standard deviation was rounded to 0.1. Accordingly, the average value was rounded to 15.1 to match the decimal places of the standard deviation.

Table 6.1: Measured concentrations from the diluted dissolved BZCYYb solutions and their corresponding molar ratio to measured barium in ICP-OES experiments.

	BZCYYb-cal	**BZCYYb-HA**	**BZCYYb-pellet**
Measured Ba concentration(ppm)	15.1(1)	15.6(1)	15.3(2)
Measured Zr concentration(ppm)	1.00(1)	1.02(1)	1.02(1)
Measured Ce concentration(ppm)	10.7(1)	11.2(1)	10.9(1)
Measured Y concentration(ppm)	1.05(1)	1.04(1)	1.02(1)
Measured Yb concentration(ppm)	2.06(1)	2.02(1)	1.91(1)
Measured Zr:Ba molar ratio	0.10(1)	0.10(1)	0.10(1)
Measured Ce:Ba molar ratio	0.70(1)	0.70(1)	0.70(1)
Measured Y:Ba molar ratio	0.10(1)	0.10(1)	0.10(1)
Measured Yb:Ba molar ratio	0.10(1)	0.10(1)	0.10(1)

The measured concentrations were converted into molar concentrations using the relationship described in Equation 6.1, where $Ba_{mol-conc}$ represents the calculated molar concentration of barium, Ba_{conc} is the measured barium concentration, and MW_{Ba} is the

molar mass of barium. The uncertainties in the molar ratios were estimated using the standard error propagation:

$$Ba_{mol-conc}\ (mol/L) = \frac{Ba_{conc}\ (ppm)}{1000 * MW_{Ba}} \tag{6.1}$$

$$Err_{Ba-perc} = \frac{Err_{Ba}}{Ba - mol} \tag{6.2}$$

$$Err_{Ce-perc} = \frac{Err_{Ce}}{Ce - mol} \tag{6.3}$$

$$Ratio_{Ce-Ba} = \frac{Ce - mol}{Ba - mol} \tag{6.4}$$

$$Err_{Ce-Ba-ratio} = Ratio_{Ce-Ba} * \sqrt{Err^2_{Ba-perc} + Err^2_{Ce-perc}} \tag{6.5}$$

where Err_{Ba} is the error value of the measured concentration of barium, $Err_{Ba-perc}$ and $Err_{Ce-perc}$ are the error percentages of the measured barium and cerium concentration respectively, $Ratio_{Ce-Ba}$ is the error value of the molar ratio between cerium and barium. In conclusion, the calculated molar ratios in Table 6.1 confirm that the elemental compositions of the prepared samples (BZCYYb-cal, BZCYYb-HA, and BZCYYb-pellet) match the theoretical stoichiometry of $BaZr_{0.1}Ce_{0.7}Y_{0.1}Yb_{0.1}O_{3-\delta}$.

While ICP-OES provides accurate measurements of bulk stoichiometry, it does not offer spatial information on elemental distribution within the sample. To visualise the elemental distribution, energy-dispersive X-ray spectroscopy (EDS) was conducted on the surface of the dense BZCYYb-pellet sample. EDS mapping and stoichiometric quantification were performed exclusively on the pellet rather than on the BZCYYb-cal and BZCYYb-HA powders, as the irregular and rough morphology of powder particles affect the spatial resolution. Moreover, the interaction volume of the incident high-energy electron beam is unpredictable across individual powder grains, leading to unreliable quantification of elemental ratios.

As shown in Figure 6.2, the homogeneous colour distributions across all elemental maps confirm uniform elemental dispersion in the BZCYYb-pellet. The corresponding molar ratios obtained from EDS analysis are presented in Table 6.2, indicating that most elements are present in proportions close to the theoretical stoichiometry. However, it is worth noting that the measured molar ratio between Ce and Ba slightly deviates from the ideal value. This discrepancy is likely due to the close proximity of the L-line emission energies of barium (4.47 keV) and cerium (4.84 keV), which can lead to peak overlapping in the EDS spectrum and consequently affect quantitative accuracy.

In addition to the chemical compositional analysis, the crystal structures of BZCYYb-cal, BZCYYb-HA, and BZCYYb-pellet were characterised using X-ray diffraction (XRD) to confirm the successful formation of the targeted BZCYYb1711 phase following calcina-

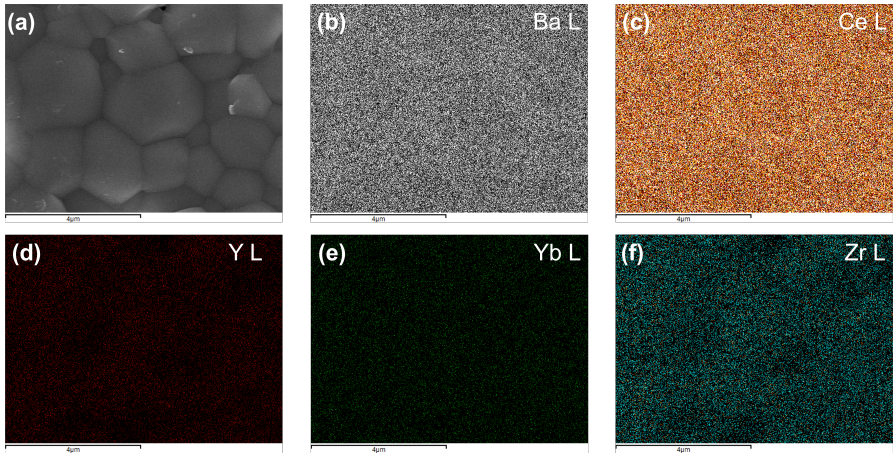


Figure 6.2: The SEM-EDS result of dense BZCYYb-pellet sample. (a) The secondary electron image of a selected region for EDS mapping, and the EDS elemental mapping of (b) barium, (c) cerium, (d) yttrium, (e) ytterbium, (f) zirconium

Table 6.2: The stoichiometry of BZCYYb-pellet measured by EDS.

	BZCYYb-pellet	**theoretical molar ratio**
Ce:Ba molar ratio	0.67(1)	0.70
Zr:Ba molar ratio	0.09(1)	0.10
Y:Ba molar ratio	0.09(1)	0.10
Yb:Ba molar ratio	0.11(1)	0.10

tion, humid treatment, and sintering. The room-temperature XRD patterns for all three samples are presented in Figure 6.3, with their intensities normalised to the [0,1] range for comparison. Across the 2θ range from approximately 28° to 90° the peak shapes and positions appear consistent among the three samples. All patterns exhibit diffraction profiles that are in excellent agreement with those reported for BZCYYb1711 compositions using the same X-ray wavelength ($\lambda = 1.5406$ Å) in published literature[8, 76, 73, 72, 155, 156].

Although most diffraction peaks exhibit the same shapes and positions in both BZCYYb-cal and BZCYYb-HA, a minor peak at $2\theta = 23.8°$ in the BZCYYb-HA pattern stands out as an anomaly. Interestingly, a peak at a similar position has been previously reported in BZCYYb1711 systems exposed to pure CO_2 atmosphere, and this peak was attributed to the formation of $BaCO_3$ phase, as reported by Ishiyama et al.[158], VahidMohammadi et al.[155] and Zhong et al.[159].

To investigate the origin of the anomalous peak, both structural and chemical analyses were conducted using XRD and attenuated total reflectance Fourier transform infrared spectroscopy (ATR-FTIR). The XRD pattern of BZCYYb-HA was compared with that of $BaCO_3$ with the Pmcn symmetry, as shown in Figure 6.4. It is evident that the most intense peak in the $BaCO_3$ pattern aligns with the small peak observed in the BZCYYb-HA pattern. To confirm the existence of $BaCO_3$ phase in measured BZCYYb-HA sample,

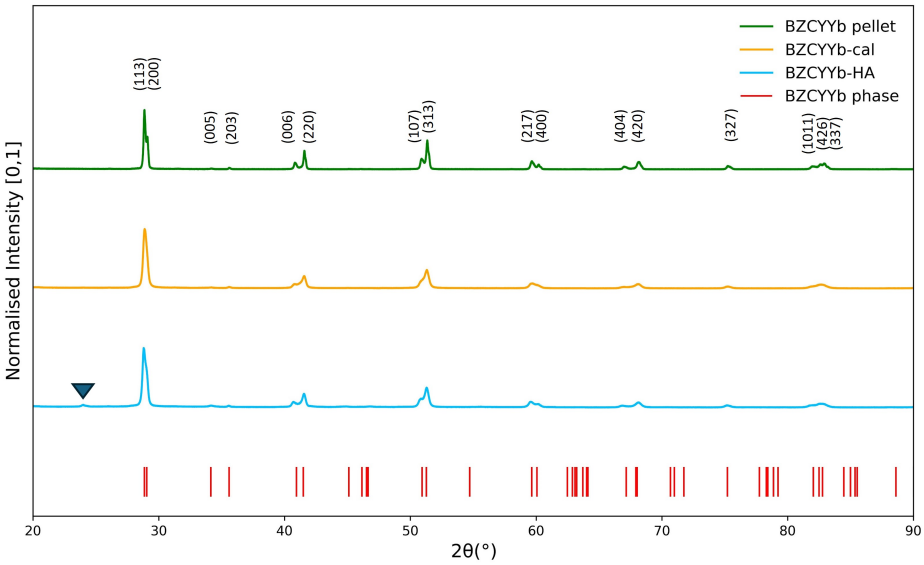


Figure 6.3: XRD patterns of sintered BZCYYb pellet (green), BZCYYb-cal powders (yellow), and BZCYYb-HA powders (blue) measured at 25°C from 20° to 90°. Intensity of all XRD patterns was normalised in [0,1]. The red stick pattern represents the BZCYYb1711 tetragonal crystallography model reported by Hamze et al.[157]. All observable peaks in XRD patterns are indexed. The small inverse triangle marks out the additional peak which was only visible in the XRD pattern of BZCYYb-HA sample.

ATR-FTIR analysis was performed to detect characteristic vibrational signatures of carbonate species.

Figure 6.5 presents the FTIR spectra of BZCYYb-cal and BZCYYb-HA powders. In the spectrum of BZCYYb-HA (blue), a broad and intense transmission band appears between 1350 cm^{-1} and 1550 cm^{-1}, corresponding to the reported v_3 asymmetric stretching characteristic mode of the inorganic carbonates[161]. Moreover, this characteristic band of inorganic carbonates was similarly reported by Yan et al. in the degraded BZCY ($BaZr_{0.1}Ce_{0.7}Y_{0.2}O_{3-\delta}$) upon the formation of $BaCO_3$[162].

Although other weaker carbonate-related peaks are expected, they were not clearly observed in the FTIR spectrum of BZCYYb-HA, likely due to the low fraction of $BaCO_3$ formed. Therefore, based on the combined evidence from XRD and ATR-FTIR, the small diffraction peak at $2\theta = 23.8°$ in the BZCYYb-HA sample can be attributed to minor $BaCO_3$ formation during the annealing process under humid (3 vol%) compressed air, while the carbon source was suspected to be the CO_2 ($\approx$ 400 ppm) in the compressed air gas (BOC, UK).

To quantitatively analyse the formed $BaCO_3$ phase and calculate the phase fraction of $BaCO_3$ in the BZCYYb-HA sample, Rietveld refinement was performed on the BZCYYb-

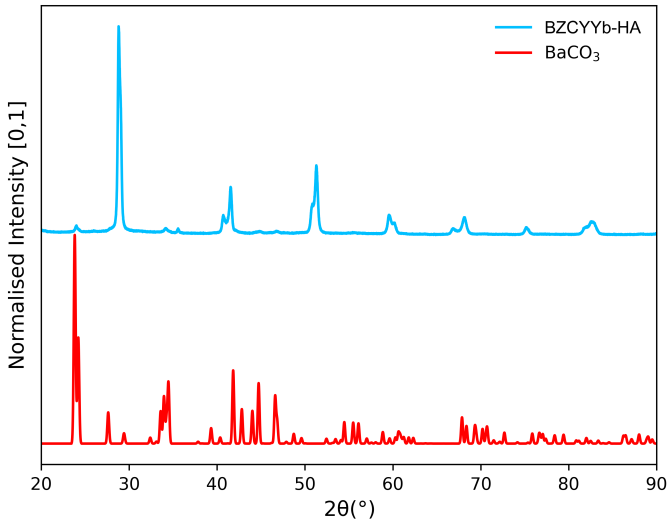


Figure 6.4: XRD patterns of BZCYYb-HA(blue) and the literature reported $BaCO_3$ (red) powders measured at 25°C from 20° to 90°. Intensity of both XRD patterns was normalised in [0,1]. The replotted $BaCO_3$ XRD pattern with the Pmcn symmetry was reported by Cai et al.[160].

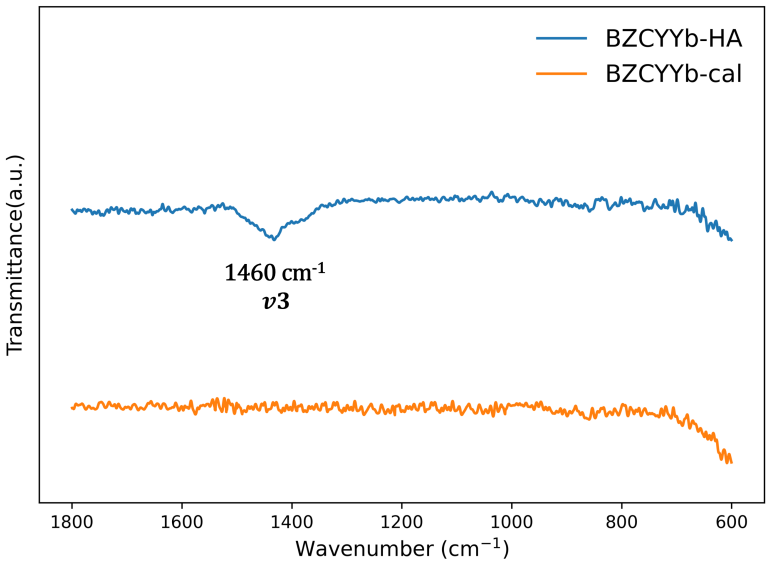


Figure 6.5: The FTIR spectra of BZCYYb-HA powder (blue) and BZCYYb-cal powder (orange).

HA XRD data. The crystallographic model used to refine the structural model against the room-temperature XRD data of BZCYYb1711 was the tetragonal (I4/mcm) phase reported recently by Hamze et al.[157].

To verify whether the reported I4/mcm tetragonal crystallographic model reliably represents the structure of BZCYYb1711, this model was first applied to the BZCYYb-cal powder prior to analysis of the BZCYYb-HA sample. According to the literature, two distinct 2θ ranges have been employed for Rietveld refinement of BZCYYb1711 XRD data. Hamze et al. scanned the diffraction pattern over the range $2\theta = 20°$ to $130°$[157], while Zhang et al. and Ivanov et al. collected the XRD pattern from $2\theta = 20°$ to $80°$[73, 163]. Rietveld refinements were performed on two XRD datasets of the same BZCYYb-cal powder, each measured over a different 2θ range, to evaluate the influence of the angular range on the refined structural parameters.

Figure 6.6 shows that, for both 2θ ranges, the calculated Bragg reflections of BZCYYb closely match the major experimental peak positions, indicating that the I4/mcm model accurately describes the BZCYYb1711 phase at room temperature. The site occupancies were not refined, as the results of chemical compositional analyses (e.g. ICP-OES and EDS) confirmed that the synthesised BZCYYb1711 sample kept the expected stoichiometry. Owing to the limited sensitivity of XRD towards oxygen atoms, the oxygen positions were fixed according to the reported crystallographic model[157] rather than refined. As summarised in Table 6.3, varying the scanned 2θ range exerted negligible influence on the refined unit cell parameters. Both refined values were within the range of those reported in the literature, which themselves exhibit variation across different studies. The atomic positions of both the A-site (Ba) and B-site cations (Ce, Y, Yb, Zr) were refined and found to be consistent with previously reported values. Among the thermal parameters, only the anisotropic thermal parameters of the Ba site were refined, since the heavy B-site co-doping may introduce uncertainties and yield unreliable refinement results. Notably, the refined anisotropic thermal parameters of Ba obtained from the $2\theta = 20°$-$90°$ dataset deviated more significantly from the literature values, indicating that extending the 2θ range improves the accuracy and reliability of the refined thermal parameters.

In the refinement of BZCYYb-cal XRD data, a noticeable discrepancy was observed between the measured and calculated diffraction profiles around $2\theta = 29°$. As highlighted in the inset of Figure 6.6, the difference primarily arises from a mismatch where the experimental data show a single broad peak, whereas the calculated pattern based on the crystallographic model predicts two distinct reflections around this 2θ position. This discrepancy can be attributed to the resolution limitation of the laboratory-based XRD instrument used in this study. In Rietveld refinement, a pseudo-Voigt profile function combining Gaussian and Lorentzian components was employed to model the peak shape, with the full width at half maximum (FWHM) parameterised according to the Caglioti

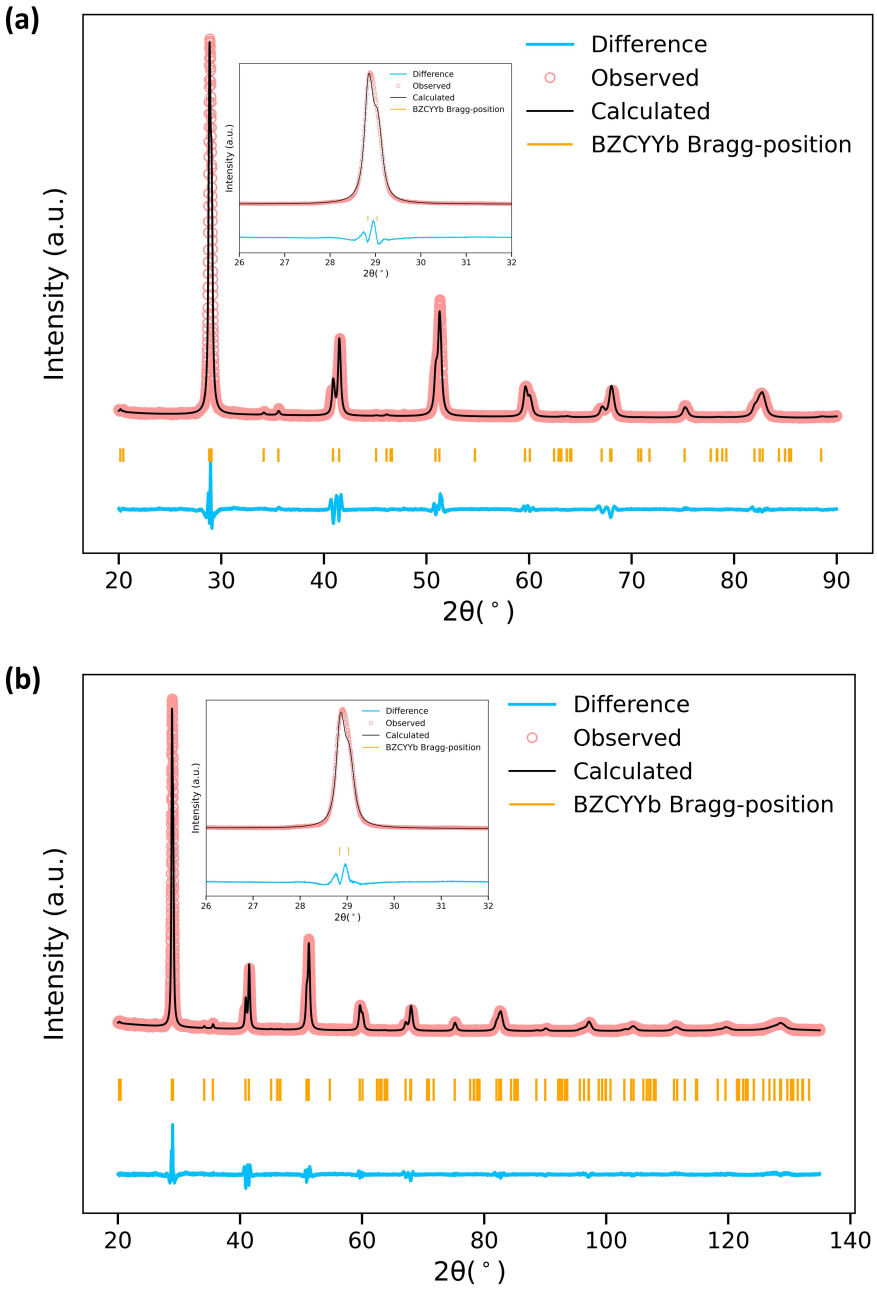


Figure 6.6: The Rietveld refinement of BZCYYb-cal powder with I4/mcm tetragonal phase model. Same powder was measured under room temperature and the scan time per step were both 250 seconds per step, but with different scanning angle, (a) is the XRD pattern scan from 20° to 90° , and (b) is the XRD pattern scan from 20° to 135°. The statistical parameters of the refinements for pattern in (a) was $R_{wp} = 9.99\%$ and $\chi^2 = 2.53$, and in (b) was $R_{wp} = 9.74\%$ and $\chi^2 = 1.81$.

Table 6.3: The refined lattice parameters, barium positions and its anisotropic thermal parameters of BZCYYb diffraction pattern with different 2θ ranges, the reported refined parameters in literature are included as a reference.

		$2\theta = 20°$ **to** $90°$	$2\theta = 20°$ **to** $135°$	**Literature reference values**
Lattice parameter a=b (Å)		6.1662(2)	6.1680(2)	6.1478(1)[157], 6.1688[73], 6.18[75]
Lattice parameter c (Å)		8.8391(4)	8.8378(3)	8.8789(2)[157], 8.834[73], 8.71[75]
Ba	x	0	0	0[157]
	y	0.5	0.5	0.5[157]
	z	0.25	0.25	0.25[157]
	U11	0.003(1)	0.0125(4)	0.012(1)[157]
	U22	0.003(1)	0.0125(4)	0.012(1)[157]
	U33	0.071(1)	0.036(1)	0.051(2)[157]
	U12	0	0	0[157]
	U13	0	0	0[157]
	U23	0	0	0[157]
B-site	x	0	0	0[157]
	y	0	0	0[157]
	z	0	0	0[157]

equation[164, 165, 166], as described below:

$$FWHM^2 = Utan^2\theta + Vtan\theta + W \tag{6.6}$$

$$FWHM = Xtan\theta + \frac{Y}{cos\theta} \tag{6.7}$$

Equation 6.6 describes the full width at half maximum (FWHM) of the Gaussian component, whereas Equation 6.7 corresponds to the FWHM of the Lorentzian component. U, V, W, X, Y are parameters closely related to the instrument resolution. A standard LaB_6 reference sample was used to refine these parameters for the Panalytical XRD instrument, as summarised in Table 6.4. Based on these refined parameters, even just considering the the Gaussian component alone, the calculated FWHM at $2\theta = 29°$ is approximately 2.26°, which exceeds the separation between the two Bragg reflections located at $2\theta = 28.86°$ and 29.04°. Consequently, the two reflections appear to be overlapped in the measured pattern, preventing the more accurate refining and inducing the observed discrepancy between the experimental and calculated diffraction profiles.

Table 6.4: Refined UVWXY parameters based on the Rietveld refinement of standard LaB_6 sample.

U	**V**	**W**	**X**	**Y**
10.829	-18.047	9.032	3.592	-0.113

Following the confirmation of the suitability of the I4/mcm crystallographic model for

the BZCYYb1711 structure, Rietveld refinement was performed on the BZCYYb-HA sample to quantitatively analyse the presence of the $BaCO_3$ phase, where the $BaCO_3$ phase was refined based on the orthorhombic model reported by Cai et al.[160]. As shown in Figure 6.7, the calculated Bragg positions for the $BaCO_3$ phase align well with the small peak observed at $2\theta = 23.8°$, and the small values of statistical refinement parameters (R_{wp} and χ^2) further confirm the reliability of the fitted phase fractions.

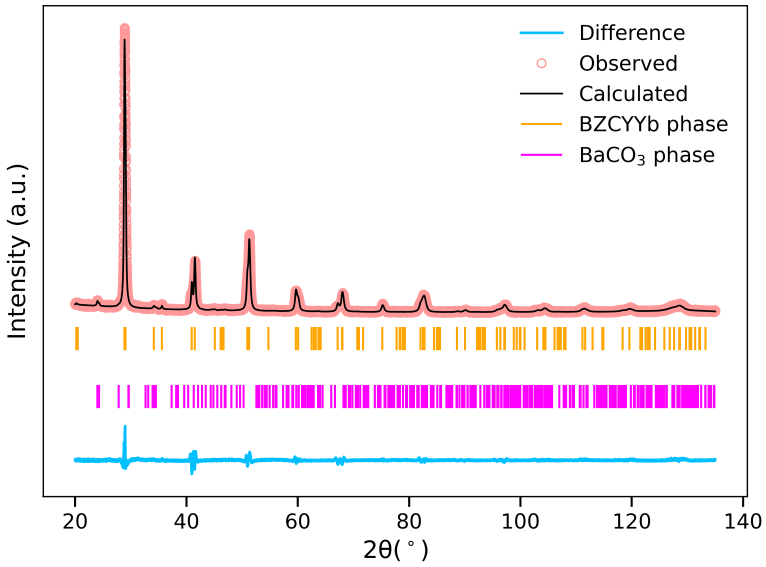


Figure 6.7: The Rietveld refinement of BZCYYb-HA XRD pattern with $BaCO_3$ phase. The BZCYYb-HA phase was refined by I4/mcm tetragonal space group reported by Hamze et al.[157], and the $BaCO_3$ phase was refined by the Pmcn orthorhombic space group reported by Cai et al.[160]. The statistical parameters of this Rietveld refinement were $R_{wp} = 9.73\%$ and $\chi^2 = 1.76$.

In the refinement, for similar reasons as discussed above, the B-site cations were not refined. Furthermore, due to the substantial overlap between the Bragg reflections of the BZCYYb phase and the $BaCO_3$ secondary phase, the corresponding peak intensities are affected, making it difficult to accurately refine the thermal parameters and site occupancy of the A-site cation, which are strongly dependent on intensity information. In view of these constraints, only the unit cell parameters of both phases and their respective phase fractions were refined, as summarised in Table 6.5.

Table 6.5: Refined unit cell parameters and phase fractions of BZCYYb-HA, BZCYYb-cal phases and $BaCO_3$ phase.

Refined unit cell parameters	**BZCYYb-HA**	**BZCYYb-cal**	$BaCO_3$
a (Å)	6.1664(1)	6.1680(2)	5.296(2)
b (Å)	6.1664(1)	6.1680(2)	8.982(5)
c (Å)	8.8315(2)	8.8378(3)	6.438(3)
Refined phase fraction	96.0(1) wt%	100 wt%	4.0(1) wt%

Compared with the refined results of BZCYYb-cal, the unit cell parameters of BZCYYb-HA are slightly smaller. This reduction can be attributed to the partial loss of barium from the BZCYYb phase and the consequent formation of a 4.0(1) wt% $BaCO_3$ secondary phase. A similar decrease in unit cell parameters resulting from barium deficiency in the BZCYYb1711 system has also been reported by Jin et al.[167].

In summary, complementary chemical composition analyses using ICP-OES and EDS confirmed that the synthesised samples retained the intended stoichiometry, with all constituent elements present in ratios closely matching their theoretical values. XRD analysed the crystal structure information (e.g. unit cell parameters) of synthesised BZCYYb samples. Furthermore, by applying FTIR analysis with XRD refinement results, the presence of the secondary $BaCO_3$ phase was confirmed, and its phase fraction quantitatively determined. Although the Rietveld refinement indicated a barium deficiency in the BZCYYb1711 matrix of the BZCYYb-HA sample due to the formation of the $BaCO_3$ phase, this deficiency was not detected by ICP-OES. This apparent discrepancy arises from the intrinsic limitation of the ICP-OES technique: when the number of moles of barium lost from BZCYYb1711 equals that incorporated into the $BaCO_3$ phase, and both phases are dissolved and analysed together during ICP-OES measurement, the resulting stoichiometric ratios appear consistent with the theoretical composition, as the technique cannot distinguish between barium ions originating from the carbonate phase and those from the perovskite matrix.

6.2 Indirect Probing of Incorporated Protons

To validate the assumption of protonic conduction in the BZCYYb-cal system, experiments were conducted to investigate the proton concentration. Thermogravimetric analysis (TGA) was performed on both BZCYYb-cal and BZCYYb-HA powders, measuring mass loss during heating from room temperature to 700°C at a rate of 10°C/min. To estimate the proton content in the samples, two assumptions were made: protons were released from the BZCYYb matrix in the form of H_2O, and the release of H_2O was entirely responsible for the mass loss recorded in the TGA measurements.

To minimise uncertainties in the measured mass loss arising from the possible evaporation of surface-adsorbed species or buoyancy effects caused by variations in atmospheric conditions within the balance during heating, the mass loss was recorded starting from 100°C. This approach was adopted because buoyancy effects are most pronounced at the onset of heating and can significantly distort the interpretation of weight changes, particularly in the low-temperature region. In some cases, the apparent mass deviation caused by buoyancy can exceed 1 %, thereby complicating the accurate determination of the true sample mass loss during thermal analysis[168]. Although this strategy may exclude poten-

tial mass loss associated with the removal of surface adsorbates, this omission is negligible in the present context, as the primary objective was to quantify the mass loss theoretically induced by the removal of incorporated hydroxyl groups.

In the absence of explicit clarification, a carrier gas that has not been passed through a humidifying source (e.i. a bubbler) is generally assumed to be "dry". However, in practice, residual moisture present in such gases can significantly influence thermogravimetric analysis (TGA), particularly for hydration-sensitive materials like BZCYYb1711. To minimise the impact of trace moisture on the TGA measurements, a drying tube was integrated into the gas delivery system, as illustrated in Figure 6.8. A gas flow controller was positioned between the drying tube and the TGA instrument to ensure that the inclusion of the drying tube did not affect the overall flow rate within the system.

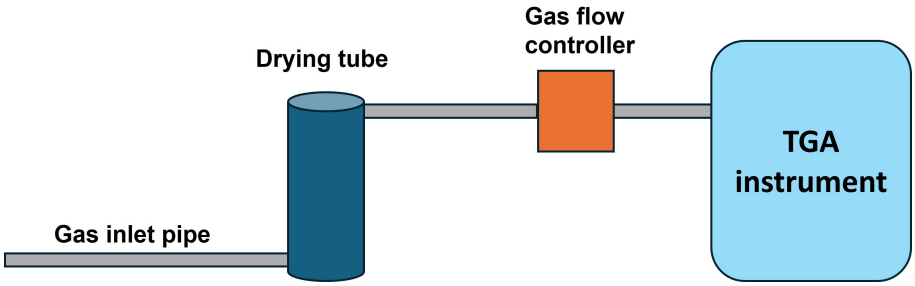


Figure 6.8: The illustration of the TGA set up with the drying tube.

To investigate the influence of the drying tube on the TGA results, two independent measurements were conducted on samples from the same batch, with all other experimental parameters, such as gas flow rate and heating programme, kept identical. The percentage mass change ($m_{\%}$) was calculated using Equation 6.8, where m_T denotes the sample mass at a given temperature, and m_{100C} represents the mass recorded at 100°C. As illustrated in Figure 6.9, the sample tested without the drying tube (orange) exhibited a smaller percentage mass change compared with the sample tested with the drying tube (blue). For instance, the difference in mass loss between the two conditions reached approximately 1.65 % after 220 minutes heating.

$$m_{\%} = \frac{m_T - m_{100C}}{m_{100C}} * 100 \tag{6.8}$$

This substantial difference highlights the significant influence of the drying tube on the TGA measurement and suggests that residual moisture in the inlet gas can contribute appreciably to the measured mass loss. The significant difference in the mass loss observed with the application of a drying tube reinforced the importance of moisture control when the TGA measurement was applied to the hydration-sensitive materials such as BZ-

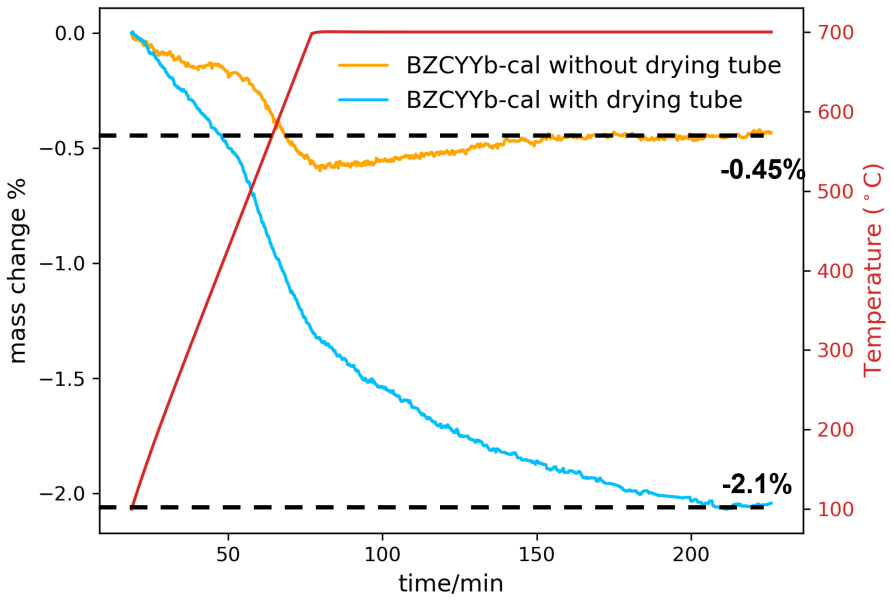


Figure 6.9: The mass loss of BZCYYb-cal powders heated from 100°C to 700°C under argon atmosphere, the red curve in data corresponds to the measured temperature, and the blue and orange curves represent the mass change percentage of measured samples. Orange curve represents the mass loss of heated BZCYYb-cal sample without applying the drying tube, while the blue curve represents the mass loss with the set up containing the drying tube.

CYYb1711.

It is also worth noting that in Figure 6.9, after reaching the plateau temperature of 700°C, the sample without the drying tube (orange curve) exhibited an upward deflection, whereas the sample with the drying tube (blue curve) continued to show a gradual increase in the mass loss. This divergence in behaviour at a constant temperature indicates that the BZCYYb-cal powder gained mass in the absence of the drying tube, resulting in a reduction in net mass loss. This observation suggested that the BZCYYb-cal sample was capable of incorporating moisture from the inlet gas at elevated temperatures up to 700°C.

Moreover, both mass changes with and without the drying tube shown in Figure 6.9 demonstrates the change of gradient when reaching the plateau temperature of 700°C. For example, in the TGA data of BZCYYb-cal with drying tube, the mass loss occurring below 700°C exhibits a steeper gradient, while the mass loss observed during the isothermal dwell at 700°C shows a slower decline. This change in slope suggests the presence of more than one unknown distinct mass-loss processes occurring during the heating stage.

To identify the possible cause of changing slopes, the variation of TGA environment was considered as an additional factor that may influence the mass-loss behaviour. The TGA results obtained for BZCYYb-cal under dry air and dry argon conditions are pre-

sented in Figure 6.10. Interestingly, unlike the continuous mass loss observed under argon, the BZCYYb-cal sample exhibited a noticeable mass gain under air after reaching 700°C (step 2). As the effect of p_{H_2O} was minimised, which was confirmed by the previous TGA measurements shown in Figure 6.9, the primary difference between the dry air and dry argon environments lies in the oxygen partial pressure (p_{O_2}). Therefore, it is reasonable to attribute the observed mass gain under air to oxygen incorporation, although direct evidence to support this hypothesis is currently lacking. In contrast, the mass-loss behaviour below 700°C (step 1) displayed a similar trend under both atmospheres, suggesting that the process responsible for this stage is not significantly affected by variations in p_{O_2}.

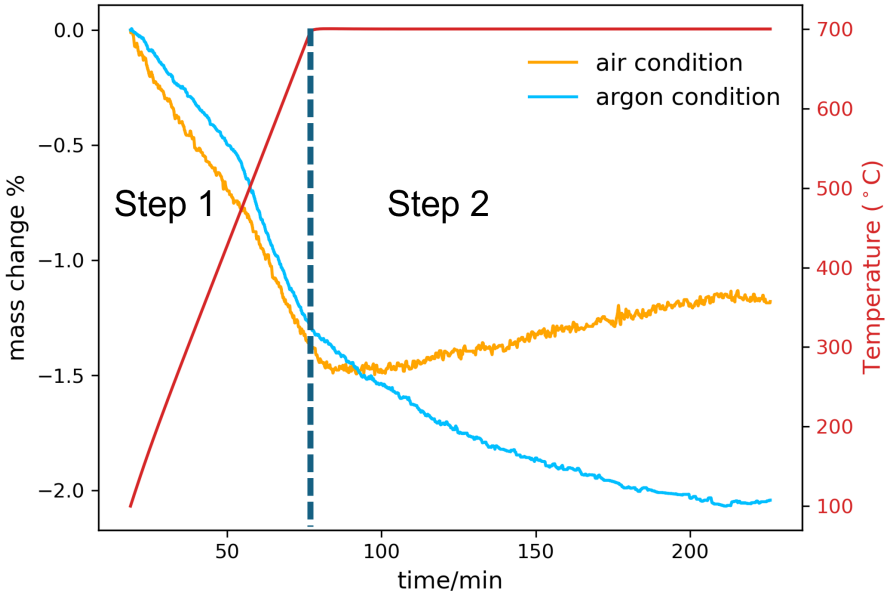


Figure 6.10: The mass loss of BZCYYb-cal powders heated from 100°C to 700°C under air (orange) and argon (blue) atmosphere with the application of drying tube. Two TGA measurements were applied on the same batch of BZCYYb-cal sample, and all experimental settings were kept the same (e.g. gas flow rate = 50 ml/min, heating rate = 10 K/min).

A key limitation of the TGA technique is that it measures only the overall mass change, without providing information about the nature or origin of that change. To overcome this limitation, residual gas analysis (RGA) was performed using quadrupole mass spectrometry (QMS) to directly monitor the gaseous species evolved from, and surrounding, the heated BZCYYb1711 sample during thermal treatment.

In RGA measurements, the as-sintered BZCYYb pellet was used instead of the BZCYYb-cal powder. This substitution was necessary due to the risk of powder loss due to the evacuation from the pump (schematic of RGA setup is available in section 5.7). Similar to the BZCYYb-cal sample, the sintered pellet had not undergone any prior hydration treatment. Once the system reached a high vacuum (approximately 10^{-6} torr), it was sealed,

and the composition of the enclosed gas environment was analysed using the calibrated q-MS system, which provided partial pressure readings for different mass-to-charge (m/z) species. To ensure compatibility with the ultra-high vacuum operating requirements of the mass spectrometer, a leak valve was employed to stabilise the pressure of the transferred gas at 10^{-5} torr, as detailed in the section 5.7.

The evolution of the mass 18 species, corresponding to the H_2O gas molecules, was monitored during the heating of the as-sintered BZCYYb pellet to 700°C, which was a temperature selected to match that used in the TGA measurements. As shown in Figure 6.11 (a), the pressure of the mass 18 species in the closed system increased upon heating, confirming the release of H_2O from the as-sintered BZCYYb material, despite the absence of prior hydration treatment. To eliminate the possible effect from alternative sources of H_2O in the RGA measurements, a control experiment was conducted in which the same heating procedure was applied to the empty system (i.e., without the BZCYYb pellet). The mass 18 signal from this blank experiment (green curve) was significantly lower than that of the sample-containing system (orange curve), thereby confirming that the experimental setup itself did not generate H_2O during heating.

In Figure 6.9, the smaller mass loss observed under conditions without the drying tube suggested that the BZCYYb1711 system was capable of incorporating moisture from the surrounding atmosphere. This hydration-absorbing behaviour was further investigated using RGA technique. As shown in Figure 6.11 (b), the partial pressure of the mass 18 species (corresponding to H_2O) decreased during the slow cooling process from 700°C to 67°C. However, it is possible that the H_2O was adsorbed on the inner surface of the sample tube.

By integrating the findings from both the TGA and RGA experiments, it can be concluded that the observed mass loss in the BZCYYb1711 system is associated with the release of hydration-related species. This observation confirms that the as-synthesised BZCYYb samples (BZCYYb-cal and the as-sintered BZCYYb-pellet) inherently contain protons, even without deliberate humidification treatment.

Following the clarification of hydration-related mass loss, the TGA results of BZCYYb-cal and BZCYYb-HA powders were compared to evaluate the effect of the humid annealing process on mass change. As shown in Figure 6.12, though two samples exhibited similar mass-loss profiles, the extent of mass loss differed between BZCYYb-cal and BZCYYb-HA within step 1 (below 700°C) and step 2 (above 700°C). This observation suggests that the species responsible for mass loss are temperature-dependent. As the only confirmed origin of mass loss thus far is the removal of hydration species, a plausible explanation for the differing mass-loss magnitudes between the two steps (below and above 700°C) is that, in BZCYYb-HA, an additional population of incorporated hydroxyl groups exists that forms stronger bonds with the BZCYYb lattice and therefore requires higher thermal energy to

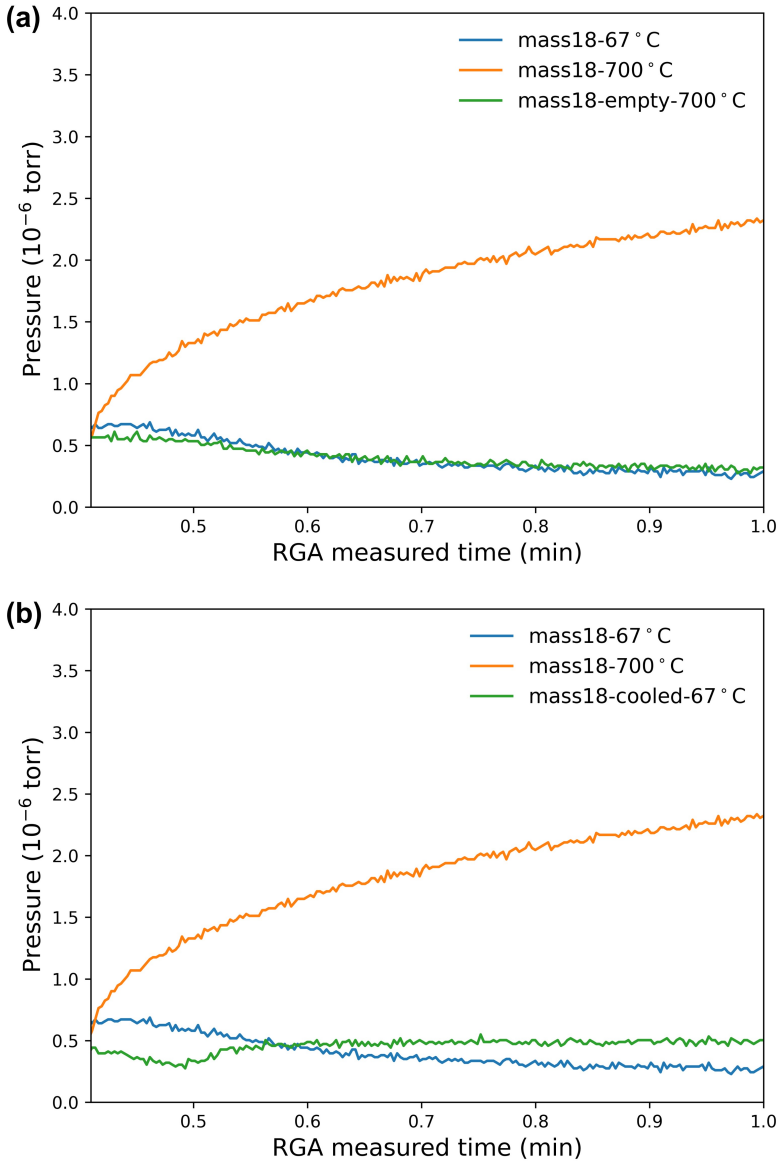


Figure 6.11: (a) The pressure of gas species with molar mass = 18 in the closed system containing BZCYYb-pellet at 67°C (blue) and 700°C (orange), and the pressure of gas species (molar mass = 18) of the empty quartz tube was measured at 700°C as the background reference (green). (b) The pressure of gas species with molar mass = 18 in the closed system containing BZCYYb-pellet at 67°C (blue) and 700°C (orange). The green curve represents the pressure of gas (mass = 18) measured when heated BZCYYb-pellet was cooled from 700°C to 67°C at 2°C/min cooling rate. One hour stabilisation period was applied before performing the RGA measurement

be released, leading to larger mass loss difference in step 2 than step 1.

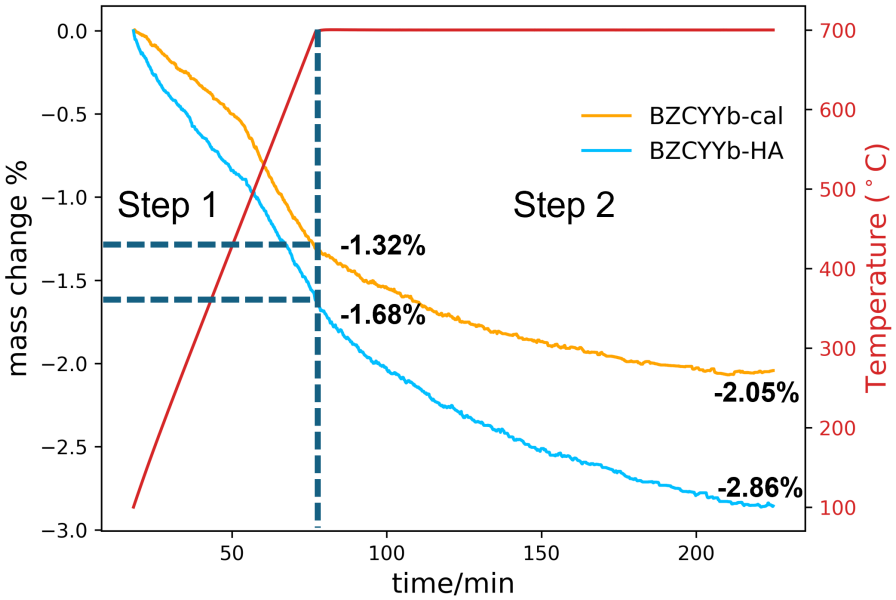


Figure 6.12: The mass loss of BZCYYb-cal (orange) and BZCYYb-HA (blue) powders heated from 100°C to 700°C under dry argon atmosphere with the application of drying tube. The gas flow rate was 50 ml/min, and the heating rate was 10 K/min

In conclusion, through combined TGA and RGA analyses, the presence of existed protons in the as-calcined BZCYYb1711 system without the intentional humid treatment, was clearly demonstrated.

6.3 Neutron Techniques to Measure Proton Concentrations

Although the TGA and RGA results clearly demonstrate the presence of incorporated protons in the BZCYYb-cal system, accurate quantification of proton content via TGA is inherently limited. This limitation is due to the fact that mass changes in TGA can be influenced by multiple factors, including surface-adsorbed species and variations in oxygen stoichiometry[81]. To address this limitation, neutron prompt gamma-ray activation analysis (PGAA), which is a technique that allows for the direct and exclusive quantification of hydrogen, was employed to determine the proton concentrations in both BZCYYb-cal and BZCYYb-HA powders.

As introduced in the section 5.10, PGAA is a technique to detect and analyse the prompt-γ ray peaks from elements and their isotopes. The calibration of the PGAA spectra was the prerequisite to the quantification analysis: The calibration of the γ peaks position and of the efficiencies of the detectors was performed by measuring the energy

standards (e.g. ^{152}Eu) with well known and precise γ-ray energies. After ensuring the precision of the detected γ peak positions, the spectroscopic database[169] developed by Budapest PGAA facility was applied to identify the identities of detected peaks based on the peak positions.

To quantitatively analyse the detected elements from the PGAA results, the relationship between the calculated mass and the net γ peak area of the element was applied, as shown in Equation 6.9, where A is the net peak area, ϵ is the counting efficiency, t is the time of measurement, m is the calculated mass of the detected nuclide, M is the atomic weight, N_A is the Avogadro constant, Φ is the thermal equivalent neutron flux and σ_γ is the partial γ-ray production cross-section. The final term σ_γ is a derived nuclear constant explained in Equation 6.10, where σ is the thermal neutron capture cross section, θ is the isotopic abundance of detected element and P_γ is the emission probability of the γ-ray[170]. Based on this framework, the mass and molar quantity of the element of interest can be accurately calculated, allowing for the determination of molar ratios and stoichiometric information.

$$\frac{A}{\epsilon t} = \frac{m}{M} N_A \sigma_\gamma \Phi \tag{6.9}$$

$$\sigma_\gamma = \sigma \theta P_\gamma \tag{6.10}$$

Although the general procedure for quantitative analysis of PGAA spectra may appear straightforward, robust and accurate data interpretation requires careful consideration of several key factors. Firstly, the definition of a peak and its corresponding background region within the data analysis procedure must be clearly established, as the accuracy of peak integration is highly sensitive to this definition. Secondly, the criteria employed by the processing software to evaluate the quality of peak-area fitting must be specified, since reliable quantification depends critically on the peak-area quantification. Furthermore, in PGAA spectra, all elements except hydrogen typically produce multiple prompt-γ peaks. This introduces the possibility of peak overlap between different elements, which needs to be taken account to ensure the reliability and reproducibility of quantitative PGAA analysis.

The criteria defining the peak and its neighbouring background were based on a commonly used peak-search algorithm shown in Equation 6.11, where C_i is the total counts in the given energy channel, B is the average value of the baseline from neighbouring channels and σ_B is the standard deviation of the calculated baseline[170].

$$C_i - B > 3\sigma_B = 3\sqrt{B} \tag{6.11}$$

The Hyperlab software[171] was applied not only in the peak defining process, but also for the peak area fitting and calculation. Although ideally the γ peaks should exhibit symmetric shapes, real spectra acquired using high-purity germanium (HPGe) detectors are often affected by low-energy tailing. This phenomenon arises when some γ-rays lose energy in the smaller energy channel, resulting in an asymmetric peak shape with a pronounced tail on the low-energy side.

To accommodate this asymmetry, HyperLab employs a composite peak shape function comprising the linear sum of a Gaussian function and an exponentially modified Gaussian (EMG). Additionally, a second-order polynomial is used to model the underlying background. Figure 6.13 shows the fitting of peaks within the energy range containing a characteristic γ peak for barium and hydrogen. To assess the quality of fitting, the normalised residual was also calculated and plotted at the bottom of Figure 6.13 based on Equation 6.12, where R_N is the calculated normalised residual, C_d is the data count and C_f is the fitting count. The fitting described well the peak shape of both barium and hydrogen γ peaks shown in Figure 6.13, and the randomly scattered normalised residuals confirmed the good quality of the fitting.

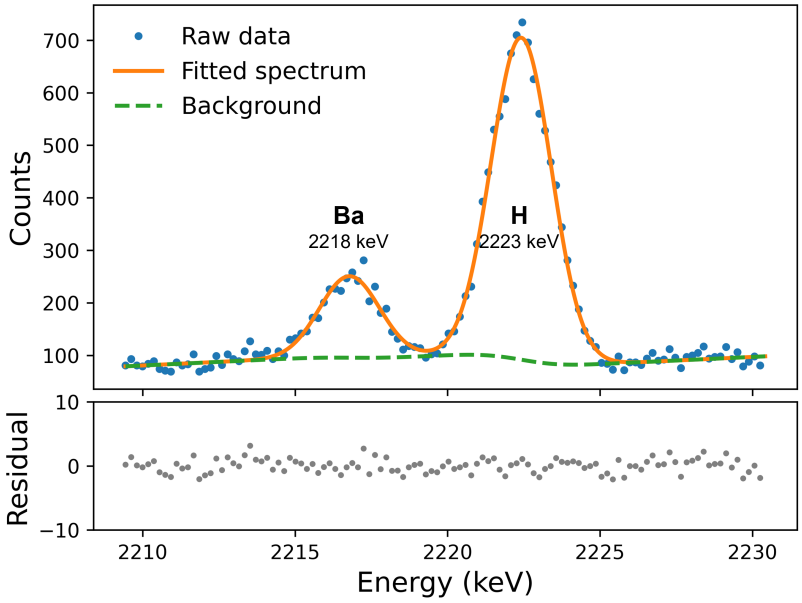


Figure 6.13: An energy spectrum measured by the PGAA technique with peak fitting and element labelling. The peak fitting includes the characteristic γ peaks of barium and hydrogen determined by the Hyperlab software. The normalised residual which was calculated based on Equation 6.12 is illustrated at the bottom to show the fitting quality.

$$R_N = \frac{C_d - C_f}{\sqrt{C_f}} \tag{6.12}$$

Following the labeling of the peak positions and the calculation of net peak areas, elemental indexing relying on the database was performed by the ProSpeRo concentration calculation Excel macro[170]. This tool compares the list of detected peak energies to a reference database to identify corresponding elements. As previously noted, hydrogen is unique in the PGAA spectrum as it possesses only one characteristic γ peak, whereas other elements exhibit multiple characteristic peaks. To minimise misidentification due to peak overlap from different elements, ProSpeRo evaluates a parameter known as the qualifier. This parameter is defined as the ratio of the sum of the squared relative peak areas for the detected peaks to the sum of squared areas for all known characteristic peaks of the corresponding element. The qualifier is heavily influenced by the inclusion of strong peaks and decreases significantly if dominant peaks are missing from the spectrum. To ensure the reliability of the automatic elemental identification, ProSpeRo only retains elements with a qualifier value greater than 0.4—an empirically established threshold[170].

By understanding the details of the data processing step in the PGAA results, the quality of the quantitative and qualitative analysis of PGAA spectra obtained from BZCYYb-cal and BZCYYb-HA powders was ensured. As illustrated by Figure 6.14, the peaks corresponding to the barium (^{138}Ba) (Figure 6.14(a)), zirconium (^{92}Zr) (Figure 6.14(a)) and cerium (^{140}Ce) (Figure 6.14(b)) exhibited slightly higher counts in BZCYYb-cal than BZCYYb-HA, due to the larger quantity of sample used (0.35 g BZCYYb-cal and 0.31 g BZCYYb-HA were measured in PGAA). The counts corresponding to the hydrogen (H) signal at its characteristic energy of 2223 keV were higher in BZCYYb-HA than in BZCYYb-cal, following the expectation that the BZCYYb-HA sample would contain more protons due to the proton incorporation via the treatment in a humid atmosphere. The non-negligible counts of hydrogen peak in BZCYYb-cal proves the existence of protons in the BZCYYb-cal system, matching well the previously reported TGA results shown in Figure 6.12.

Based on the relationship shown in Equation 6.9 mentioned above, the masses of elements were calculated from their corresponding net areas of γ peaks, thus the molar ratio between elements was obtained. To minimise the hydrogen intensity from sample container and the instrument, the intensity of hydrogen was measured on the empty container and noted as background hydrogen (H_{bg}). Table 6.6 lists the calculated molar ratios in BZCYYb-cal and BZCYYb-HA. The small molar ratios between the H_{bg} and the measured hydrogen (H) confirmed that the contribution from the background hydrogen signal was negligible to the total measured hydrogen signals from the samples. The molar ratio between the cerium (Ce) and barium (Ba) matched both the theoretical stoichiometry of BZCYYb ($BaZr_{0.1}Ce_{0.7}Y_{0.1}Yb_{0.1}O_{3-\delta}$) and the experimental results from the ICP-OES and EDS measurements, suggesting that all barium and cerium peaks were correctly indexed and not affected by the potential peak overlapping problem. Though the barium deficiency was found in BZCYYb-HA samples from the XRD refinement, the

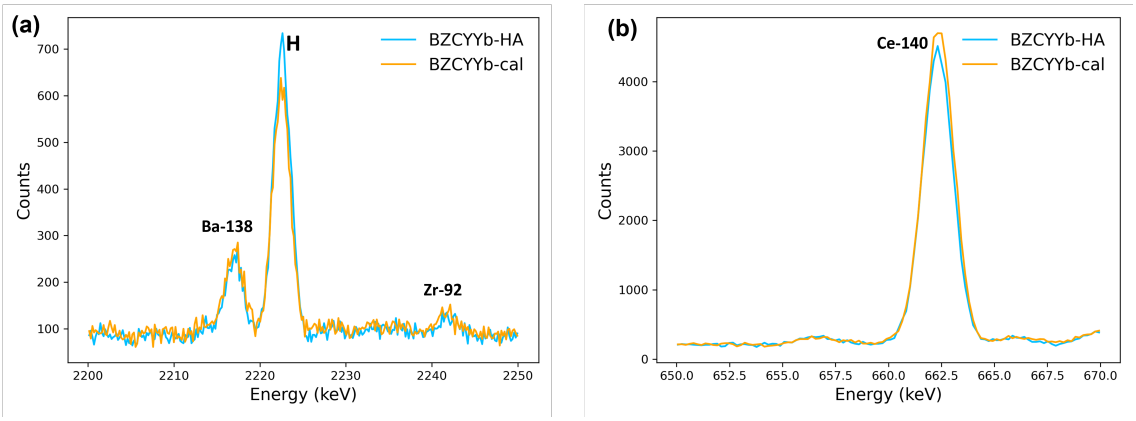


Figure 6.14: The PGAA spectra of BZCYYb-cal and BZCYYb-HA powders at room temperature. (a) The PGAA spectrum includes peaks corresponding to ^{138}Ba, ^{92}Zr with the characteristic hydrogen (H) signal presented after subtraction of the background hydrogen contribution inherent to the PGAA setup. (b) The PGAA spetrum includes the peak corresponding to ^{140}Ce, two little humps besides the ^{140}Ce peak were due to the teflon packaging of powders.

PGAA technique faced the same limitations as ICP-OES and EDS that it cannot distinguish the barium in the $BaCO_3$ phase from the BZCYYb matrix. Based on the calculated molar ratio between H and Ba, the protonated chemical compositions of BZCYYb-cal and BZCYYb-HA can be deduced as $BZCYYbO_{3-\delta}H_{0.35}$ and $BZCYYbO_{3-\delta}H_{0.44}$ respectively. Compared with the proposed protonated composition from TGA results ($BZCYYbH_{0.46}$ for BZCYYb-cal and $Ba_{0.931}ZCYYbH_{0.59}$ for BZCYYb-HA), the proton concentrations measured by PGAA in both samples are lower. This discrepancy arises from the fundamental difference between the techniques: TGA measures total mass loss, which includes contributions not only from proton-related species (e.g. H_2O), but also from other species such as surface-adsorbed components. As a result, the hydration-related mass loss and thus the inferred proton content can be overestimated in TGA, whereas PGAA directly and exclusively quantifies hydrogen nuclei, offering more specific information regarding proton content.

Table 6.6: The molar ratio calculated from the peak area of selected species in room temperature PGAA measurement.

Molar ratio	**BZCYYb-cal**	**BZCYYb-HA**
H_{bg} : H	0.015(1)	0.016(1)
Ce : Ba	0.71(4)	0.71(4)
H : Ba	0.35(2)	0.44(2)

In conclusion, PGAA, as a proton-exclusive analytical technique, provided direct quantification of hydrogen content and served as a valuable complement to the indirect measurements obtained by TGA. Although the proton concentrations calculated for the BZCYYb-cal and BZCYYb-HA samples differed between the two methods, both PGAA and TGA consistently confirmed the presence of a significant proton concentration in the BZCYYb-

cal sample.

6.4 Summary

In this chapter, a comprehensive investigation was conducted to elucidate the structural integrity, compositional homogeneity, and proton incorporation behaviour of the BZCYYb1711 system. Multi-technique characterisation, including XRD, FTIR, ICP-OES, EDS, TGA, RGA, and PGAA, was employed to establish a consistent understanding of the material's phase composition and protonic properties.

XRD and FTIR analyses confirmed the successful synthesis of BZCYYb1711, with only a minor secondary $BaCO_3$ phase detected in the humid-annealed sample. Rietveld refinement revealed that the unit cell parameters of the humid-treated (BZCYYb-HA) sample were slightly reduced relative to the as-calcined (BZCYYb-cal) sample, a trend attributed to partial barium loss and $BaCO_3$ formation. The complementary ICP-OES and EDS analyses verified that the overall stoichiometry of both samples remained consistent with the nominal composition, and the apparent barium deficiency indicated by XRD refinement was rationalised as an artefact arising from the inability of ICP-OES to differentiate barium species originating from distinct phases.

TGA and RGA techniques revealed that the observed mass loss during heating primarily originated from the release of hydration species, confirming the existence of intrinsic protons within the BZCYYb1711 lattice even in the absence of deliberate humidification. Comparison between BZCYYb-cal and BZCYYb-HA samples demonstrated that a majority of the protons are already present in the as-calcined sample, while the humid annealing still has some minor effect in increasing the proton concentrations.

Finally, PGAA provided direct quantification of the hydrogen content and validated the conclusions drawn from TGA. Although minor discrepancies were observed between the absolute proton concentrations measured by the two methods, both consistently confirmed significant proton incorporation in the as-calcined BZCYYb1711 sample.

Chapter 7: Effect of Humid Annealing on Proton Dynamics in $BaZr_{0.1}Ce_{0.7}Y_{0.1}Yb_{0.1}O_{3-\delta}$

7.1 Effect of Humid Annealing on Localised Proton Dynamics

Both PGAA and TGA measurements complementarily confirmed the presence of incorporated protons in the BZCYYb-cal sample, even though it had not been deliberately treated under humid conditions. However, while these results establish the existence of protons, they provide no direct insight into whether such protons exhibit the same dynamic behaviour as those in hydrated BZCYYb-HA (BZCYYb samples annealed under humid air conditions), which is critical for understanding why the conductivity remains comparable under both dry and humid atmospheres.

Whereas impedance spectroscopy can probe long-range total conductivities, accessing the corresponding localised dynamics is far more challenging. Such information is essential, as it links proton transport directly to atomic-scale interactions and structural features. The processes within atomic-scale perform fast in timescale as well, thus probing these process requires techniques sensitive to very short timescales (faster than the nanosecond regime). To explore the localised proton dynamics, two complementary neutron-based techniques were employed: neutron Compton scattering (NCS), which probes proton momentum distributions at timescales of $10^{-16} - 10^{-15}$ s[172], and backscattering quasielastic neutron scattering (QENS), which resolves proton hopping dynamics on the nanosecond timescale ($\sim 10^{-9}$ s)[152].

As noted in the section 5.12, Vesuvio employs two sets of detectors: forward detectors positioned downstream of the sample, and backscattered detectors located between the sample and the neutron source. Figure 7.1 shows the raw ToF spectra of BZCYYb-HA powders collected by both detector banks. While both forward and backscattered spectra display distinct peaks in the 300-400 μs range, a broad feature with additional fine peaks between 100-350 μs is observed exclusively in the forward spectrum. This forward-spectrum exclusive counts originates from the unique kinematic constraints of neutron–hydrogen scattering. Because the neutron mass ($m_n = 1.0087, u$) is only slightly larger than that of hydrogen ($m_H = 1.0079, u$), collisions result in neutrons being preferentially scattered in the forward direction. Consequently, the broad peak visible only in the forward spectra is a distinct signature of hydrogen, enabling NCS to isolate and study the NMD of hydrogen specifically.

Based on the sequential fitting strategy described in section 5.12, the backward scattering data were first analysed prior to fitting the hydrogen recoil peak in the forward spectrum. The backscattered data were fitted using the normalised 1D Gaussian function,

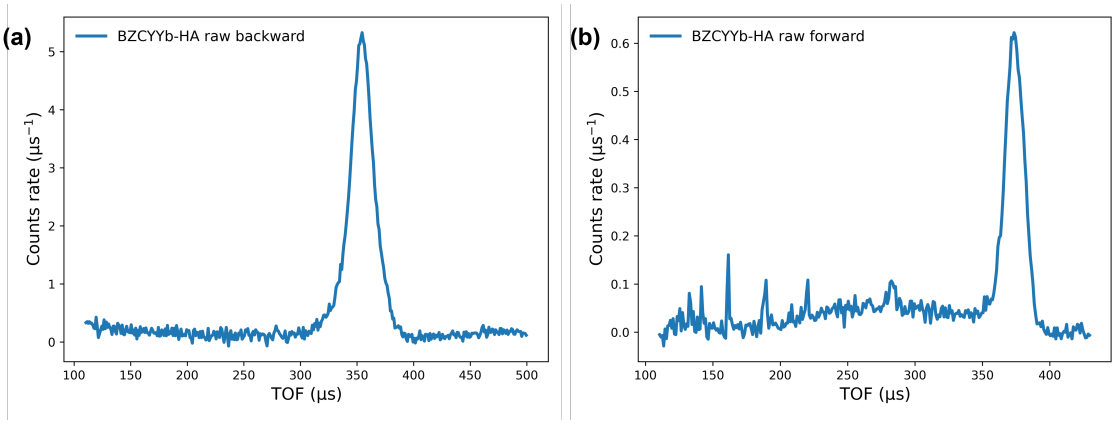


Figure 7.1: The raw ToF spectrum of BZCYYb-HA measured by (a) backward detectors and (b) forward detectors. The NCS experiment was performed at room temperature and the BZCYYb-HA powders was sealed in the aluminium sample holder.

representing the Compton profiles of all elements present in the sample, including the aluminium sample holder but excluding hydrogen. As shown in Figure 7.2, the fitted recoil peaks were converted into the corresponding ToF peaks for direct comparison with the measured data. The excellent agreement between the overall fit (grey line) and the experimental points confirms the high quality of the backward scattering fit, thereby providing reliable fixed parameters for the subsequent hydrogen fitting in the forward spectrum.

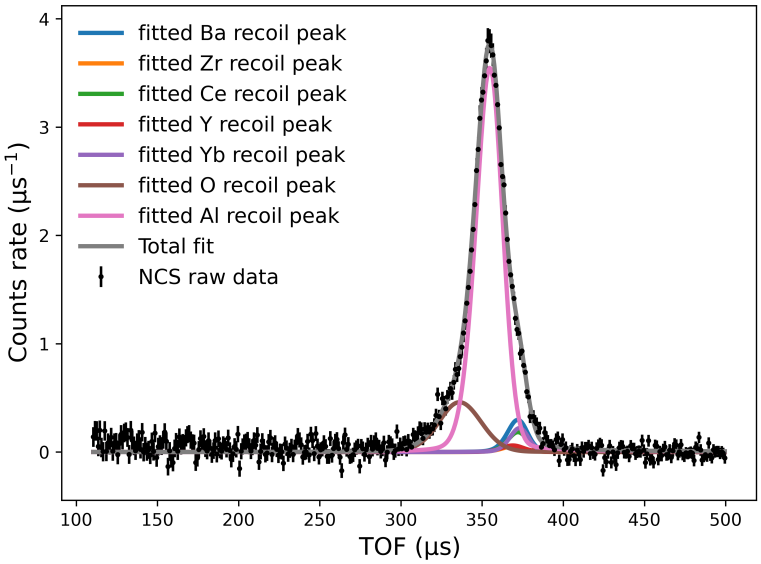


Figure 7.2: The fitting of BZCYYb backward scattering data. Recoil peaks of all elements except hydrogen were fitted based on the normalised 1D Gaussian function (Equation 5.50), and then all fitted recoil peaks were convoluted and converted back to the ToF domain to form the final fit (Grey line).

The quantitative results of the backscattered fitting are summarised in Table 7.1. For validation, these fitted recoil peak widths can be compared with literature values. Wallis et al. reported room-temperature (298 K) NCS data for a related system, $BaZr_{0.7}Ce_{0.2}Y_{0.1}O_{3-\delta}$

(BZCY721), measured on the Vesuvio beamline, where the fitted widths of heavy-element recoil peaks (Ba, Zr, Ce, Y, O, Al) were found to be consistent with the present results[98]. This agreement is expected, as recoil peak width reflects the localised dynamics of the element, and for immobile heavy atoms at room temperature, these dynamics should remain nearly identical across similar perovskite systems. Nevertheless, while the fitted widths appear reasonable, the precision of the results is limited. All fitted intensities in Table 7.1 show large standard deviations. This uncertainty originates from the broad, overlapping ToF peaks in the raw backscattering data, which contain contributions from multiple elements that must be fitted simultaneously. The heavily doped composition of BZCYYb1711 exacerbates this issue, as the large number of distinct atomic species introduces significant fitting complexity. In addition, the strong background signal from the aluminium sample holder further obscures quantitative accuracy. These challenges highlight the importance of applying the sequential fitting strategy, whereby the recoil peak parameters obtained from the backward fit are fixed and subsequently used in the forward fitting step, thus isolating the hydrogen contribution and improving the robustness of the hydrogen Compton profile analysis.

Table 7.1: The fitted intensity of recoil peaks of atoms in BZCYYb-cal samples except hydrogen measured in backward scattering at room temperature (298K). The aluminium signal was originated from the sample holder, and its recoil peak width was well calibrated at 298K, hence the error value of fitted peak width of aluminium is zero.

Element	**Fitted width of recoil peak of the element($Å^{-1}$)**	**fitted intensity of recoil peak of the element(a.u.)**
Ba	34(3)	0.03(3)
Zr	26(4)	0.006(5)
Ce	34(3)	0.02(2)
Y	25(4)	0.007(6)
Yb	40(1)	0.02(2)
O	14(1)	0.1(1)
Al	13.5	0.4(2)

Following the backward fitting, attention was turned to the forward scattering spectrum, where the broad hydrogen recoil peak is clearly observed (Figure 7.1b). Unlike the relatively smooth recoil peaks of heavier elements, the hydrogen signal in the forward data is complicated by numerous spike-shaped features. These artefacts arise from the specific design of the Vesuvio forward detectors, which are cerium-activated yttrium-aluminium-perovskite (YAP) scintillators. Importantly, these detectors are sensitive not only to neutrons but also to prompt γ-rays emitted following resonance neutron absorption by certain nuclei[173]. This effect is analogous to the principle of PGAA (prompt-gamma activation analysis), discussed in the previous chapter, where epi-thermal neutrons at specific

resonance energies are absorbed by target atoms, leading to the emission of characteristic γ-rays. In Vesuvio, such resonance events appear as sharp absorption features superimposed on the neutron ToF spectrum, thereby complicating the fitting of the hydrogen Compton profile.

To mitigate these effects, resonance-contaminated regions were excluded from the fit by applying ToF masking. As shown in Figure 7.3a, the anomalously high count-rate points correspond to resonance peaks, which were masked before performing the Compton profile fitting. The improvement brought by this approach is evident in Figures 7.3c and d, where the reduced chi-squared values increase after masking, confirming that more reliable fits are obtained when resonance artefacts are removed. As summarised in the overall fitting workflow (Figure 5.14), the optimised Compton profiles were then converted back into the time domain to generate the final fitted ToF spectra.

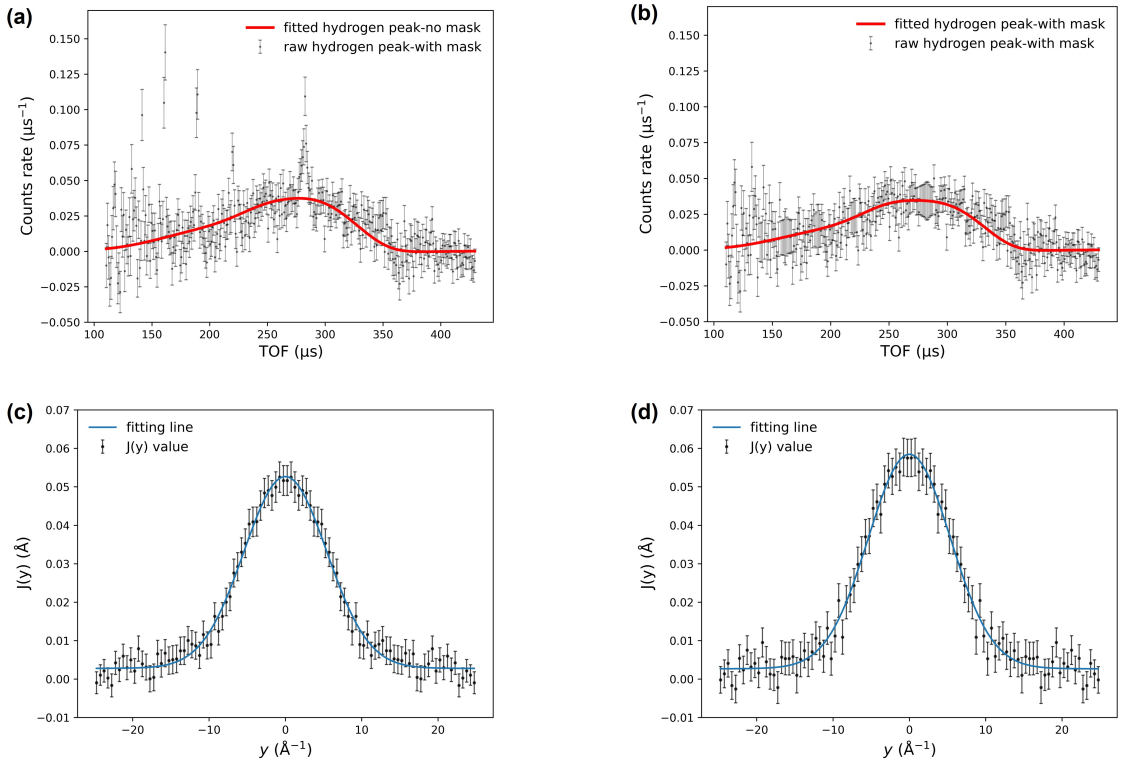


Figure 7.3: The hydrogen peak in the ToF spectra of BZCYYb-cal sample at room temperature fitted (a) without masking the ToF range locating absorption resonance peaks, (b) with masking the ToF range locating absorption resonance peaks. And the corresponding Compton profile J(y) of hydrogen fitted (c) without masking the ToF range locating absorption resonance peaks with reduced chi-squared value = 0.47, (d) with masking the ToF range locating absorption resonance peaks with reduced chi-squared value = 0.53. All fittings were performed based on the normalised 1D Gaussian function shown in Equation 5.50.

The final fits in the forward scattering data are shown in Figure 7.4 in the ToF domain. In both cases, the total fitting curves reproduce the experimental spectra well, confirming

the reliability of the applied procedure. The extracted fitting parameters are summarised in Table 7.2.

Table 7.2: The fitted width and intensity of the H recoil peak in BZCYYb-cal and BZCYYb-HA samples at room temperature.

Sample	Fitted width of the recoil peak of H ($Å^{-1}$)	Fitted intensity of the recoil peak of H (a.u.)
BZCYYb-cal	4.9(4)	0.4(1)
BZCYYb-HA	4.8(6)	0.5(1)

However, the fitted parameters presented in Table 7.2 exhibit relatively large error values, resulting in similar fitted width and intensity values for the BZCYYb-cal and BZCYYb-HA samples. These large uncertainties likely stem from the heavily doped nature of the BZCYYb system. In neutron Compton scattering (NCS) analysis, the Compton profiles of all constituent elements are fitted simultaneously. Thus, in a multicomponent and heavily doped system, parameter correlations and overlapping contributions from different atomic species can introduce substantial fitting errors.

In contrast to NCS, quasielastic neutron scattering (QENS) selectively probes the dynamics of mobile species; hence, protons contribute most significantly to the measured signal, whereas heavier matrix cations have negligible influence. Consequently, QENS effectively overcomes the limitations encountered by NCS in analysing multicomponent, heavily doped systems such as BZCYYb1711.

As introduced in section 5.13, the broadening of the QENS signal reflects atomic motion within the measured system. Although QENS does not selectively isolate individual elements, in the case of BZCYYb1711 it is reasonable to attribute the observed broadening predominantly to hydrogen. This attribution is justified by two principal considerations: first, hydrogen has a much larger incoherent neutron scattering cross-section than the other constituent elements, meaning that QENS is particularly sensitive to the dynamics of individual protons (Table 5.2). Second, hydrogen exhibits substantially higher mobility than heavier cations in the structure.Consequently, the quasielastic broadening detected in BZCYYb1711 can be reliably interpreted as a direct manifestation of proton dynamics.

While QENS provides a powerful means to probe the localised dynamics of mobile species such as protons, its applicability depends strongly on the characteristic time and length scales accessible to a given instrument. Therefore, the choice of QENS beamline must be guided by an estimate of the protonic motion expected in the BZCYYb1711 system. Assuming a Grotthuss-type transport mechanism, where protons hop between adjacent oxygen ions, the relevant hopping length can be approximated by the O-O distance. From a simulation perspective, Yang et al. reported that the DFT-optimised cubic

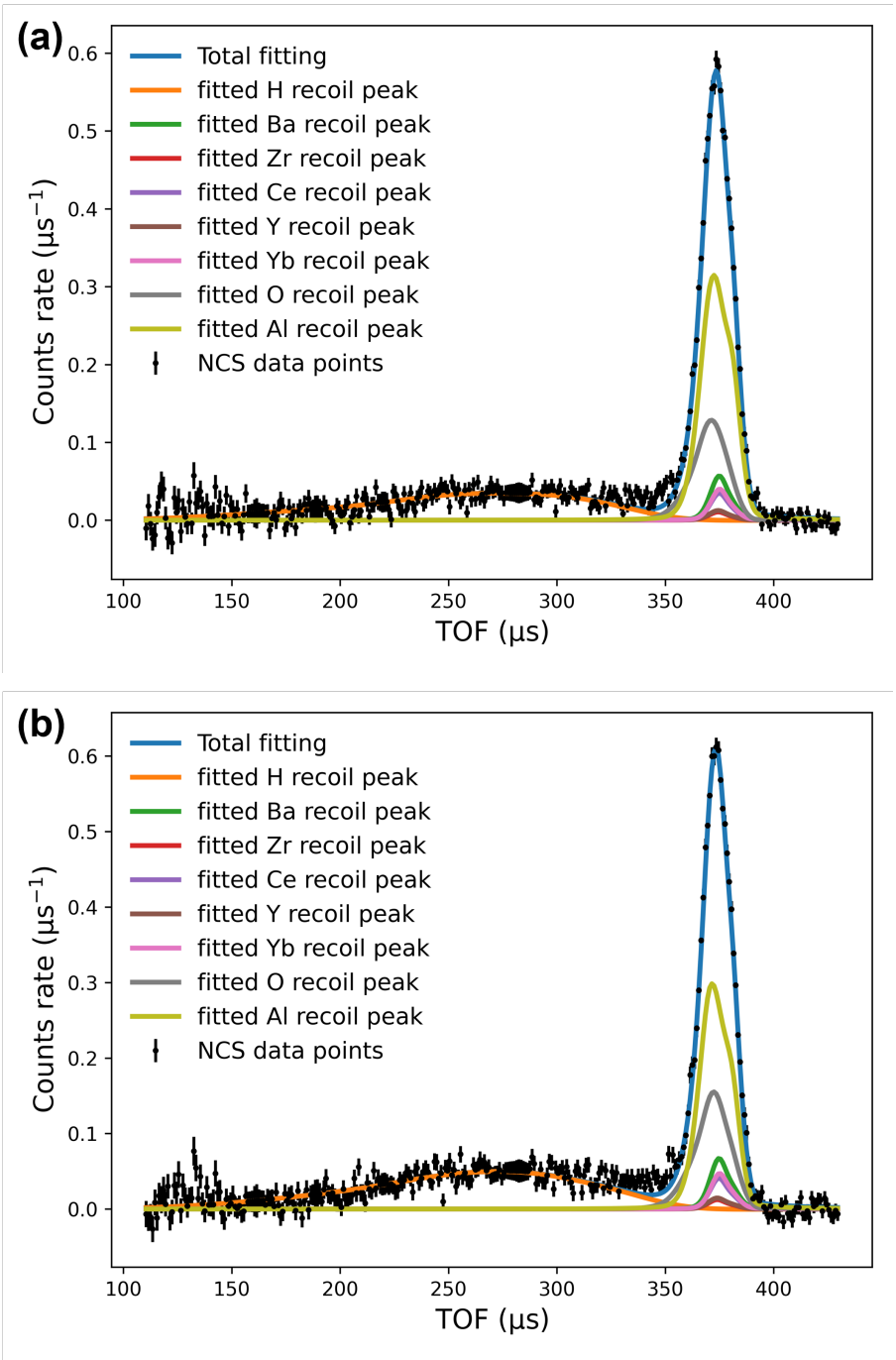


Figure 7.4: The NCS spectrum consists of the fitted recoil peaks of atomic species in (a) BZCYYb-cal based on normalised 1D Gaussian model and (b) BZCYYb-HA based on anisotropic Gaussian model at room temperature. The Al recoil peak comes from the aluminium sample container provided by Vesuvio beamline.

BZCYYb1711 structure yielded an adjacent O-O distance of approximately 3.17 Å[174], while neutron diffraction refinements of the cubic phase by Hamze et al. suggested a value of about 3.11 Å[157].

In terms of timescale, previous QENS studies on related proton-conducting perovskites have consistently reported localised proton dynamics occurring within the picosecond to nanosecond range[175]. Examples include the proton diffusion in $BaZr_{0.85}M_{0.15}O_{2.925}$ (M = Y, In, Ga) by Groβ et al.[176], local proton diffusion coefficients in $BaCa_{0.39}Nb_{0.61}O_{2.91}$ by Pionke et al.[177], and the dynamics of $BaZr_{0.9}Y_{0.1}O_{2.95}$ studied by Wilmer et al.[178], as well as activation energies for proton hopping in $BaZr_{0.90}M_{0.10}O_{2.95}$ (M = Y, Sc) reported by Karlsson et al.[179]. Taken together, these findings suggest that in BZCYYb1711 the relevant protonic motion occurs on timescales of ∼picoseconds to nanoseconds and over distances of a few Angstroms, providing a strong rationale for selecting QENS beamlines optimised for these dynamical regimes.

Building on this estimation of proton dynamics, it is important to select a neutron spectrometer that matches the relevant time and length scales. Neutron spectrometers are generally classified into three categories: time-of-flight, backscattering, and spin-echo instruments. Each type of QENS spectrometer is optimised for probing different dynamical regimes, as illustrated in Figure 7.5. Given that proton motion in BZCYYb1711 is expected to occur on picosecond-nanosecond timescales and over distances of a few Angstroms, backscattering spectrometers are the most suitable choice. Accordingly, the IN16b beamline at the Institut Laue-Langevin (ILL, France) was employed in this PhD project.

The suitability of backscattering spectrometers such as IN16b arises from their extremely high energy resolution, which allows access to slow dynamical processes on the nanosecond timescale. This relationship between instrumental energy resolution and the corresponding observable time window is expressed in Equation 7.1, where t_{res} is the characteristic observation time, h is Planck's constant (4.135×10^{-15} eV · s), and Γ_{res} is the full-width at half maximum (FWHM) of the elastic resolution function[180]. Thus, by selecting IN16b, it was possible to directly probe the proton hopping dynamics in BZCYYb1711 within the expected picosecond-nanosecond time window.

$$t_{res} \approx \frac{h}{2\pi(\Gamma_{res})} \tag{7.1}$$

In addition to the energy resolution of the selected beamline, the accessible range of energy transfer also plays a crucial role in experimental design, particularly in determining the temperature window for measurements. Ideally, a QENS instrument would capture

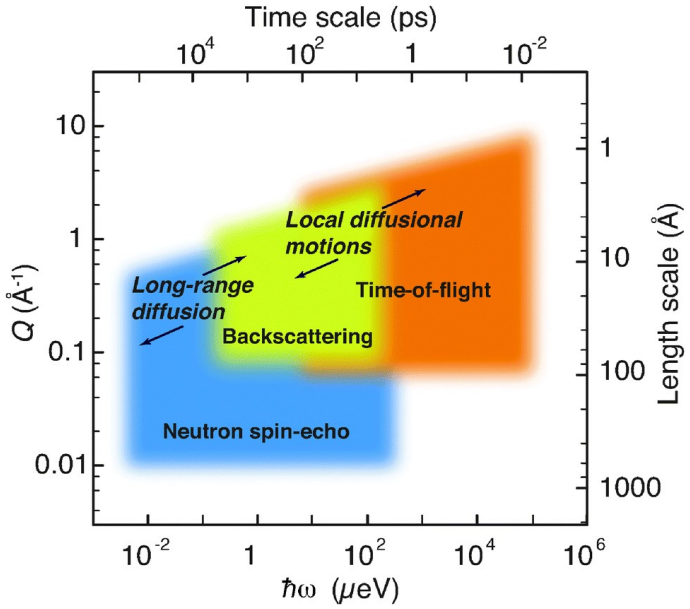


Figure 7.5: Timescale and length scale of different neutron spectroscopy techniques[181].

an infinite range of energy transfers ($\Delta\hbar\omega = \pm\infty$), allowing the full spectrum of dynamic processes to be observed. In practice, however, the measurable energy transfer is limited by the beamline instrumentation. Since the energy transfer of scattered neutrons directly reflects the kinetics of mobile species in the sample, this limitation becomes increasingly important at elevated temperatures, where proton dynamics accelerate. As illustrated in Figure 7.6, higher temperatures lead to broader QENS peaks due to faster proton mobility. Consequently, careful selection of the measurement temperature range is essential: if the proton dynamics become too fast, the associated energy transfers may exceed the instrumen's detection window, preventing signal observation.

While conducting QENS measurements at every temperature point would be the most reliable way to ensure that spectral broadening remains within the detection limits, such an approach is highly time-consuming, as each scan must cover the entire energy transfer range. A more efficient strategy is to employ the fixed window scan (FWS) method, which provides a rapid estimate of the suitable temperature window by monitoring the temperature dependence of the scattering signal at selected energy transfers[152]. Two types of FWS are commonly used: elastic FWS (EFWS), which records the structure factor $S(Q, \hbar\omega)$ at the elastic line ($\hbar\omega = 0$), and inelastic FWS (IFWS), which tracks the structure factor at a chosen finite energy transfer. These concepts are illustrated in Figure 7.6.

As illustrated by figure 7.6, increasing temperature broadens and lowers QENS peaks. Consequently, EFWS signals decrease with temperature, as shown in Figure 7.7(a). The IFWS results, presented in Figure 7.7(b), show a slightly different trend: the signal at $\hbar\omega = 0.002$ meV initially increases with temperature but then declines beyond ~380°C.

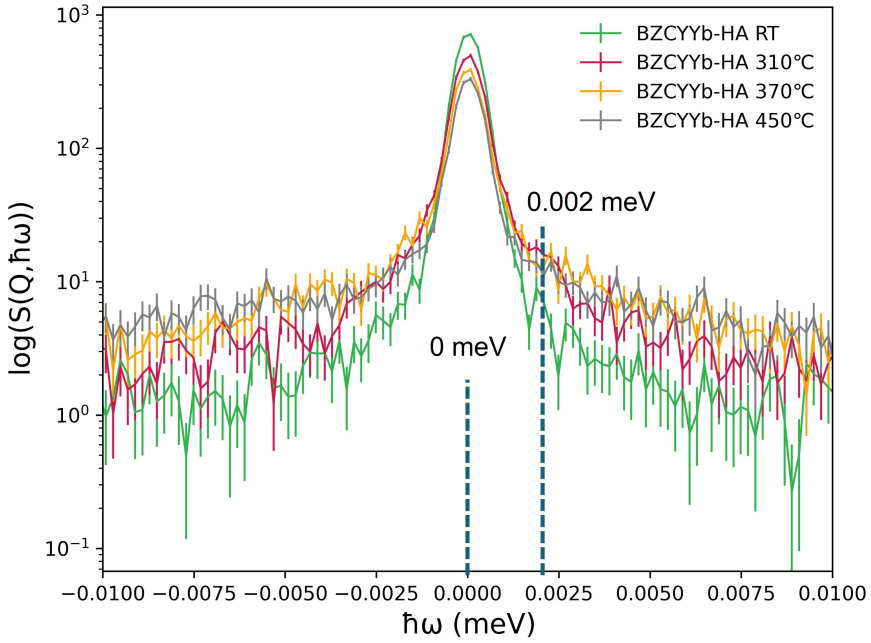


Figure 7.6: The illustration of the QENS spectra broadening of BZCYYb-HA powders measured at RT, 310°C, 370°C and 450°C in IN16b beamline (ILL, France). The indicating lines demonstrate the focused energy transfer value of elastic fixed window scan (EFWS) at 0 meV and inelastic fixed window scan (IFWS) at 0.002 meV.

This turnover occurs because the QENS peak broadens beyond the resolution window of the spectrometer, reducing the measured intensity at that energy transfer. From this behaviour, it can be inferred that the suitable upper temperature for reliable measurements on IN16b is around 450°C.

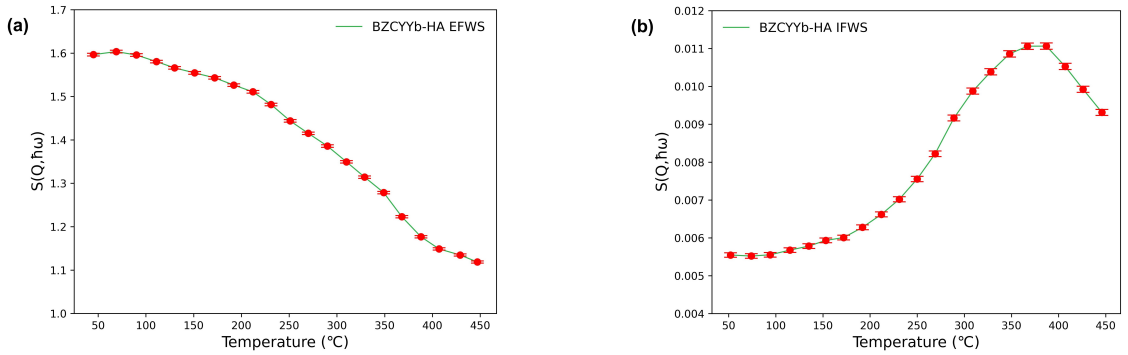


Figure 7.7: (a) The elastic fixed window scan (EFWS) of BZCYYb-HA sample from 50°C to 450°C. (b) The inelastic fixed window scan (IFWS) at energy transfer ($\hbar\omega$) = 0.002 meV of BZCYYb-HA sample from 50°C to 450°C. Both FWS experiments were performed at the IN16b beamline, ILL, France.

Once the appropriate temperature range for QENS measurements had been established, the next step was to analyse the raw neutron scattering data. However, the signal directly recorded by the detectors is not the true scattering from the sample alone. As

expressed in Equation 7.2, the measured intensity I_{S+C}^{meas}, where $S+C$ denotes the combined contributions of the sample and the container, includes both genuine scattering and attenuation effects arising from interactions within the sample and container. In other words, the measured spectrum reflects not only the intrinsic scattering but also the loss of neutrons due to absorption and scattering in the sample and container.

This attenuation effect can be exemplified by Equation 7.3, which describes the measured contribution from the sample I_{S+C}^{S}. Here, I^S is the true sample scattering, and A_{S+C}^{S} is the attenuation coefficient that depends on the scattering angle, sample and container geometry, and neutron cross-sections[182]. A similar treatment applies to the container, as shown in Equation 7.4. To isolate the pure sample signal I^S, the true container scattering I^C must first be determined from an independent measurement of the empty container I_C^{meas} (Equation 7.5), where A_C^C accounts for the container's own attenuation.

By combining Equations 7.2-7.5, the corrected sample signal I^S can be calculated as expressed in Equation 7.6, which can be further rearranged into Equation 7.7. In this form, two key correction terms are introduced: the self-attenuation factor ($SAF = \frac{A_{S+C}^C}{A_C^C}$) and the self-shielding factor ($SSF = A_{S+C}^S$). These factors are essential for correcting raw QENS data, ensuring that the extracted scattering truly reflects the dynamics of the sample.

$$I_{S+C}^{meas} = I_{S+C}^{S} + I_{S+C}^{C} \tag{7.2}$$

$$I_{S+C}^{S} = A_{S+C}^{S} I^S \tag{7.3}$$

$$I_{S+C}^{C} = A_{S+C}^{C} I^C \tag{7.4}$$

$$I_C^{meas} = A_C^C I^C \tag{7.5}$$

$$I^S = \frac{1}{A_{S+C}^S}(I_{S+C}^{meas} - \frac{A_{S+C}^C}{A_C^C} I_C^{meas}) \tag{7.6}$$

$$I^S = \frac{I_{S+C}^{meas} - SAF \times I_C^{meas}}{SSF} \tag{7.7}$$

Building on the framework described above, the attenuation coefficients were calculated by considering the cylindrical scattering geometry of the quartz container, as reported in the literature[182]. The mathematical expressions for A_{S+C}^S, A_{S+C}^C, and A_C^C are given in Equations 7.8-7.10, where R denotes the inner radius of the cylindrical container (excluding wall thickness), K is the ratio between the total diameter (including wall thickness) and the inner diameter (excluding wall thickness), μ_c and μ_s are the linear absorption coefficients of the container and sample materials, respectively, l_c and l_s are the optical path lengths in the container and sample, and r and r' represent radius vectors.

In practice, these coefficients were computed using the *PaalmanPingsMonteCarloAbsorption* algorithm in the MANTID software package, which first defines the shape, geome-

try, and composition of both the container and the sample. These parameters are then used in the *MonteCarloAbsorption* algorithm to simulate neutron trajectories and determine the attenuation correction factors[183, 184, 182]. As shown in Figure 7.8, the calculated attenuation coefficients oscillated slightly within confined limits across the measured q-range, demonstrating that they were essentially q-independent. Accordingly, each coefficient was approximated by its mean value and applied throughout the QENS data reduction process.

$$A^S_{S+C} = \frac{1}{\pi R^2} \int_0^R \int_0^{2\pi} e^{-\mu_s l_s(r,\omega) - \mu_c l_c(r,\omega)} r dr d\omega \tag{7.8}$$

$$A^C_{S+C} = \frac{1}{\pi R^2 (K^2 - 1)} \int_R^{KR} \int_0^{2\pi} e^{-\mu_s l_s(r,\omega) - \mu_c l_c(r,\omega)} r dr d\omega \tag{7.9}$$

$$A^C_C = \frac{1}{\pi R^2 (K^2 - 1)} \int_R^{KR} \int_0^{2\pi} e^{-\mu_c l_c(r',\omega)} r' dr' d\omega \tag{7.10}$$

As outlined in Equation 7.7, subtraction of the measured scattering from the empty container I_C^{meas} is essential to isolate the true scattering signal of the sample I^S. While quartz containers were chosen for their superior high-temperature stability and chemical inertness compared with aluminium, they also introduce a substantial background signal that complicates data processing. This effect is clearly illustrated in Figure 7.9(a): the QENS spectrum of the empty quartz container (red) shows a non-negligible intensity when compared with the spectrum of the BZCYYb-cal sample (green) at $q = 0.59$ Å^{-1}.

To assess whether this background is restricted to specific q values or persists across the full q-range, the QENS spectra of both the empty quartz container and the BZCYYb-cal sample were integrated over the measured energy transfer window (± 0.03 meV). The resulting $I(q)$ values, shown in Figure 7.9(b), confirm that the quartz container contributes a significant background signal across all probed q values. Moreover, the variation of $I(q)$ with q indicates that this background is not uniform but q-dependent, further highlighting the need for rigorous container subtraction during data analysis.

As shown above, the quartz container introduced a significant, q-dependent background signal. Importantly, this contribution was also temperature dependent, making its subtraction more challenging. Although some previous QENS studies have employed quartz containers, the details of background correction were rarely discussed[185, 186]. To address this gap, a dedicated protocol and a custom analysis script were developed in this PhD project to ensure reliable subtraction of the quartz background.

Ideally, background measurements should be performed at every temperature of interest; however, limited beamtime made this impractical. Instead, the empty quartz container was measured at three representative temperatures (25°C, 300°C, and 600°C), and the dependence of the background signal on temperature was modelled by interpolation.

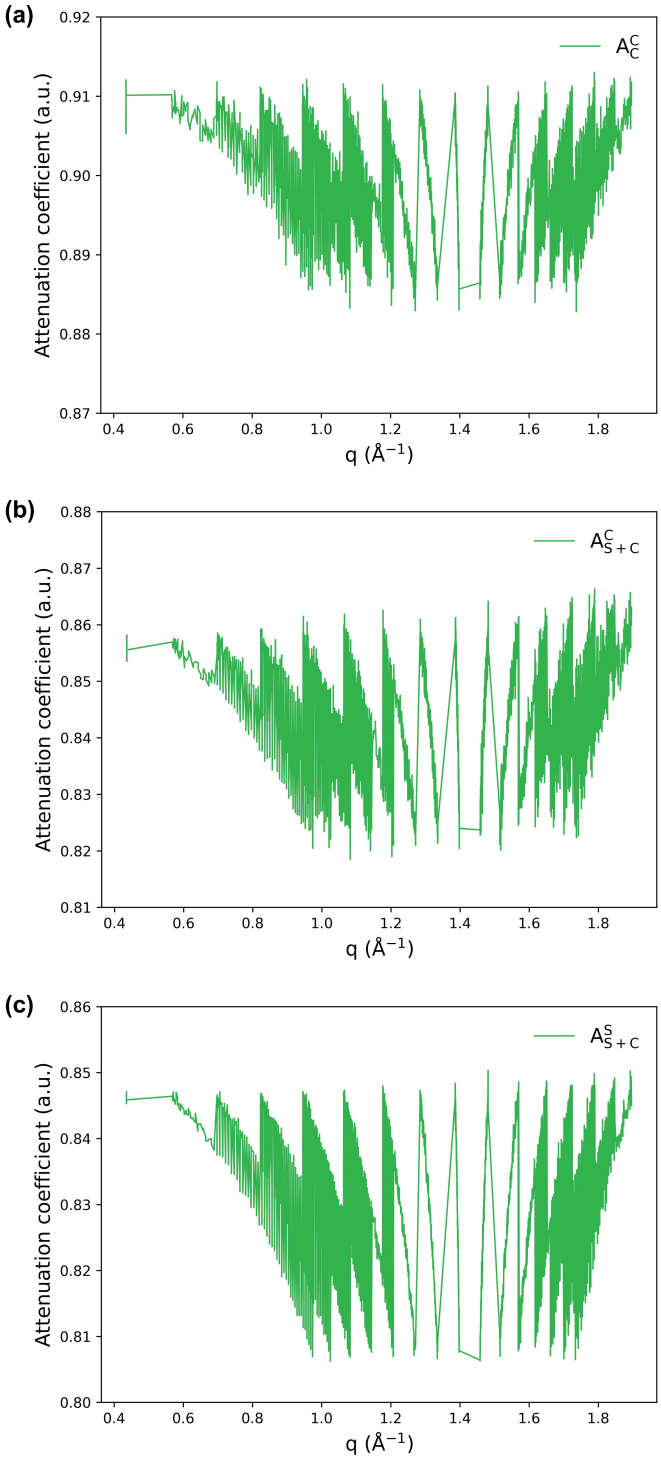


Figure 7.8: The calculation of the attenuation coefficients based on Palmann Ping's method[182] via the *PaalmanPingsMonteCarloAbsorption* algorithm in MANTID software[183, 184]: (a) the attenuation coefficient of container from container itself (A_C^C) (b) the attenuation coefficient of container from container itself and the sample (A_{S+C}^C), (c) the attenuation coefficient of container from the sample from itself and the container(A_{S+C}^S).

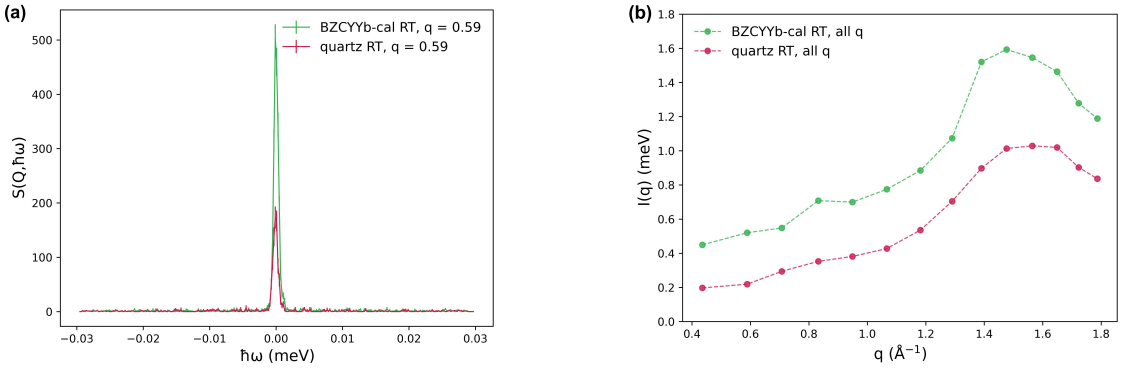


Figure 7.9: (a) Room temperature QENS spectra of BZCYYb-cal (green) and empty quartz container (red) at q = 0.59 $\mathring{A}^{-1}$ in IN16b beamline, ILL, France. (b) The integration of the room temperature QENS spectra of BZCYYb-cal and empty quartz container over all energy channels.

Figure 7.10(a) shows the peak height decreases with increasing temperature, which can be explained by the stronger thermal vibration of SiO_2 atoms. This confirmed that the quartz background depends on both q (Figure 7.9(b)) and T.

To quantify this dependence, the elastic peak intensity was integrated across the full energy transfer window ($\hbar\omega = \pm 0.03$ meV) at each temperature. The integrated values were then normalised to 25°C to obtain the intensity ratio $I_r(q, \omega, T)$ (shown in Equation 7.11), enabling direct comparison of the temperature dependence at different q values. As illustrated in Figure 7.10(b), the ratios generally followed a linear relationship with T, with high correlation coefficients ($R^2 > 0.99$) supporting this assumption. This allowed interpolation of the background intensity at the actual measurement temperatures. At some q values, however, the R^2 fell below 0.99 (Figure 7.10(c)), and in such cases the background subtraction was deemed unreliable and excluded from further analysis.

Finally, for data meeting the correlation criterion, the corrected sample intensity was obtained using Equation 7.12, where $S_a(q, \omega, T, sample)$ is the attenuation-corrected signal of sample, $S_a(q, \omega, T, quartz)$ is the attenuation-corrected signal of the empty container, and $S_{bg}(q, \omega, T, \text{sample})$ represents the measured sample signal after applying both attenuation and background subtraction. This ensured that only the scattering of sample remained after removal of the quartz contribution.

$$I_r(q, T) = \frac{I(q, T)}{I(q, 25°C)} \tag{7.11}$$

$$S_{bg}(q, \omega, T, sample) = S_a(q, \omega, T, sample) - S_a(q, \omega, T, quartz) \tag{7.12}$$

After completing the attenuation correction and background subtraction, the final step in QENS data reduction is the calibration of detector efficiency. This is typically

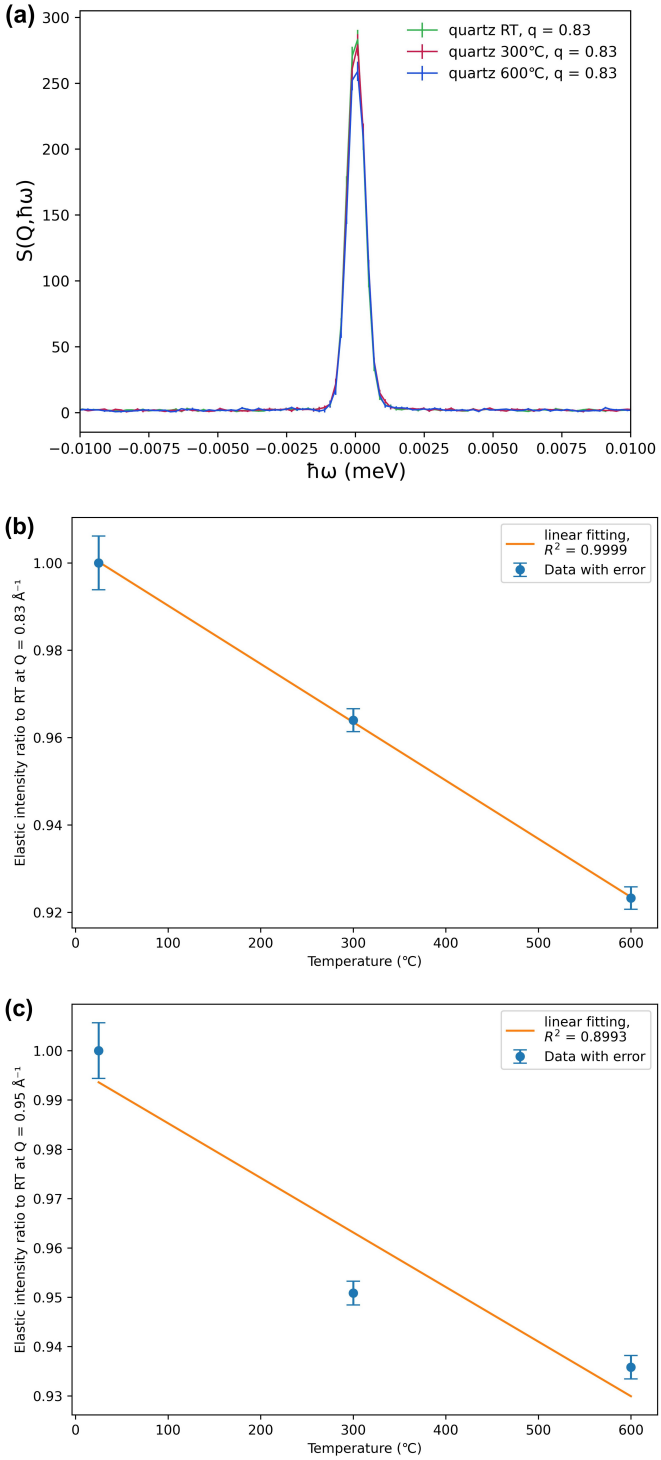


Figure 7.10: (a) The example of the QENS spectra of empty quartz container measured at 25°C, 300°C and 600°C at q = 0.83 Å^{-1} measured in IN16b beamline (ILL, France). (b) The linear fitting between the ratio of the integration to the whole energy transfer range ($\hbar\omega = \pm 0.03$ meV) at each measured temperature to the integration value at 25°C at q = 0.83 Å^{-1} of measured empty quartz container in IN16b beamline (ILL, France). (c) The linear fitting between the ratio of the integration to the whole energy transfer range ($\hbar\omega = \pm 0.03$ meV) at each measured temperature to the integration value at 25°C at q = 0.94 Å^{-1} of measured empty quartz container in IN16b beamline (ILL, France).

carried out using a vanadium cylinder, which serves as the standard because vanadium scatters neutrons both elastically and incoherently. Its elastic scattering makes the signal temperature-independent, facilitating normalisation, while its incoherent nature ensures that the scattering is free from structural contributions such as Bragg peaks. As a result, the vanadium signal should in theory be q-independent.

In practice, however, variations in detector efficiency lead to differences in the measured intensity at different q values. Figure 7.11(a) shows the integrated elastic intensity of the vanadium spectrum ($\hbar\omega = \pm 0.002$ meV) across q, clearly revealing this instrumental dependence. To correct for it, the vanadium spectrum $S(q, \omega, \text{vanadium})$ was divided by its integrated elastic intensity $I(q, \text{vanadium})$, as expressed in Equation 7.13. The resulting normalised vanadium spectrum $S_v(q, \omega, \text{vanadium})$ was then re-integrated over the same energy range (Equation 7.14), yielding $I_v(q, \text{vanadium})$. As illustrated in Figure 7.11(b), the q-independence of $I_v(q, \text{vanadium})$ confirmed that detector normalisation was performed correctly.

Finally, this calibration was applied to the sample data: the background-corrected and attenuation-corrected spectrum $S_{bg}(q, \omega, \text{sample})$ was divided by $I(q, \text{vanadium})$, producing the fully reduced spectrum $S_v(q, \omega, \text{sample})$ (Equation 7.15), which was subsequently used for data fitting.

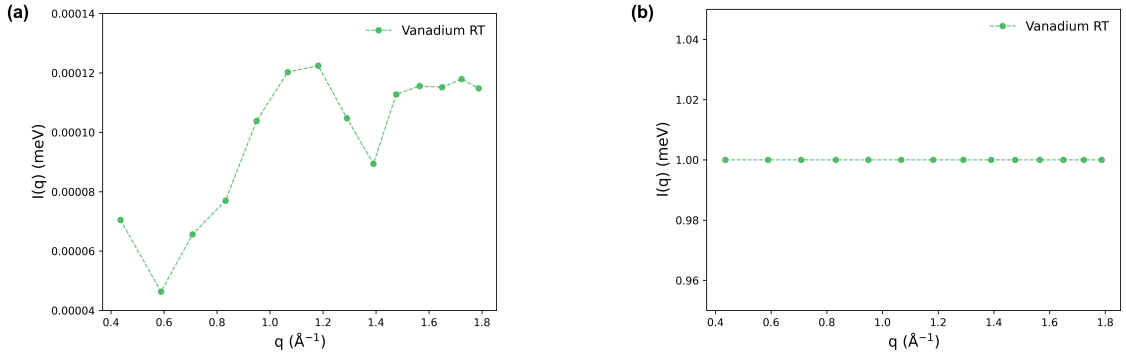


Figure 7.11: (a) The integration of vanadium QENS spectrum in the elastic energy tranfer range ($\hbar\omega = \pm 0.002$ meV) at different q values. (b) The integration of the normalised vanadium QENS spectrum after the division by the integration of raw vanadium QENS spectrum in the elastic energy tranfer range ($\hbar\omega = \pm 0.002$ meV), this result proves the correct normalisation of detectors' efficiencies.

$$S_v(q,\omega,vanadium) = \frac{S(q,\omega,vanadium)}{I(q,vanadium)} \tag{7.13}$$

$$I_v(q,vanadium) = \int_{-0.002}^{0.002} S_v(q,\omega,vanadium)d\hbar\omega \tag{7.14}$$

$$S_v(q,\omega,sample) = \frac{S_{bg}(q,\omega,sample)}{I(q,vanadium)} \tag{7.15}$$

After completing the data reduction, the QENS spectra of the BZCYYb samples were ready for detailed analysis. Based on the assumption that protons dominate the scattering response, the measured total structure factor $S^{meas}(q,\omega)$ can be approximated by the incoherent structure factor $S_i^{meas}(q,\omega)$. In practice, this measured signal is expressed as the convolution of the intrinsic incoherent dynamic structure factor of the sample, $S_i(q,\omega)$, with the instrumental resolution function, $R(q,\omega)$, as shown in Equation 7.16.

$$S_i^{meas}(q,\omega) = R(q,\omega) \otimes S_i(q,\omega) \tag{7.16}$$

To obtain the resolution function, the BZCYYb sample measured at room temperature (RT) was used. At this condition, the protons are essentially immobile, and the signal resembles a purely elastic response similar to that of the vanadium standard. Consequently, the RT spectrum exhibits no detectable broadening of the QENS peak, as illustrated in Figure 7.12, and can therefore be reliably employed to describe the instrumental resolution.

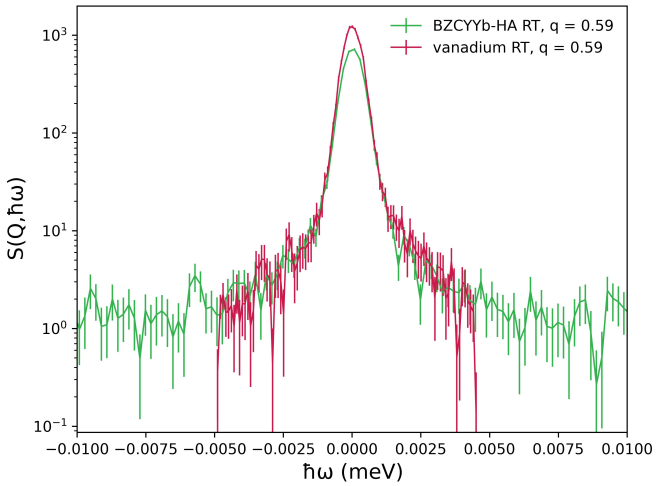


Figure 7.12: The example of QENS spectra of BZCYYb-HA powders and vanadium standard at q = 0.59, both experiments were measured at room temperature in IN16b beamline(ILL, France).

As outlined in Equation 7.17, the incoherent QENS signal can generally be decomposed into two principal contributions: an elastic term, represented by a delta function $\delta(\omega)$ with

amplitude $A_0(Q)$, and a incoherent quasielastic term, $S_i^{qe}(q,\omega)$, with corresponding amplitude A_1[152]. The elastic component captures immobile species or protons confined in static sites, as it corresponds to zero energy transfer. In contrast, the quasielastic broadening, which carries the information on dynamic processes, is usually described by one or more Lorentzian functions $L(q,\omega)$, as shown in Equation 7.18. Each Lorentzian contribution reflects a distinct dynamic process, and its width, expressed as the half-width-at-half-maximum (HWHM) $\Gamma(q)$ in Equation 7.19, correlates to the timescale of the motion[181]. Narrow Lorentzian peaks therefore indicate slower proton dynamics, while broader peaks correspond to faster motions.

$$S_i(q,\omega) = A_0(q)\delta(\omega) + (1 - A_0)S_i^{qe}(q,\omega) \tag{7.17}$$

$$S_i^{qe}(q,\omega) = \sum_{l=1} A_l(q)L_l(q,\omega) \tag{7.18}$$

$$L(q,\omega) = \frac{1}{\pi}\frac{\Gamma(q)}{(\hbar\omega)^2 + (\Gamma(q))^2} \tag{7.19}$$

$$S_i^{meas}(q,\omega) = R(q,\omega) \otimes [(A_0(Q)\delta(\omega) + A_1 S_i^{qe}(q,\omega))] + B \tag{7.20}$$

By combining these relationships (Equations 7.16-7.19), the full expression of the incoherent measured structure factor is obtained, as illustrated in Equation 7.20. In this form, the measured signal is represented as the convolution of the instrumental resolution with both the delta (elastic) and Lorentzian (quasielastic) terms, together with an additional flat background B, which accounts for ultrafast motions occurring beyond the detection window of the spectrometer.

The fitting procedure described in Equation 7.20 relies on the assumption that the measured structure factor can be approximated solely by the incoherent contribution. However, in practice, coherent scattering from the BZCYYb sample can influence the results at certain q values. To examine this, neutron diffraction of the BZCYYb-cal sample was carried out at room temperature on the XTREMED beamline (ILL, France) using an incident neutron wavelength of 2.45 Å, as shown in Figure 7.13. In addition to a relatively flat signal, which is due to the incoherent scattering from the incorporated protons in the BZCYYb-cal system, Bragg peaks were observed at $q \approx 1.43$ Å^{-1} and $q \approx 2.04$ Å^{-1}. These peaks confirm the presence of coherent scattering contributions at specific q regions. Importantly, the Bragg peak at $q \approx 1.43$ Å^{-1} lies within the q range probed by the IN16b beamline used for QENS measurements. Consequently, QENS data around this q value were excluded from fitting, as the measured scattering could not be attributed purely to incoherent processes.

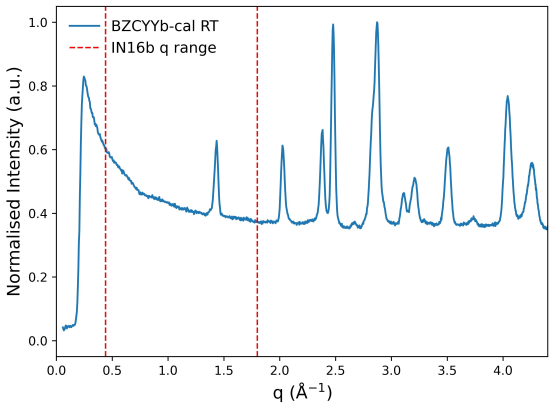


Figure 7.13: The neutron diffraction pattern of BZCYYb-cal sample with normalised intensity [0,1] measured at RT in XTREMED beamline (ILL, France), the wavelength of the incident neutron was 2.45 Å. The q-range of IN16b beamline is outlined by red dashed line.

Figures 7.14 (a) and (b) shows the QENS spectra of BZCYYb-HA and BZCYYb-cal samples fitted with a single Lorentzian function, from which the q-dependent half-width at half-maximum (HWHM) values were extracted to quantify the spectral broadening. To interpret these HWHM parameters in terms of proton dynamics, theoretical jump-diffusion models are commonly employed. The most widely applied is the Chudley-Elliott (CE) model, which assumes successive proton hops occur over a constant distance l and are independent of one another[187]. The CE model is mathematically expressed in Equation 7.21, where $\hbar$ is the reduced Planck constant, τ is the mean residence time between successive hops, q is the momentum transfer of scattered neutrons, and l is the fixed jump length. For practical reasons, the comparison between BZCYYb-cal and BZCYYb-HA was only performed at 310°C, as the limited beamtime available allowed QENS measurements to be collected at this temperature for both systems.

In addition to the CE model, the Hall-Ross (HR) jump-diffusion model can also be applied to solid-state systems[188]. Unlike the CE model, which assumes a uniform jump distance, the HR model accounts for random diffusion processes in which the jump length follows a Gaussian distribution, as expressed in Equation 7.22, where $\langle l^2 \rangle$ denotes the mean squared jump length. In this work, both CE and HR models were employed in parallel to evaluate which model described better the localised proton hopping behaviour in the BZCYYb samples.

$$\Gamma(q) = \frac{\hbar}{\tau}(1 - \frac{sin(ql)}{ql}) \tag{7.21}$$

$$\Gamma(q) = \frac{\hbar}{\tau}(1 - exp\frac{-Q^2\langle l^2 \rangle}{6}) \tag{7.22}$$

The fitting results obtained using the Chudley–Elliott (CE) and Hall–Ross (HR) mod-

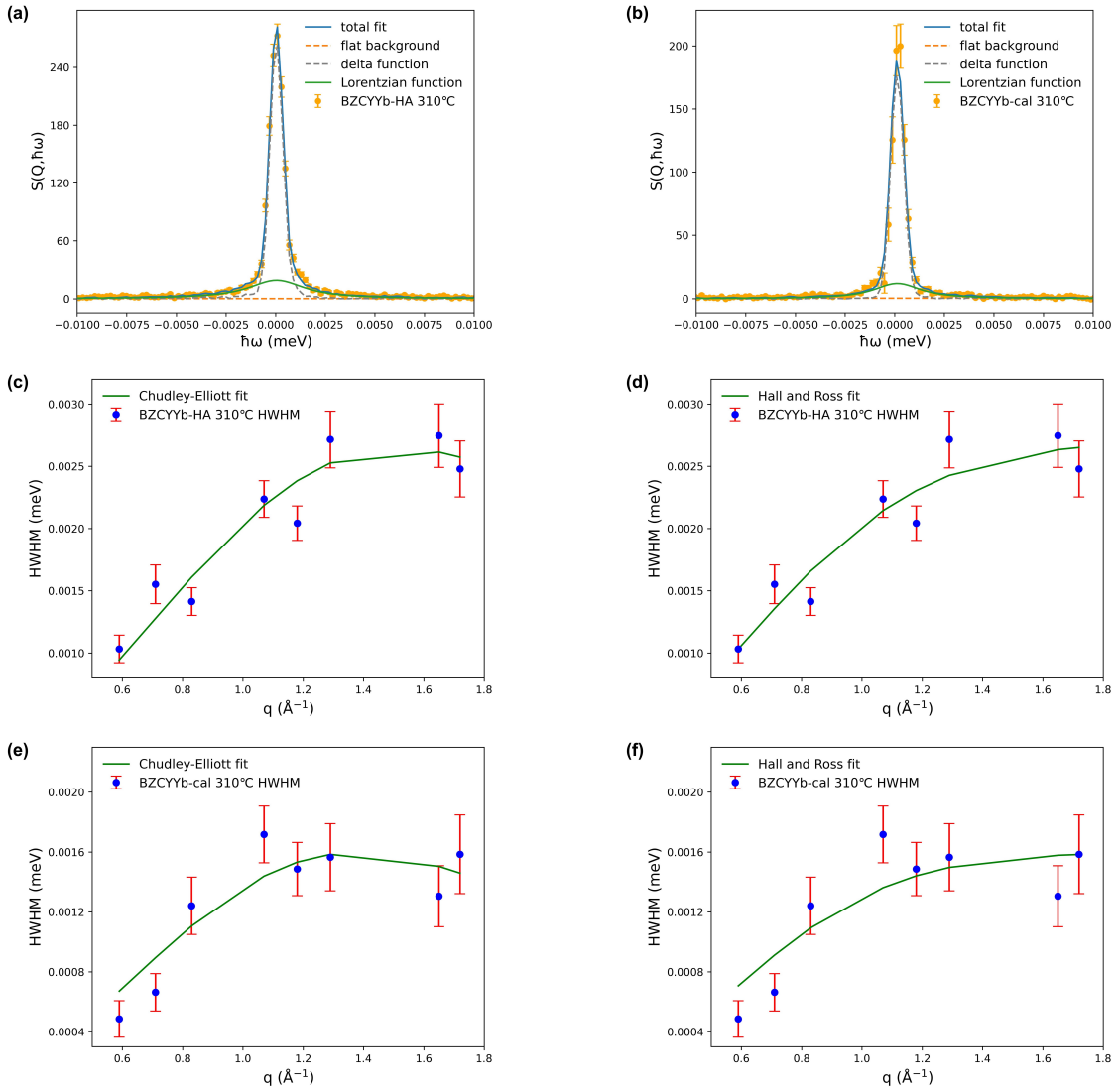


Figure 7.14: (a) The fit of the QENS spectrum of BZCYYb-HA sample measured at 310°C in IN16b (ILL, France) using a flat background, a delta function for the elastic term and a Lorentzian function for the quasielastic term which both are convoluted with the resolution function. (b) The fit of the QENS spectrum of BZCYYb-cal sample measured at 310°C using a flat background, a delta function for the elastic term and a Lorentzian function for the quasielastic term which both are convoluted with the resolution function. (c) The HWHM of the BZCYYb-HA sample measured at 310°C in IN16b (ILL, France) fitted with the Chudley-Elliot jump diffusion model, the reduced χ^2 value is 1.458. (d) The HWHM of the BZCYYb-HA sample measured at 310°C in IN16b (ILL, France) fitted with the Hall and Ross jump diffusion model, the the reduced χ^2 value is 1.682. (e) The HWHM of the BZCYYb-cal sample measured at 310°C in IN16b (ILL, France) fitted with the Chudley-Elliot jump diffusion model, the reduced χ^2 value is 1.708. (f) The HWHM of the BZCYYb-cal sample measured at 310°C in IN16b (ILL, France) fitted with the Hall and Ross jump diffusion model, the the reduced χ^2 value is 2.213.

els are presented in Figure 7.14 (c–f). For both BZCYYb-cal and BZCYYb-HA, the CE model consistently yielded reduced χ^2 values closer to one, indicating a statistically superior fit. However, as summarised in Table 7.3, no significant difference was observed in the fitted jump lengths between the two models, and the corresponding diffusion coefficients were of comparable magnitude. These results suggest that both models fit the localised protonic motion in BZCYYb-cal and BZCYYb-HA equivalently. However, based on the underlying theoretical assumptions of the two models, the CE model is preferred, as it is widely applied to describe dynamics in crystalline materials where the hopping distance remains relatively constant. In contrast, the HR model assumes a continuous Gaussian distribution of jump lengths, representing less constrained motion typical of disordered or amorphous systems.

As shown in Table 7.3, the jump lengths derived from QENS fitting for both BZCYYb-cal and BZCYYb-HA are very similar. This indicates that protons in both systems hop between comparable adjacent oxygen sites, and that the additional humid annealing applied to BZCYYb-HA did not alter the fundamental hopping distance or available transport pathways. However, the fitted mean residence time is significantly shorter in BZCYYb-HA, pointing to a faster proton hopping rate and, consequently, enhanced local diffusion.

Table 7.3: The fitted jump diffusion length (l), mean residence time (tau) and corresponding calculated diffusion coefficient ($D = \frac{l^2}{6\tau}$) of BZCYYb-cal and BZCYYb-HA QENS results with Chudley-Elliot (CE) jump diffusion model and Hall and Ross (HR) jump diffusion model. The * represents the root mean square average jump diffusion length fitted based on HR model as shown in Equation 7.22

Sample	**fitted jump length /Å**	**fitted mean residence time /ps**	**fitted diffusion coefficients /cm^2s^{-1}**
BZCYYb-cal with CE model	3.3(2)	502(29)	$3.5(5)\times 10^{-7}$
BZCYYb-cal with HR model	3.2(5)*	413(41)	$4(1)\times 10^{-7}$
BZCYYb-HA with CE model	3.0(2)	303(13)	$5.0(6)\times 10^{-7}$
BZCYYb-HA with HR model	2.9(3)*	244(16)	$6(1)\times 10^{-7}$

In summary, the QENS analysis demonstrates that while the hopping distance of protons in BZCYYb-cal and BZCYYb-HA remains essentially unchanged, the dynamics of the hopping process differ markedly. The humid-annealed BZCYYb-HA exhibits a substantially shorter mean residence time, indicating a higher hopping frequency and enhanced local proton diffusion compared with the as-calcined sample.

7.2 Effect of Humid Annealing on Total Conductivity

While neutron techniques provide insight into localised proton hopping, electrochemical impedance spectroscopy (EIS) was employed to assess the influence of hydration on overall conductivity and to probe the long-range proton dynamics in the BZCYYb1711 system.

Reliable impedance measurements require careful optimisation of several experimental parameters, including the frequency range of the applied sinusoidal voltage and the selected temperature range[189].

To verify the suitability of the experimental settings described above, the Lin-KK (linear Kramer-Kronig) test was employed, based on the Kramers-Kronig (KK) relations. Examples of the KK test will be shown in the following section[190, 191]. The KK relations enable the calculation of the real part of impedance from the imaginary part, and vice versa, as expressed in Equations 7.23-7.24[190]. This interconvertibility between $Z_{Re}(\omega)$ and $Z_{Im}(\omega)$ relies on three conditions being satisfied: linearity, which represents a proportional response to the applied sinusoidal voltage. Causality stands for the response originates solely from the applied perturbation. Stability demands that the impedance remains reproducible under repeated testing. The Lin-KK test therefore serves as a practical tool to validate the reliability of measured impedance spectra, while also allowing the impact of different experimental settings on data quality to be systematically evaluated.

$$Z_{Re}(\omega) = \frac{2}{\pi}\int_0^\infty \frac{\omega' \cdot Z_{Im}(\omega')}{\omega^2 - \omega'^2} d\omega' \tag{7.23}$$

$$Z_{Im}(\omega) = \frac{-2\omega}{\pi}\int_0^\infty \frac{\omega \cdot Z_{Re}(\omega')}{\omega^2 - \omega'^2} d\omega' \tag{7.24}$$

The selection of the frequency range for the applied sinusoidal voltage is directly linked to the working principle of EIS. In theory, each electrochemical process can be represented by an equivalent circuit consisting of a resistor and a capacitor connected in parallel (as detailed in the section5.11)[192]. Such an RC element is characterised by a distinct time constant, as defined in Equation 7.25:

$$\tau = R \cdot C \tag{7.25}$$

$$f = \frac{1}{\tau} = \frac{1}{R \cdot C} \tag{7.26}$$

Here, τ represents the characteristic time constant of a given electrochemical process, with R and C denoting its resistance and capacitance, respectively. The capacitance values associated with different electrochemical processes span a wide range, as reported by Irvine et al.[193]. As shown in Table 7.4, capacitances can vary from as small as 10^{-12} F to as large as 10^{-4} F. According to the relationship between capacitance, time constant, and the frequency of the applied sinusoidal voltage (Equation 7.26), processes with smaller capacitances, such as bulk conduction, require higher probing frequencies, while processes with larger capacitances, such as electrode effects, are accessible at lower frequencies. Consequently, employing a broad frequency range is essential to fully resolve and characterise the different electrochemical processes occurring within the sample.

Table 7.4: Capacitance values and their possible interpretation of electrochemical process[193].

Capacitance/F	Corresponding process
10^{-12}	Bulk
10^{-11}	Minor, second phase
10^{-11} - 10^{-8}	Grain boundary
10^{-10} - 10^{-9}	Bulk ferroelectric
10^{-9} - 10^{-7}	Surface layer
10^{-7} - 10^{-5}	Sample-electrode interface
10^{-4}	Electrochemical reactions

Although most commercial instruments claim the capability to measure frequencies above 1 MHz, in practice it is difficult to obtain reliable data in this range. At very high frequencies, the data quality can be compromised by parasitic effects such as the inductance of leads and connections in the setup[194]. This limitation is demonstrated in the EIS results of the BZCYYb-cal symmetric cell shown in Figure 7.15. In Figure 7.15 (a), the Nyquist plot obtained within the frequency window of 1 Hz-1 MHz shows smooth and consistent data points. In contrast, Figure 7.15 (b) displays an abrupt jump in the high-frequency region when frequencies above 10^6 Hz are included. This artefact directly affects the Kramers-Kronig (KK) validation: as shown in Figure 7.15 (d), the residual error becomes significantly larger above 10^6 Hz, while remaining small and acceptable between 1 Hz and 10^6 Hz. These results confirm that the data collected above 10^6 Hz fail to satisfy the KK relations and are therefore invalid. For this reason, the upper frequency limit used in the EIS measurements of the BZCYYb system was set to 10^6 Hz.

Adjusting the measuring temperature provides a practical way to probe fast electrochemical processes requiring frequencies above 1 MHz, since lowering the temperature slows down the kinetics. Figure 7.16 illustrates how temperature affects which processes can be captured within the fixed frequency window (1 MHz-1 Hz). It is worth noting that a constant phase element (CPE) was used instead of an ideal capacitor (C) to fit the deformed semicircles observed in the Nyquist plots. The relationship between the CPE and the equivalent capacitance is described in section 5.11. At 426°C (Figure 7.16 (a)), an RC equivalent circuit was applied with the fitted capacitance of approximately 2.1×10^{-3} F. This relatively large capacitance corresponds to a slower process, most likely related to electrode-electrolyte interfacial reactions, indicating that the faster protonic processes in the bulk or grain boundaries could not be resolved at this temperature. This limitation arises because proton mobility in the BZCYYb symmetric cell is too fast to be captured within the 1 MHz upper frequency limit, restricting the measurement to slower contributions instead. Under such circumstances, the only practical way to estimate the total

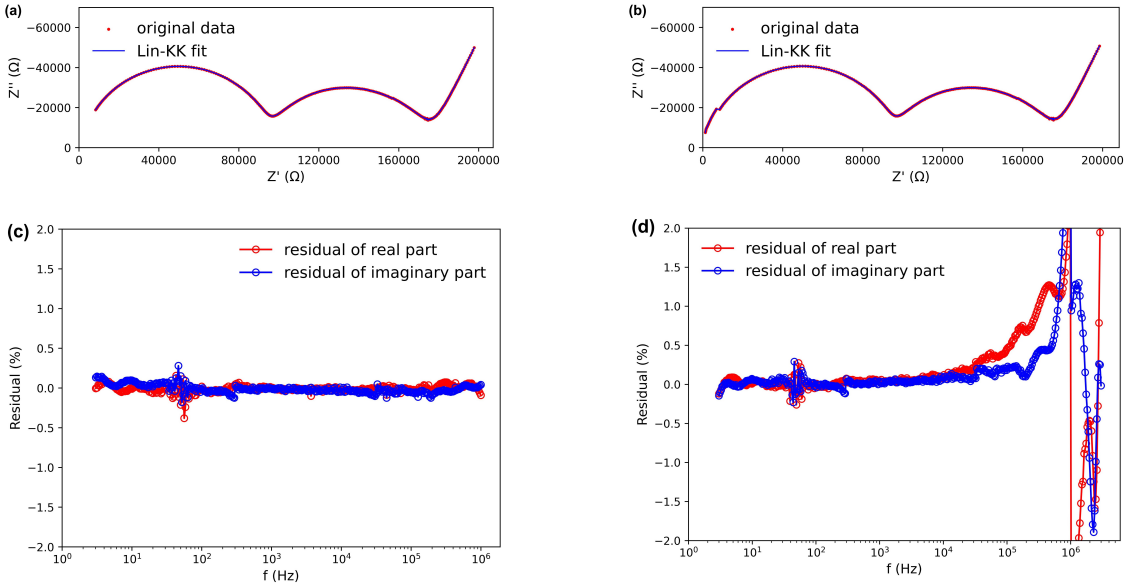


Figure 7.15: The effect of selected measured frequency on the data validity tested by Lin-KK tool. The BZCYYb-cal symmetric cell with Pt electrodes was measured at 150°C under dry compressed air condition. (a) The Nyquist plot of EIS data measured from 1 MHz to 1 Hz. (b) The Nyquist plot of EIS data measured from 3 Mhz to 1 Hz. (c) The residual, representing the difference of measured and calculated real and imaginary part of impedance, of data measured from 1 MHz to 1 Hz. (d) The residual, representing the difference of measured and calculated real and imaginary part of impedance, of data measured from 3 MHz to 1 Hz.

conductivity of the BZCYYb1711 electrolyte is to take the intercept value (highlighted in the blue circle) between the impedance data and the real axis (corresponds to the resistive component). Although this intercept value inevitably includes overlapping contributions from bulk transport, grain boundaries, and electrode processes, it is here approximated as the total resistance of the BZCYYb1711 electrolyte within the constrained frequency window.

While at higher temperatures the rapid proton mobility prevents fast electrochemical processes from being resolved within the measured frequency window, lowering the temperature slows down proton migration and allows additional processes to emerge in the EIS spectra. As shown in Figure 7.16 (b), the data at 166°C could be fitted with a two-RC equivalent circuit, yielding capacitance values of 5.5×10^{-10} F and 6.1×10^{-7} F. According to the ranges reported in Table 7.4, these correspond to grain boundary conduction and the sample-electrode interface, respectively. When the temperature was further reduced to 118°C (Figure 7.16 (c)), the slower kinetics enabled resolution of an additional process. The data were fitted with a three-RC equivalent circuit, revealing a smaller capacitance of 4.5×10^{-11} F, which can be attributed to bulk proton transport in the BZCYYb1711 electrolyte.

Thus, varying the measurement temperature not only enabled the conductivity of the BZCYYb symmetric cell to be evaluated across different thermal conditions, but also al-

lowed inaccessible electrochemical processes to be resolved within the limited frequency window (1 MHz-1 Hz).

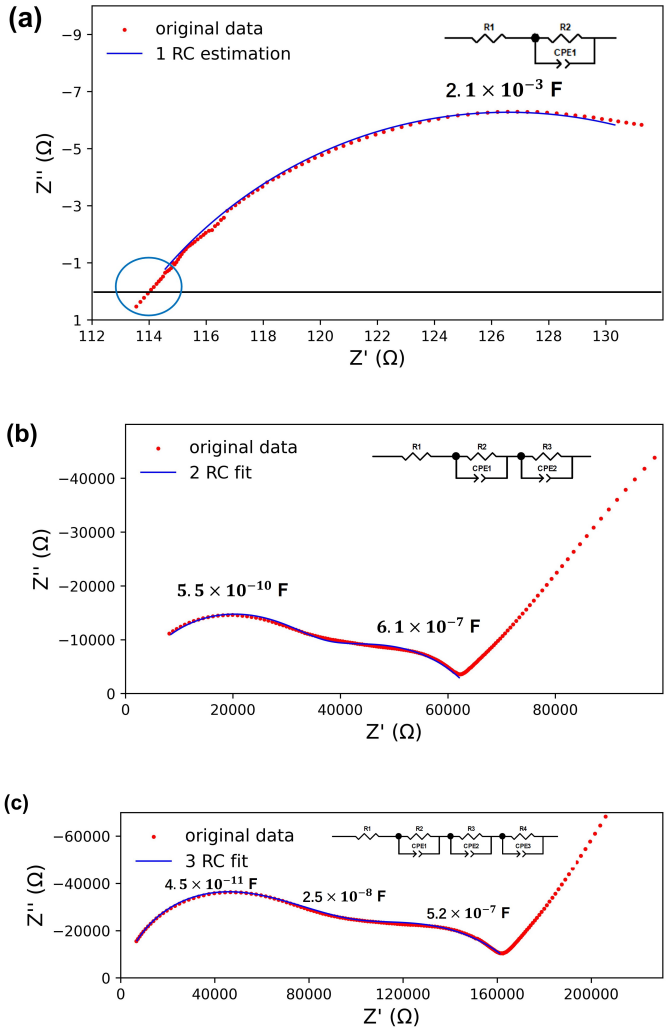


Figure 7.16: The fitted EIS data of BZCYYb-cal symmetric cell measured under dried (passed through drying tube) compressed air from 1 MHz to 1 Hz at (a) 426°C, (b) 166°C with chi-squared value of fitting = 4.4×10^{-5} and (c) 118°C with chi-squared value of fitting = 1.6×10^{-5}. The measured temperatures were probed by the thermocouple positioned close to the measured symmetric cell.

Using the fitting strategy described above, the total conductivity of the BZCYYb-Pt symmetric cell was determined from electrochemical impedance spectroscopy (EIS) measurements. Although BZCYYb1711 has been reported as a mixed ionic conductor, supporting both protonic and oxide-ion transport[8], the measured total conductivity can be attributed predominantly to proton conduction. This is because electronic contributions are negligible (>97% ionic transport number[75]), while oxide-ion conduction is strongly suppressed below 550°C. As shown in Figure 7.17, the conductivity measured under dry air was close to that under humid air across the full temperature range of 517°C to 95°C. This very small difference between dry and humid conditions is consistent with findings

reported in the literature[68, 72, 73], further indicating that the humid annealing did not improve the conductivity significantly. Moreover, a distinct change in Arrhenius slope is observed at ≈323°C, indicating a lower proton hopping activation energy at high temperature regime (>323°C). This changing activation energy may be explained from the electrostatic attraction between protons (positively charged) and accpetor dopants (negatively charged), which may form the dopant-proton pairs. At lower temperatures, the binding energy of these pairs exceeds thermal energy, reducing the effective mobile proton fraction and increasing the apparent activation energy. As temperature increases, partial dissociation occurs, which facilitates long-range proton transport and leads to lower activation energy.

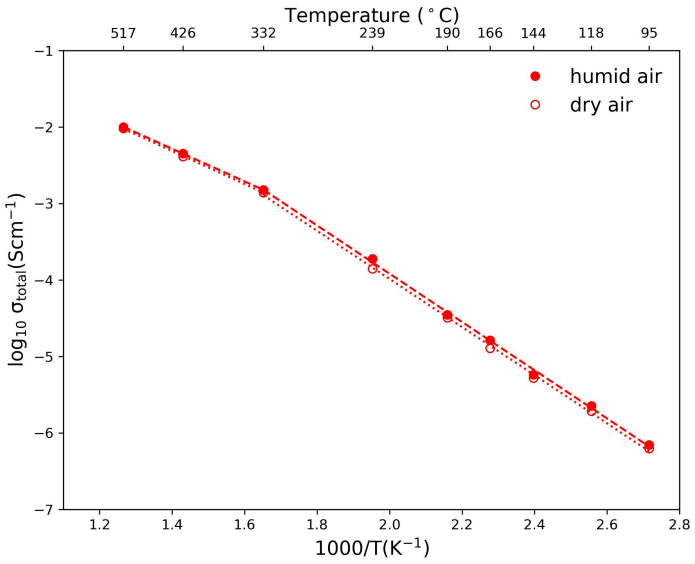


Figure 7.17: The total conductivity of BZCYYb symmetric cells coated with Pt electrodes measured under humid air (3 vol% H_2O) and dry air ($pH_2O \approx 10^{-5}$ mbar) condition from temperature range 517°C to 95°C.

The small difference in conductivity between dry and humid conditions indicates that the presence of 3 vol% H_2O did not significantly affect the measured total conductivity. A plausible explanation for this behaviour is that the sintered BZCYYb pellets (used to fabricate the BZCYYb symmetric cell for EIS measurements) already contained a non-negligible amount of protons, which contributed predominantly to the total conductivity, while the additional protons introduced under humid conditions played only a minor role. This observation is consistent with the findings discussed in Section 6.

As discussed in Section 3.1, proton dynamics in the BZCYYb1711 system have generally been analysed indirectly using electrochemical impedance spectroscopy (EIS), through measurements of total conductivity. However, only a limited number of studies have reported protonic rather than total conductivity for BZCYYb at medium-to-low temperatures (<400°C), as illustrated in Figure 7.17. This gap raises an important question: Do protons remain mobile and contribute to transport in this medium-low temperature

regime? Although QENS enables direct probing of localised proton hopping, the dynamics it captures occur on different time and length scales compared with EIS measurements. To bridge this gap, the isotopic exchange depth profiling (IEDP) technique was employed, in which hydrogen isotopic diffusion is monitored using secondary ion mass spectrometry (SIMS). This method provides direct information on hydrogen isotope transport information and the measured length scales are comparable to those probed by EIS.

As described in Section 5.9, deuterium (D) has an atomic mass of 2.014 amu. Figure 7.18(a) shows that the measured signal intensity at $m/z = 2.014$ was significantly higher in the deuterium-exchanged BZCYYb pellet compared with the unexchanged reference, confirming the capability of the SIMS technique to effectively detect and trace deuterium. The two-dimensional (2D) scan of the cross-sectional surface of the exchanged BZCYYb sample (sample preparation details shown in section 5.9), shown in Figure 7.18(b), reveals that the D signal intensity decreases progressively along the Y direction, corresponding to the depth from the pellet surface toward the centre. This gradient clearly indicates deuterium diffusion within the BZCYYb lattice.

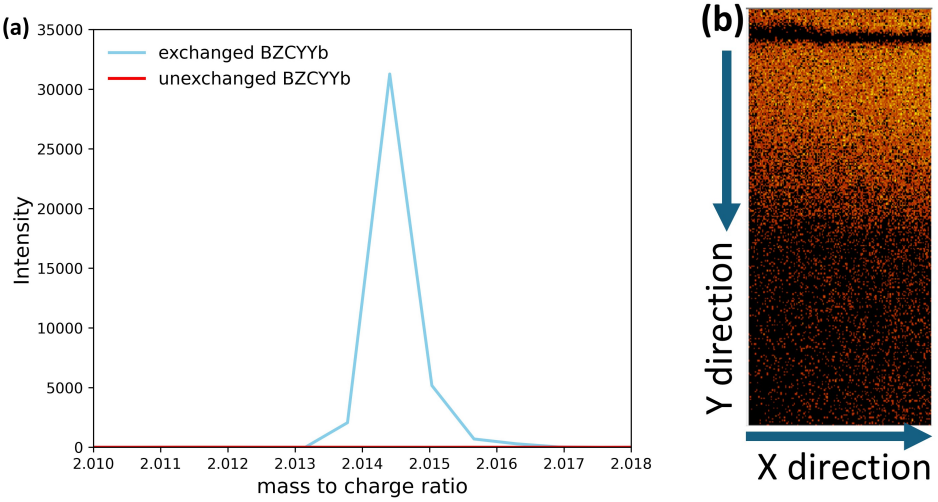


Figure 7.18: (a) SIMS mass spectrum of the exchanged BZCYYb pellet and the unexchanged pristine reference. (b) 2D SIMS image of the cross-sectional side of exchanged BZCYYb sample. In the 2D scanning, the SIMS technique measured the intensity of m/z = 2.014 signal along each point with (x,y) position, and the blue arrows illustrate the X and Y directions.

The 2D scan data shown in Figure 7.18(b), which display the deuterium signal intensity as a function of (x, y) position, were converted into one-dimensional (1D) profiles to analyse the diffusion path of exchanged deuterium along the Y direction from the pellet surface. This was achieved by grouping all data points with the same Y-coordinate across the X direction.

To quantitatively analyse the isotopic diffusion and achieve the transport parameters such as isotopic tracer diffusion coefficient (D^*), the semi-infinite diffusion model developed

by Crank[195] was applied, which is shown below:

$$C'(x,t) = \frac{C(x,t) - C_{bg}}{C_g - C_{bg}} = erfc[\frac{x}{2\sqrt{D^*t}}] - [exp(\frac{kx}{D^*} + \frac{k^2t}{D^*}) \times erfc(\frac{x}{2\sqrt{D^*t} + k\sqrt{\frac{t}{D^*}}})] \tag{7.27}$$

where x is the diffusion depth from the surface of the sample, t is the time taken of the diffusion of exchanged species, $C'(x,t)$ is the normalised isotopic fraction, $C(x,t)$ is the measured isotopic fraction of deuterium, C_{bg} is the natural abundance of deuterium (0.0156%), C_g is the isotopic fraction of deuterium in the deuterium oxide (99.9 atom% D, Sigma Aldrich, UK) applied in exchange annealing environment, D^* is the isotopic tracer diffusion coefficient and k is the surface exchange coefficient.

Figures 7.19(a) and (b) present the fitted isotopic diffusion profiles of samples exchanged at 260°C and 320°C, respectively. Clear diffusion gradients are evident in both cases, confirming the occurrence of isotopic diffusion at these temperatures. When compared with the green dashed line representing $C'(x,t)$ calculated from the natural abundance of deuterium, the measured $C'(x,t)$ values of the exchanged samples are substantially higher, further verifying successful isotope exchange.

It is noteworthy that, due to the conversion of 2D image data into 1D diffusion profiles, the surface isotopic fraction could not be determined precisely, as each surface value corresponds to the averaged intensity of all data points sharing the same Y-coordinate. To obtain a more accurate surface isotopic fraction, depth-profile measurements were additionally performed (details provided in Section 5.9), and the resulting normalised isotopic fraction is presented in the inset of each figure. The nearly constant horizontal $C'(x,t)$ values within 0.25 µm from the surface indicate that the measured surface isotopic fraction was not influenced by surface-adsorbed species. The $C'(x,t)$ value obtained from the depth-profile experiments was subsequently used to define the surface $C'(x,t)$ (diffusion depth = 0 µm) in the 2D image-based diffusion analyses.

Moreover, the tracer diffusion coefficient obtained from IEDP for the D_2O-exchanged BZCYYb pellet was $1.21(4)\times10^{-7}$ cm^2s^{-1} at 320°C, while the localised diffusion coefficient derived from QENS for the humid-air-annealed BZCYYb powders (BZCYYb-HA) was $5.0(6)\times10^{-7}$ cm^2s^{-1} at 310°C (see section 7.1). Although IEDP probes long-range diffusion over micrometre-length scales, whereas QENS captures localised proton motion on the Angstrom scale, the comparable magnitudes of the fitted diffusion coefficients suggest that proton mobility remains consistent across different length scales, assuming that the deuteron diffusion adequately represents the protonic diffusion.

The reported high ionic transport number (>97%) and low oxide-ion transport number

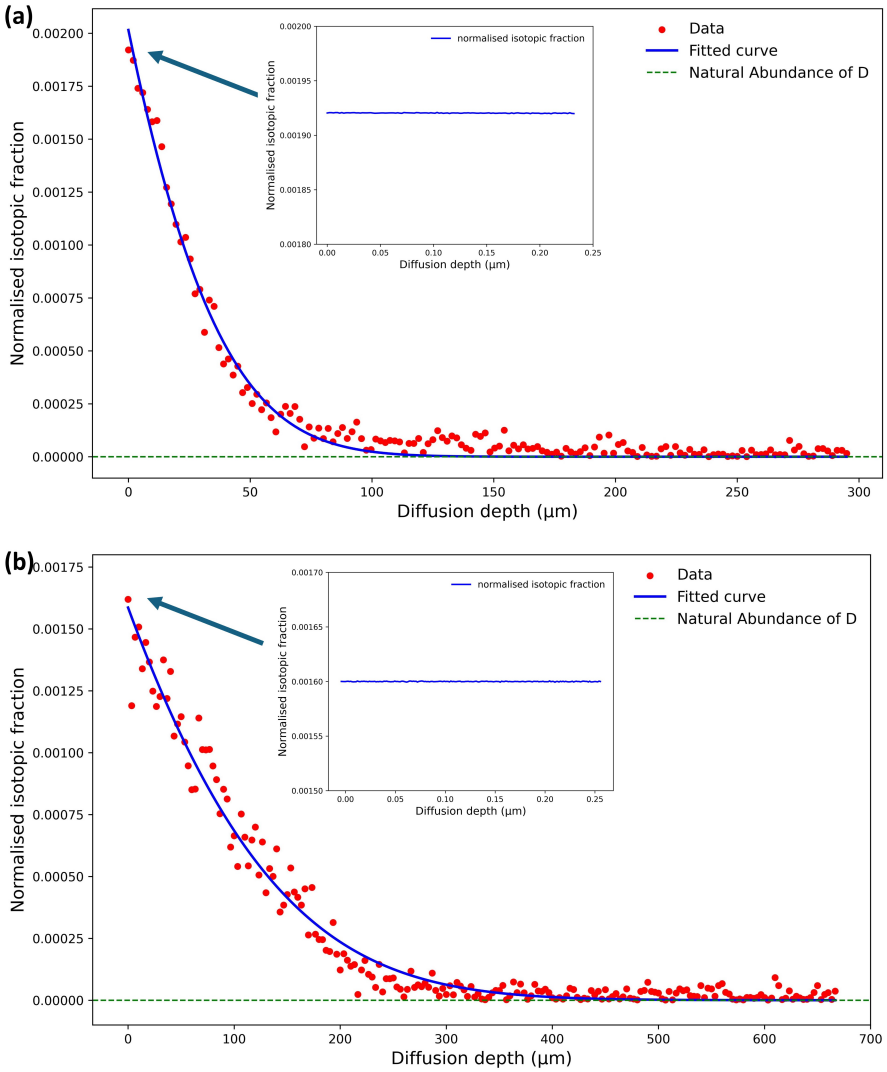


Figure 7.19: (a) The fitted isotopic diffusion profile measured in BZCYYb pellet exchanged in pD_2O = 22 torr environment for 25 minutes at 260°C. The inset image shows the normalised isotopic fraction depth profile from the surface of the exchanged pellet. The fitted D^* = 4.35(3) $\times 10^{-8}$ cm^2s^{-1}, fitted k = 4.48(2) $\times 10^{-7}$ cms^{-1}, the R^2 value of the fitting is 0.99. (b) The fitted isotopic diffusion profile measured in BZCYYb pellet exchanged in pD_2O = 22 torr environment for 25 minutes at 320°C. The inset image shows the normalised isotopic fraction depth profile from the surface of the exchanged pellet. The fitted D^* = 1.21(4) $\times 10^{-7}$ cm^2s^{-1}, fitted k = 1.41(2) $\times 10^{-8}$ cms^{-1}, the R^2 value of the fitting is 0.99. The green dashed line represents the natural abundance of deuterium.

($\approx 10\%$) of BZCYYb1711 system at 600°C under humid atmosphere[75] suggested that the total conductivity was majorly contributed by the protonic conduction, hence it is possible to approximate the measured total conductivity from EIS to the protonic conductivity. By applying the Nernst-Einstein relation (Equation 7.28), the protonic diffusion coefficient can be estimated from the measured conductivity value:

$$D_\sigma = \sigma(T)\frac{k_B T}{e^2 N} \tag{7.28}$$

where k_B is the Boltzmann constant, $\sigma(T)$ is the conductivity at temperature T, e is the proton charge, N is the density of mobile protons, and D_σ is the proton diffusion coefficient. To calculate the density of mobile protons, the measured hydrogen-barium molar ratio from PGAA needs to be converted based on the following equation:

$$N = m_H * \frac{\rho N_A}{M} \tag{7.29}$$

where m_H is the measured hydrogen-barium molar ratio (representing the number of protons per formula unit), ρ is the calculated density of BZCYYb1711 system from XRD refinement, N_A is the Avogadro constant and M is the molar mass of BZCYYb1711 system. The m_H measured by PGAA (data in section 6) of BZCYYb-HA sample was 0.44(2), and the ρ calculated from the Rietveld refinement of BZCYYb-HA powders was 6.27 gcm$^-$3, which is close to the reported theoretical density in literature[196, 197].

By combining the Equation 7.28-7.29, the estimated protonic diffusion coefficient at 323°C was calculated to be 9.38 $\times 10^{-8}$ cm^2s^{-1}, based on the measured total conductivity values illustrated in Figure 7.17. This estimated diffusion value was hard to be 100% accurate, as the calculation was based on multiple assumptions: first, the total conducitvity was approximated to the protonic conductivity. Second, the measured room temperature hydrogen-barium molar ratio by PGAA was assumed to be the same at 323°C. Third, the calculated proton concentration from Equation 7.29 assumed that all protons in the BZCYYb1711 system were mobile and no protons were trapped. Fourth, the estimated proton concentration based on the powder sample was assumed to be applied to the dense BZCYYb symmetric cell. Though the calculation required many assumptions, the estimated protonic diffusion coefficient from EIS (9.38×10^{-8} cm^2s^{-1} at 323°C) was close to the isotopic tracer diffusion coefficient from SIMS ($1.21(4)\times10^{-7}$ cm^2s^{-1} at 320°C) and the localised proton diffusion coefficient from QENS ($5.0(6)\times10^{-7}$ cm^2s^{-1} at 310°C). This cross-technique convergence suggesting that the majority of incorporated protons participate in long-range transport. It further suggests that microstructural bottlenecks, particularly grain-boundary blocking, are limited under these conditions, enabling local proton hopping observed by QENS to translate efficiently into macroscopic conductivity.

In summary, the two measured isotopic diffusion profiles not only confirm the successful

incorporation of deuterium (D) ions into the dense BZCYYb pellet but also demonstrate that D ions are mobile and can diffuse at 260°C. Assuming that deuterium exhibits diffusion behaviour comparable to that of protons, these IEDP results address the existing research gap regarding the lack of evidence for proton mobility in the medium-to-low temperature range (<400°C).

7.3 Summary

In this chapter, neutron Compton scattering (NCS) and quasielastic neutron scattering (QENS), were employed to investigate the effect of humid annealing on the localised proton dynamics in BZCYYb-cal (as-calcined sample) and BZCYYb-HA (humid air-annealed sample). Although NCS is capable of probing localised dynamics on the femtosecond timescale (10^{-15} s), the heavily doped nature of the BZCYYb system, combined with the inherent fitting approach of NCS, which involves simultaneous modelling of the Compton profiles of all constituent elements, introduced substantial uncertainties in the fitted results. Consequently, no discernible difference in localised dynamics could be identified between BZCYYb-cal and BZCYYb-HA using NCS. In contrast, the QENS technique is not significantly affected by compositional complexity and successfully revealed that humid annealing shortened the relaxation time of localised proton hopping, indicating enhanced proton mobility in BZCYYb-HA compared with BZCYYb-cal.

Electrochemical impedance spectroscopy (EIS) was employed to investigate the total conductivity of Pt-coated BZCYYb symmetric cells under dry and humid air atmospheres, in order to evaluate the effect of humid annealing on total conductivity. Consistent with previous reports, the difference in total conductivity between the humid and dry conditions was minimal, indicating that the presence of 3 vol% H_2O did not significantly influence the measured conductivity. A plausible explanation for this behaviour is that the sintered BZCYYb pellets (used to fabricate the symmetric cells for EIS measurements) already contained a non-negligible concentration of protons, which contributed predominantly to the total conductivity, whereas the additional protons introduced under humid conditions had only a minor effect.

Moreover, the isotopic exchange depth profiling (IEDP) technique was employed to probe exclusively the long-range diffusion of proton isotopes. The clear diffusion profiles of exchanged deuterium ions confirmed the occurrence of isotopic diffusion down to 260°C, demonstrating that protonic species remain mobile at such low temperatures. Assuming that the diffusion behaviour of protons and deuterium ions does not differ significantly, these IEDP results address the existing research gap concerning the lack of direct evidence for proton mobility in BZCYYb1711 system in the medium-to-low temperature range (<400°C).

Chapter 8: Effect of Partial Pressure of Oxygen on Proton Dynamics in $BaZr_{0.1}Ce_{0.7}Y_{0.1}Yb_{0.1}O_{3-\delta}$

8.1 Effect of Partial Pressure of Oxygen on Total Conductivity

The influence of oxygen partial pressure (p_{O_2}) on the total conductivity of the BZCYYb1711 system was evaluated by comparing the electrochemical impedance spectroscopy (EIS) responses of a Pt-coated BZCYYb symmetric cell measured under humid (3 vol % H_2O) air and humid (3 vol % H_2O) hydrogen-nitrogen mixed gas (5 % H_2/95 % N_2) atmospheres.

Similar to the conditions described in Section 7.2, the impedance of the Pt-coated BZCYYb symmetric cell under humid hydrogen-nitrogen mixed gas was measured over the temperature range of 517-95°C and a frequency range of 1 MHz to 1 Hz. The overlapping data points representing the total conductivities measured under humid air and humid hydrogen-nitrogen atmospheres, as shown in Figure 8.1, indicate that variations in p_{O_2} exerted no significant influence on the total conductivity. This negligible difference in conductivity within the BZCYYb1711 system is consistent with previous findings by Zhang et al.[73], who reported total conductivities of 0.0036 Scm^{-1} in humid (3 vol % H_2O) air and 0.0032 Scm^{-1} in humid hydrogen-nitrogen gas (5 % H_2/95 % N_2) at 550°C. Moreover, a similar change of conductivity slope was also observed in Figure 8.1, indicating the change of apparent proton hopping activation energy was not caused by change of p_{O_2}.

8.2 Effect of Partial Pressure of Oxygen on Localised Proton Hopping

In addition to the long-range (in μm) conductivity measured by EIS, quasielastic neutron scattering (QENS) was employed to investigate the effect of oxygen partial pressure (p_{O_2}) on localised proton dynamics. The data reduction procedures for the BZCYYb-HH sample (annealed under humid hydrogen-nitrogen gas, 5 % H_2/95 % N_2), including vanadium normalisation, background subtraction, and attenuation correction, followed the same steps as those applied to BZCYYb-HA (annealed under humid air), as described in Section 7.1. A representative fit of the full width at half maximum (FWHM) of the BZCYYb-HH QENS spectrum using the Chudley-Elliott model is shown in Figure 8.2, and the corresponding fitted parameters for BZCYYb-HH and BZCYYb-HA are summarised in Table 8.1.

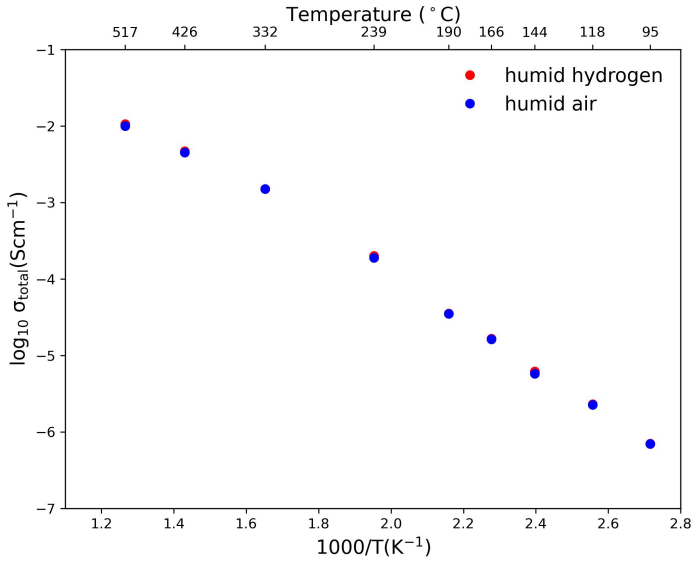


Figure 8.1: The comparison of total conductivities of Pt-coated BZCYYb pellet measured under humid (3vol% H_2O) air and humid (3vol% H_2O) hydrogen mixed gas (5%H_2/95%N_2) conditions from 517°C to 95°C.

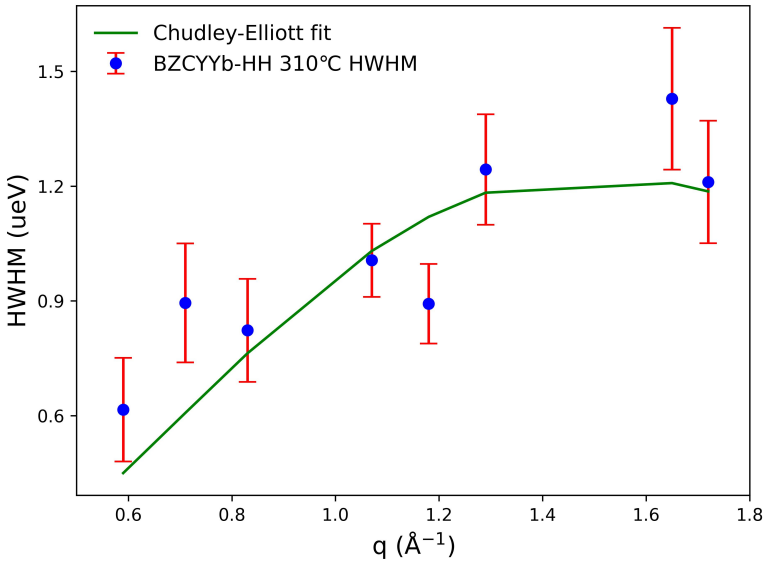


Figure 8.2: The fitted HWHM (half width half maximum) versus q (change of momentum) of BZCYYb-HH measured at 310°C based on the Chudley-Elliot model[187]. The fitted constant jump length is 3.0(2) Å, fitted relaxation time of hopping is 652(43) ps, and the fitted diffusion coefficient is 2.3(4)×10^{-7} cm^2s^{-1}. The reduced chi-squared value of the fitting is 1.927.

With respect to the fitted jump length, BZCYYb-HH and BZCYYb-HA exhibited comparable values, indicating that the change in annealing atmosphere did not significantly influence the average proton hopping distance. However, comparison of the fitted relaxation times reveals that proton motion in BZCYYb-HA was considerably faster than in BZCYYb-HH, suggesting that annealing under humid hydrogen conditions induced slower localised proton hopping relative to the humid air environment.

Table 8.1: Fitted constant jump length and relaxation time based on the Chudley-Elliot model from BZCYYb-HA (annealed in humid air) and BZCYYb-HH (annealed in humid hydrogen mixed gas 5%H_2/95%N_2) QENS results, which were measured at IN16b (ILL, France) at different temperatures.

		BZCYYb-HA	**BZCYYb-HH**
Fitted constant jump length (Å)	310°C	3.0(1)	3.0(2)
	370°C	3.2(1)	3.6(1)
	450°C	4.4(1)	4.6(2)
Fitted relaxation time (ps)	310°C	312(14)	652(43)
	370°C	166(5)	245(7)
	450°C	124(2)	143(5)

Moreover, as the fitted jump length and relaxation time were obtained, the diffusion coefficient can be calculated based on the relationship $D = \frac{r^2}{6\tau}$, where D is the diffusion coefficient, r is the jump length and τ is the relaxation time of hopping. Figure 8.3 shows the calculated diffusion coefficients and their corresponding proton localised hopping activation energy in both samples. The protonic localised activation energy in BZCYYb-HA sample illustrated in Figure 8.3 (a) was 0.46 eV, lower than the activation energy of BZCYYb-HH sample shown in Figure 8.3 (b), indicating that the different pO_2 of the annealing condition can affect the localised proton hopping.

To rationalise the lower activation energy of localised proton hopping observed in the BZCYYb-HA sample compared with the BZCYYb-HH sample, the influence of oxygen partial pressure (p_{O_2}) must be considered. To quantify the p_{O_2} of hydrogen-nitrogen mixed gas, the H_2/H_2O redox reaction must be considered:

$$H_2 + \frac{1}{2}O_2 \leftrightarrow H_2O \tag{8.1}$$

$$K_p(T) = \frac{p_{H_2O}}{p_{H_2}(p_{O_2})^{\frac{1}{2}}} \tag{8.2}$$

$$p_{O_2} = (\frac{p_{H_2O}}{K_p(T)p_{H_2}})^2 \tag{8.3}$$

where $K_p(T)$ is the equilibrium constant, p_{H_2O} is the partial pressure of the humidity in humid hydrogen-nitrogen mixed gas, and p_{H_2} is the partial pressure of hydrogen in

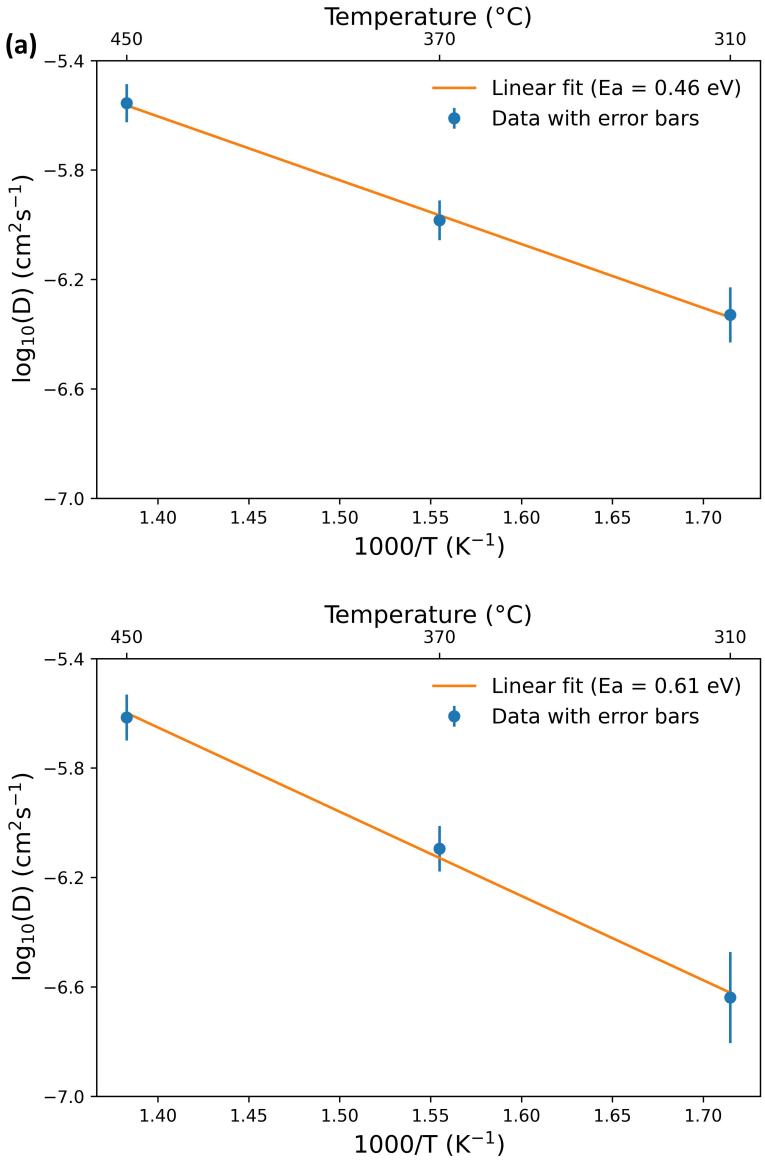


Figure 8.3: (a) The fitted diffusion coefficients of BZCYYb-HA (annealed in humid air) sample measured by QENS at IN16b (ILL, France) at 310°C, 370°C and 450°C. The R^2 value of the linear relationship is 0.99, and the fitted activation energy is 0.46 eV. (b) The fitted diffusion coefficients of BZCYYb-HH (annealed in humid hydrogen) sample measured by QENS at IN16b (ILL, France) at 310°C, 370°C and 450°C. The R^2 value of the linear relationship is 0.98, and the fitted activation energy is 0.61 eV.

humid hydrogen-nitrogen mixed gas. At 450°C, the corresponding $K_p(T)$ is $\approx 10^{15}\ atm^{-\frac{1}{2}}$ according to the NIST-JANAF Thermochemical Tables[198]. The p_{H_2O} is $\approx 0.03\ atm$ and the p_{H_2} of applied 1 atm hydrogen-nitrogen mixed gas is 0.05 atm, hence the calculated p_{O_2} is $3 \times 10^{-31}\ atm$. According to literature, this is the level of p_{O_2} which can reduce the cerium element[199, 200], leading to the formation of oxygen vacancies to balance the negative charges induced by cerium reduction:

$$2Ce_{Ce}^{x} + O_{O}^{x} \rightarrow 2Ce_{Ce}^{\prime} + V_{O}^{\bullet\bullet} + \frac{1}{2}O_2 \tag{8.4}$$

The formation of oxygen vacancies would reduce the number of neighbouring oxygen sites available for proton hopping, thus, the higher activation energy of localised protonic hopping in BZCYYb-HH may due to the formation of oxygen vacancies during the cerium reduction.

As discussed in the IFWS (inelastic fixed window scan) results in Section 7, the QENS broadening of the BZCYYb-HA sample above 450°C exceeded the accessible energy transfer range of the IN16B spectrometer, indicating that a beamline with a wider dynamic range was required to capture the faster localised proton dynamics at higher temperatures. Therefore, QENS measurements of both BZCYYb-HA and BZCYYb-HH were also conducted on the BASIS spectrometer (ORNL, USA) because of its broader energy transfer window ($\pm$ 100 μeV) compared with the energy transfer range ($\pm$ 30 μeV) probed by IN16B spectrometer (ILL, France), which enabled the investigation of faster proton dynamics.

During the BASIS QENS measurements, some anomalous data were observed, as shown in Figure 8.4, where the empty quartz container exhibited a higher scattering intensity than the BZCYYb-HH sample (sample plus container). This unexpected result is likely attributable to the higher mass or density of quartz used for the empty-container reference compared with the quartz tube that contained the BZCYYb-HH sample. Although the background subtraction could not be reliably performed due to the abnormally high intensity from the empty container, it remained reasonable to fit the QENS broadening of both BZCYYb-HH and BZCYYb-HA, since the principal contribution to the observed quasielastic broadening arises from proton dynamics within the samples.

The fitted half-width at half-maximum (HWHM) values of the BZCYYb-HA sample at 370°C, 450°C, and 550°C are presented in Figure 8.5. Unlike the datasets at 370°C and 450°C shown in Figures 8.5(a) and (b), respectively, the HWHM values of the QENS spectrum at 550°C could not be satisfactorily fitted using the Chudley–Elliott model. As highlighted in Figure 8.5(c) by the red squares, the fitted HWHM values at $q = 1.5$ Å^{-1} and $q = 1.7$ Å^{-1} approached 100 μeV, which corresponds to the total accessible energy transfer range of the BASIS spectrometer. This indicates that the quasielastic broadening

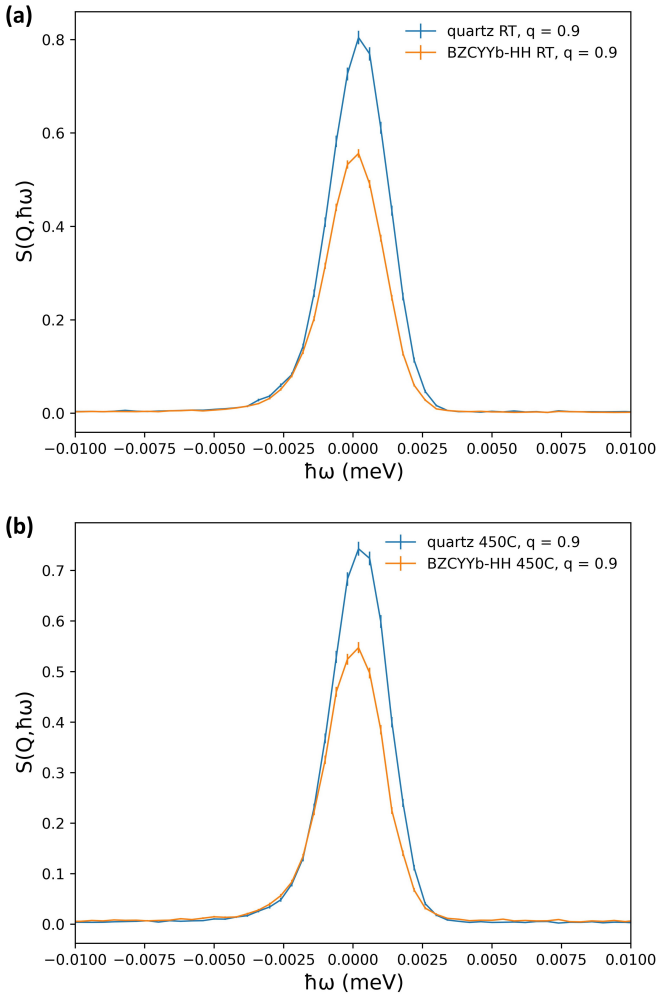


Figure 8.4: (a) QENS spectra of empty quartz container and BZCYYb-HH sample with q (change of momentum) = 0.9 measured at room temperature. (b) QENS spectra of empty quartz container and BZCYYb-HH sample with q (change of momentum) = 0.9 measured at 450°C.

associated with proton hopping at 550°C exceeded the instrumental energy window of BASIS at these momentum transfer values.

Table 8.2 compares the fitted diffusion coefficients of the BZCYYb-HA sample measured on the BASIS and IN16B spectrometers. The close agreement of the diffusion coefficients at both 370°C and 450°C not only demonstrates the reproducibility of the QENS data obtained from two independent instruments, but also confirms that the same localised proton-hopping process was probed in both measurements.

Table 8.2: Fitted diffusion coefficients based on the Chudley-Elliot model between BZCYYb-HA samples measured at BASIS (BZCYYb-HA-BASIS) and at IN16b (BZCYYb-HA-IN16b) at 370°C and 450°C.

	Fitted D at 370°C (cm^2s^{-1})	**Fitted D at 450°C** (cm^2s^{-1})
BZCYYb-HA-BASIS	$1.7(8) \times 10^{-6}$	$6(2) \times 10^{-6}$
BZCYYb-HA-IN16b	$1.04(8) \times 10^{-6}$	$2.8(2) \times 10^{-6}$

Compared with BZCYYb-HA, the QENS spectral broadening of BZCYYb-HH was smaller, which enabled a fitting of the HWHM at 550°C, as shown in Figure 8.6(c). However, at 650°C (Figure 8.6(d)), the measurement again approached the instrumental limitation of the BASIS spectrometer. However, in Table 8.3, it is noteworthy that the diffusion coefficients fitted from the BASIS measurements exhibited uncertainties comparable to the fitted values. These large error values suggest fitted parameters should not be quantitatively interpreted. The increased uncertainties are likely attributable to the lower energy resolution of BASIS relative to IN16B; as a result, for localised dynamics that fall within the optimal measurement range of IN16B, the broader energy window but poorer resolution of BASIS limits the precision of the fitting. Furthermore, the uncertainties in the diffusion coefficients obtained from BASIS increased with temperature. This trend may be explained by the gradual loss of protons from the system during heating, which reduces the signal intensity and consequently increases the fitting error.

Table 8.3: Fitted diffusion coefficients based on the Chudley-Elliot model between BZCYYb-HH samples measured at BASIS (BZCYYb-HH-BASIS) and at IN16b (BZCYYb-HH-IN16b) at 370°C, 450°C and 550°C.

	Fitted D at 370°C (cm^2s^{-1})	**Fitted D at 450°C** (cm^2s^{-1})	**Fitted D at 550°C** (cm^2s^{-1})
BZCYYb-HH-BASIS	$2(2) \times 10^{-6}$	$3(3) \times 10^{-6}$	$5(5) \times 10^{-6}$
BZCYYb-HH-IN16b	$8.0(7) \times 10^{-7}$	$2.4(2) \times 10^{-6}$	Not accessible

8.3 Summary

In this chapter, electrochemical impedance spectroscopy (EIS) measurements on Pt-coated BZCYYb pellets demonstrated that variations in oxygen partial pressure (p_{O_2})

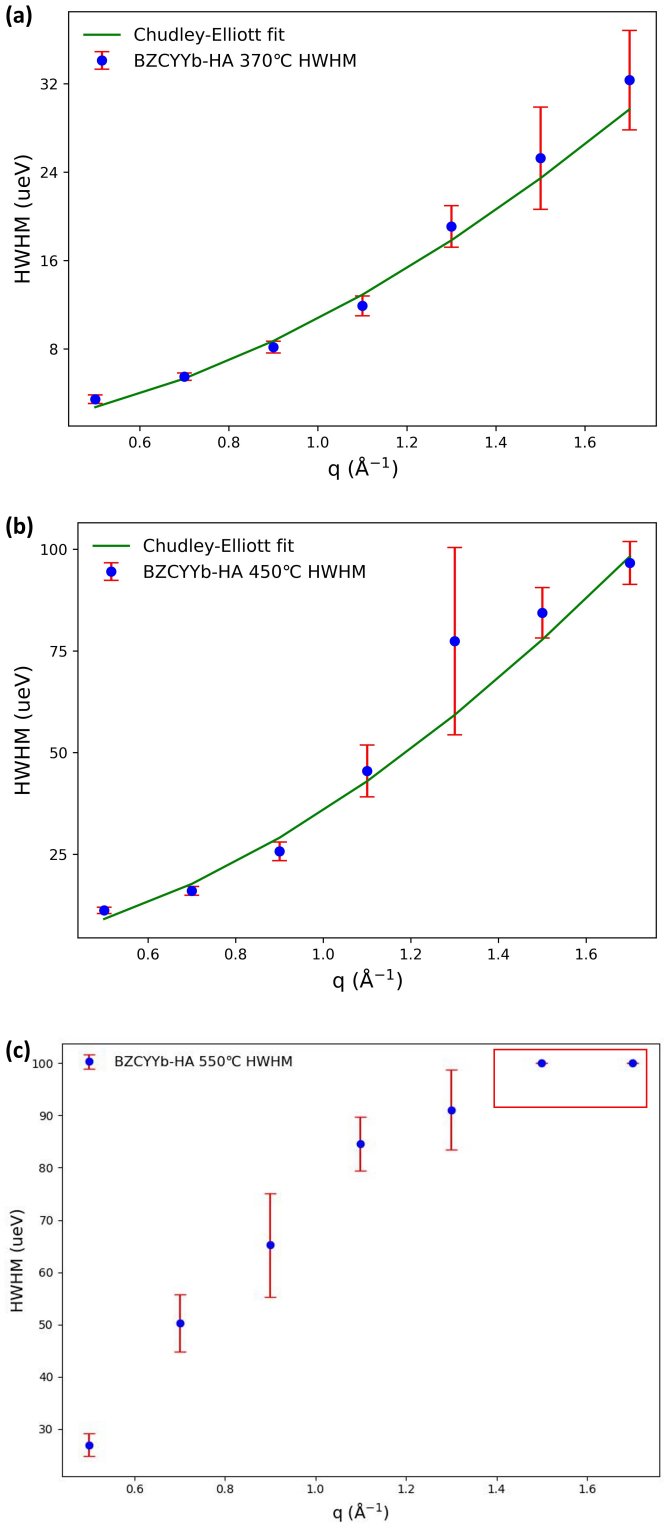


Figure 8.5: The fitted HWHM (half width half maximum) versus q (change of momentum) of BZCYYb-HA sample based on Chudley-Elliot model measured by BASIS beamline at (a) 370°C and reduced chi-squared is 1.405, (b) at 450°C and reduced chi-squared is 2.889, (c) at 550°C, the red box highlights fitted HWHM which equal to the energy tranfer range of BASIS beamline (± 200 μeV), indicating the failure of fitted QENS broadening, thus the HWHM fitted results cannot be fitted by Chudley-Elliot model at this temperature.

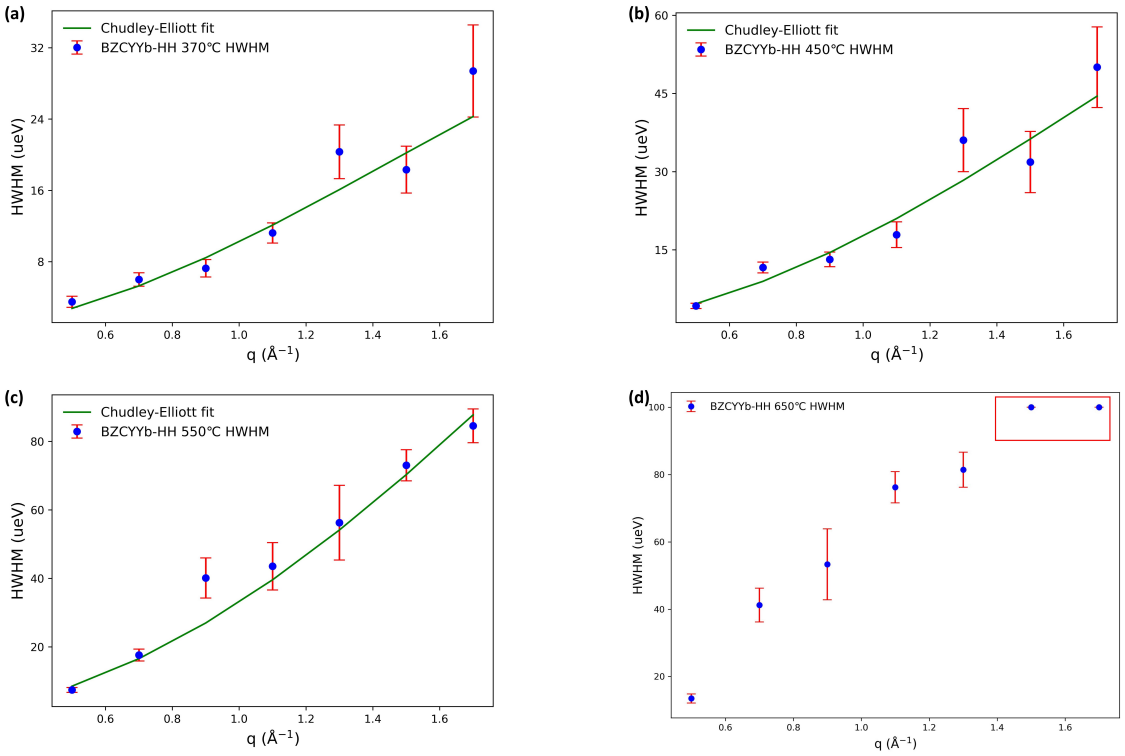


Figure 8.6: The fitted HWHM (half width half maximum) versus q (change of momentum) of BZCYYb-HH sample based on Chudley-Elliot model measured by BASIS beamline at (a) 370°C and reduced chi-squared is 1.575, (b) at 450°C and reduced chi-squared is 2.483, (c) at 550°C and reduced chi-squared is 1.794, (d) at 650°C, the red box highlights fitted HWHM which equal to the energy tranfer range of BASIS beamline (± 200 μeV), indicating the failure of fitted QENS broadening, thus the HWHM fitted results cannot be fitted by Chudley-Elliot model at this temperature.

exerted a negligible influence on the total conductivity. Quasielastic neutron scattering (QENS) measurements performed on the IN16B spectrometer revealed that the activation energy for localised proton hopping was lower in BZCYYb-HA (powders annealed under humid air) than in BZCYYb-HH (powders annealed under humid hydrogen-nitrogen gas), while the BASIS spectrometer enabled the investigation of faster proton dynamics at higher temperatures in both samples. The higher localised hopping activation energy observed in BZCYYb-HH is likely associated with the formation of oxygen vacancies induced by partial cerium reduction, which reduces the number of available oxygen sites for proton hopping and consequently decreases proton mobility. For future work, techniques capable of directly determining the oxidation state of cerium, such as X-ray photoelectron spectroscopy (XPS) or X-ray absorption spectroscopy (XAS), would be valuable in verifying this hypothesis.

Chapter 9: Conclusions and Outlook

9.1 Conclusions

This thesis presented a comprehensive investigation into the structural stability, proton incorporation behaviour, and proton transport dynamics of the BZCYYb1711 system. Through a combination of advanced characterisation techniques, the inherent protonic concentrations, localised dynamics, and long-range transport phenomena were systematically examined across different atmospheric and thermal conditions. The findings collectively contribute to a deeper understanding of the fundamental proton conduction mechanisms in this complex perovskite material and provide valuable insights for its optimisation in proton-conducting solid oxide fuel cells (PCFCs).

Multi-technique characterisation, including XRD, FTIR, ICP-OES, EDS, TGA, RGA, and PGAA, established a consistent picture of the structural and compositional stability of BZCYYb1711. XRD and FTIR confirmed the successful synthesis of single-phase perovskite BZCYYb1711, with only a trace amount of secondary $BaCO_3$ detected in the humid-annealed sample. Rietveld refinement indicated a slight contraction of the lattice parameters upon humid annealing (BZCYYb-HA), attributed to partial barium loss and $BaCO_3$ formation. Complementary chemical analyses (ICP-OES and EDS) verified that the overall elemental stoichiometry remained consistent with the nominal composition, and the apparent barium deficiency inferred from XRD was rationalised as an artefact of the analytical limitation of ICP-OES, which cannot distinguish between barium originating from different phases.

Thermogravimetric (TGA) and residual gas analysis (RGA) revealed that the primary mass loss during heating was due to dehydration, confirming the presence of inherent protons in the BZCYYb1711 lattice even without deliberate humidification. Comparisons between as-calcined (BZCYYb-cal) and humid-annealed (BZCYYb-HA) samples showed comparable proton concentrations, suggesting that proton incorporation occurs inherently during synthesis. Prompt gamma activation analysis (PGAA) further provided direct quantification of hydrogen content, validating the TGA-derived conclusions and reinforcing the presence of significant proton incorporation in the as-synthesised BZCYYb1711.

To investigate proton dynamics at the atomic scale, neutron Compton scattering (NCS) and quasielastic neutron scattering (QENS) were employed. Although NCS can, in principle, probe femtosecond-scale dynamics, the heavily doped and compositionally complex nature of BZCYYb led to large fitting uncertainties arising from the simultaneous modelling of multiple elemental Compton profiles. Consequently, no meaningful difference in localised proton dynamics could be resolved between the BZCYYb-cal and BZCYYb-HA

samples using NCS.

In contrast, QENS provided a more sensitive and direct characterisation of localised proton hopping. The results demonstrated that humid annealing shortened the relaxation time of localised proton motion, indicating enhanced proton mobility in the BZCYYb-HA sample compared with BZCYYb-cal. These findings confirm that water vapour exposure facilitates more dynamic proton behaviour at the atomic scale, even though the overall conductivity remained largely unchanged.

Electrochemical impedance spectroscopy (EIS) was used to measure the total conductivity of Pt-coated BZCYYb symmetric cells under both dry and humid conditions. Consistent with prior studies, only a minor difference was observed between the two environments, indicating that the presence of 3 vol% H_2O did not significantly alter the measured conductivity. This observation supports the hypothesis that the sintered BZCYYb pellets already contained a substantial inherent proton population, contributing predominantly to the total conductivity, while the contribution from additional protons introduced under humid conditions was negligible.

To directly probe long-range proton transport, isotopic exchange depth profiling (IEDP) was employed. The clear diffusion profiles of exchanged deuterium confirmed active isotopic diffusion down to 260°C, providing the first direct evidence of proton mobility in BZCYYb1711 within the medium-to-low temperature regime (<400°C). Assuming comparable diffusivities for protons and deuterons, these findings bridge a critical knowledge gap by demonstrating that proton mobility persists at temperatures lower than previously verified by macroscopic techniques such as EIS.

Further investigations were conducted to evaluate the effect of oxygen partial pressure (p_{O_2}) on both total conductivity and localised proton hopping. EIS measurements confirmed that variations in p_{O_2} had a negligible impact on total conductivity. However, QENS experiments performed on the IN16B and BASIS spectrometers revealed subtle differences in activation energy between samples annealed under humid air (BZCYYb-HA) and humid hydrogen (BZCYYb-HH). The higher activation energy in BZCYYb-HH was attributed to the formation of oxygen vacancies caused by partial cerium reduction, which reduced the number of available oxygen sites for proton hopping. Future work employing oxidation-state-sensitive techniques such as X-ray photoelectron spectroscopy (XPS) or X-ray absorption spectroscopy (XAS) is recommended to verify this hypothesis and quantify the extent of cerium reduction.

Collectively, this body of work provides a coherent, multi-scale understanding of proton behaviour in the BZCYYb1711 system, from structural integrity and inherent proton concentrations to localised dynamics and long-range transport.

9.2 Outlook

The results presented in this thesis confirmed that the BZCYYb1711 system incorporates a significant number of protons even without intentional humid annealing. While this discovery is novel, two critical questions remain: First, is this phenomenon unique to BZCYYb1711, or is it a more general feature of proton-conducting materials? Second, beyond hydration-based uptake, could BZCYYb1711 also incorporate protons directly, thereby opening the possibility of its application in hydrogen storage?

Addressing the first question is essential for advancing the fundamental understanding of proton conduction. If inherent proton concentration is a general property of proton-conducting materials, then the additional conductivity expected from deliberate hydration may be less significant than previously assumed. A practical way to explore this would be to conduct TGA measurements on as-calcined PCFC materials, including both brownmillerite systems such as protonated strontium cobaltites and perovskite candidates such as barium cerates. However, TGA alone cannot provide a direct and exclusive quantification of incorporated protons, as its results may also be influenced by decomposition or oxygen loss. To overcome this limitation, TGA should be coupled with mass spectrometry, enabling sensitive detection of hydrogen and oxygen in the exhaust gases from the TGA. Preliminary insights obtained from such combined measurements could then be validated and quantified through prompt gamma-ray activation analysis (PGAA), which directly probes the molar ratios of incorporated protons.

The second question links this work to the broader challenge of hydrogen storage. The large-scale deployment of fuel cell technologies is currently constrained by limitations in hydrogen storage and transport, as conventional methods: compressed hydrogen and cryogenic liquefaction, which remain costy and hold safety risks[201, 202]. If materials such as BZCYYb1711 can directly incorporate hydrogen, it is possible to apply this property to the alternative, safer, and potentially cheaper storage approaches. To test this hypothesis, isotopic labelling using deuterium (D_2) is essential, since deuterium can be distinguished from protons by its mass-to-charge ratio. Annealing BZCYYb samples under D_2, followed by SIMS analysis, would enable the detection of incorporated deuterium and provide evidence for direct hydrogen uptake. Here, the key assumption is that D_2 and H_2 follow similar incorporation mechanisms.

Finally, this work should be viewed in the wider context of PCFC development. Considerable recent effort has been directed towards lowering the operating temperature of solid oxide fuel cells to enhance cost-effectiveness and practical applicability. For example, Tsujikawa et al. recently demonstrated that heavily Sc-doped cubic perovskites exhibit

exceptional proton conductivity (0.01 Scm^{-1} at 300°C) by enabling rapid proton transport pathways[203]. Their findings highlight that fundamental investigations of proton hopping mechanisms are vital for the rational design of next-generation PCFC systems. In this context, the systematic framework established in this PhD project, which linked proton incorporation, crystal structure, localised proton dynamics, and macroscopic conductivity, provides a transferable methodology for probing and optimising proton transport in other candidate materials. This approach is expected to support the discovery and design of future PCFC electrolytes with improved performance.

References

[1] J. A. Turner, "Sustainable Hydrogen Production," *Science*, vol. 305, no. 5686, pp. 972–974, 2004.

[2] I. Staffell, D. Scamman, V. A. Abad *et al.*, "The role of hydrogen and fuel cells in the global energy system," *Energy & environmental science*, vol. 12, pp. 463–491, 2019.

[3] A. Kraytsberg and Y. Ein-Eli, "Review of Advanced Materials for Proton Exchange Membrane Fuel Cells," *Energy & Fuels*, vol. 28, no. 12, pp. 7303–7330, 2014.

[4] S. Singhal, "Advances in solid oxide fuel cell technology," *Solid State Ionics*, vol. 135, no. 1-4, pp. 305–313, 2000.

[5] B. C. H. Steele and A. Heinzel, "Materials for fuel-cell technologies," vol. 414, pp. 345–352, 2001.

[6] H. Iwahara, "Prospect of hydrogen technology using proton-conducting ceramics," *Solid State Ionics*, vol. 168, no. 3-4, pp. 299–310, 2004.

[7] H. Iwahara, T. Esaka, H. Uchida *et al.*, "Proton conduction in sintered oxides and its application to steam electrolysis for hydrogen production," *Solid State Ionics*, vol. 3–4, pp. 359–363, 1981.

[8] L. Yang, M. Liu, S. Wang *et al.*, "Enhanced sulfur and coking tolerance of a mixed ion conductor for sofcs $BaZr_{0.1}Ce_{0.7}Y_{0.2-x}Yb_xO_{3-\delta}$," *Science*, vol. 326, no. 5949, pp. 126–129, 2009.

[9] J.-T. Zhang, F.-L. Liang, B. Chi *et al.*, "Enhanced electrochemical performance of $BaZr_{0.1}Ce_{0.7}Y_{0.1}Yb_{0.1}O_{3-\delta}$ electrodes for hydrogen and methane oxidation in solid oxide fuel cells by $Cu_{0.5}Pd_{0.5}$ impregnation," *Journal of Power Sources*, vol. 200, pp. 29–33, 2012.

[10] S. Wang, L. Zhang, L. Zhang *et al.*, "Two-step sintering of ultrafine-grained barium cerate proton conducting ceramics," *Electrochimica Acta*, vol. 87, pp. 194–200, 2013.

[11] I. Energy. 2025 Statistical Review of World Energy. [Online]. Available: https://www.energyinst.org/statistical-review

[12] K. Vohra, A. Vodonos, J. Schwartz *et al.*, "Global mortality from outdoor fine particle pollution generated by fossil fuel combustion: Results from GEOS-Chem," *Environmental Research*, vol. 195, p. 110754, 2021.

[13] F. Perera, "Pollution from Fossil-Fuel Combustion is the Leading Environmental Threat to Global Pediatric Health and Equity: Solutions Exist," *International Journal of Environmental Research and Public Health*, vol. 15, no. 1, p. 16, 2017.

[14] Y. Zhang, A. Han, S. Deng *et al.*, "The impact of fossil fuel combustion on children's health and the associated losses of human capital," *Global Transitions*, vol. 5, pp. 117–124, 2023.

[15] M. A. Azni, R. Md Khalid, U. A. Hasran *et al.*, "Review of the Effects of Fossil Fuels and the Need for a Hydrogen Fuel Cell Policy in Malaysia," *Sustainability*, vol. 15, no. 5, p. 4033, 2023.

[16] LJ. Pietrafesa, C. Gallagher, S. Bao *et al.*, "Global Surface Temperature Variability And Trends And Attribution To Carbon Emissions," *Journal of Environmental Science Current Research*, vol. 2, no. 2, pp. 1–8, 2019.

[17] S. A. Bandh, F. A. Malla, I. Qayoom *et al.*, "Importance of Blue Carbon in Mitigating Climate Change and Plastic/Microplastic Pollution and Promoting Circular Economy," *Sustainability*, vol. 15, no. 3, p. 2682, 2023.

[18] J. L. Holechek, H. M. E. Geli, M. N. Sawalhah *et al.*, "A Global Assessment: Can Renewable Energy Replace Fossil Fuels by 2050?" *Sustainability*, vol. 14, no. 8, p. 4792, 2022.

[19] E. B. Agyekum, C. Nutakor, A. M. Agwa *et al.*, "A Critical Review of Renewable Hydrogen Production Methods: Factors Affecting Their Scale-Up and Its Role in Future Energy Generation," *Membranes*, vol. 12, no. 2, p. 173, 2022.

[20] V. K. Visvanathan, K. Palaniswamy, D. Ponnaiyan *et al.*, "Fuel Cell Products for Sustainable Transportation and Stationary Power Generation: Review on Market Perspective," *Energies*, vol. 16, no. 6, p. 2748, 2023.

[21] A. E. Lutz, R. S. Larson, and J. O. Keller, "Thermodynamic comparison of fuel cells to the Carnot cycle," *International Journal of Hydrogen Energy*, vol. 27, no. 10, pp. 1103–1111, 2002.

[22] L. Pingkuo and G. Junqing, "Comparative analysis on the development potential of green hydrogen industry in China, the United States and the European Union," *International Journal of Hydrogen Energy*, vol. 84, pp. 700–717, 2024.

[23] O. Z. Sharaf and M. F. Orhan, "An overview of fuel cell technology: Fundamentals and applications," *Renewable and Sustainable Energy Reviews*, vol. 32, pp. 810–853, 2014.

[24] M. Alhassan and M. U. Garba, "Design of an Alkaline Fuel Cell," *Leonardo Electron. J. Pract. Technol*, no. 99–106, 2006.

[25] A. T. Hamada, M. F. Orhan, and A. M. Kannan, "Alkaline fuel cells: Status and prospects," *Energy Reports*, vol. 9, pp. 6396–6418, 2023.

[26] N. Sammes, R. Bove, and K. Stahl, "Phosphoric acid fuel cells: Fundamentals and applications," *Current Opinion in Solid State and Materials Science*, vol. 8, no. 5, pp. 372–378, 2004.

[27] A. M. Herring, "Inorganic–Polymer Composite Membranes for Proton Exchange Membrane Fuel Cells," *Journal of Macromolecular Science, Part C: Polymer Reviews*, vol. 46, no. 3, pp. 245–296, 2006.

[28] Y. Shao, G. Yin, Z. Wang *et al.*, "Proton exchange membrane fuel cell from low temperature to high temperature: Material challenges," *Journal of Power Sources*, vol. 167, no. 2, pp. 235–242, 2007.

[29] M. A. Hickner, H. Ghassemi, Y. S. Kim *et al.*, "Alternative Polymer Systems for Proton Exchange Membranes (PEMs)," *Chemical Reviews*, vol. 104, no. 10, pp. 4587–4612, 2004.

[30] S. Mekhilef, R. Saidur, and A. Safari, "Comparative study of different fuel cell technologies," *Renewable and Sustainable Energy Reviews*, vol. 16, no. 1, pp. 981–989, 2012.

[31] R. R. Contreras, J. Almarza, and L. Rincón, "Molten carbonate fuel cells: A technological perspective and review," *Energy Sources, Part A: Recovery, Utilization, and Environmental Effects*, pp. 1–15, 2021.

[32] J. J. Baschuk and X. Li, "Carbon monoxide poisoning of proton exchange membrane fuel cells," *International Journal of Energy Research*, vol. 25, no. 8, pp. 695–713, 2001.

[33] E. Fabbri, D. Pergolesi, and E. Traversa, "Materials challenges toward proton-conducting oxide fuel cells: A critical review," *Chemical Society Reviews*, vol. 39, no. 11, p. 4355, 2010.

[34] W. C. Heraeus, "Über die elektrolytische Leitung fester Körper bei sehr hohen Temperaturen," *Zeitschrift für Elektrochemie*, vol. 6, no. 2, pp. 41–43, 1899.

[35] E. Baur and H. Preis, "Über Brennstoff-Ketten mit Festleitern," *Zeitschrift für Elektrochemie und angewandte physikalische Chemie*, vol. 43, no. 9, pp. 727–732, 1937.

[36] V. C. Waonr, "Über den mechanismus der elektrischen Stromleitung im Nernststift," 1943.

[37] B. C. H. Steele and A. Heinzel, "Materials for fuel-cell technologies," vol. 414, 2001.

[38] S. C. Singhal, "Solid Oxide Fuel Cells: Past, Present and Future," in *Solid Oxide Fuels Cells: Facts and Figures*, J. T. Irvine and P. Connor, Eds. London: Springer London, 2013, pp. 1–23.

[39] B. Timurkutluk, C. Timurkutluk, M. D. Mat *et al.*, "Novel structured gadolinium doped ceria based electrolytes for intermediate temperature solid oxide fuel cells," *Journal of Power Sources*, vol. 196, no. 22, pp. 9361–9364, 2011.

[40] K. Huang, J.-H. Wan, and J. B. Goodenough, "Increasing Power Density of LSGM-Based Solid Oxide Fuel Cells Using New Anode Materials," *Journal of The Electrochemical Society*, vol. 148, no. 7, p. A788, 2001.

[41] M. Yashima, T. Tsujiguchi, Y. Sakuda *et al.*, "High oxide-ion conductivity through the interstitial oxygen site in Ba7Nb4MoO20-based hexagonal perovskite related oxides," *Nature Communications*, vol. 12, no. 1, pp. 1–7, 2021.

[42] B. Schwaighofer, M. Appel, M. A. Gonzalez *et al.*, "Oxide ion dynamics in hexagonal perovskite mixed conductor $Ba_7\ Nb_4\ MoO_{20}$: A comprehensive Ab Initio molecular dynamics study," *Materials Advances*, vol. 5, no. 4, pp. 1676–1682, 2024.

[43] J. Zhang, S. Ricote, P. V. Hendriksen *et al.*, "Advanced Materials for Thin-Film Solid Oxide Fuel Cells: Recent Progress and Challenges in Boosting the Device Performance at Low Temperatures," *Advanced Functional Materials*, vol. 32, no. 22, p. 2111205, 2022.

[44] K. Kreuer, "Proton-Conducting Oxides," *Annual Review of Materials Research*, vol. 33, no. 1, pp. 333–359, 2003.

[45] E. C. C. D. Souza and R. Muccillo, "Properties and applications of perovskite proton conductors," *Materials Research*, vol. 13, no. 3, pp. 385–394, 2010.

[46] H. Iwahara, T. Esaka, H. Uchida *et al.*, "Proton conduction in sintered oxides and its application to steam electrolysis for hydrogen production," *Solid State Ionics*, vol. 3–4, pp. 359–363, 1981.

[47] S. Fop, "Solid oxide proton conductors beyond perovskites," *Journal of Materials Chemistry A*, vol. 9, pp. 18 836–18 856, 2021.

[48] M. P. Arciniegas and L. Manna, "Designing Ruddlesden–Popper Layered Perovskites through Their Organic Cations," *ACS Energy Letters*, vol. 7, no. 9, pp. 2944–2953, 2022.

[49] N. Lu, Z. Zhang, Y. Wang *et al.*, "Enhanced low-temperature proton conductivity in hydrogen-intercalated brownmillerite oxide," *Nature Energy*, vol. 8, no. 10, pp. 1168–1168, 2023.

[50] C. Duan, J. Huang, N. Sullivan *et al.*, "Proton-conducting oxides for energy conversion and storage," *Applied Physics Reviews*, vol. 7, no. 1, 2020.

[51] J. Bao, H. Ohno, N. Kurita *et al.*, "Proton conduction in Al-doped CaZrO3," *Electrochimica Acta*, vol. 56, no. 3, pp. 1062–1068, 2011.

[52] H. Iwahara, H. Uchida, K. Ono *et al.*, "Proton Conduction in Sintered Oxides Based on BaCeO3," *Journal of The Electrochemical Society*, vol. 135, no. 2, pp. 529–533, 1988.

[53] S. V. Bhide and A. V. Virkar, "Stability of BaCeO3-Based Proton Conductors in Water-Containing Atmospheres," *Journal of The Electrochemical Society*, vol. 146, no. 6, pp. 2038–2044, 1999.

[54] E. Fabbri, L. Bi, D. Pergolesi *et al.*, "Towards the Next Generation of Solid Oxide Fuel Cells Operating Below 600 °C with Chemically Stable Proton-Conducting Electrolytes," *Advanced Materials*, vol. 24, no. 2, pp. 195–208, 2012.

[55] H. Iwahara, T. Yajima, T. Hibino *et al.*, "Protonic conduction in calcium, strontium and barium zirconates," *Solid State Ionics*, vol. 61, no. 1-3, pp. 65–69, 1993.

[56] K. Katahira, Y. Kohchi, T. Shimura *et al.*, "Protonic conduction in zr-substituted $BaCeO_3$," *Solid State Ionics*, vol. 138, no. 1-2, pp. 91–98, 2000.

[57] J. Tong, D. Clark, M. Hoban *et al.*, "Cost-effective solid-state reactive sintering method for high conductivity proton conducting yttrium-doped barium zirconium ceramics," *Solid State Ionics*, vol. 181, no. 11-12, pp. 496–503, 2010.

[58] J. Tong, D. Clark, L. Bernau *et al.*, "Solid-state reactive sintering mechanism for large-grained yttrium-doped barium zirconate proton conducting ceramics," *Journal of Materials Chemistry*, vol. 20, no. 30, p. 6333, 2010.

[59] N. Kane, Z. Luo, Y. Zhou *et al.*, "Durable and High-Performance Thin-Film BHYb-Coated BZCYYb Bilayer Electrolytes for Proton-Conducting Reversible Solid Oxide Cells," *ACS Applied Materials & Interfaces*, vol. 15, no. 27, pp. 32 395–32 403, 2023.

[60] Z. Luo, Y. Zhou, X. Hu *et al.*, "Critical role of acceptor dopants in designing highly stable and compatible proton-conducting electrolytes for reversible solid oxide cells," *Energy & Environmental Science*, vol. 15, no. 7, pp. 2992–3003, 2022.

[61] S. Choi, C. J. Kucharczyk, Y. Liang *et al.*, "Exceptional power density and stability at intermediate temperatures in protonic ceramic fuel cells," *Nature Energy*, vol. 3, no. 3, pp. 202–210, 2018.

[62] B. Guan, H. Tian, Y. N. Picard *et al.*, "Unraveling the conundrum of electronic leakage in protonic ceramic cells: Operation-specific insights and rational design strategies," *Journal of Power Sources*, vol. 604, p. 234454, 2024.

[63] P. Babilo and S. M. Haile, "Enhanced Sintering of Yttrium-Doped Barium Zirconate by Addition of ZnO," *Journal of the American Ceramic Society*, vol. 88, no. 9, pp. 2362–2368, 2005.

[64] Y. Liu, L. Yang, M. Liu *et al.*, "Enhanced sinterability of $BaZr_{0.1}Ce_{0.7}Y_{0.1}Yb_{0.1}O_{3-\delta}$ by addition of nickel oxide," *Journal of Power Sources*, vol. 196, no. 23, pp. 9980–9984, 2011.

[65] Z. Liu, X. Wang, M. Liu *et al.*, "Enhancing sinterability and electrochemical properties of $BaZr_{0.1}Ce_{0.7}Y_{0.1}Yb_{0.1}O_{3-\delta}$ proton conducting electrolyte for solid oxide fuel cells by addition of NiO," *International Journal of Hydrogen Energy*, vol. 43, no. 29, pp. 13 501–13 511, 2018.

[66] M. Asmare, M. Ilbas, F. M. Cimen *et al.*, "Three-dimensional numerical simulation and experimental validation on ammonia and hydrogen fueled micro tubular solid oxide fuel cell performance," *International Journal of Hydrogen Energy*, vol. 47, no. 35, pp. 15 865–15 874, 2022.

[67] C. Chen, Y. Dong, L. Li *et al.*, "Electrochemical properties of micro-tubular intermediate temperature solid oxide fuel cell with novel asymmetric structure based on $BaZr_{0.1}Ce_{0.7}Y_{0.1}Yb_{0.1}O_{3-\delta}$ proton conducting electrolyte," *International Journal of Hydrogen Energy*, vol. 44, no. 31, pp. 16 887–16 897, 2019.

[68] K. Yang, J. X. Wang, Y. J. Xue *et al.*, "Synthesis, sintering behavior and electrical properties of $BaZr_{0.1}Ce_{0.7}Y_{0.2}O_{3-\delta}$ and $BaZr_{0.1}Ce_{0.7}Y_{0.1}Yb_{0.1}O_{3-\delta}$ proton conductors," *Ceramics International*, vol. 40, no. 9, pp. 15 073–15 081, 2014.

[69] R. Stafford, S. Rothman, and J. Routbort, "Effect of dopant size on the ionic conductivity of cubic stabilised ZrO_2," *Solid State Ionics*, vol. 37, no. 1, pp. 67–72, 1989.

[70] F. Yuan, J. Wang, H. Miao *et al.*, "Investigation of the crystal structure and ionic conductivity in the ternary system (Yb_2O_3)x –(Sc_2O_3)(0.11-x)–(ZrO_2)0.89 (x= 0–0.11)," *Journal of Alloys and Compounds*, vol. 549, pp. 200–205, 2013.

[71] M. Oishi, S. Akoshima, K. Yashiro *et al.*, "Defect structure analysis of B-site doped perovskite-type proton conducting oxide $BaCeO_3$," *Solid State Ionics*, vol. 179, no. 39, pp. 2240–2247, 2008.

[72] F. He, Z. Teng, G. Yang *et al.*, "Manipulating cation nonstoichiometry towards developing better electrolyte for self-humidified dual-ion solid oxide fuel cells," *Journal of Power Sources*, vol. 460, p. 228105, 2020.

[73] Y. Zhang, D. Xie, B. Chi *et al.*, "Basic properties of proton conductor $BaZr_{0.1}Ce_{0.7}Y_{0.1}Yb_{0.1}O_{3-\delta}$ (BZCYYb) material," *Asia-Pacific Journal of Chemical Engineering*, vol. 14, no. 4, pp. 1–10, 2019.

[74] I.-H. Kim, D.-K. Lim, H. Bae *et al.*, "Determination of partial conductivities and computational analysis of the theoretical power density of $BaZr_{0.1}$ $Ce_{0.7}$ $Y_{0.1}$ $Yb_{0.1}$

$O_{3-\delta}$ (BZCYYb1711) electrolyte under various PCFC conditions," *Journal of Materials Chemistry A*, vol. 7, no. 37, pp. 21 321–21 328, 2019.

[75] H. Guo, Y. Li, L. Jiang *et al.*, "Transport properties of the Ba(Zr,Ce,Y,Yb)$O_{3-}\delta$ proton conductor: The real role of co-substitution of Y and Yb," *Journal of Materials Chemistry A*, vol. 12, no. 10, pp. 5875–5884, 2024.

[76] T. Ishiyama, H. Kishimoto, K. Develos-Bagarinao *et al.*, "Correlation between Dissolved Protons in nickel-doped $BaZr_{0.1}Ce_{0.7}Y_{0.1}Yb_{0.1}O_{3-\delta}$ and Its Electrical Conductive Properties," *Inorganic Chemistry*, vol. 56, no. 19, pp. 11 876–11 882, 2017.

[77] J. Müller, K. Kreuer, J. Maier *et al.*, "A conductivity and thermal gravimetric analysis of a y-doped $SrZrO_3$ single crystal," *Solid State Ionics*, vol. 97, no. 1-4, pp. 421–427, 1997.

[78] K. Kreuer, E. Schonherr, and J. Maier, "Proton and oxygen diffusion in BaCeO3 based compounds: A combined thermal gravimetric analysis and conductivity study," *Solid State Ionics*, vol. 70–71, pp. 278–284, 1994.

[79] S. Ricote, N. Bonanos, and G. Caboche, "Water vapour solubility and conductivity study of the proton conductor $BaCe_{0.9-x}Zr_xY_{0.1}O_{3-\delta}$," *Solid State Ionics*, vol. 180, no. 14-16, pp. 990–997, 2009.

[80] I. Ahmed, S. Eriksson, E. Ahlberg *et al.*, "Synthesis and structural characterization of perovskite type proton conducting $BaZr_{1-x}In_xO_{3-\delta}$ ($0.0 \leq x \leq 0.75$)," *Solid State Ionics*, vol. 177, no. 17-18, pp. 1395–1403, 2006.

[81] M. Karlsson, "Perspectives of neutron scattering on proton conducting oxides," *Dalton Transactions*, vol. 42, no. 2, pp. 317–329, 2013.

[82] Z. Révay and T. Belgya, "Principles of the PGAA method," in *Handbook of Prompt Gamma Activation Analysis*, G. L. Molnár, Ed. Boston, MA: Springer US, 2004, pp. 1–30.

[83] R. L. Paul, "Hydrogen Measurement by Prompt Gamma-ray Activation Analysis A Review," *The Analyst*, vol. 122, no. 3, pp. 35R–41R, 1997.

[84] D. L. Anderson and Z. Kasztovszky, "Applications of PGAA with Neutron Beams," in *Handbook of Prompt Gamma Activation Analysis*, G. L. Molnár, Ed. Boston, MA: Springer US, 2004, pp. 137–172.

[85] R. Paul and R. Lindstrom, "Prompt gamma-ray activation analysis: Fundamentals and applications," *Journal of Radioanalytical and Neclear Chemistry*, vol. 243, no. 1, pp. 181–189, 2000.

[86] D. L. Anderson, W. C. Cunnigham, and E. A. Mackey, "Neutron capture prompt-γ activation analysis of foods," *Biological Trace Element Research*, vol. 26–27, no. 1, pp. 613–622, 1990.

[87] D. L. Anderson, W. C. Cunningham, and T. R. Lindstrom, "Concentrations and Intakes of H, B, S, K, Na, Cl, and NaCl in Foods," *Journal of Food Composition and Analysis*, vol. 7, no. 1-2, pp. 59–82, 1994.

[88] D. Anderson, Y. Sun, M. Failey *et al.*, "Neutron-Capture Prompt Gamma-Ray Multielement Analysis of Twenty-Two Geochemical Reference Standards," *Geostandards Newsletter*, vol. 9, no. 2, pp. 219–228, 1985.

[89] D. L. Anderson, G. E. Gordon, and E. A. Lepel, "Analyses of construction materials by neutron-capture prompt γ-ray activation analysis," *Canadian Journal of Chemistry*, vol. 61, no. 4, pp. 724–728, 1989.

[90] C. Y. Jones, J. Wu, L. Li *et al.*, "Hydrogen content in doped and undoped BaPrO3 and BaCeO3 by cold neutron prompt-gamma activation analysis," *Journal of Applied Physics*, vol. 97, no. 11, p. 114908, 2005.

[91] M. Coduri, M. Karlsson, and L. Malavasi, "Structure–property correlation in oxide-ion and proton conductors for clean energy applications: Recent experimental and computational advancements," *Journal of Materials Chemistry A*, vol. 10, no. 10, pp. 5082–5110, 2022.

[92] B. Schwaighofer, M. A. Gonzalez, M. R. Johnson *et al.*, "Ionic Mobility in Energy Materials: Through the Lens of Quasielastic Neutron Scattering," *Chemistry of Materials*, vol. 37, no. 10, pp. 3575–3593, 2025.

[93] R. Hempelmann, "Hydrogen diffusion mechanism in proton conducting oxides," *Physica B: Condensed Matter*, vol. 226, no. 1-3, pp. 72–77, 1996.

[94] C. Karmonik, R. Hempeimann, J. Cook *et al.*, "Investigation of the Proton Migration Mechanism in the perovskite proton conductor $Ba_3Ca_{1.18}Nb_{1.82}H_{0.2}O_{8.83}$ by means of Quasielastic Neutron Scattering," *Ionics*, vol. 2, pp. 69–74, 1996.

[95] N. Malikova, C.-K. Loong, J.-M. Zanotti *et al.*, "Proton-Containing Yttrium-Doped Barium Cerate: A Simultaneous Structural and Dynamic Study by Neutron Scattering," *The Journal of Physical Chemistry C*, vol. 111, no. 17, pp. 6574–6580, 2007.

[96] J. Wallis, A. Kruth, and F. Demmel, "Proton dynamics in a spark-plasma sintered $BaZr_{0.7}Ce_{0.2}Y_{0.1}O_{3-\delta}$ proton conductor investigated by quasi-elastic neutron scattering," *Physical Chemistry Chemical Physics*, vol. 25, no. 18, pp. 13 155–13 163, 2023.

[97] C. Andreani, M. Krzystyniak, G. Romanelli *et al.*, "Electron-volt neutron spectroscopy: Beyond fundamental systems," *Advances in Physics*, vol. 66, no. 1, pp. 1–73, 2017.

[98] J. Wallis, A. Kruth, I. Da Silva *et al.*, "Nuclear dynamics in BaZr0.7 Ce0.2Y0.1O3-δ proton conductor as observed by neutron diffraction and Compton scattering," *Journal of Physics Communications*, vol. 4, no. 4, p. 045004, 2020.

[99] A. Perrichon, E. Jedvik Granhed, G. Romanelli *et al.*, "Unraveling the Ground-State Structure of $BaZrO_3$ by Neutron Scattering Experiments and First-Principles Calculations," *Chemistry of Materials*, vol. 32, no. 7, pp. 2824–2835, 2020.

[100] W. D. Kingery, H. K. Bowen, and D. R. Uhlmann, *Introduction to Ceramics*. John wiley & sons, 1976.

[101] K. S. Randhawa, "A state-of-the-art review on advanced ceramic materials: Fabrication, characteristics, applications, and wettability," *Pigment & Resin Technology*, vol. 53, no. 6, pp. 768–785, 2024.

[102] J. Livage and C. Sanchez, "Sol-gel chemistry," *Journal of Non-Crystalline Solids*, vol. 145, no. C, pp. 11–19, 1992.

[103] A. E. Danks, S. R. Hall, and Z. Schnepp, "The evolution of 'sol-gel'chemistry as a technique for materials synthesis," *Materials Horizons*, vol. 3, pp. 91–112, 2016.

[104] C. J. Brinker and G. W. Scherer, *Sol-Gel Science: The Physics and Chemistry of Sol-Gel Processing*. Gulf Professional Publishing, 1990.

[105] S. Kulkarni, S. Duttagupta, and G. Phatak, "Sol–gel synthesis and protonic conductivity of yttrium doped barium cerate," *Journal of Sol-Gel Science and Technology*, vol. 74, no. 1, pp. 94–102, 2015.

[106] Á. Triviño-Peláez, D. Pérez-Coll, M. Aparicio *et al.*, "Processing and characterisation of $BaZr_{0.8}Y_{0.2}O_{3-\delta}$ proton conductor densified at 1200 °C," *Journal of Materials Chemistry A*, vol. 10, no. 8, pp. 4428–4439, 2022.

[107] Y. Guo, R. Ran, Z. Shao *et al.*, "Effect of Ba nonstoichiometry on the phase structure, sintering, electrical conductivity and phase stability of $Ba_{1\pm x}Ce_{0.4}Zr_{0.4}Y_{0.2}O_{3-\delta}$ proton conductors ($0 \leq x \leq 0.20$)," *International Journal of Hydrogen Energy*, vol. 36, no. 14, pp. 8450–8460, 2011.

[108] Y. Yamazaki, R. Hernandez-Sanchez, and S. M. Haile, "Cation non-stoichiometry in yttrium-doped barium zirconate: Phase behavior, microstructure, and proton conductivity," *Journal of Materials Chemistry*, vol. 20, no. 37, p. 8158, 2010.

[109] Y. Zou and J. Malzbender, "Development and optimization of porosity measurement techniques," *Ceramics International*, vol. 42, no. 2, pp. 2861–2870, 2016.

[110] J.-C. Lee and S.-H. Ahn, "Bulk density measurement of porous functionally graded materials," *International Journal of Precision Engineering and Manufacturing*, vol. 19, no. 1, pp. 31–37, 2018.

[111] S. Singhal, "Solid oxide fuel cells for stationary, mobile, and military applications," *Solid State Ionics*, vol. 152–153, pp. 405–410, 2002.

[112] S. Zarabi Golkhatmi, M. I. Asghar, and P. D. Lund, "A review on solid oxide fuel cell durability: Latest progress, mechanisms, and study tools," *Renewable and Sustainable Energy Reviews*, vol. 161, p. 112339, 2022.

[113] P. Echilin, C. E. Fiori, and J. Goldstein, *Advanced Scanning Electron Microscopy and X-Ray Microanalysis*. Springer Science & Business Media, 2013.

[114] L. Reimer, "Scanning Electron Microscopy: Physics of Image Formation and Microanalysis, Second Edition," *Measurement Science and Technology*, vol. 11, no. 12, pp. 1826–1826, 2000.

[115] B. Steele, "Appraisal of $Ce_{1-y}Gd_yO_{2-y/2}$ electrolytes for IT-SOFC operation at 500°C," *Solid State Ionics*, vol. 129, no. 1-4, pp. 95–110, 2000.

[116] K. Bae, D. H. Kim, H. J. Choi *et al.*, "High-Performance Protonic Ceramic Fuel Cells with 1 µm thick Y:Ba(Ce,Zr)O_3 Electrolytes," *Advanced Energy Materials*, vol. 8, no. 25, p. 1801315, 2018.

[117] K. Vernon-Parry, "Scanning electron microscopy: An introduction," *III-Vs Review*, vol. 13, no. 4, pp. 40–44, 2000.

[118] W. Zhou, R. Apkarian, Z. L. Wang *et al.*, "Fundamentals of Scanning Electron Microscopy (SEM)," in *Scanning Microscopy for Nanotechnology: Techniques and Applications.*, W. Zhou and Z. L. Wang, Eds. New York, NY: Springer New York, 2006, pp. 1–40.

[119] D. C. Joy, *Monte Carlo Modeling for Electron Microscopy and Microanalysis*. Oxford University Press, 1995.

[120] J. Goldstein, D. E. Newbury, J. R. Michael *et al.*, *Scanning Electron Microscopy and X-ray Microanalysis*, fourth edition ed. New York, NY, U.S.A: Springer, 2018.

[121] H. Seiler, "Secondary electron emission in the scanning electron microscope," *Journal of Applied Physics*, vol. 54, no. 11, pp. R1–R18, 1983.

[122] K.-R. Peters, "Generation, collection and properties of an SE-I enriched signal suitable for high resolution SEM on bulk specimens," *Scanning Electron Microscopy*, vol. 1982, no. 1, p. 31, 1982.

[123] D. A. Moncrieff and P. R. Barker, "Secondary electron emission in the scanning electron microscope," *Scanning*, vol. 1, no. 3, pp. 195–197, 1978.

[124] J. I. Goldstein, D. E. Newbury, J. R. Michael *et al.*, *Energy Dispersive X-ray Spectrometry: Physical Principles and User-Selected Parameters.* New York, NY: Springer New York, 2018, pp. 209–234.

[125] D. Bell and A. Garratt-Reed, *Energy Dispersive X-ray Analysis in the Electron Microscope*, 0th ed. Garland Science, 2003.

[126] D. E. Newbury and N. W. M. Ritchie, "Is Scanning Electron Microscopy/Energy Dispersive X -ray Spectrometry (SEM / EDS) Quantitative?" *Scanning*, vol. 35, no. 3, pp. 141–168, 2013.

[127] B. D. Cullity and R. Smoluchowski, "Elements of X-Ray Diffraction," *Physics Today*, vol. 10, no. 3, pp. 50–50, 1957.

[128] V. K. Pecharsky and P. Y. Zavalij, *Fundamentals of Powder Diffraction and Structural Characterization of Materials.* Boston, MA: Springer US, 2005.

[129] A. A. Bunaciu, E. G. Udriştioiu, and H. Y. Aboul-Enein, "X-Ray Diffraction: Instrumentation and Applications," *Critical Reviews in Analytical Chemistry*, vol. 45, no. 4, pp. 289–299, 2015.

[130] W. H. Bragg and W. L. Bragg, "The reflection of X-rays by crystals," *PROCEEDINGS OF THE ROYAL SOCIETY A*, vol. 88, no. 605, pp. 428–438, 1913.

[131] S. R. Khan, B. Sharma, P. A. Chawla *et al.*, "Inductively Coupled Plasma Optical Emission Spectrometry (ICP-OES): A Powerful Analytical Technique for Elemental Analysis," *Food Analytical Methods*, vol. 15, no. 3, pp. 666–688, 2022.

[132] P. J. Goodhew and J. Humphreys, *Electron Microscopy and Analysis THIRD EDITION.* CRC Press, 2000.

[133] T. Hatakeyama and F. X. Quinn, *Thermal Analysis: Fundamentals and Applications to Polymer Science*, 2nd ed. Chichester Weinheim: Wiley, 2000.

[134] M. E. Brown and P. K. Gallagher, *Handbook of Thermal Analysis and Calorimetry.* Amsterdam: Elsevier, 2008.

[135] Z. Shen and S. Fearn, "Back-to-basics tutorial: Secondary ion mass spectrometry (SIMS) in ceramics," *Journal of Electroceramics*, 2024.

[136] T. Grehl, "Improvement in TOF-SIMS Instrumentation for Analytical Application and Fundamental Research," Ph.D. dissertation, Universität Münster, 2003.

[137] S. Fearn, *An Introduction to Time-of-Flight Secondary Ion Mass Spectrometry (ToF-SIMS) and Its Application to Materials Science.* IOP Publishing, 2015.

[138] J. A. Kilner, S. J. Skinner, and H. H. Brongersma, "The isotope exchange depth profiling (IEDP) technique using SIMS and LEIS," *Journal of Solid State Electrochemistry*, vol. 15, no. 5, pp. 861–876, 2011.

[139] R. Chater, S. Carter, J. Kilner *et al.*, "Development of a novel SIMS technique for oxygen self-diffusion and surface exchange coefficient measurements in oxides of high diffusivity," *Solid State Ionics*, vol. 53–56, pp. 859–867, 1992.

[140] G. L. Molnár, *Handbook of prompt gamma activation analysis with neutron beams*. Dordrecht: Kluwer Academic Publishers, 2004.

[141] J. R. Macdonald, "Impedance spectroscopy," *Annals of Biomedical Engineering*, vol. 20, no. 3, pp. 289–305, 1992.

[142] M. Shoar Abouzari, F. Berkemeier, G. Schmitz *et al.*, "On the physical interpretation of constant phase elements," *Solid State Ionics*, vol. 180, no. 14-16, pp. 922–927, 2009.

[143] G. Brug, A. Van Den Eeden, M. Sluyters-Rehbach *et al.*, "The analysis of electrode impedances complicated by the presence of a constant phase element," *J. Electroanal. Chem. Interf. Electrochem.*, vol. 176, no. 1-2, pp. 275–295, 1984.

[144] S. M. Gateman, O. Gharbi, H. Gomes De Melo *et al.*, "On the use of a constant phase element (CPE) in electrochemistry," *Curr. Opin. Electrochem*, vol. 36, p. 101133, 2022.

[145] C. H. Hsu and F. Mansfeld, "Technical Note: Concerning the Conversion of the Constant Phase Element Parameter Y into a Capacitance," *Corrosion*, vol. 57, no. 9, pp. 747–748, 2001.

[146] M. Krzystyniak, M. J. Gutmann, K. Refson *et al.*, "Nuclear quantum dynamics in Hexamethylenetetramine and its deuterated counterpart: A DFT-augmented neutron study," *Physica Scripta*, vol. 98, no. 2, p. 025707, 2023.

[147] M. Krzystyniak, G. Romanelli, and F. Fernandez-Alonso, "Non-destructive quantitation of hydrogen via mass-resolved neutron spectroscopy," *The Analyst*, vol. 144, no. 13, pp. 3936–3941, 2019.

[148] G. B. West, "Electron scattering from atoms, nuclei and nucleons," *Physics Reports*, vol. 18, no. 5, pp. 263–323, 1975.

[149] M. Krzystyniak and C. A. Chatzidimitriou-Dreismann, "A new data treatment scheme for integrated intensities in neutron Compton scattering," *Journal of Physics: Condensed Matter*, vol. 20, no. 10, p. 104249, 2008.

[150] J. Mayers and T. Abdul-Redah, "The measurement of anomalous neutron inelastic cross-sections at electronvolt energy transfers," *Journal of Physics: Condensed Matter*, vol. 16, no. 28, pp. 4811–4832, 2004.

[151] S. Jackson, M. Krzystyniak, A. G. Seel *et al.*, "VESUVIO Data Analysis Goes MANTID," *Journal of Physics: Conference Series*, vol. 571, p. 012009, 2014.

[152] M. T. Telling, *A Practical Guide to Quasi-elastic Neutron Scattering*. Royal Society of Chemistry, 2020.

[153] J. Wind, R. A. Mole, D. Yu *et al.*, "Liquid-like Ionic Diffusion in Solid Bismuth Oxide Revealed by Coherent Quasielastic Neutron Scattering," *Chemistry of Materials*, vol. 29, no. 17, pp. 7408–7415, 2017.

[154] V. F. Sears, "Neutron scattering lengths and cross sections," *Neutron News*, vol. 3, no. 3, pp. 26–37, 1992.

[155] A. VahidMohammadi and Z. Cheng, "Fundamentals of Synthesis, Sintering Issues, and Chemical Stability of $BaZr_{0.1}Ce_{0.7}Y_{0.1}Yb_{0.1}O_{3-\delta}$ Proton Conducting Electrolyte for SOFCs," *Journal of The Electrochemical Society*, vol. 162, no. 8, pp. F803–F811, 2015.

[156] Z. Zhong, X. Xu, Z. Zhang *et al.*, "Microwave sintering of high-performance $BaZr_{0.1}Ce_{0.7}Y_{0.1}Yb_{0.1}O_{3-\delta}$ (BZCYYb) electrolytes for intermediate-temperature solid oxide fuel cells," *International Journal of Hydrogen Energy*, p. S0360319922024934, 2022.

[157] L. Hamze, E. Suard, O. Joubert *et al.*, "Synthesis and temperature dependence of the crystal structure of proton conductor $BaZr_{0.1}Ce_{0.7}Y_{0.1}Yb_{0.1}O_{3-\delta}$ (BZCYYb1711) by combined neutron and X-ray diffraction," *Solid State Ionics*, vol. 417, p. 116682, 2024.

[158] T. Ishiyama, H. Kishimoto, K. Develos-Bagarinao *et al.*, "Decomposition reaction of $BaZr_{0.1}Ce_{0.7}Y_{0.1}Yb_{0.1}O_{3-\delta}$ in carbon dioxide atmosphere with nickel sintering aid," *Journal of the Ceramic Society of Japan*, vol. 125, no. 4, pp. 247–251, 2017.

[159] Z. Zhong, Z. Li, J. Li *et al.*, "A facile method to synthesize $BaZr_{0.1}Ce_{0.7}Y_{0.1}Yb_{0.1}O_{3-\delta}$ (BZCYYb) nanopowders for the application on highly conductive proton-conducting electrolytes," *International Journal of Hydrogen Energy*, vol. 47, no. 94, pp. 40 054–40 066, 2022.

[160] G. Cai, A. E. Phillips, M. G. Tucker *et al.*, "Neutron scattering study of the orientational disorder and phase transitions in barium carbonate," *Journal of Physics: Condensed Matter*, vol. 32, no. 37, p. 374014, 2020.

[161] G. Socrates and G. Socrates, *Infrared and Raman Characteristic Group Frequencies: Tables and Charts*, 3rd ed. Chichester ; New York: Wiley, 2001.

[162] N. Yan, Y. Zeng, B. Shalchi *et al.*, "Discovery and Understanding of the Ambient-Condition Degradation of Doped Barium Cerate Proton-Conducting Perovskite Oxide in Solid Oxide Fuel Cells," *Journal of The Electrochemical Society*, vol. 162, no. 14, pp. F1408–F1414, 2015.

[163] I. Ivanov, D. Tsvetkov, V. Sereda *et al.*, "Temperature- and water-induced structural transformations in $BaZr_{0.1}Ce_{0.7}Y_{0.1}Yb_{0.1}O_{3-\delta}$ proton conducting electrolyte," *Chimica Techno Acta*, vol. 11, no. 4, pp. 202 411 422, 8307, 2024.

[164] L. B. Mccusker, R. B. Von Dreele, D. E. Cox *et al.*, "Rietveld refinement guidelines," *Journal of Applied Crystallography*, vol. 32, no. 1, pp. 36–50, 1999.

[165] G. Caglioti, A. Paoletti, and F. Ricci, "Choice of collimators for a crystal spectrometer for neutron diffraction," *Nuclear Instruments*, vol. 3, no. 4, pp. 223–228, 1958.

[166] P. Thompson, D. E. Cox, and J. B. Hastings, "Rietveld refinement of Debye–Scherrer synchrotron X-ray data from Al_2 O_3," *Journal of Applied Crystallography*, vol. 20, no. 2, pp. 79–83, 1987.

[167] C. Jin, Z. Huizhu, D. Lei *et al.*, "Effect of Ba nonstoichiometry on the phase composition, microstructure, chemical stability and electrical conductivity of $BaZr_{0.1}Ce_{0.7}Y_{0.1}Yb_{0.1}O_{3-\delta}$ ($0.9 \leq x \leq 1.1$) proton conductors," *Ceramics International*, vol. 41, no. 6, pp. 7796–7802, 2015.

[168] J. D. Menczel and R. B. Prime, *Thermal Analysis of Polymers: Fundamentals and Applications*. Hoboken, N.J: John Wiley, 2009.

[169] International Atomic Energy Agency, Ed., *Database of Prompt Gamma Rays from Slow Neutron Capture for Elemental Analysis*. Vienna: International Atomic Energy Agency, 2007.

[170] Z. Révay, "Determining Elemental Composition Using Prompt γ Activation Analysis," *Analytical Chemistry*, vol. 81, no. 16, pp. 6851–6859, 2009.

[171] L. Szentmiklósi, Z. Révay, J. Östör *et al.*, "Improved analytical workflow for prompt gamma activation analysis," *Journal of Radioanalytical and Nuclear Chemistry*, vol. 333, no. 7, pp. 3325–3333, 2024.

[172] E. B. Karlsson, C. A. Chatzidimitriou-Dreismann, T. Abdul-Redah *et al.*, "Anomalous neutron Compton scattering in Nb hydride: Indications of proton correlations," *Europhysics Letters (EPL)*, vol. 46, no. 5, pp. 617–623, 1999.

[173] E. M. Schooneveld, J. Mayers, N. J. Rhodes *et al.*, "Foil cycling technique for the VESUVIO spectrometer operating in the resonance detector configuration," *Review of Scientific Instruments*, vol. 77, no. 9, p. 095103, 2006.

[174] X. Yang, L. Jia, B. Pan *et al.*, "Mechanism of Proton Conduction in Doped Barium Cerates: A First-Principles Study," *Journal of Physical Chemistry C*, vol. 124, no. 14, pp. 8024–8033, 2020.

[175] G. L. Squires, *Introduction to the Theory of Thermal Neutron Scattering*, 3rd ed. Cambridge: Cambridge University Press, 2012.

[176] B. Groß, C. Beck, F. Meyer *et al.*, "$BaZr_{0.85}Me_{0.15}O_{2.925}$ (Me = Y, In and Ga): Crystal growth, high-resolution transmission electron microscopy, high-temperature X-ray diffraction and neutron scattering experiments," p. 7, 2001.

[177] M. Pionke, T. Mono, W. Schweika *et al.*, "Investigation of the hydrogen mobility in a mixed perovskite: $Ba[Ca_{(1+x)/3}Nb_{(2-x)/3}]O_{3-x/2}$ by quasielastic neutron scattering," *Solid State Ionics*, vol. 97, no. 1-4, pp. 497–504, 1997.

[178] D. Wilmer, T. Seydel, and K.-D. Kreuer, "Proton Diffusion in Hydrated Acceptor-Doped Barium Zirconate," *MRS Proceedings*, vol. 972, pp. 0972–AA01–04, 2006.

[179] M. Karlsson, I. Ahmed, A. Matic *et al.*, "Short-range structure of proton-conducting $BaM_{0.10}Zr_{0.90}O_{2.95}$ (M=Y, In, Sc and Ga) investigated with vibrational spectroscopy," *Solid State Ionics*, vol. 181, no. 3-4, pp. 126–129, 2010.

[180] R. J. Newport, B. D. Rainford, R. Cywinski *et al.*, "Neutron Scattering at a Pulsed Source," *Physics Today*, vol. 42, no. 10, pp. 127–128, 1989.

[181] M. Karlsson, "Proton dynamics in oxides: Insight into the mechanics of proton conduction from quasielastic neutron scattering," *Physical Chemistry Chemical Physics*, vol. 17, no. 1, pp. 26–38, 2015.

[182] H. H. Paalman and C. J. Pings, "Numerical Evaluation of X-Ray Absorption Factors for Cylindrical Samples and Annular Sample Cells," *Journal of Applied Physics*, vol. 33, no. 8, pp. 2635–2639, 1962.

[183] O. Arnold, J. Bilheux, J. Borreguero *et al.*, "Mantid—Data analysis and visualization package for neutron scattering and μ SR experiments," *Nuclear Instruments and Methods in Physics Research Section A: Accelerators, Spectrometers, Detectors and Associated Equipment*, vol. 764, pp. 156–166, 2014.

[184] F. Akeroyd, S. Ansell, S. Antony *et al.*, "Mantid: Manipulation and Analysis Toolkit for Instrument Data." Mantid Project, 2013.

[185] S. NaraseGowda, C. M. Brown, M. Tyagi *et al.*, "Quasi-Elastic Neutron Scattering Studies of Hydrogen Dynamics for Nanoconfined $NaAlH_4$," *The Journal of Physical Chemistry C*, vol. 120, no. 27, pp. 14 863–14 873, 2016.

[186] T. Tominaga, M. Sahara, Y. Kawakita *et al.*, "Evaluation of sample cell materials for aqueous solutions used in quasi-elastic neutron scattering measurements," *Journal of Applied Crystallography*, vol. 54, no. 6, pp. 1631–1640, 2021.

[187] C. T. Chudley and R. J. Elliott, "Neutron Scattering from a Liquid on a Jump Diffusion Model," *Proceedings of the Physical Society*, vol. 77, no. 2, pp. 353–361, 1961.

[188] P. L. Hall and D. Ross, "Incoherent neutron scattering functions for random jump diffusion in bounded and infinite media," *Molecular Physics*, vol. 42, no. 3, pp. 673–682, 1981.

[189] D. Klotz, A. Weber, and E. Ivers-Tiffée, "Practical Guidelines for Reliable Electrochemical Characterization of Solid Oxide Fuel Cells," *Electrochimica Acta*, vol. 227, pp. 110–126, 2017.

[190] M. Schönleber, D. Klotz, and E. Ivers-Tiffée, "A Method for Improving the Robustness of linear Kramers-Kronig Validity Tests," *Electrochimica Acta*, vol. 131, pp. 20–27, 2014.

[191] M. Schönleber and E. Ivers-Tiffée, "Approximability of impedance spectra by RC elements and implications for impedance analysis," *Electrochemistry Communications*, vol. 58, pp. 15–19, 2015.

[192] D. A. Harrington and P. Van Den Driessche, "Mechanism and equivalent circuits in electrochemical impedance spectroscopy," *Electrochimica Acta*, vol. 56, no. 23, pp. 8005–8013, 2011.

[193] J. T. S. Irvine, D. C. Sinclair, and A. R. West, "Electroceramics: Characterization by Impedance Spectroscopy," *Advanced Materials*, vol. 2, no. 3, pp. 132–138, 1990.

[194] V. Vivier and M. E. Orazem, "Impedance Analysis of Electrochemical Systems," *Chemical Reviews*, vol. 122, no. 12, pp. 11 131–11 168, 2022.

[195] J. Crank, *The Mathematics of Diffusion*. Oxford University Press, 1979.

[196] F. Bagioni, E. Mercadelli, A. Bartoletti *et al.*, "Synthesis strategies for BaCe0.7Zr0.1Y0.1Yb0.1O3- for the development of high-conducting solid oxide cell electrolyte," *International Journal of Hydrogen Energy*, vol. 193, p. 152384, 2025.

[197] D. Clark, J. Tong, A. Morrissey *et al.*, "Anomalous low-temperature proton conductivity enhancement in a novel protonic nanocomposite," *Phys. Chem. Chem. Phys.*, vol. 16, no. 11, pp. 5076–5080, 2014.

[198] T. C. Allison, "NIST-JANAF Thermochemical Tables - SRD 13," 2013.

[199] M. Mogensen, N. M. Sammes, and G. A. Tompsett, "Physical, chemical and electrochemical properties of pure and doped ceria," *Solid State Ionics*, vol. 129, no. 1-4, pp. 63–94, 2000.

[200] Z. Wang, Z. Luo, H. Xu *et al.*, "New Understanding and Improvement in Sintering Behavior of Cerium-Rich Perovskite-Type Protonic Electrolytes," *Advanced Functional Materials*, vol. 34, no. 38, p. 2402716, 2024.

[201] A. Züttel, "Materials for hydrogen storage," *Materials Today*, vol. 6, no. 9, pp. 24–33, 2003.

[202] M. R. Usman, "Hydrogen storage methods: Review and current status," *Renewable and Sustainable Energy Reviews*, vol. 167, p. 112743, 2022.

[203] K. Tsujikawa, J. Hyodo, S. Fujii *et al.*, "Mitigating proton trapping in cubic perovskite oxides via ScO_6 octahedral networks," *Nature Materials*, 2025.